Kuwait J.Sci., Vol.50, No.(1B),January.2023,pp(1-18)

Applications of well logging techniques to evaluate the groundwater aquifers in the area between southwest Bani Sweif and west Asyoute governorate, upper Egypt

Safi Eldein.M. Metwally [1], Shimaa. M. Elska [1, *], Fardous. M. Zarif [1], Abdallah. F. Saad [2]

[1] *Dept. of geophysical exploration, Desert Research Center, Cairo, Egypt*
[2]*Dept of Physics., Faculty of Science, Zagazig University, Zagazig, Egypt*

**Corresponding author: Shimaa_Elska@yahoo.com*

Abstract

The relevance of detecting aquifer characterization and aquifer potential has risen with the application of well logging technique as the demand for water has increased. Apart from pumping data, 16 geophysical well logs (resistivity, gamma ray, self-potential, and nuclear logs) are utilized to achieve the main goal of estimating petrophysical parameters (porosity (∅), effective porosity ($\emptyset_{eff}$), hydraulic conductivity (k), permeability (K) and shale volume (V_{sh})) of the Apollonia (Eocene fractured limestone aquifer), Upper and Lower Bahariya (Nubian sandstone aquifer) formations. The findings show that the Eocene fractured limestone aquifer has a carbonate in soft chalk with high K and ∅ as well as high k of 4974.39 mD at well ST-188 (a highly productive aquifer), whereas the Lower Bahariya formation is mostly fine to medium-grained sandstone and clay, suggesting that it formed in shallow marine environments with low K. On the other hand, Upper Bahariya was noted that having poor sand succession. As results shown, K of the most examined wells range from 2609.69 to 1486.812 mD at ST-258 and ST-38 wells respectively. The study appears that V_{sh}, such as ∅ and K parameters, is regarded as an important attribute in aquifer evaluation where, estimated V_{sh} over the studied area is ranges between 5.96% and 31.7% at ST-48 and WBS1 wells respectively. Overall, this study provides an important insight into the importance of evaluating groundwater aquifers over time to help in making decisions to save and protect groundwater aquifers in the future for sustainable development.

Keywords: Bahariya formation; gamma; groundwater; neutron; Egypt

1. Introduction

Egypt is classed as a water-scarce country, despite its strategic location. It has a serious and long-standing water shortage, which might obstruct its economic growth (World Bank, 2018). The study area has been exposed to substantial deep groundwater extraction over the past three years as one of the new targeted reclamation areas. As a result, aquifer (s) appraisal as a dependable supply of water for agricultural and industrial sustainable development is urgently needed in such field region (Nisar *et al*., 2021). Geophysical well logging is the most important method for determining

subsurface petrophysical parameters, allowing researchers as Twfiq *et al*., (2021); and Zainab *et al*., (2019) to maximize field exploitation.

Little is known about the study area's aquifer, and its unclear what metrics are used to determine groundwater sustainability. Herein lies the significance of the current study, the primary purpose of which is to learn more about groundwater potential in various zones, as well as its lithological, petrophysical, and hydraulic properties. This was done by the examination and interpretation of all available geophysical well logs (nuclear logs, gamma ray, self-potential, and resistivity), as well as hydrogeological data. Consequently, evaluation of deep groundwater aquifers relates to the determination of aquifer properties such as porosity (∅), effective porosity ($\emptyset_{eff}$), hydraulic conductivity (k), permeability (K) and shale volume (V_{sh}) (Farrag *et al.,*2019).

2. Study area and geological setting

The investigated area is located between Southwest Bani Sweif and West Asyoute in the western desert fringes of the North part of Upper Egypt (Figure 1).

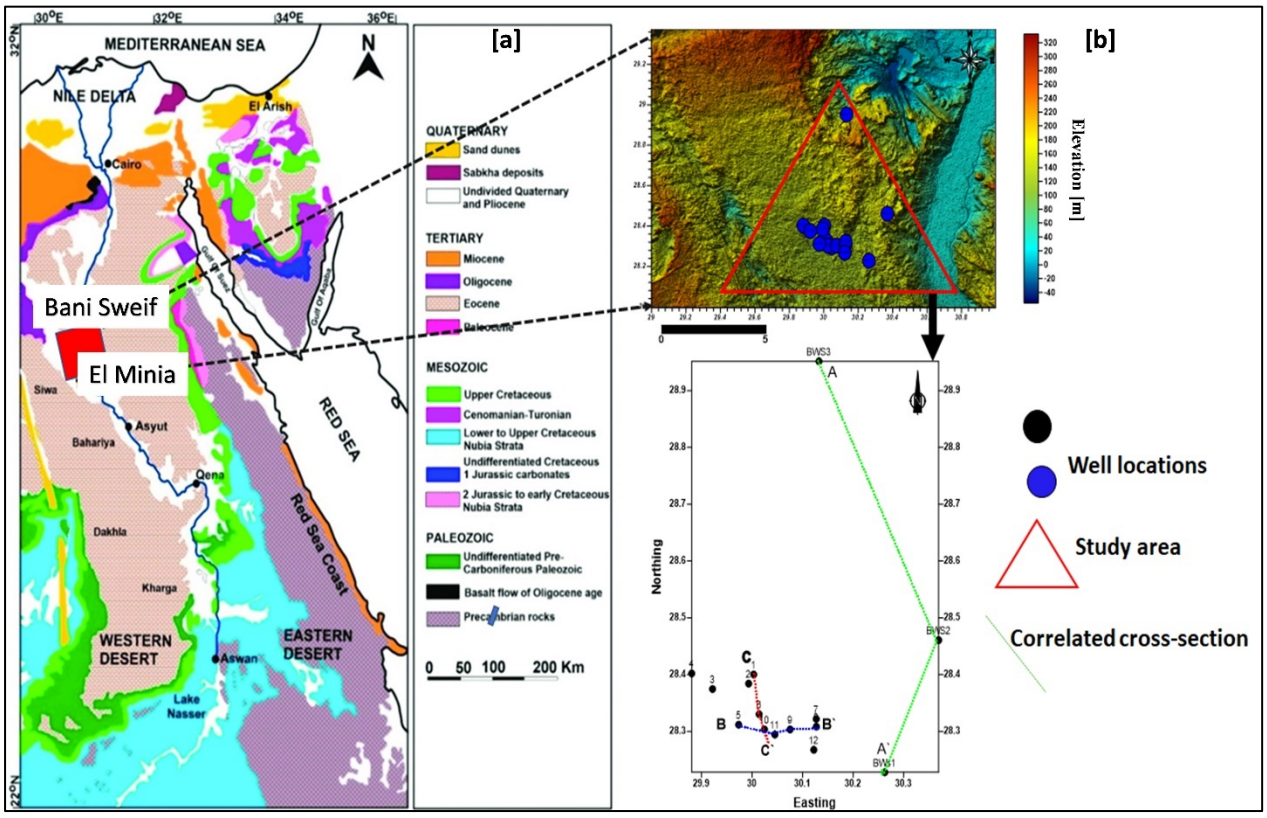

Fig.1. [a] a geological map with the location of study area modified after (Conoco,1987), [b]; a digital elevation map [DEM] of the study area with well locations

According to Yousif *et al*., (2018), the study area has four geomorphological units: tableland, floodplain (gravely, silt, and sandy plain), isolated hills, and a sand dunes belt (Figure 3). The Middle Eocene limestone aquifer, which is composed of the Samalut deposit (chalky

limestone with thin clay intercalations), was identified as a water-bearing structure (Al-Ruwain, 1996). There were also several lithological units spanning in age from the Middle Eocene to the Quaternary (Figure 4). The study area is influenced by a network of faulting systems (NW-SE). These faults have a significant impact on the occurrences of groundwater aquifers in this region (Yousif *et al*., 2018). Figure (4) depicts a composite log tapped into West El Minia's shallow Bahariya aquifer in the Western Desert. The Bahariya Formation is classified into upper and lower units, and is mostly composed of fine to medium sandstone and clay (Wehr *et al*., 2002). The pre-Cambrian basement, a Cretaceous sequence that comprises the majority of the stratigraphic succession across the studied region, and the Apollonia formation, which is followed by Oligocene shales of the El Dabaa formation, make up the stratigraphy of the investigated area (Makky *et al*., 2014).

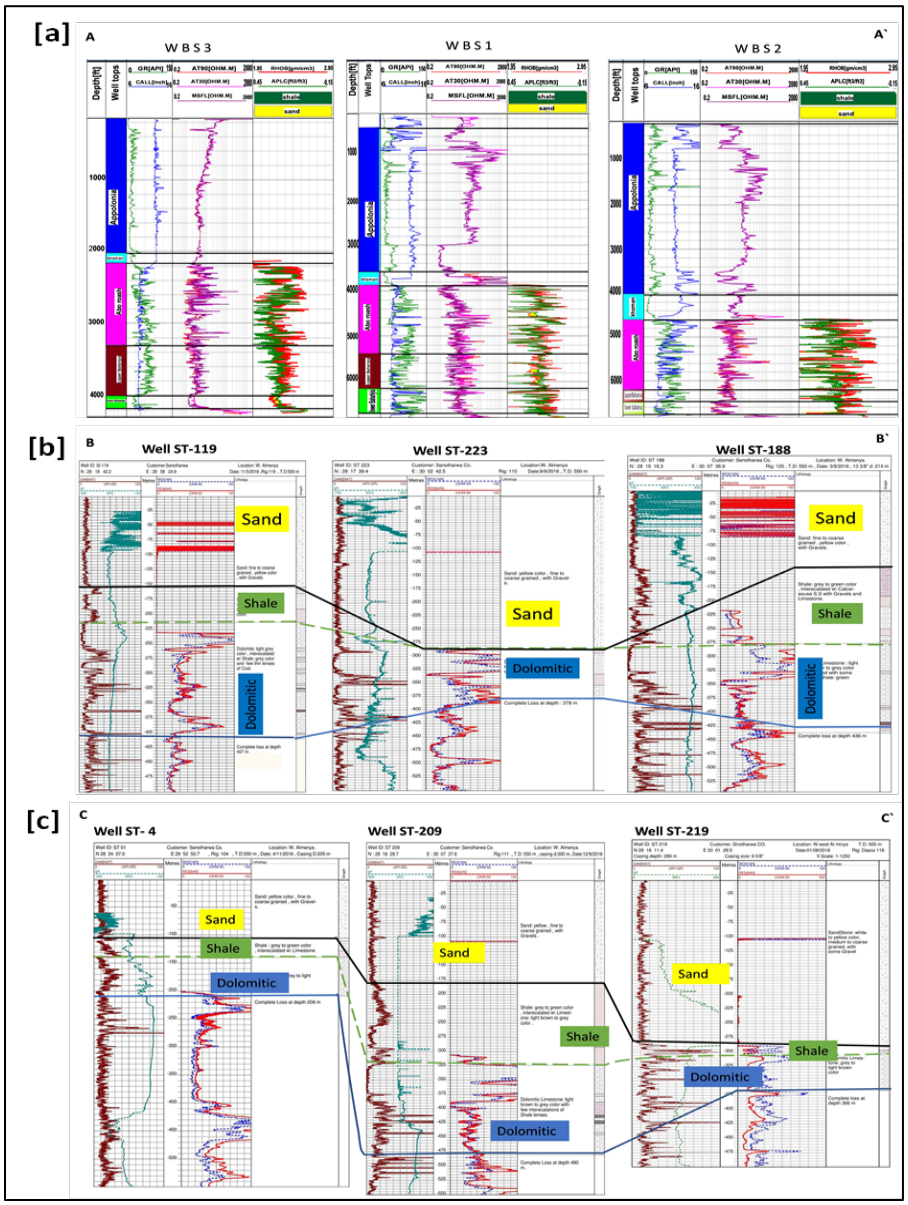

Fig. 2. Correlations among the tending well logs cross sections AA`, BB` and CC`

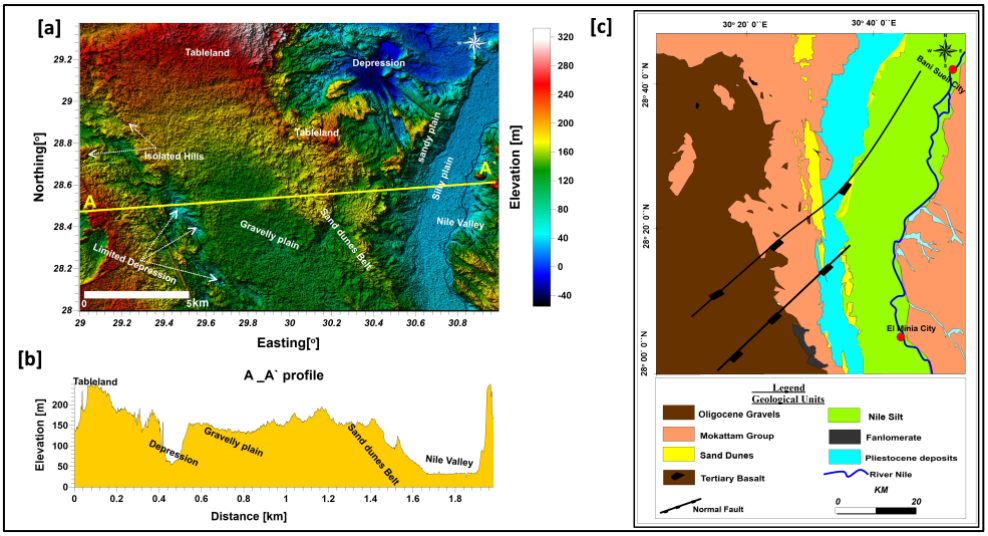

Fig. 3. (a) Geomorphology map of study area, (b) Geomorphic unit crossing study area along A-A` profile, (c) Geological unit of study area.

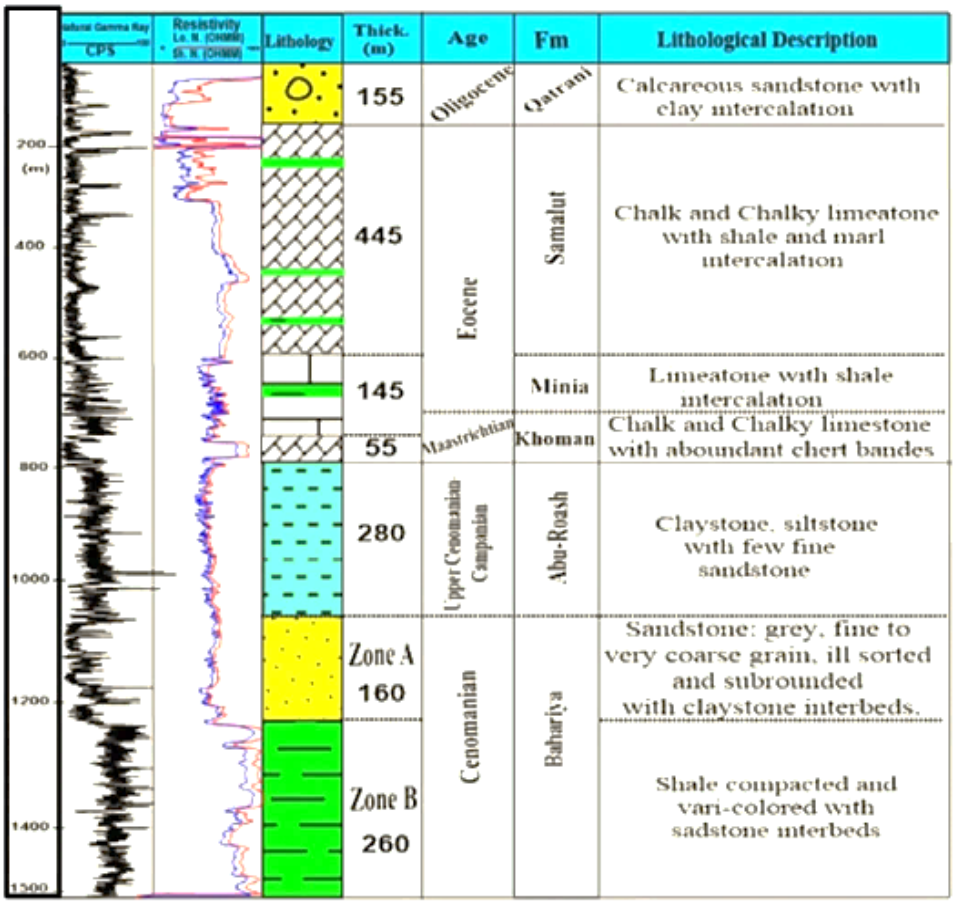

Fig. 4. Composite log tapping shallow Bahariya aquifer of west El Minia (Yousif *et al*., 2018)

3. Materials and methods

3.1 Data Acquisition

Sixteen Well logs were collected and depicted in Table (1). Some wells are correlated to demonstrate the subsurface stratigraphic strata (Figure 2) in the investigated area. The analysis of these well logs and 13 pumping test data were used to estimate the petrophysical and hydraulic parameters of the study aquifers.

Table 1. Available data for the study area

No	*name*	*Available data*
1	WBS 1	Density (RHOB), neutron (APLC), gamma ray (GR), resistivity (AT60-AT30-AT90), caliper (CAL), sonic (DT) logs
2	WBS 2	
3	WBS 3	
4	ST-13	GR, SP, long normal resistivity R46, short normal resistivity R16
5	ST -209	
6	ST-118	
7	ST-38	
8	ST-48	
9	ST119	
10	ST-180	
11	ST-188	
12	ST-214	
13	ST-223	
14	ST-258	
15	ST-1	
16	ST-219	

3.2. Data processing and interpretation

Well logs are collected in form of soft copies (Las files) and hard copies. To give a more realistic and accurate formation evaluation, the data of hard copies was digitized and stored in data files using the Golden Software Didger (V. 2.23) at depth intervals (0.5m in deep wells to 2m in shallow wells) and interactive petrophysics^{TM} (IP) software (http://www.senergyltd.com) was used to integrate all available data to understand and compute the input of the different petrophysical parameters. Self-potential, resistivity and gamma-ray logging curves were investigated in well logging data, with an emphasis on nuclear logs (density and neutron). The geophysical well logs are critical for determining the depth and thickness of viable zones as calculated aquifer characteristic (Shalaby, 2021; and Farrag *et al*.,2019).

3.2.1. Lithology identification

The lithology is determined from cross plots methods of the neutron-density, neutron-sonic, and M-N cross-plots.

3.2.2. Petrophysical parameters estimation

3.2.2.1. Shale volume

V_{sh} percentage is estimated from Gamma ray (GR) log by using equation of Schlumberger (1997):

$$V_{sh} = O.5 * I_{GR}/(1.5 - I_{GR}) \quad (1)$$

$$I_{GR} = \frac{GR_{log} - GR_{min}}{GR_{max} - GR_{min}} \quad (2)$$

Where (I_{GR}) is gamma ray index, GR_{log} is the gamma ray log reading, GR_{min}, GR_{max} are the minimum and the maximum gamma ray reading.

The GR logs could discriminate between clean aquifer and poor one using shale base lines and identify the zone of water bearing. In these cases, the GR values in the water-bearing zones for studied well logs range from 120 American Petroleum Institute (API) in ST-119 well to150 API in WBS 3 well.

3.2.2.2. Porosity (∅): -

It can be calculated from neutron or density logs where ∅ equal to neutron logs reading or from density logs ($\emptyset_D$) by using the following equation of Asquith and Gibson (1982).

$$\emptyset_D = \frac{\rho_{ma} - \rho_b}{\rho_{ma} - \rho_f} \quad (3)$$

Where ρ_{ma} is matrix density, ρ_b is (bulk density) density log value, (ρ_f) is fluid density=1 g/cm^3 and from resistivity logs by using Archie´s formula (1942):

$$F = a * \emptyset^{m} \quad (4)$$

Where, a is a constant =1; F formation factor= $R_t R_w$and m is a constant called cementation factor = 2 (empirically)

$$\emptyset = (1/(R_t/R_w)\ \text{^}1/2 \quad (5)$$

Where (R_t) is true resistivity in ohm m, and it obtained from comparing between long normal resistivity (R_{long}) and short normal resistivity (R_{short}) (Schlumberger ,1997)

$R_t = 1.7R_{long} - 0.7R_{short}$ (If R_{long}>R_{short}) (6)

and R_w is a formation water resistivity in ohm m which can be calculated from electrical resistivity (R) logs

$R_w = (R_{mf} \times R_t)/R_{short}$ (7)

Where, R_{mf} is mud filtrate resistivity and R_t is the true resistivity which was estimated from R_{long} and R_{short} curves.

3.2.2.3. Effective Porosity ($\emptyset_{eff}$):

It's calculated from the following equation (Schlumberger, 1997)

$\emptyset_{eff} = \emptyset * (1 - V_{sh})$ (8)

3.2.2.4. Hydraulic conductivity (*K*)

K calculates from $\emptyset_{eff}$ due to Schlumberger, (1997) by the following equation

$\emptyset_{eff} = 0.462 + 0.045lnK$ (9)

3.2.2.5. The permeability (K)

K calculates from ∅ based on Timur (1968) formula:

$K\text{^}1/2 = 100 * \emptyset^{2.25} / S_{wirr} * 1000$ (10)

Where $S_{wirr}$is irreducible water saturation=5.2297 ∅

The water saturation (s_w) in the study area is~1. The depth to water (water bearing zone) can measure at specific depth based on R_t of induction log, SP, ∅ of density and neutron logs and Gamma ray log responses.

3.3. Pumping test

Firstly, the water level was monitored directly 2 hours before the pumping test was performed. The transmissivity will be estimated from specific capacity (Q/s) based on 13 pumping and recovery tests (Verbovsek, 2008).

T = C (Q/s). (11)

Where T is transmissivity m^2/day, Q/s is specific capacity m^3/day/m and C is constant at 0.9:1.5 value and an average of 1.2 (Jalludin and Razack, 2004). With the use of GWW software, T, *k*, and storage coefficient S were calculated using the Theis method (1935).

4. Results and discussion

The petrophysical properties of the Nubian sandstone aquifer were elucidated by the well-logging study. A variety of cross plots were created and interpreted. The Eocene carbonate aquifer was assessed using the standard archie (1942) and schlumberger (1997) equations.

4.1. Apollonia formation Evaluation

Due to the shortage of neutron, sonic, and density log recordings. The following contour maps will be depended mainly on the above equations. Figure (5a) shows the distribution of depth to Apollonia waterbearing that increases in south and south east direction. Figure (5b) depicts the water level contour map which displays that water level values range from 8m to - 259m. The water flow direction is towards the southwest direction where the recharge source is the Nile valley where, Figure (5c) represents the distribution of porosity ($\emptyset$) which increases in the south and southeast of the study area, reaching a maximum of 46.96 % at ST-258 well and a minimum of 18.31 % at ST-38 well. Estimated effective porosity ($\emptyset_{eff}$) over the study area is shown in (Figure 5d), which shows the similar trend of ($\emptyset$). Table (2) summarized the estimated petrophysical parameters for Eocene carbonate aquifer. The permeability contour map is depicted in Figure (5e). It increases in the south and east directions, where it has a high value of 2609.69 mD at ST-258 well, and decreases in the southwest direction, where the minimum value is 1486.81 mD at ST-38 well. The hydraulic conductivity contour map (Figure.5f) has the same trend of permeability distribution. Iso resistivity contour map is shown in Figure (5g). The resistivity values are increase in west and northwest direction with maximum value 138. 89 Ohm.m at well ST-19. The results show also the distribution of V_{sh} Figure (5h) which increases towards east and northeast direction (Nile valley direction). The low V_{sh}% meaning that Apollonia formation is mainly carbonate rocks with little intercalation of shale.

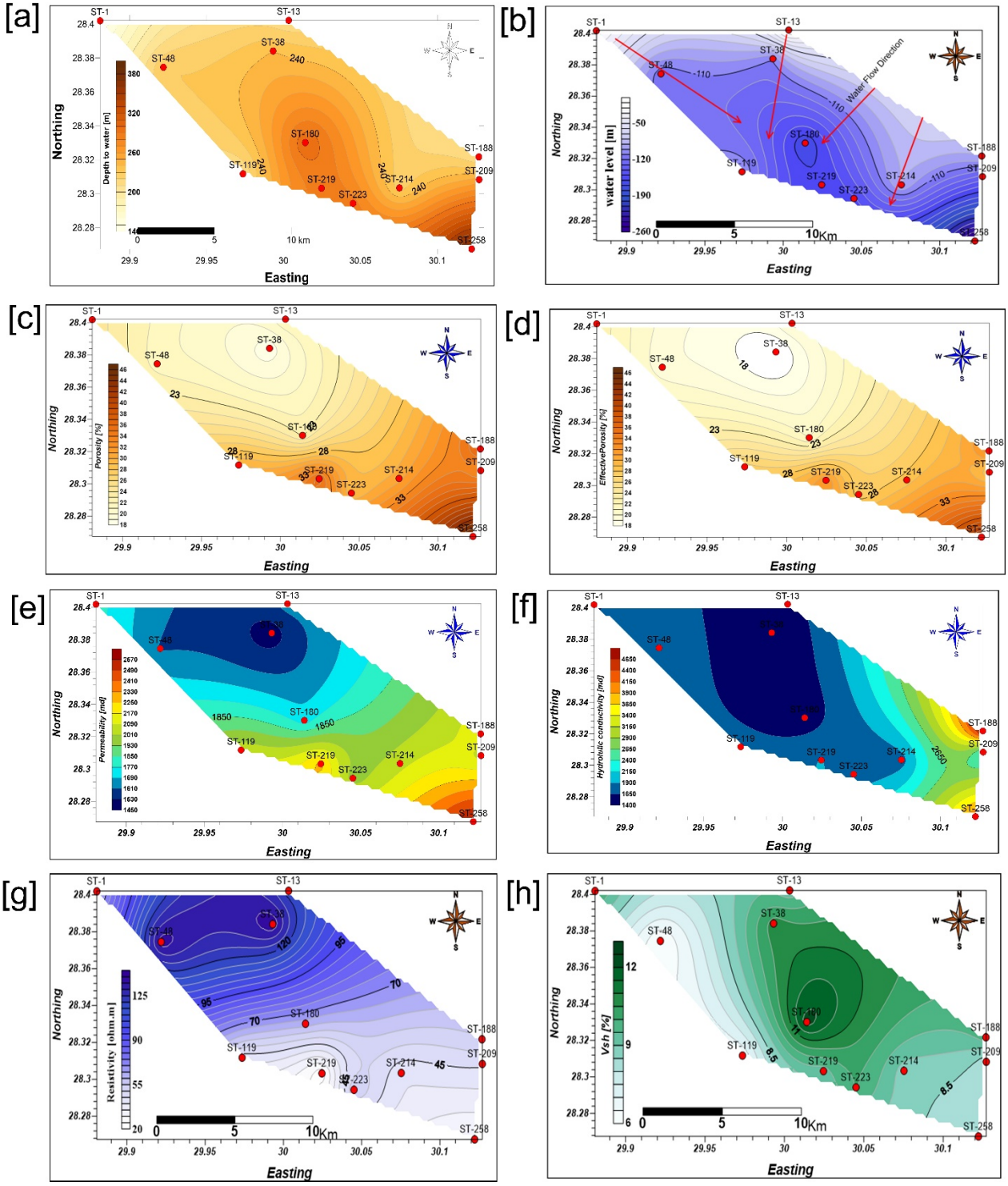

Fig. 5. [a] depth to water. [b] water level. [c] porosity, [d] effective porosity, [e] permeability [f] hydraulic conductivity, [g] Isoresistivty and [h] shale volume percentage contour maps for Apollonia formation.

The estimated V_{sh} of the studied wells (Figures. 6a & b) demonstrate that Apollonia and Upper Bahariya formations are classified as clean aquifers have low shale content. The Apollonia Formation's shale volume was shown in Figure (6a). It reveals that the formation has the least amount of shale, followed by the upper and lower Bahariya formations in decreasing depth order (Figure.6b). The average V_{sh} values for the three formations are 8%, 20%, and 26 %, respectively.

Table 2. Summarized petrophysical parameters of geophysical well logs:

Well	Aquifer	Coordinate N	E	Total thickness(m)	Total depth (m)	Depth to water(m)	water level(m)	Ø (%)	$Ø_{eff}$(%)	k (mD)	k (mD)	V_{sh}(%)
WBS1	UPPER	30.2623	28.2279	99.3648	2072.64	1644.0912	*	21.721	14.9232	1695.4956	1348.8905	31.5812
WBS2	BAHARIYA	30.3690	28.4607	82.6008	2103.12	1892.5032	*	17.903601	17.7547	3087.6849	1523.8235	14.7649
WBS3		30.1324	28.9517	214.2744	1310.64	1009.1928	*	27.9716	18.1721	1878.5813	1345.0364	31.0552
WBS1	LOWER	30.2623	28.2279	302.3616	2072.64	1743.456	*	24.536	13.2508	1585.3528	1310.1223	32.0335
WBS2	BAHARIYA	30.3690	28.4607	86.8395	2103.12	1975.104	*	19.39167	17.5610	1964.3312	1440.1947	26.0592
WBS3		30.1324	28.9517	53.0352	1310.64	1223.4672	*	24.7386	18.0292	1750.9523	1460.8821	22.9095
WBS1		30.2623	28.2279	963	2072.64	102	37.68	*	*	*	*	5.0433
WBS2		30.3690	28.4607	1189	2103.12	129	44	*	*	*	*	4.9527
WBS3		30.1324	28.9517	618	1310.64	108.32	38.28	*	*	*	*	12.0628
ST13		30.0033	28.4022	365	580	98.95	33.05	22.04855	20.3482	1647.970	1528.0260	9.1357
ST38		29.9932	28.3841	305	550	96.74	34.26	18.30979	16.5387	1486.817	1397.3693	10.7701
ST48		29.9219	28.3745	280	540	80.48	32.52	21.50817	19.3537	1604.814	1902.4103	5.9646
ST1	APOLLONIA	29.8807	28.4019	348	550	91.9	35.1	24.79189	22.7151	1804.375	1622.8801	10.1588
ST119		29.9736	28.3117	270	500	76.9	33.1	30.02235	27.3983	2064.033	1737.3048	6.5722
ST180		30.0141	28.3301	170	500	97.4	33.6	22.80661	20.9547	1725.351	1521.9702	12.264
ST188		30.1269	28.3217	325.5	550	85.4	34.6	36.74754	33.0401	2165.998	4974.3917	9.7705
ST209		30.1271	28.3083	245	550	85.21	35.79	32.60873	27.9922	2060.183	2254.0058	8.1773
ST214		30.0753	28.3034	275.5	500	99.69	36.31	30.6382	28.4832	2064.033	1785.2611	8.7479
ST219		30.0246	28.3032	210	530	88.15	36.85	35.50314	32.0514	2275.824	1912.2649	9.2288
ST223		30.0451	28.2943	325	550	97.2	35.8	29.03656	27.3328	1970.151	1784.8808	10.0485
ST258		30.1222	28.2674	233.172	700	83.25	37.75	46.96442	42.56449	2609.695	4171.2785	8.4168

* No data, mdarcy (mD), Porosity (Ø), Effective Porosity (Øeff), permeability(k), hydraulic conductivity(k), Shale Volume $\boldsymbol{V_{sh}}$

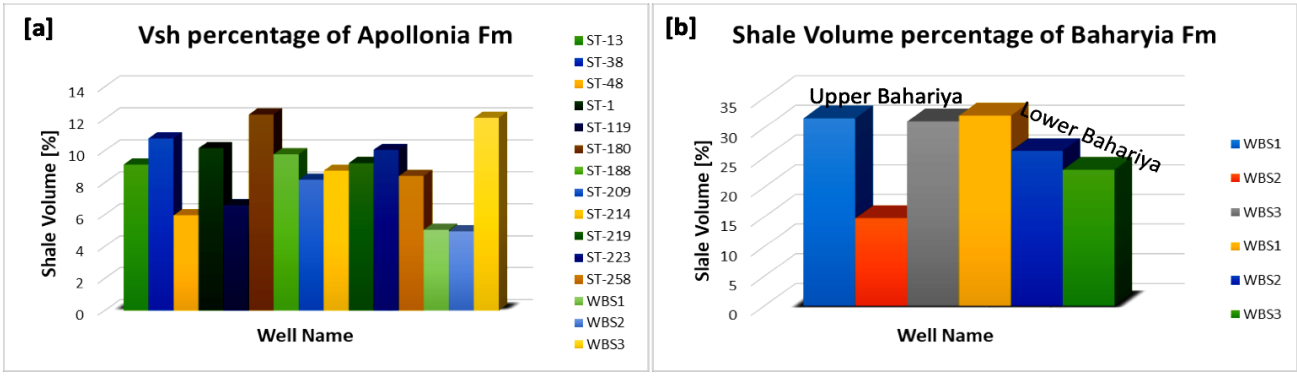

Fig. 6. Clustered column for [a] percentage of shale volume of Apollonia Fm of available wells, [b] the percentage of shale volume of upper and lower Bahariya Fm for three deep wells.

4.2. Bahariya formation evaluation

The Nubian sandstone aquifer was evaluated using the derived petrophysical characteristics. Figure (7) illustrates the findings of the neutron density cross plot, which demonstrates how groundwater affects the plotted data as it migrates northwestern from the limestone line. A drop in the phi neutron ($\emptyset_N$) and a rise in the phi density ($\emptyset_D$) are both signs of this phenomenon. The highest ($\emptyset_D$) for the upper Bahariya formation is 0.45 at well WBS1 (Figure.7a) and the lowest is 0.0038 at well WBS3 (Figure.7c). At well WBS1 (Figure.7a), the highest ($\emptyset_N$) is 0.451, while the minimum is 0.093 (Figure.7b). Due to the movement of displayed data toward the southwest of the cross plot, the shale impact in WBS3 is higher than in WBS1 and WBS2.

The lower Bahariya formation's highest ($\emptyset_D$) is 0.4478 at well WBS1 (Figure.7a), while the lowest ($\emptyset_D$) is 0.000645 at well WBS2 (Figure.7b). In addition, the highest ($\emptyset_N$) for the lower Bahariya formation is 0.447 at well WBS1 (Figure.7a), while the minimum ($\emptyset_N$) is 0.067 at well WBS2 (Figure.7b). It was discovered that shale affects WBS2 more than WBS1 and WBS3 wells.

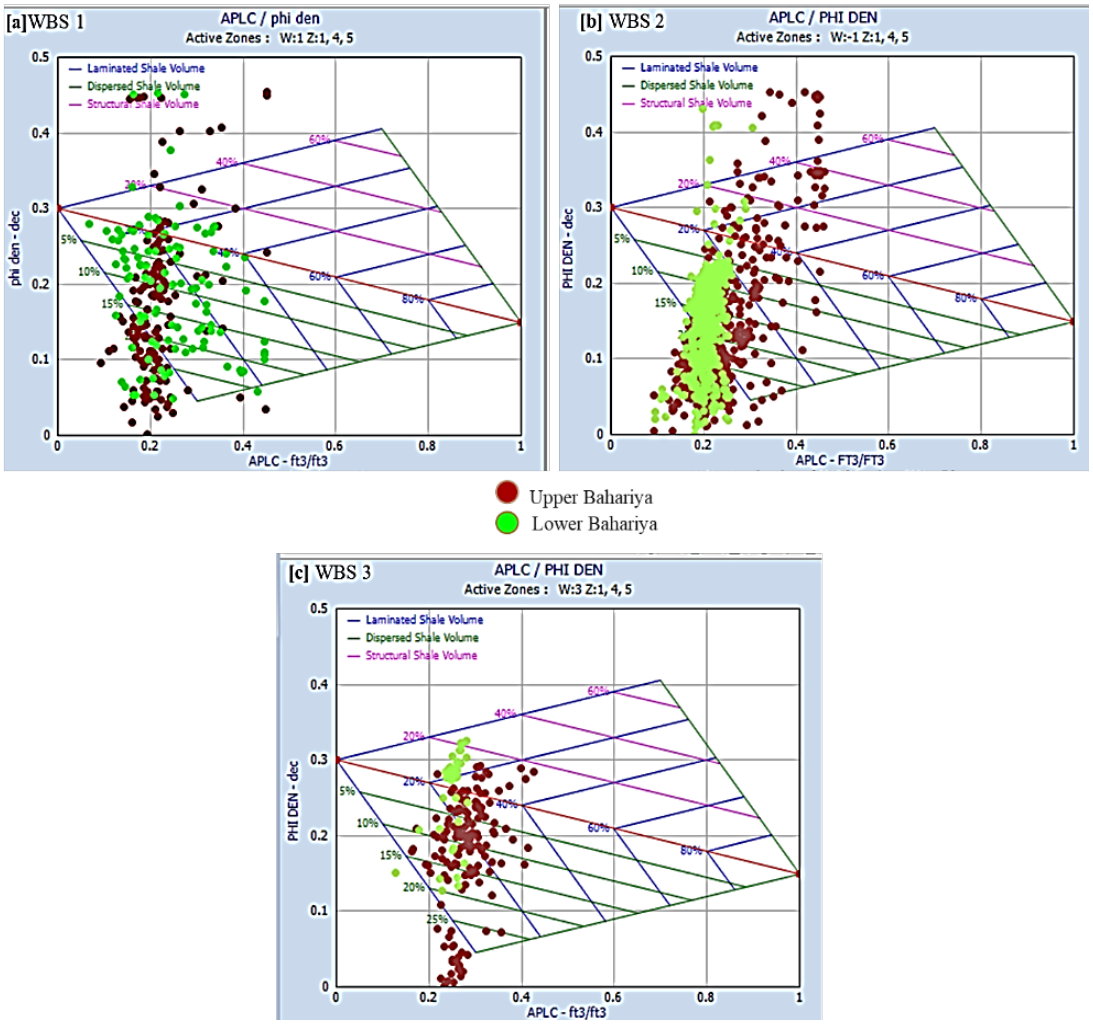

Fig. 7. Shale type cross plot of upper and lower Bahariya formation; [a] WBS 1, [b]; WBS 2 and [c]; WBS 3 wells.

Figure (8) depicts the relationship between GR and $\emptyset_N$ in terms of energy (APLC). This cross plot shows that the presence of limestone and dolomite is indicated by low GR and low (APLC) points. Sandstone rock units are indicated by medium GR and medium APLC points, whereas shale is indicated by high GR and high APLC points. The WBS1 at figure (8a) exhibits a moderate GR and APLC for the upper and lower Bahariya formations, indicating that the lithology of this formation is mostly sandstone.

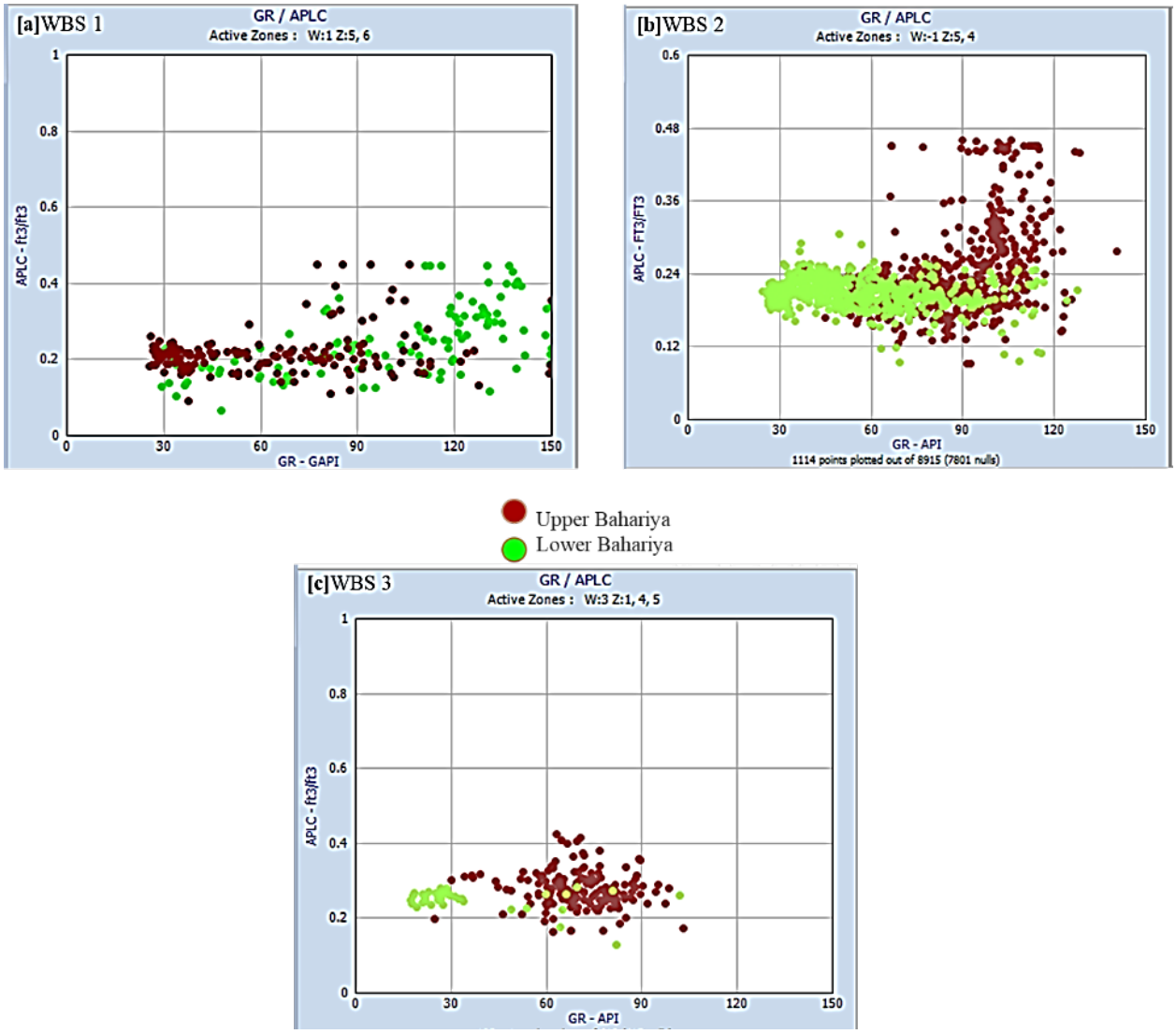

Fig. 8. GR- APLC cross plot [a]; WBS 1 [b]; WBS 2 and [c]; WBS3 wells.

Figure (9) clarifies the results of the GR and density logs (RHOB), where plots reveal that points of limestone and dolomite are displayed in the left direction. As a result, the major lithology of this aquifer may be concluded to be sandstone with shale and carbonate streaks based on plotted sites along the sandstone line are the highest.

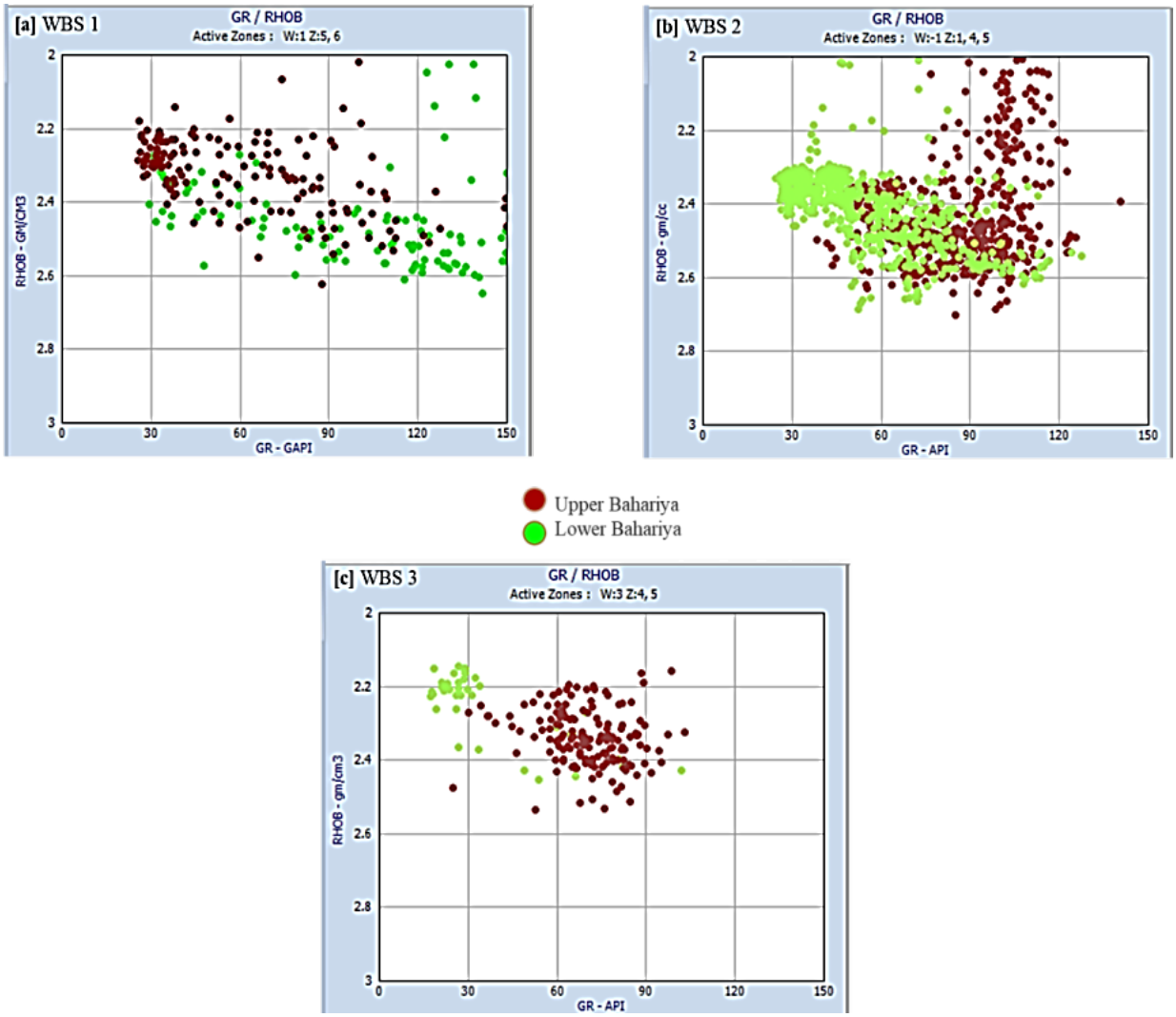

Fig. 9. GR-RHOB cross plot [a]; WBS 1 [b]; WBS 2 and [c]; WBS3 wells

Figure (10) shows a cross plot of porosity and lithology for the upper and lower Bahariya formations. Figure (10a) shows plotted data from the upper Bahariya well at WBS1, which is dispersed between sandstone and limestone and has a porosity value varying from 9.3 to 46.1%. The bulk of points appear to be spread downward along the dolomite line due to the impacts of shale. This indicates the presence of shale lithology in sandstone and limestone lines. The data from the lower Bahariya aquifer's neutron–density cross plot is distributed between the sandstone line and limestone, with porosity values ranging from 6.7 to 44.7 %. The upper Bahariya formation is therefore cleaner than the lower Bahariya formation. These findings match with those of Ghoubachi (2017) and Yousif *et al.* (2018), who found that the Bahariya formation is separated into two units as documented in well logs, and that their productivity is mostly determined by the proportion of (V_{sh}).

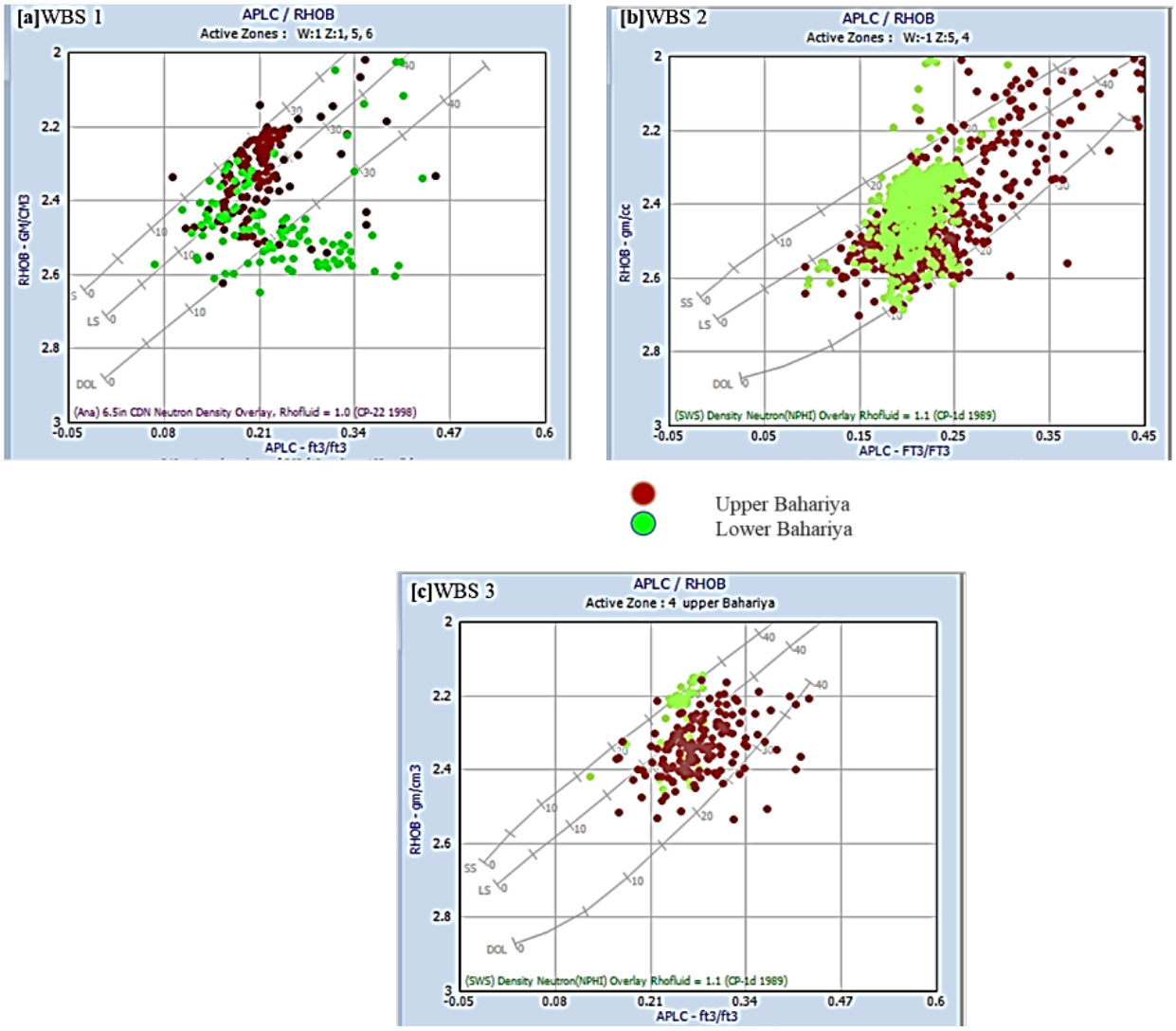

Fig. 10. APLC/RHOB cross-plots of Bahariya formation for [a] WBS 1, [b] WBS 2 and [c] WBS 3 wells

5. Hydrology

Table (3) shows the results of the preliminary analysis of pumping tests using equation (11) for unconfined Eocene aquifer. The quick time recovery (29:120 min), (Figure. 11), is most likely due to the secondary porosity of the fissured limestone aquifer. This aquifer is distinguished by two types of water flow (laminar and turbulent flows) (Ibrahim *et al*., 2020). *K*, T, and S were calculated using long-duration pumping test of 13 wells. According to the fitted models of these wells, the tested *K* values range from 0.25×10^1 to 4.15×10^1 m/d with an average of 2.1×10^1 m/d (Table 3). The wide range of *K* values can be explained by permeable zones caused by the karstification process, which is accompanied with fast changes in the high density of fractures and joints as observed in wells ST38, 214, and 48 (Figure. 11).

Table 3. Finding of pumping test analysis of Eocene fractured limestone aquifer.

WELL NO.	FORMATION	AQUIFER	PUMPING RATE Q (M^3/H)	DRAWDOWN S (M)	SPECIFIC CAPACITY ($M^3/H/M$)	LOSS FACTOR B (M)	T (M^2/DAY)	SALINITY (MG/L)	SAFE YIELD K (M/D)	WELL PRODUCTIVITY CLASSIFICATION (IBRAHIM, 2020)
ST1	Eocene	Apollonia	215	3.5	61.43	345	9400	2304	2.75×10^0	150	High
ST13			220	2.7	81.5	0	229	2384	2.65×10^0	150	High
ST38			215	7.20	29.86	200	937	2320	0.25×10^3	150	High
ST48			210	1.39	151.079	200	8300	2194	4.15×10^1	150	High
ST119			220	21.18	10.387	280	348	2048	4.57×10^0	150	High
ST180			210	10.85	19.35	202	2540	2285	1.46×10^1	150	High
ST188			210	13.22	15.885	337	2240	2208	7.27×10^0	150	High
ST209			200	6.98	28.65	250	3140	2426	1.27×10^1	150	High
ST214			200	10.06	18.87	275	2990	2304	1.10×10^1	150	High
ST219			240	12.15	19.75	241	1790	2340	8.30×10^0	150	High
ST223			190	13.90	13.669	267	1140	2342	4.87×10^0	150	High
ST258			180	42.71	4.21	358	598	2451	1.68×10^0	150	High

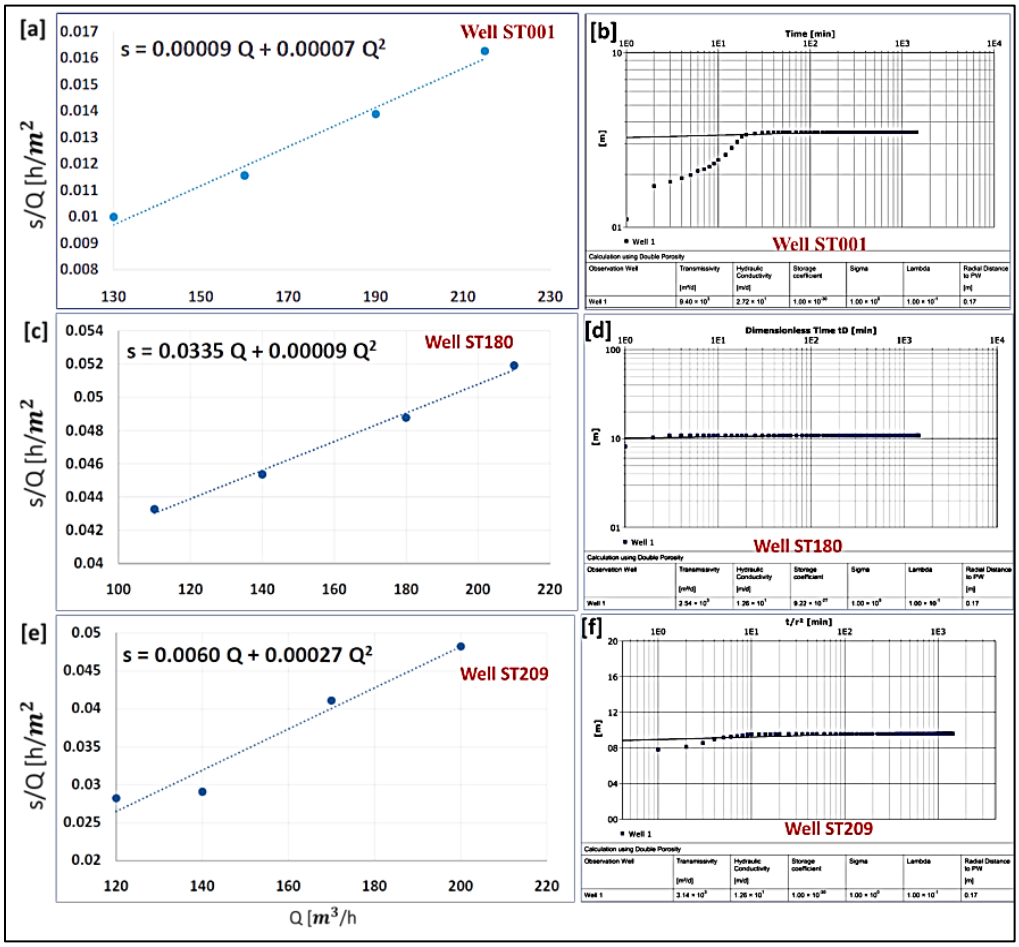

Fig.11. Long-duration tests data analysis for some Eocene aquifer over the investigated area. a, c and d represent the relationship between the rate of withdrawal and qualitative decline, while b, d and f represent the results of the analysis of long pumping test using the Theis method.

6. Conclusion

The available geophysical well logging data and pumping tests were complementary each other to obtain the detailed hydrogeological characteristics of the Eocene and Nubian sandstone aquifers in the study area. The lower Bahariya unit has the lowest hydraulic characteristics and the most modest petrophysical qualities. For any future well drilling/production activity, the study strongly recommends extracting from the Upper Bahariya unit of the Nubian sandstone aquifer of low V_{sh} with a priority of WBS2 well, whereas in the Eocene aquifer, the total extraction rate per day should not exceed 150 m^3/day in the entire study area to prevent depletion of the concerned aquifer. As a result, the implied geophysical well logging technique and its accompanying detailed petrophysical analysis contributed to a better understanding of the characteristics of the Eocene and Nubian sandstone aquifers in this specific area of Egypt's western Desert, where many complex geological and hydrogeological aspects occur. Furthermore, the current study indicated that $\emptyset_{eff}$, k, and $v_{sh}$are the primary determinants of Eocene and Nubian sandstone aquifers quality, all of which are critical in optimizing sustainable groundwater resource management techniques.

References

Archie, G. E., (1942). The electrical resistivity log as an aid in determining some reservoir characteristics. Trans., AIME, 146, 54-67.

Asquith, G. & Gibson, C. (1982). Basic Well Log Analysis for Geologists. AAPG Publications, Tulsa, OK, 216 pp.

F.M. Al-Ruwain. (1996) Hydrogeology and ground water modeling of the carbonate aquifer of Al-Sulibiya, Kuwait. Kuwait J.Sci. &Eng.23, 1996.

Farrag, A. A., Ebraheem, M. O., Sawires, R., Ibrahim, H. A., & Khalil, A. L. (2019). Petrophysical and aquifer parameters estimation using geophysical well logging and hydrogeological data, Wadi El-Assiuoti, Eastern Desert, Egypt. Journal of African Earth Sciences, 149, 42–54. https://doi.org/10.1016/j.jafrearsci.2018.07.023

Ghoubachi, S.Y., (2017). The hydrogeological characteristics of the Nubian Sandstone System in Sahl Karawein Area and Its Vicinities, El-Farafra Oasis, Western Desert, Egypt. Ann. Geol. Surv. Egypt. 36, 175–187.

Ibrahem, S. M. M., Elalfy, M., Hagras, M. A., & Company, A. (2020). Groundwater Potentials of Eocene, 82(1), 59–82.

Jalludin, M., and Razack, M., (2004): Assessment of hydraulic properties of sedimentary and volcanic aquifer systems under arid conditions in the Republic of Djibouti (Horn of Africa),Hydrogeol. J.,12(2), 159-170.

Makky, A. F., El Sayed, M. I., Abu El-Ata, A. S., Abd El-Gaied, I. M., Abdel-Fattah, M. I., & Abd-Allah, Z. M. (2014). Source rock evaluation of some upper and lower Cretaceous sequences, West Beni Suef Concession, Western Desert, Egypt. Egyptian Journal of Petroleum, 23(1), 135–149. https://doi.org/10.1016/j.ejpe.2014.02.016

Twfiq Mohamed Z., Zarif Fardous. M., Massoud A. and Al Temamy Ayman M., (2021). Determination of the petrophysical and natural radioactivity properties of Nubian sandstone Aquifer at the area of the Northwest El Ain village, Sharq El Oweinat area, southwestern Desert, Egypt. Asian journal of Environment &Ecology.15(4):37 55,2021. Doi:10.9734/AJEE/2021/v15i430236.

Nisar, U. B., Khan, M. J., Imran, M., Khan, M. R., Farooq, M., Ehsan, S. A., Ahmad, A., Qazi, H. H., Rashid, N., & Manzoor, T. (2021). Groundwater investigations in the Hattar industrial estate and its vicinity, Haripur district, Pakistan: An integrated approach. Kuwait Journal of Science, 48(1), 51–61. https://doi.org/10.48129/KJS.V48I1.7820.

Schlumberger (1997), L Interpretation, Principles/Applications. Houston, Texas, U.S.A.

Shalaby, M. R. (2021). Petrophysical characteristics and hydraulic flow units of reservoir rocks: Case study from the Khatatba Formation, Qasr field, North Western Desert, Egypt. Journal of Petroleum Science and Engineering, 198, 108143. https://doi.org/10.1016/j.petrol.2020.108143.

Theis, V., (1935). The relation between the lowering of the piezometric surface and the rate and duration of discharge of a well using groundwater storage. Transaction of the American Geophysical Union. 16:519-524.https://doi org/10.1/29623

Timur, A. (1968): An investigation of permeability, porosity, and residual water saturation relationships. Log Anal. 9(4), 8–17.

Verbovsek, T., (2008): Estimation of transmissivity and hydraulic conductivity from specific capacity and specific capacity index in Dolomite aquifers. J. Hydrologic Eng., 13(9).

Wehr, F., Youle, J. and Pemberton, G. (2002). Sequence stratigraphy and sedimentology of the Bahariya Formation, Khalda Concession, Western Desert, Egypt. American Association of Petroleum Geologists, International meeting, Cairo, Egypt, (Abstract Volume unpaginated).

World Bank. (2018). Water scarce Cities: Thriving in a finite world.

Yousif, Mohamed, Hassan S. Sabet, Saad Y. Ghoubachi, and Ameer Aziz (2018). "Utilizing the Geological Data and Remote Sensing Applications for Investigation of Groundwater Occurrences, West El Minia, Western Desert of Egypt." NRIAG Journal of Astronomy and Geophysics 7(2):318–33.

Zainab, M. H. A. L., Almallah, I. A., & Al-Najm, F. M. (2019). Petrophysical properties evaluation using well logging of the upper sand member of Zubair Formation in Zubair oil Field, Southern Iraq. Basrah Journal of Science, 37(3), 457–480.

Submitted: 21/11/2021
Revised: 21/02/2022
Accepted: 09/03/2022
DOI: 10.48129/kjs.17333

Climate vulnerability index of the coastal subdistricts of Badin, Sindh, Pakistan

Noor Fatima[1], Aamir Alamgir[1,*], Moazzam Ali Khan[1], Muhammad Owais[2]

[1]*Institute of Environmental Studies, University of Karachi, Karachi, Pakistan*
[2]*Institute of Business Administration, Karachi, Pakistan*

**Corresponding author: aamirkhan.ku@gmail.com*

Abstract

The frequent occurrence of climate related events and changes in average temperature, are predicted to increase the vulnerability of the coastal population of Sindh. A climate vulnerability index (CVI) was established and applied to the coastal subdistricts of Badin, Sindh, Pakistan. This study aimed to recognize the vulnerabilities of the coastal population of Sindh exposed to climate change. According to the study, the subdistricts of Badin have been exposed to high temperatures and significant climatic tragedies during the last two decades. The highest vulnerability to climate variability was found in Tando Bago (0.72) and Badin (0.70). Matli is better off in adaptive capacity through socio-demographic (0.29). The vulnerability to resource dependency and knowledge and skill was low in the sub-district of Talhar. In terms of sensitivity, Tando Bago is the most sensitive subdistrict in terms of health (0.55) and resource variability (0.80). The study raises concerns related to coastal communities and their aptitude to address present and upcoming challenges connected with climate change and increased insecurity. The CVI calculated (0.59) can be utilized to improve adaptive capacity, minimize sensitivity, and mitigate exposure to climatic extremes in adaptation planning.

Keywords: Badin; climate change; coastal districts; Sindh; vulnerability index.

1. Introduction

The prolonged consequences of climate change on the socio-economic system have become a major concern, prompting an array of vulnerability assessments to be started in various locations in order to protect vulnerable communities facing climatological extremes (Reed *et al.,* 2013). Climate vulnerability is the result of the combination of climate exposure, sensitivity and the adaptive capacity of the communities (Fatima *et al.*, 2021). Exposure to climate disasters (droughts, floods, and heavy rains) are regarded to pose the biggest harm to agriculture-based communities (Rehman *et al.,* 2015, Fatima *et al.,* 2021). Climate change and fluctuations in average temperature have already had a severe impact on community vulnerability and livelihood, particularly in the coastal areas (IPCC, 2014). Like in Pakistan, the coastal areas of Sindh are highly susceptible to these changes and frequently experience extreme events. Major climate variability concerns in the coastal areas of Sindh are the alteration in temperature (Rehman *et al.,* 2015), precipitation (Gajbhiye *et al*., 2016), and other meteorological parameters (Fatima *et al.,* 2021). These long-term and drastic changes in climatological parameters across multiple geographical areas have caused heat waves (Chaudhry *et al*., 2009), flash floods (Kazi, 2014), droughts (Khan *et al.,* 2013), cyclones (NDMA, 2019), food insecurity (Gelan & Atkinson, 2021), as well as damage to water and land resources on which

livelihood of the coastal communities are largely dependent. For instance, damage to agricultural crops (Fatima *et al.*, 2021), livestock and water resources is widely reported (reference missing). A climate change scenario changed the outlook of the environmental factors in the coastal areas of Sindh, thus affecting the livelihood, natural resources, and other sectors of life (Alamgir *et al.,* 2017). Climate variability in the coastal areas of Sindh has been widely studied in association with its impacts (e.g., floods, cyclone, drought). However, few of the studies in Pakistan have assessed livelihood vulnerability at the community level (Salik *et al.,* 2015; Sattar *et al.,* 2017; Qaisrani *et al.,* 2018). A simple human vulnerability index (HVI) for 103 districts in Pakistan was developed by (Khan & Salman, 2012) to study the spatial analysis of vulnerability to climate change hazards in the country. Similarly, the Pakistan Institute of Development Economics (PIDE) in 2013 estimated a district level vulnerability to climate change index for 22 districts in Pakistan.

Multiple indicators of community vulnerability are used in vulnerability assessments to quantify multifaceted challenges that cannot be characterized by a single metric. The models are also increasingly used in the identification and mapping of vulnerable hotspots (Hinkel, 2011). The top priorities are given to the communities experiencing vulnerability, increasing awareness of where adaptation measures should be placed and identifying mechanisms for monitoring adaptation policies.

This study developed a climate vulnerability index (CVI) for the coastal subdistricts of Badin, Sindh Pakistan. The region has been exposed to the consequences of climate change in the last two decades (Alamgir *et al.,* 2017). The objective of the study was to identify and compare the vulnerabilities in the light of coastal communities expose to climate change. It investigates how vulnerability in the context of climate change may alert measures to reduce vulnerability in climate-vulnerable region(s). This research focused on assessing household vulnerability in coastal subdistricts, which enhances the application of vulnerability assessment literature based on indicators.

2. Methodology

2.1 Study area and sample size

The coastal district of Badin was selected for this study and identified as vulnerable hotspot. According to Pakistan NHDR 2017, the human development index (HDI) of Badin is 0.4, placing it in the low development category. The substantial populations in subdistricts of Badin living in poverty, have low adaptive capacity and their socio-economic activities are heavily influenced by climate change issues. These subdistricts are located in Pakistan's southern area, between 23°43' and 25°26' N, and 67°05' and 68°45'E. The coastal district of Badin was stratified into five sub-districts (Badin, Golarchi, Matli, Talhar and Tando Bago) and a total of 235 households were surveyed.

2.2 Index computation

2.2.1 Selection of Indicators

Based on IPCC tripartite typology of vulnerability (Hahn *et al.*, 2009), 10 indicators baskets (Figure 1) were categorized in terms of adaptive capacity: (1) socio-demographic (SD), (2) socio-political networks (SP), (3) livelihood strategies (LS), (4) infrastructure (IS), (5) resource dependency (RD), (6) knowledge and skills (KS); sensitivity: (7) health (HE), (8) natural asset (NA), (9) resource

variability (RV); and exposure: (10) climate variability (CV). Definition and explanation of major indicator basket and its subcomponent are given in Appendix A.

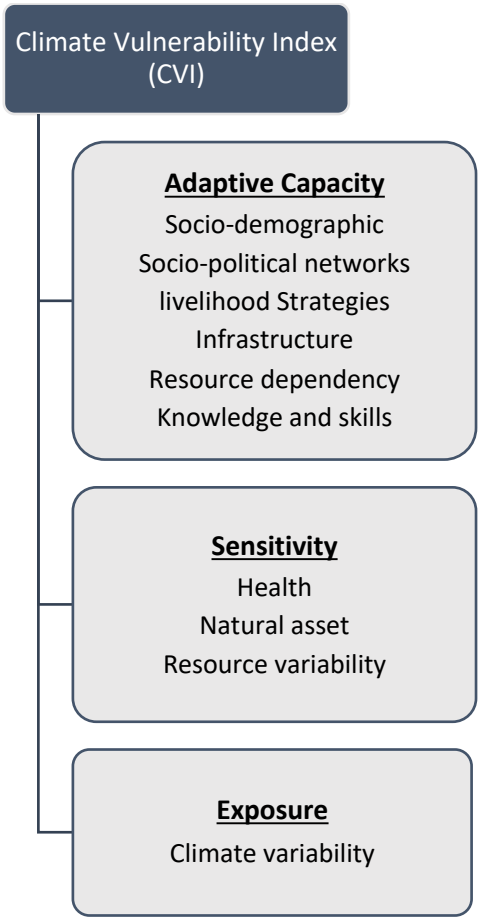

Fig. 1. Major Indicator Baskets used for CVI

2.2.2 Data collection

A field survey was conducted to identify the practicality of gathering the required data through questionnaires. Appendix-B outlines the mechanism through which each indicator was quantified and standardized. Also, secondary data were added on climate change variables such as average maximum monthly temperature (^{0}C) and average monthly precipitation (mm) over the period 2001–2020 from Badin station of the Pakistan Metrological Department (PMD).

2.2.3 Standardization

Primary household survey data were transformed into suitable measurement units (percentages, ratio and indices) to quantify the indicators. The CVI uses indicators that were scaled differently and standardized to make the indicators to a uniform, equivalent scale and aggregate into a single index by using the following equation (Hahn *et al*., 2009):

$$\text{Index Si} = \frac{S - S_{min}}{S_{max} - S_{min}} \quad (1)$$

Where Si is a sub-indicator of Indicator Basket i, and S_{max} and S_{min} are maximum and minimum values, reflecting high and low vulnerability, respectively.

2.2.4 Weighting Indicator Basket

Assuming an equal contribution of each indicator basket to overall vulnerability, equal weights were applied (Hahn *et al.*, 2009). The weighting approach is an important aspect for indexing (Hinkel, 2011) based on different settings. In this regard, it is appropriate for climate-prone settings where comparisons between groups that were similarly exposed can be made.

2.2.5 Composite Index Calculation

The value for the indicator baskets was computed by taking the average scores of the standardized subcomponent in each basket using Eq. 2:

$$Ib = \frac{\sum_i^n indexSi}{n} \quad (2)$$

Where Ib represent each of the 10 major indicator baskets, indexSi is the sub-indicator for the i making up each indicator basket and n represents the number of indicators for a specific basket. The values of the indicating baskets were calculated to obtain the CVI score for each coastal subdistrict (Eq. 3).

$$\mathrm{CVI} = \frac{\sum_{i=1}^{10} \mathrm{WiIbi}}{\sum_{i=1}^{10} \mathrm{Wi}} \quad (3)$$

Where CVI is the computed climate vulnerability index, equivalent to the average weight of all 10 indicator baskets, and Wi is the weight of each major indicator basket (Ibi), which is calculated from the sum of all sub-indicators present in each indicator basket which contributes equally to the overall climate vulnerability index. The vulnerability score was computed for each subdistrict. The CVI is scaled from 0 (least vulnerable) to 1 (most vulnerable). Based on indicator baskets defined in section 2.2.1, the equation 3 for CVI can be expressed as:

$$\mathrm{CVI} = \frac{[W_{SD}SD + W_{SP}SP + W_{LS}LS + W_{IS}IS + W_{RD}RD + W_{KS}KS + W_{HE}HE + W_{NA}NA + W_{RV}RV + W_{CV}CV]}{W_{SD} + W_{SP} + W_{LS} + W_{IS}IS + W_{RD} + W_{KS} + W_{HE} + W_{NA} + W_{RV} + W_{CV}} \quad (4)$$

A comprehensive example for CVI estimation of major Indicator basket resource variability (RV) for sub-district Badin is given in Appendix B.

3. Results

The values for CVI and each indicator basket of subdistricts of Badin are presented in Table 1, and Figure 2. The results of each sub-indicator in the indicator basket are given in Appendix C. Starting with the socio-demographic (SD) indicator basket of the district Badin, the greater vulnerability was shown by subdistricts Golarchi (0.36), followed by Talhar (0.34), Badin (0.32), Tando Bago (0.32) and Matli (0.29). The age dependency ratio (SD1) in Golarchi (0.37) was higher than in other sub-districts, indicating that it has a higher ratio of economically dependent population to productive population. The vulnerability score for education (SD2) is higher in Talhar (0.70), where the majority

of the household heads did not have primary school education. Similarly, more than half of the household heads in Badin, Golarchi and Tandgo Bago, and half of the household heads in Matli were also uneducated, with index values of 0.52, 0.65, 0.64 and 0.50, respectively. The majority of the household heads have more than two years' experience in their respective fields (farming/fishing/herding). This showed a low vulnerability score for experience (SD3) in Badin, Golarchi and Matli and zero for other subdistricts.

Table 1. Climate Vulnerability Index (CVI) of coastal subdistricts of Badin, Sindh, Pakistan.

Vulnerability	Indicator Basket	Index Value					
		Badin	Golarchi	Matli	Talhar	Tando Bago	District Badin
Adaptive Capacity	Socio Demographic	0.32	0.36	0.29	0.34	0.32	0.32
	Socio-Political Networks	0.60	0.64	0.57	0.59	0.64	0.61
	Livelihood Strategies	0.70	0.77	0.67	0.73	0.72	0.71
	Infrastructure	0.54	0.62	0.59	0.63	0.61	0.59
	Resource Dependency	0.35	0.38	0.35	0.23	0.35	0.34
	Knowledge and Skills	0.35	0.48	0.42	0.30	0.41	0.40
Sensitivity	Health	0.46	0.47	0.43	0.49	0.55	0.48
	Natural Assets	0.76	0.78	0.74	0.74	0.77	0.76
	Resource Variability	0.80	0.80	0.80	0.80	0.80	0.80
Exposure	Climate Variability	0.70	0.68	0.69	0.69	0.72	0.70

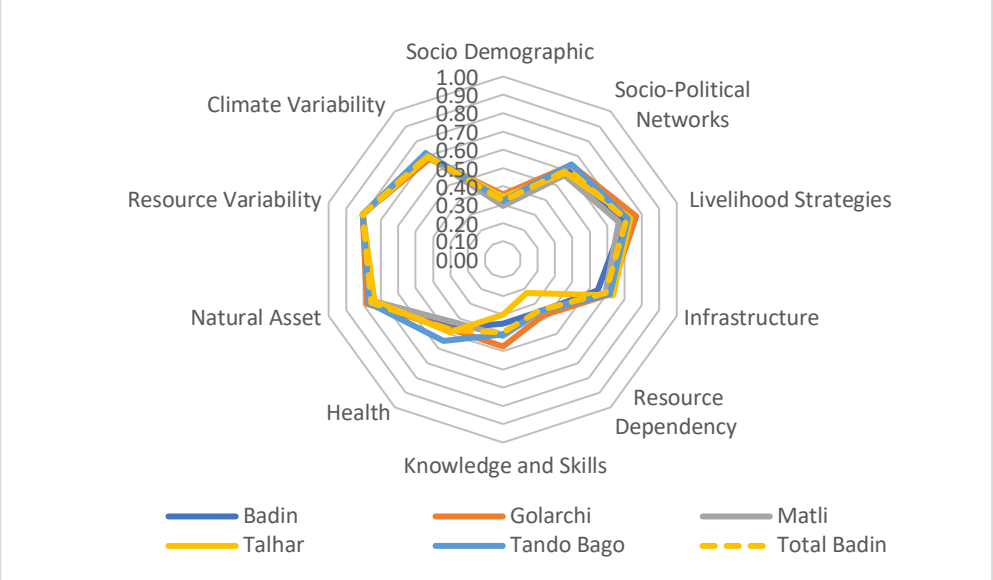

Fig. 2. The CVI values for Subdistricts of Badin

The vulnerability score for socio-political (SP) support during hard times is similar and higher in Golarchi (0.64) and Tando Bago (0.64). Except for a few, the majority of respondents were not members of any official local organization or group (SP1). More than 70% of households in each sub-district did not approach local government and NGOs in the last five years for any kind of assistance or external support (SP2). The majority of them had no access to information regarding climate, security, aid support programs (SP3) and had no contact with local government (SP4). Moreover, households borrowed money and received assistance from their landlords (Zamindars) in hard times (SP5). Cooperation was also observed among villagers of all subdistricts during periods of harsh weather conditions and scarcity (SP6). About 54-65% of households in each subdistrict had access to social media/information through TV, radio, telephone/mobile phone (SP7), Overall, Golarchi and Tando Bago were more vulnerable than other subdistricts in the social-political network basket (SP8).

Subdistrict Golarchi showed more vulnerability in the livelihood strategy (LS) basket than the other subdistricts (Table 1). The majority of households in all subdistricts did not receive remittances (LS1) in the last two years in the form of cash or in-kind assistance from family members or friends living in urban regions. Some of the households that are active in socio-political networks find assistance from other sources like landlords, NGOs or any funding agencies. Moreover, they have low annual net income to cover major domestic expenditures (LS2) and Golarchi showed a higher vulnerability score (0.85) as compared to other subdistricts.

In terms of savings (LS3), households in all sub-districts had no savings to cope with natural disasters, showing high vulnerability index values (Appendix C) for Tando Bago (0.91) followed by Golarchi (0.90), Talhar (0.90), Badin (0.87) and Matli (0.82). Further, more than half of the households stated that they did not have access to any financial institution for credit/loans (LS4) to support their activities. In terms of livelihood dependency (LS5), a major proportion of households in Talhar were dependent on farming and fishing as a primary source of income, making them more vulnerable (0.95) to the consequences of climate change. On the other hand, recent floods also forced landless farmers into debit/loans (35-47%), which they usually borrow from landlords and private money lenders.

The infrastructure of all coastal subdistricts is inadequate and they are vulnerable to future climate induced disasters. Infrastructure that is unable to withstand a severe climatic event (e.g., heavy rains or flood, cyclone and storms) has low adaptive capacity and therefore is more vulnerable. More than 50% of households reported in all sub-districts that they travel a long distance to reach the nearest vehicle station (IS1) and it takes more than 30 mins (Appendix A). More than 70% households in Talhar and Tando Bago reported that the village roads were not properly paved (IS2). The houses owned by respondents have wood and bamboo-based roofs, and walls were mainly composed of mud bricks (IS3). Basic government facilities were present but generally disseminated, inactive and poorly equipped.

In terms of resource dependency (RS), Matli showed the highest vulnerability score (0.6) where most of the households were dependent on electricity (RS1). However, subdistrict Golarchi was more vulnerable (0.93) and dependent on natural gas (RS2) for its domestic. The results of knowledge and skills (KS) also showed that a majority of households were satisfied with recent efforts

made by local government and NGOs to share knowledge (KS1) about climate change, while 50% of households in Badin and 45% in Golarchi have not received any type of vocational training to improve their skills (KS2), making them more adaptable to sudden livelihood changes.

The vulnerability index in terms of health was high in Golarchi, where half of the households with members reported chronic diseases (HE1). On the other hand, households in all sub-districts except in Badin did not use healthcare facilities at all or once in a while due to access constraints (too far away, too costly, unsuitable, lack of tools or staff, not enough facilities) (HE2).

The vulnerability score for the natural asset (NA) was similar for Matli and Talhar (0.74) and higher in Golarchi (0.78). It was found that more than half of the households in Talhar and Tando Bago did not have access to backup private wells or piped water (NA1). In terms of land ownership (NA2), more than half of the households in all subdistricts did not own the land where they currently live, farm, or graze animals (or are unable to access/rent land legally). House ownership (NA3) was high in Talhar, resulting in low vulnerability scores (0.35) and similarly for other subdistricts like Tando Bago (0.40), Matli (0.43), Golarchi (0.45), and Badin (0.48). Livestock ownership was high in the households for the animals they were using for grazing (NA4). Around 50% of households reported that they saved grain crops like wheat, rice, and barley and had no food shortages in the last 30 days (NA5).

The influence of resource variability (RV) on the coastal communities and their livelihoods has also been studied with reference to water resources. As shown in Table 1, the vulnerability score for all sub-district was similar (0.80), indicating that more than 80% household were experiencing nearly the same issues related to the water system (RV1), resource scarcity (RV2), distance to water resources (RV3), and income-based changes (RV4). The vulnerability score for the public water system was high in Badin (0.88), followed by Golarchi, Matli (0.85), Matli (0.82), Tando Baggo (0.73), and Talhar (0.70), and more than 35% of households reported a long distance to the water point (RV3). Moreover, around 95% of households considered resource scarcity a big problem, showing a high vulnerability score (0.90-0.95) in all subdistricts (RV2). Consequently, around 32% of farmers in Badin district reported that they have experienced income-based changes resulting from the decreasing fresh water resources used for agriculture activities. The vulnerability score for livelihood changes was high and similar in Tando Bago (0.90) and Matli (0.90), showing a large dependency on water (RV4).

Shifts in temperature and rainfall indices were generally similar for all subdistricts of Badin. However, Tando Bago showed the greatest vulnerability (0.72) in the climate variability (CV) basket than other subdistricts because of the reported higher climate-related losses to crops and livestock. Most of the households noticed long-term shifts or changes ($\leq$ 20 years) in temperature (CV1) and precipitation (CV2), indicating high vulnerability scores (0.95-0.98) (Appendix C). On the basis of the mean standard deviation of monthly average maximum daily temperature (CV3) and monthly average precipitation (CV4), the index value was the same for all subdistricts and was calculated as 0.46 and 0.24, respectively. However, the vulnerability score for the number of hot months with an average monthly temperature above 30 °C (2001–2020) was 0.80 for all sub-districts. The results also showed a high vulnerability score for climate related losses to crop damage (CV7) and livestock (CV8) in all subdistricts. More than 80% of households reported ground water salinity due to sea

water intrusion in the last 20 years (CV9). Some households (20%) reported villagers migrating due to climate change and natural disasters, but their vulnerability index was low (CV8).

4. Discussion

This study assessed an integrated vulnerability analysis with multiple indicators of climate variability and social system vulnerability at the household level. The results in (Figure 3) showed that the exposure to climatological events and their losses were high in subdistricts of Badin. The subdistricts were better off in adaptive capacity through socio-demographic, adequate infrastructure and resource dependency, but highly sensitive in terms of health, natural assets and resource variability. The households showed high access constraints to healthcare facilities, less land ownership, and high-water scarcity in Badin.

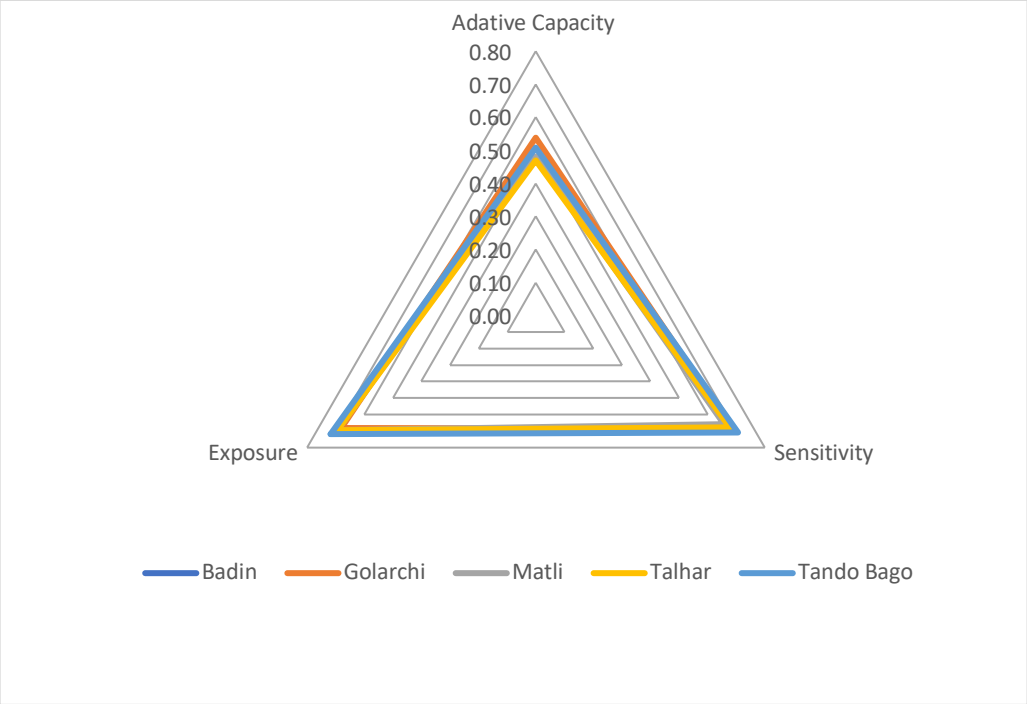

Fig.3. The vulnerability triangle of Adaptive Capacity, Exposure and Sensitivity

The livelihood strategy and resource variability are two of the major contributors to the vulnerability index of Badin. Livelihood vulnerability occurs due to income diversification being lower. The results specify that households involved in more than one livelihood activity, especially those dynamic in socio-political networks, are relatively less likely to be vulnerable. Vulnerable households have less access to local organizations, external support, and NGOs than those less vulnerable (Agrawal, 2008). This condition is applicable to the subdistricts of Golarchi, where households had low annual income, less savings, livelihood dependency, and low remittance opportunities, as well as limited involvement in political participation, all of which contributed to their low adaptive capacities. Moreover, the villagers have less access to information regarding climate, security, and aid support programs due to the high influence of the landlords in the region. At the regional level, the federal

government has a weak role, and most of the information dissemination is under the control of the landlords. Thus, households active in socio-political networks with landlords have more access.

Furthermore, one of the factors also contributing to livelihood vulnerability was a credit or loan that farmers had taken for crop inputs with a huge profit margin. Moreover, due to any constraint, if the quality of the crop is reduced and they have not paid the credit on time, the credit goes to the next crop season or year with an even larger interest. The land lord (Zamindar) frequently provides these loans to farmer households and also binds them to deliver further labor services (Oxfam & ADPC, 2014). Due to these loans the farmers and Zamindar are locked into a long-term contractual relationship. As a result, poor households remain to be poor due to indebtedness, and their adaptive capacity remains low, making them more vulnerable and less resilient (Fatima *et al.,* 2021). The vulnerability score for the credit/loan was found to be higher in all subdistricts of Badin.

Resource variability and natural assets (houses, land, livestock, etc.) could be easily converted into other assets and play a crucial role in determining the sensitivity of communities (Lemos *et al.,* 2013). Households in the subdistrict of Tando Bago were the most sensitive in terms of resource variability and natural assets. The coastal districts showed higher vulnerability to the public water supply, water-related income changes, and community perspective on water scarcity. The local government has publicized a number of water supply schemes, but none of them has been executed due to unavailability of funds. Land ownership was rare in the region, which would increase their adaptive capacity by enhancing diverse crop productivity (Fischer *et al.,* 2007). Another important indicator of vulnerability is health (Lemos *et al.,* 2013) in terms of chronic diseases and access to healthcare centers. Tando Bago is the most sensitive subdistrict in terms of the health index. During a field survey, it was observed that an increasing temperature has made most of the regions suitable for a number of vectors and extended their season. In addition, seawater intrusion into freshwater is also responsible for increasing waterborne diseases, which include vomiting, diarrhea, gastroenteritis, skin and kidney problems reported in these regions (Memon *et al.,* 2011).

Climatological events also contributed to major vulnerability in the coastal districts of Sindh. The sub-district of Tando Bago showed higher vulnerability to climate exposure (Figure 3), as evidenced by high losses of land, crops and livestock. Based on statistical evidence, it has been found that the hot days frequency index in coastal areas of Sindh has significantly increased (0.15) during a 36-year time period (Abbas *et al.,* 2018). Since rising temperatures have already affected the natural resources in the area, particularly the agriculture sector, the livelihood opportunities in the area have become limited (Fatima *et al.,* 2021). The decline of the Indus deltaic region is mostly due to diminished downstream flow, which has resulted in seawater encroaching over 1,700 km^2 of the delta over the last five decades (Alamgir *et al.,* 2017). The groundwater and soils in coastal areas are becoming salinized, rendering them useless for agriculture, resulting in an involuntary migration of the local population. If the Indus River's flow continues to dwindle, the scenario will become even more dangerous due to seawater intrusion into freshwater, groundwater, and land resources.

5. Conclusion

This study has evaluated the usefulness of the climate vulnerability index for understanding the numerous dimensions of vulnerability to climate change and factors connected with the socio-

economic and human development of communities. The CVI can be used as a valuable tool for exploring climatic interactions as well as contrasting coastal community vulnerability and climate change adaption. The tool is designed in response to livelihood perceptions and takes a prescriptive approach that is consistent with the unique social context and spatiotemporal character of vulnerability. The coastal district of Badin is more vulnerable in terms of sensitivity due to high resource variability (0.8) and low natural assets (0.76), which make them more vulnerable to the climatological exposure (0.7). Golarchi is more vulnerable in terms of adaptive capacity (0.54), while Tando Bago showed high vulnerability to climatic exposure (0.72) and sensitivity (0.71). The CVI computed in this study can be used in adaptation planning to improve adaptive capacity, reduce sensitivity, and mitigate exposure to climate extremes.

References

Abbas, F., Rehman, I. Adrees, M. Ibrahim, M. Saleem, F. Ali, S & Salik, M.R. (2018). Prevailing trends of climatic extremes across Indus-Delta of Sindh-Pakistan. Theoretical and Applied Climatology, 131**(3)**: 1101-1117.

Agrawal, A. (2008). The Role of Local Institutions in Adaptation to Climate Change. World Bank, Washington, DC. https://openknowledge.worldbank.org/handle/10986/28274 License: CC BY 3.0 IGO.

Alamgir, A., Khan, M.A. Shaukat, S.S. Khan, T.M.A & Zubair, S. (2017). Water quality appraisal of Keti Bandar and Shah Bandar creeks of Indus delta, Sindh, Pakistan. Desalination and Water Treatment, 70: 95-105.

Chaudhry, Q. U. Z., Mahmood, A. Rasul, G. & Afzaal, M. (2009). Climate change indicators of Pakistan. Pakistan Meterological Department.

Fatima, N., Alamgir, A. Khan, M.A. & Mahmood, K. (2021). Conceptual Framework for Climate Vulnerability and Conflicts in the Coastal Districts of Thatta and Sujawal, Sindh, Pakistan. International Journal of Biosciences. 18*(4):* 60-76.

Fatima, S.U., Khan, M.A. Majeed, R. Alamgir, A. & Shaukat, S.S. (2021). Multi-factoral OSLR and MLR modelling of climatological and crop production trends in coastal areas of Pakistan. Pakistan Journal of Botany. 53*(2)*:641-653.

Gajbhiye, S., Meshram, C. Singh, S.K. Srivastava, P.K. & Islam, T. (2016). Precipitation trend analysis of Sindh River basin, India, from 102-year record (1901–2002). Atmospheric Science Letters. 17*(1):* 71-77.

Gelan, A., & Atkinson, G. (2021). Climate change, global warming and food security: Assessing the prospect for Kuwait using an economy-wide model. Kuwait Journal of Science.

Hahn, M.B., Riederer, A.M. & Foster, S.O. (2009). The Livelihood Vulnerability Index: A pragmatic approach to assessing risks from climate variability and change—A case study in Mozambique. Global Environmental Change. 19*(1)*: 74-88.

Hinkel, J. (2011). "Indicators of vulnerability and adaptive capacity": Towards a clarification of the science–policy interface. Global Environmental Change. 21*(1):* 198-208.

IPCC (2014). Climate Change: Synthesis Report. Contribution of Working Groups I, II and III to the Fifth Assessment Report of the Intergovernmental Panel on Climate Change.

Kazi, A. (2014). A review of the assessment and mitigation of floods in Sindh, Pakistan. Natural Hazards. 70*(1)*: 839-864.

Khan, M.A., & Gadiwala, M.S. (2013). A study of drought over Sindh (Pakistan) using standardized precipitation index (SPI) 1951 to 2010. Pakistan Journal of Meteorology. 9*(18)*: 15-22.

Khan, F.A., Salman, A. A. (2013). Simple human vulnerability index to climate change hazards for Pakistan. International Journal of Disaster Risk Science. 3*(3)***:** 163–176.

Lemos, M.C., Agrawal, A. Eakin, H. Nelson, D.R. Engle, N.L. & Johns, O. (2013). Building adaptive capacity to climate change in less developed countries. In: Asrar, G., Hurrell, J. (eds) Climate Science for Serving Society. Springer, Dordrecht. 437-457 https://doi.org/10.1007/978-94-007-6692-1_16

Memon, M., Soomro, M. S. Akhtar, M. S. & Memon, K. S. (2011). Drinking water quality assessment in Southern Sindh (Pakistan). Environmental Monitoring and Assessment, 177*(1)*: 39-50.

NDMA (2019). Disaster Management in Sindh with historical perspective. National Disaster Management Authority, Pakistan

Oxfam & ADPC (2014). Climate Change Risks and Vulnerabilities of Badin District in Sindh Province, Pakistan. http://www.adpc.net/igo/category/ID650/doc/2014-wBRd72-ADPC-publication_CCAPakistan-2_(1).pdf

Pakistan Institute of Development Economics (2013). A District Level Climate Change Vulnerability Index of Pakistan. Centre for Environmental Economics and Climate Change Pakistan Institute of Development Economics, Islamabad, Pakistan. Https://Www.Pide.Org.Pk/Pdf/Working%20paper/Ceecc%20working%20paper-5.Pdf

Rehman, Z., Kazmi, S.J.H. Khanum, F. & Samoon, Z.A. (2015). Analysis of land surface temperature and NDVI using geo-spatial technique: A case study of Keti Bunder, Sindh, Pakistan. Journal of Basic & Applied Sciences.11: 514-527.

Reed, M. S., Podesta, G. Fazey, I. Geeson, N. Hessel, R. Hubacek, K. & Thomas, A. D. (2013). Combining analytical frameworks to assess livelihood vulnerability to climate change and analyse adaptation options. Ecological Economics. 94: 66-77.

Salik, K.M., Jahangir, S. & Hasson, S. (2015). Climate change vulnerability and adaptation options for the coastal communities of Pakistan. Ocean & Coastal Management. 112: 61-73.

Submitted: 28/06/2021
Revised: 03/01/2022
Accepted: 07/01/2022
DOI: 10.48129/kjs.17873

Kuwait J.Sci., Vol.50, No.(1A),January.2023,pp(31-48)

Evaluation of Seawater Quality of Kuwait Bay Using Physio-Chemical Parameters

Haider Liri[1], Dhary S. Al-Kandary[2, *], Jasem M. Al-Awadhi[2]

[1]*Kuwait Coast Guard, Flotilla Department, Kuwait*
[2] *Dept. of Earth and Environmental Sciences, Faculty of Science, Kuwait University, Kuwait.*

**Corresponding author: dhary.alkandary@ku.edu.kw*

Abstract

This study emphasizes on the effects of current anthropogenic activities altering seawater physio-chemical parameters around Kuwait Bay. The research aims to evaluate the spatial variations in seawater quality in Kuwait Bay. Fifty-two seawater samples were collected from 1-meter depth, between April and May 2017 and analyzed for Total Suspended Solids (TSS), nutrients: Ammonia (NH_3), Nitrate (NO_3), Nitrite (NO_2) and Silicate (SiO_2), and designated trace elements: Chromium (Cr), Zinc (Zn), Selenium (Se), Nickel (Ni), Arsenic (As), and Mercury (Hg). In addition, five real-time monitoring buoys data were used to assess seawater quality based on Kuwait Environmental Public Authority (KEPA) standards to evaluate six parameters: turbidity, Dissolved Oxygen, pH, salinity, conductivity, and seawater temperature. The results of this study reveal that: (1) average level of physio-chemical parameters: temperature, salinity, conductivity, turbidity, Dissolved Oxygen and pH in Kuwait Bay water were 27.8 ^{0}C, 40.2 ppt, 60.2 µs/cm, 5.9 NTU, 6 mg/l and 8.2, respectively; (2) average level of nutrients; silicate, nitrate, nitrite and ammonia were 333 µg/l, 83 µg/l, 235 µg/l and 43.5 µg/l, respectively; (3) average level of elements found in Kuwait Bay's seawater were 14.7 mg/l for Barium (Ba), 380 mg/l for Calcium (Ca), 9727 mg/l for Sodium (Na), 411 mg/l for Potassium (K) and 1432 mg/l for Magnesium (Mg); (4) The total suspended solids (TSS) had an average of 25.3 mg/l; (5) mean concentrations of the elements in TSS decrease in the order of Cr (15.6), Zn (5.4), Se (4.5), Ni (3.3), As (1.2), Co (0.2) and Hg (0.1mg/kg) and they are 1.6 to 22 times lower than their soil background values in, while Pb was detected in 2 samples only with average concentration of 0.7 mg/kg; and (6) Cr shows maximum enrichment relative to the upper continental crustal component (Mn). The distribution of pollutants in Kuwait Bay seems to be controlled and produced mainly by the anthropogenic and recreational activities.

Keywords: Elements; enrichment; nutrients; physio-chemical parameters; pollutants

1. Introduction

Kuwait Bay is located at the northwestern corner of the Arabian Gulf and provides the most species diversity in the region; therefore, it is considered as the highest productive ecosystem in Kuwait seawater (Al-Yamani *et al.,* 2004). It is an elliptical-shape, semi-closed body of water, extending approximately 35 km inland and covering approximately an area of 750 km^2, with an average depth

of 5 m (Al-Ghadban, 2004). Tidal current is the dominant force which effects the water movement in the Bay (Anderlini, *et al.,* 1982), with tidal range difference of 4 m vertically and 8 km horizontally. The maximum current speed in Kuwait Bay's entrance reaches approximately 1 m/s, with currents slowing toward the western portion of the Bay to less than 40 cm/s (Pokavanich and Al-Banaa, 2012; Al-Yamani *et al*., 2004). The study of Rakha *et al*. (2010) illustrated that the inner part of Kuwait Bay takes more than two years to flush.

Both anthropogenic and natural factors can cause marine pollution in Kuwait Bay (Al-Mutairi, *et al*. 2014a). However, the anthropogenic factors, associated with sewage discharge and effluent discharge from the rain sewers, and desalination and power plants, impose major environmental impacts on Kuwait Bay besides recreational facilities, hospitals and other urban and industrial buildings existing along its coast (Al-Mussalam, 1999; Al-Mutairi *et al*., 2014a; El–Anbaawy, *et al*., 2017). The natural pollution factors like the discharges from Shatt Al-Arab and dust fallout also play significant role in increasing the input of nutrients such as nitrate (NO_3) and phosphate (PO_4) as well as suspended sediments and multiple pollutants into Kuwait Bay (Al-Ghadban and El-Sammak, 2005; Al-Yamani, 2008).

In general, the main threats of pollution sources along the coast of Kuwait Bay include the following: (1) twelve rain sewers, (2) nine emergency sewage discharges, (3) five marinas and two ports, and (4) three desalination and power plants. Thus, the need for this research arises from its two main aims: (1) intensive assessing current physio-chemical status of water quality on spatial bases including total suspended solid (TSS), pH, conductivity, salinity, silicate, nitrite, nitrate, ammonia, turbidity, temperature and Dissolved Oxygen (DO), and (2) examining trace element concentrations in the seawater and TSS.

2. Materials and Methods

2.1 Data source

Kuwait Environmental Public Authority (KEPA) installed five real-time monitoring buoys in Kuwait Bay (Figure 1), their data was used for a period of one-month (April-May, 2017). Water quality data, assessed by KEPA guidelines and standards, represented six parameters. The procedures to measure concentrations of turbidity and Dissolved Oxygen were based on Manual of Oceanographic Observations and Pollutant Analyses Methods (ROPME, 1999), while the pH, salinity, conductivity and seawater temperature were measured using the hydro-lab multi-parameters field instrument.

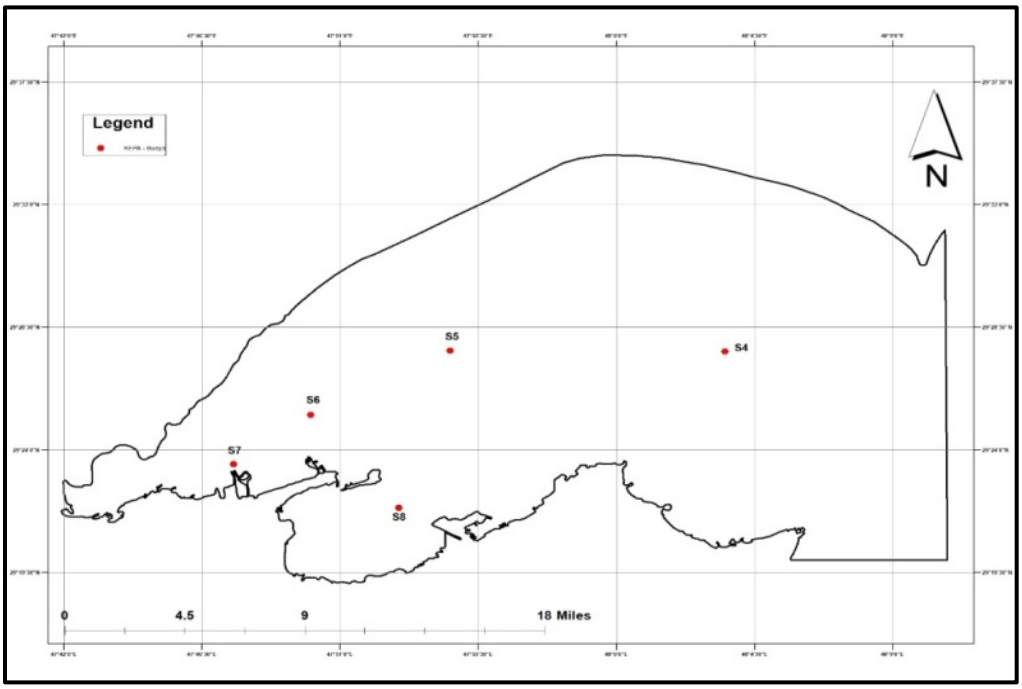

Fig. 1. Locations of marine water monitoring buoys of KEPA in Kuwait Bay.

In addition, 52 seawater samples were collected during the same period, at depth of 1 meter below sea surface at different locations covering the majority of Kuwait Bay area (Figure 2). The samples were examined and analysed in the Kuwait University laboratories to determine the following parameters: Total Suspended Solids (TSS), nutrients and selected trace elements.

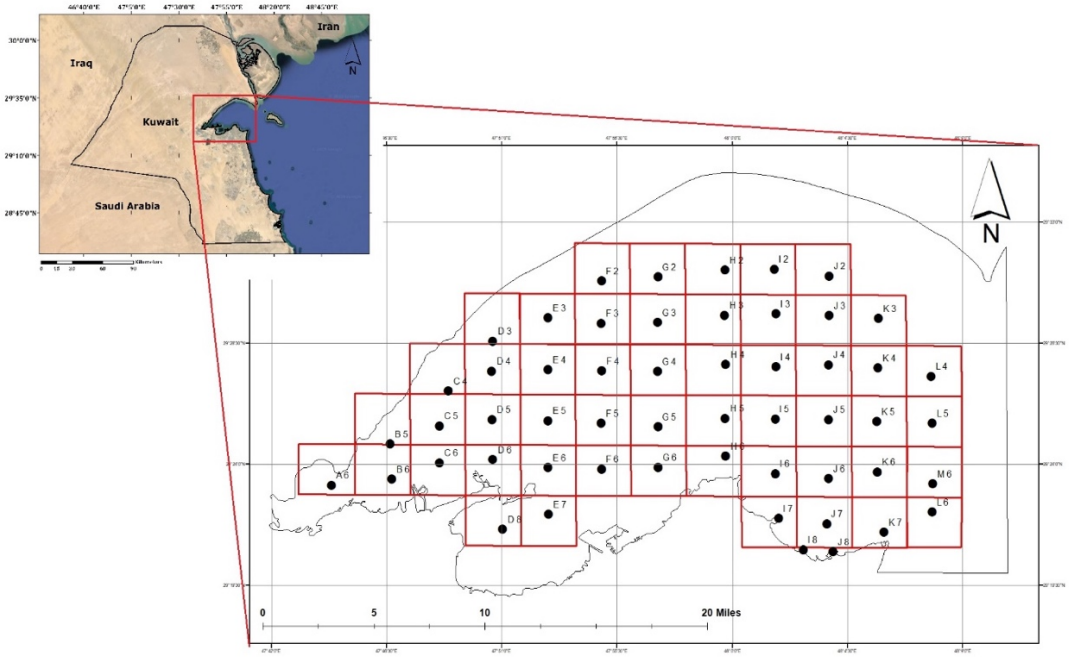

Fig. 2. Locations of seawater sampling sites in the Kuwait Bay.

TSS was measured according to the method of (MOOPA, 1999). TSS was determined by filtration of 100 ml of water through a previously dried and weighed Millipore membrane filter (porosity 0.45 µm). Filtration was done by using vacuum system under reduced pressure. The residue on the filter paper was washed several times by deionized water. The filters were then air dried in a desiccator, for at least 48 hours until constant weight was achieved. The filter papers were weighed to the nearest 3 decimal places and accordingly, the values of TSS were determined in mg/l. Inductively Coupled Plasma – Optical Emission Spectrometer (ICP-OES), Perkin Elmer, Optima 7300 was used to determine trace elements in 52-seawater samples and 24-TSS samples (Figure 3). According to US EPA method IO-3.2 (USEPA, 1999), two methods (No.3010A) and (No.3050B) were used for preparing water and TSS samples, respectively. The procedures were done by taking 0.5 g of TSS and 50 ml of seawater samples and place them in a polypropylene digestion vessel along with deionized water, 1:1 concentrated nitric (HNO_3) and hydrochloric (HCl) acids, and 30% hydrogen peroxide (H_2O_2) (for TSS sample) was added while heating at 95 ^oC then analysed by ICP.

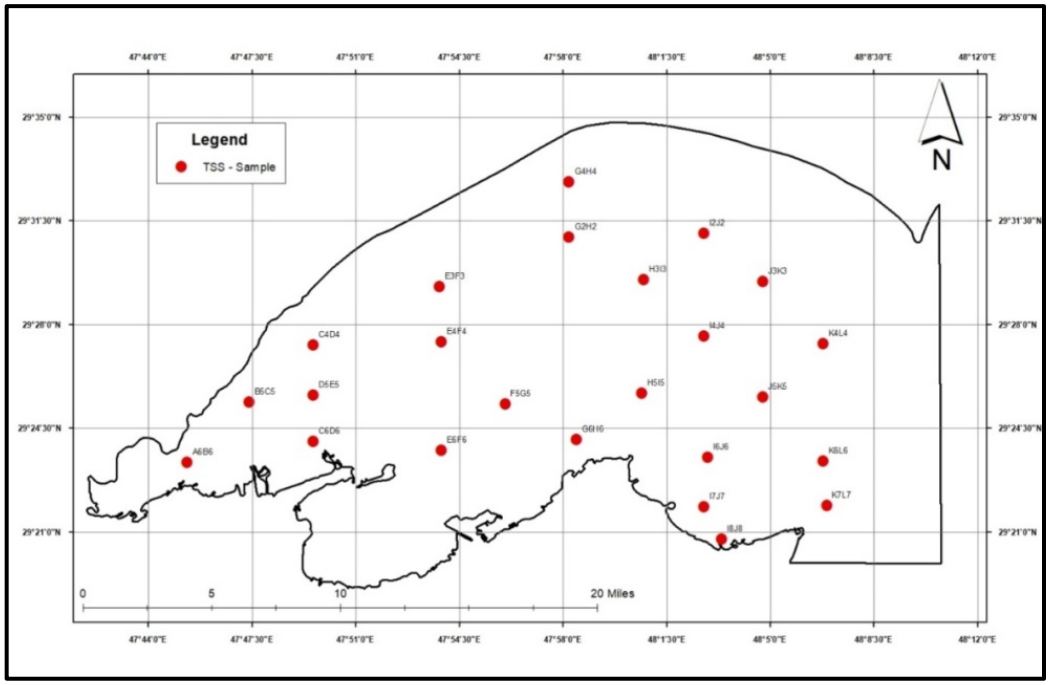

Fig. 3. Locations of the TSS samples used for ICP-OES analysis.

Seawater samples from each location were also analysed for nutrients, including Ammonia (NH_3), Nitrate (NO_3), Nitrite (NO_2) and Silicate (SiO_2), according to HACH DR/2500 method. Enrichment Factor (EF) method described by Sutherland (2000) was used to evaluate the potential impact of total suspended solids (TSS). The EF element can be compared with a pre-selected reference element and it is calculated using the following equation:

$$EF = [C_n \text{ (sample)}/ C_{ref} \text{ (sample)}] / [B_n \text{ (baseline)}/B_{ref} \text{ (baseline)}] \quad (1)$$

Where C_n (sample) is the determined value of a specific element in the TSS, C_{ref} (sample) is the preselected reference element value in the TSS, B_n (baseline) is the background value of the examined element in Kuwait sediments, B_{ref} (baseline) is the preselected reference element background value in Kuwait sediments.

3. Results

3.1 Seawater Quality

Table 1 describes statistics of elemental and physio-chemical parameters measured in Kuwait Bay water.

Table 1. Summary statistics of parameters measured for evaluating seawater quality in Kuwait Bay

	TSS	Ba	Ca	Na	K	Mg	Silicate	Nitrite	Nitrate	Ammonia
Units			Trace Elements mg/l					Nutrients µg/l		
Mean	25.3	14.75	380.5	9727.4	411.4	1432.3	333	235	83	43.5
Maximum	39.2	14.76	526.1	10510	639.1	1669.1	1270	791	1519	165
Minimum	13.2	14.73	223.1	8698	78	648.37	94.1	0	0	7.58
Std. Deviation	5.2	0.01	75.4	459	81.5	152.8	248	309	297	48
Median	24.7	14.75	385.9	9757.5	407.4	1449.5	268	154	8	15.7

	pH	Turbidity	Conductivity	DO	Salinity	Temperature
Units		NTU	ms/cm	mg/l	ppt	ºC
Mean	8.2	5.9	60.2	6	40.2	27.8
Maximum	8.5	17.4	66.7	7.8	43.9	30.8
Minimum	8	1.9	46	4.5	30.1	23.9
Std. Deviation	0.1	3.4	4.8	0.5	3.6	1.8
Median	8.2	4.7	62.1	6.1	41.9	28.3

3.1.1 Elemental analysis of seawater

Heavy elements in seawater samples at surface layers were only obtained for barium (Ba); other targeted elements were undetectable. Figure 4 shows the values and distributions of elements measured in Kuwait Bay. The concentration of total dissolved Ba ranged from 14.73 to 14.76 mg/l, with an average value of 14.75 mg/l; indicating similar concentration of Ba all over the Bay. The concentration of Ba is more than seven times higher than the KEPA maximum limits of Ba in industrial water waste permissible to be discharged into the seawater (2 mg/l). High standard deviation of other measured elements in seawater, include: Calcium (Ca), Magnesium (Mg), Potassium (K) and Sodium (Na), clarifies the wide range of data. Lower values of concentrations of these elements are found in the middle area of the Bay, while the higher concentrations are measured at the west side near Al-Doha power plants and Sulaibikhat Bay.

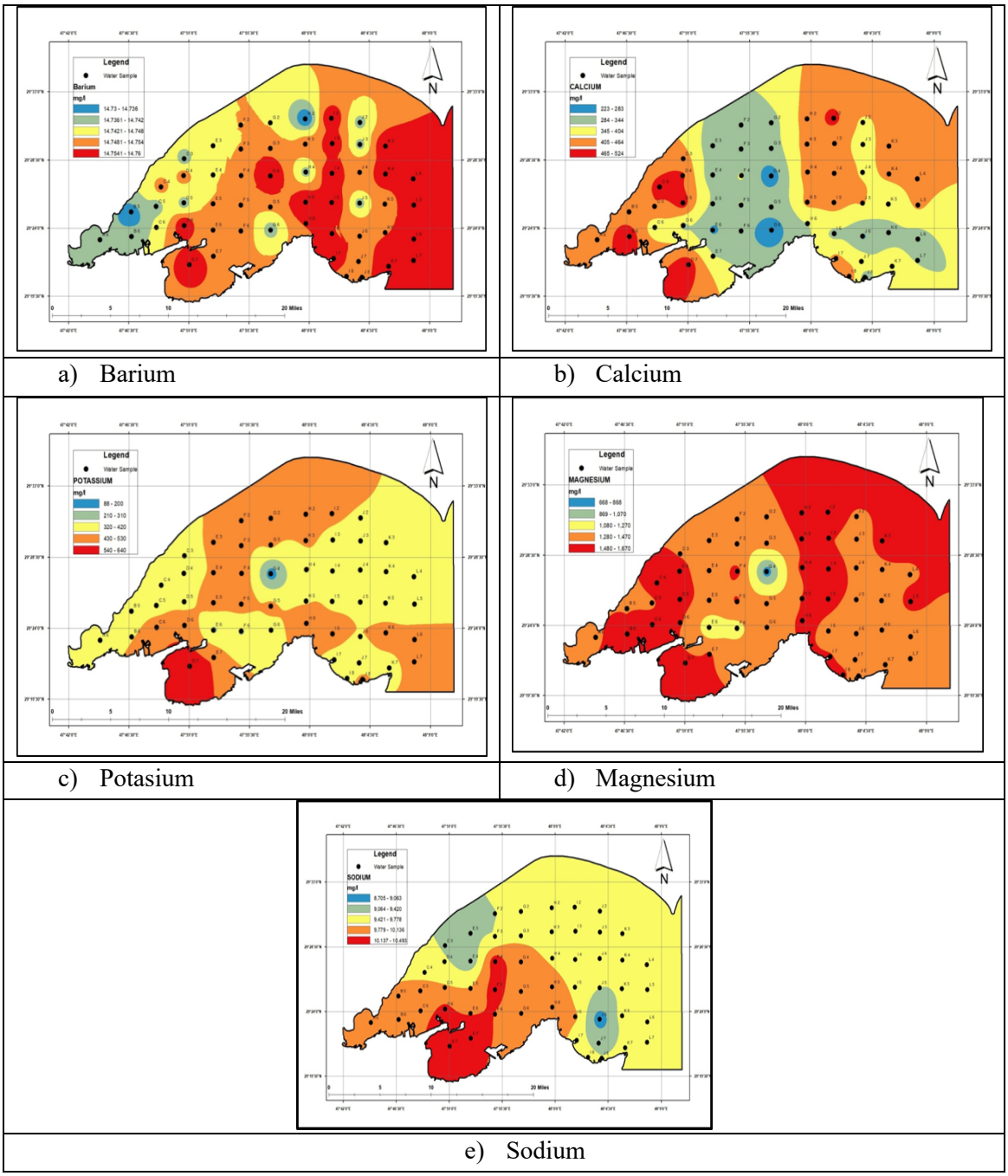

Fig. 4. Distribution of elements measured in Kuwait Bay's seawater.

3.1 Nutrients in seawater

Figure 5 shows the values and distributions of the following nutrient contents: Nitrate (NO_3), Ammonia (NH_3), Nitrite (NO_2), and Silicate (SiO_4) in seawater of Kuwait Bay. The mean concentrations of NO_3, NH_3, Nitrite NO_2, and SiO_4 are 83, 43.5, 235 and 333 µg/l, respectively. Higher values of nutrient contents are displayed around Sulaibikhat Bay and Al-Doha and Subiyah power plants in the south-west of the Bay. Furthermore, the maximum concentration of NO_3, 1519 µg/l, exceeded the K-EPA limits, 94.7 µg/l.

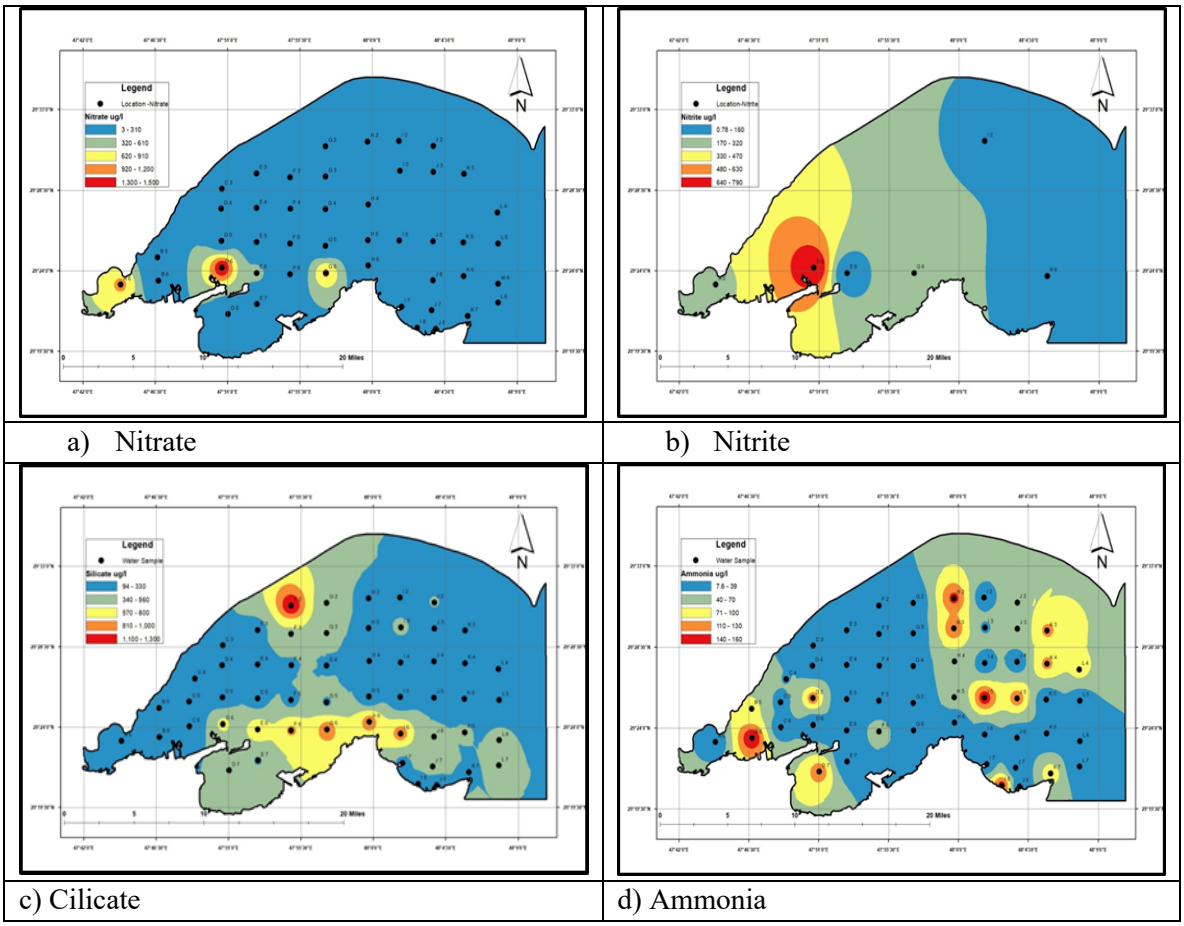

a) Nitrate | b) Nitrite

c) Cilicate | d) Ammonia

Fig. 5. Distribution of measured nutrients in Kuwait Bay's seawater.

3.2 Physio–chemical analysis of seawater

Figure 6 shows the distribution of physio-chemical parameters in the surface water of Kuwait Bay. The Dissolved Oxygen (DO) variations are minimal across the Bay with a mean value of 6.03 mg/l. Minimum concentration of DO (4.5 mg/l) was recorded at the west of the Bay near the power plants and sewer discharges, where organic matter degradation is common. This value is close to the KEPA standard limit (> 4.5 mg/l). The mean pH in Kuwait Bay was calculated at 8.2 with a maximum value of 8.5 recorded near the power and desalination plants in the west side of the Bay. The pH value decreases towards the Bay's entrance at the east side with limited spatial variation in pH value (0.5). The pH range between 6.5 and 8.5 is acceptable according to KEPA standards.

The mean surface water temperature was calculated to be 27.8 ^{0}C. The lower temperatures (23.9 ^{0}C) were recorded at the mouth of Kuwait Bay where water mixing is well, while higher values of water temperature (30.8 ^{0}C) were recorded near Doha and Subiya desalination and power plants and along the shore areas where water mixing is less. In general, the water temperature decreases towards the Bay's entrance at the east side with considerable spatial variation in temperature value (approximately 7 ^{0}C).

Highest salinity value (42.2 ppt) was located in the north western area, where the power and desalinization plants are controlling factor of salinity. The mean salinity value was calculated to be 40.2 ppt, while the minimum value was recorded at Sulaibikhat Bay (30.1 ppt); minimum conductivity value (55.6 mS/cm) was also recorded in the same area. In general, spatial distribution of conductivity values coincides with the salinity distribution pattern in Kuwait Bay seawater (Figures 6.c and 6.d).

The highest turbidity (8.4 NTU) was found in waters in the middle of the Bay; i.e., near Khor Al-Sabiya where the water circulation pattern and sediment transport are higher than other parts of the Bay and decrease southwards. Accordingly, Kuwait water clarity increased gradually from south to north and from near-shore to off-shore with minimal value of 4.4 NTU and a mean value of 5.9 NTU.

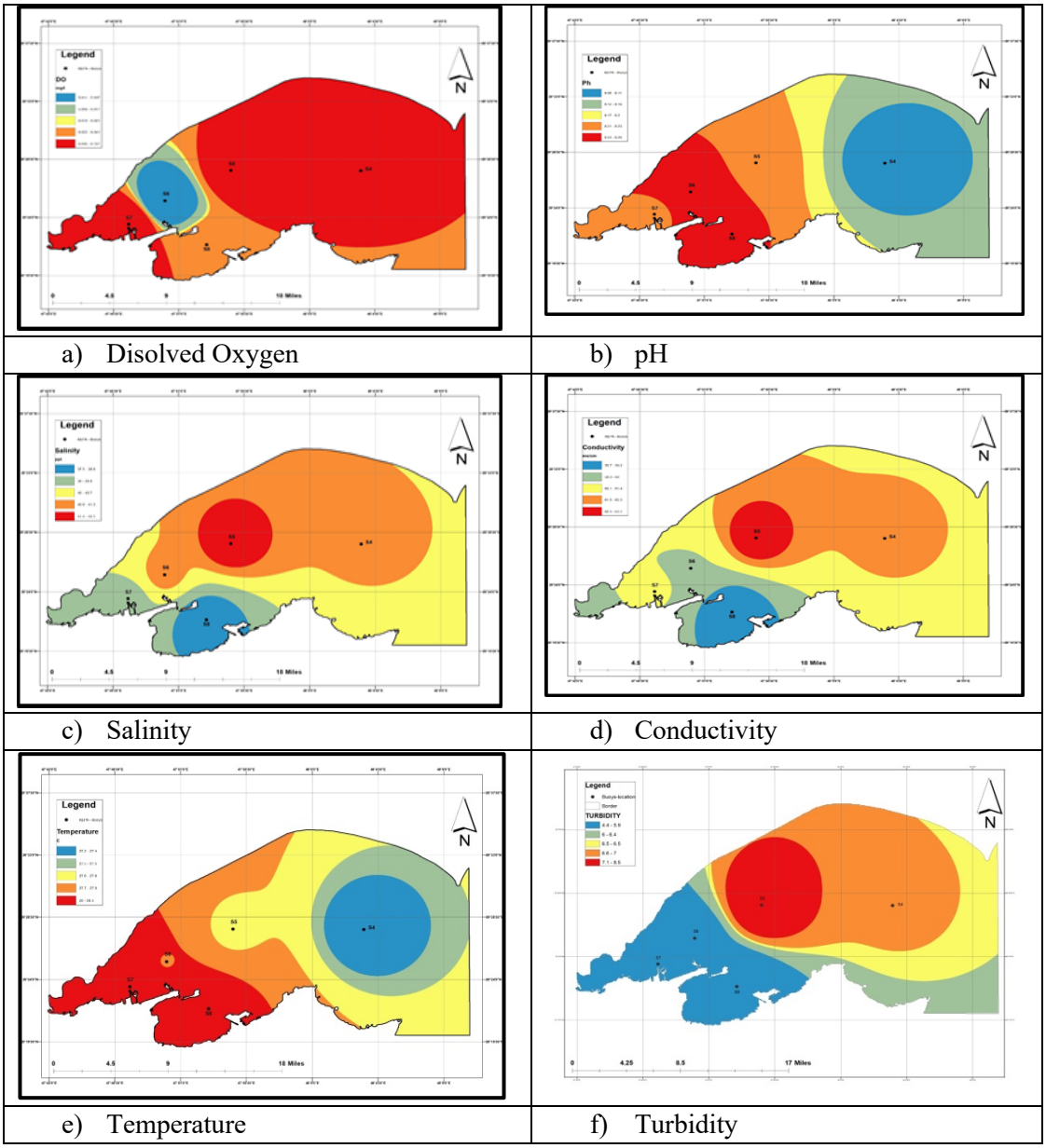

a) Disolved Oxygen
b) pH
c) Salinity
d) Conductivity
e) Temperature
f) Turbidity

Fig. 6. Distribution of physio-chemical parameters in Kuwait Bay's seawater.

Table 2 presents the analysis of correlations of the measured physio-chemical parameters in the Kuwait Bay. The analysis showed that negative correlations occurred among temperature, salinity and turbidity, while there is a weak positive correlation between pH and salinity as well as between salinity and turbidity. Such negative and week correlations indicate that the variation of each measured parameter is controlled by different source input. The week correlation between pH and salinity may be attributed to a similar input of waste brine planned for production at the three power plants erected along Kuwait Bay.

Table 2. Pearson correlations between Kuwait Bay physical parameters

Correlations					
pH		Turbidity	DO	Salinity	Temperature
pH	1				
Turbidity	-0.136	1			
DO	0.116	-.174*	1		
Salinity	0.104	.215**	-.221**	1	
Temperature	-.258**	-.415**	.277**	-.389**	1

**. Correlation is significant at the 0.01 level (2-tailed).

3.4 Total suspended solids (TSS)

Figure 7 shows the distribution of the TSS concentrations in the seawater of Kuwait Bay. The TSS has range concentration values of a minimum 13.2 mg/l and a maximum of 39.2 mg/l, with a mean value of 25.3 mg/l. The highest value of TSS concentration occurs along the south onshore of the Bay where ports, power plants and sewer discharges are erected as well as in the middle of the Bay where the turbidity is high.

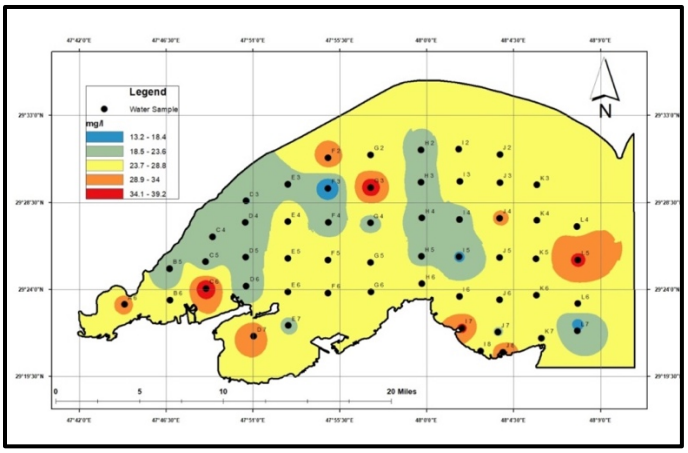

Fig. 7. Distribution map of TSS in Kuwait Bay.

3.4.1 Elemental concentration in the TSS and its distribution

The element concentrations in the TSS show that Cr and Fe concentrations were the highest in the samples collected from all sites with average concentration values of 15.6 and 13.8 mg/kg,

respectively (Table 3). The concentrations of the elements ranged from 0.1 (Hg) to 15.6 mg/kg (Cr). The mean concentrations of the elements in TSS decrease in the order of Cr (15.6), Zn (5.4), Se (4.5), Ni (3.8), As (1.2), Co (0.2) and Hg (0.1mg/kg); Pb was detected in 2 samples only with average concentration of 0.7 mg/kg (Figure 8). Ar and Se show high values at the Bay entrance in the eastside of the Bay and their values decrease in a systematic manner towards the west side of the Bay, while Ni, Co, Fe and Mn show high values at the south coast of the Bay as well as in Sulaibikhat Bay. On the other hand, Cr, Hg and Zn show higher values in the west part of the Bay near Al-Doha power plant and Shuwaikh port.

Table 3. Arithmetic mean concentrations and standard deviation of elements in TSS.

	Arsenic As	Cobalt Co	Chromium Cr	Iron Fe	Mercury Hg	Manganese Mn	Nickel Ni	Selenium Se	Zinc Zn
Units					mg/kg				
Mean	1.2	0.2	15.6	13.8	0.1	3	3.8	4.5	5.4
Maximum	1.8	0.7	19.3	36.4	0.36	4.4	12.9	10.3	19.5
Minimum	0.8	0	12.9	1.2	0	2.2	0	2.4	1
Std. Deviation	0.2	0.2	1.6	7.8	0.1	0.5	4	1.7	4.1
Median	1.2	0.1	15.6	14	0.1	2.9	1.3	4.3	5.1

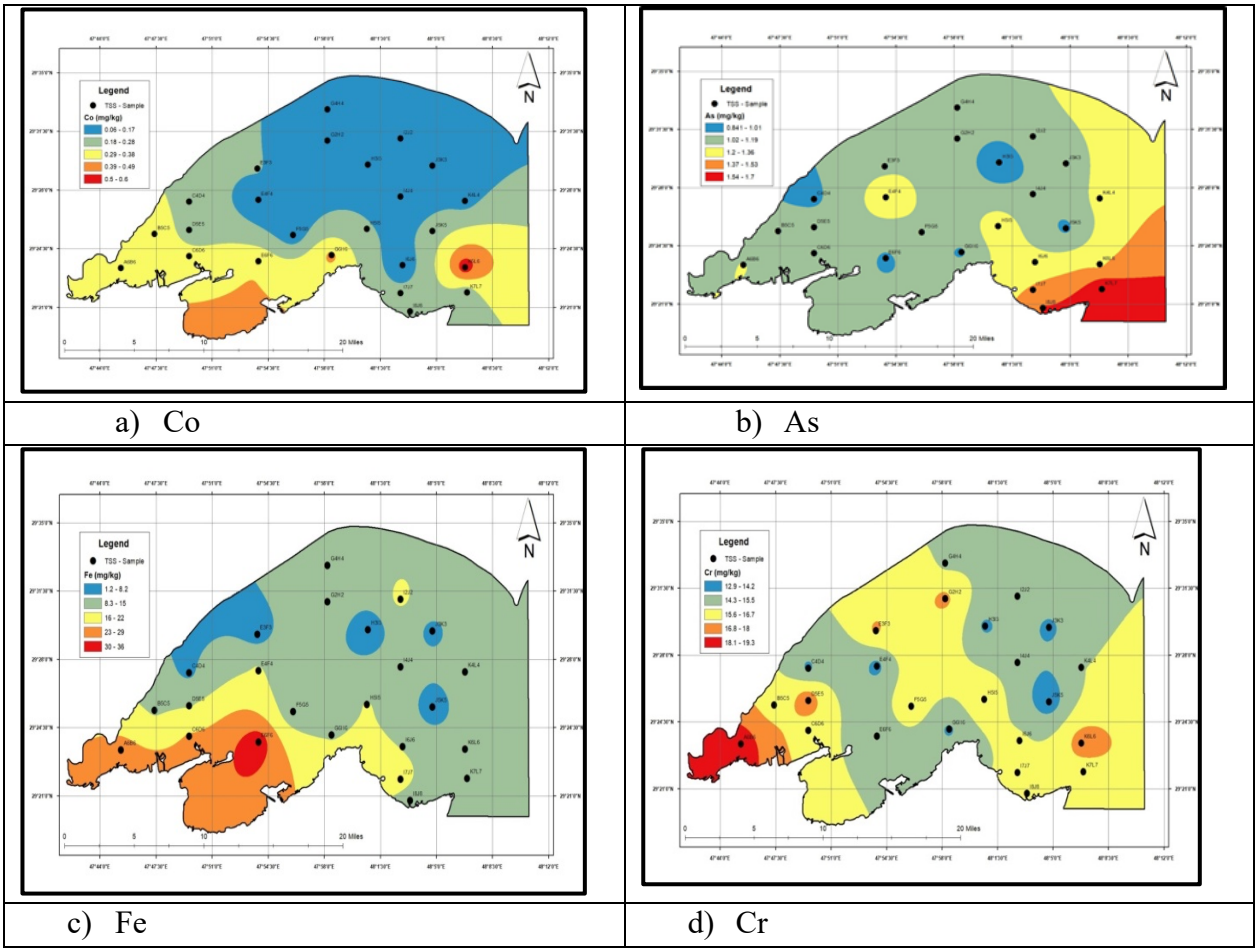

a) Co b) As

c) Fe d) Cr

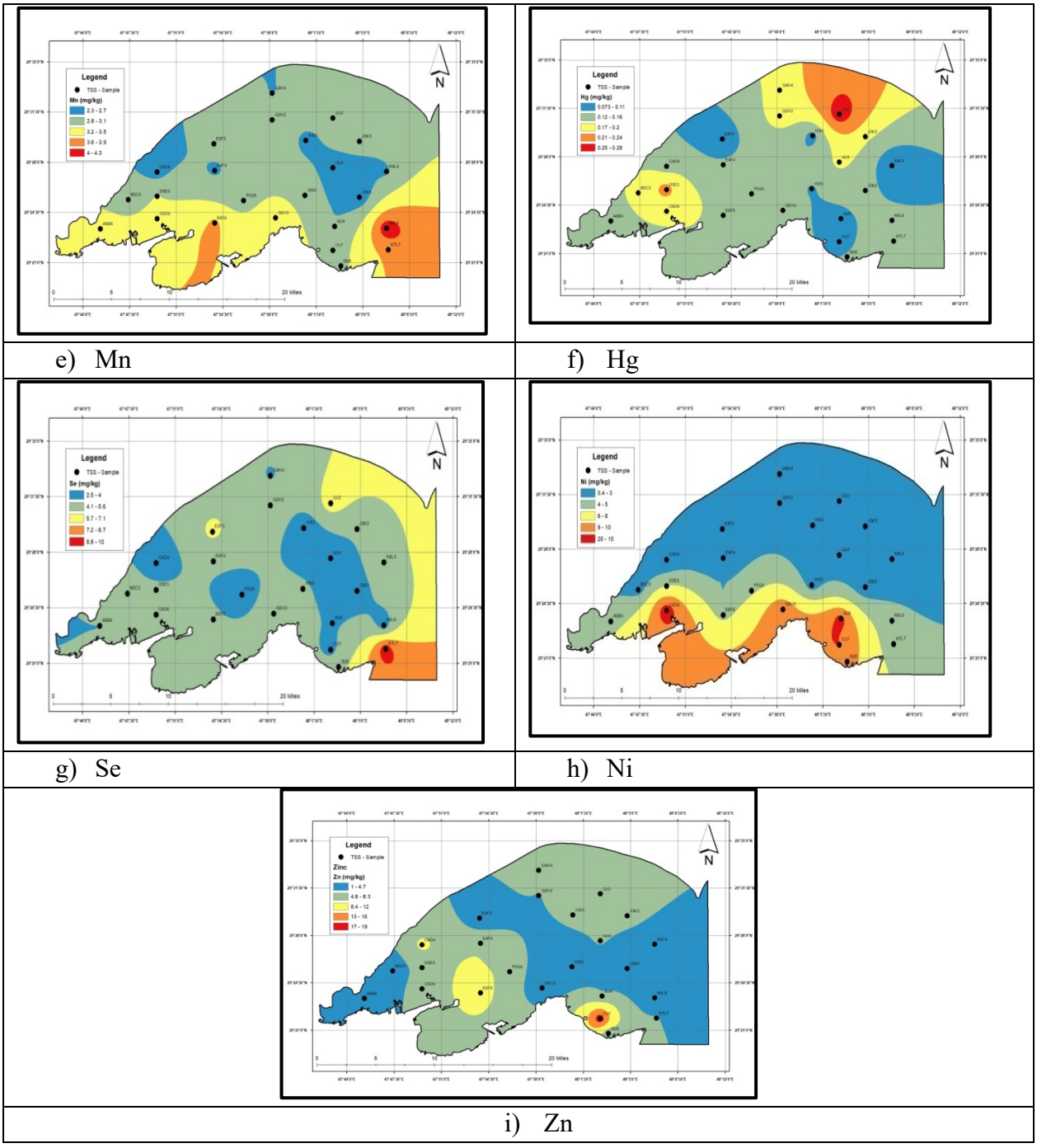

Fig. 8. Distribution map of elements concentration in TSS in Kuwait Bay's seawater.

On comparison of the measured trace elements in the TSS with the Marine Sediment Quality Guideline (1999) and Ontario Provincial Sediment Quality Guideline (2018) (Table 3), it was found that the heavy elements in the TSS, except for Hg, are within acceptance limits. The result also shows that the heavy element contamination in TSS is higher than the contamination in seawater. This indicates that the sediments can adsorb and adhere to the contaminants to their bodies more than seawater.

Table 4. Comparison of the trace element concentration in the TSS in Kuwait Bay with Marine Sediment Quality Guideline (ISQGs) and Ontario Provincial Sediment Quality Guideline (OPSGs) (Ontario, 2018; CCME, 1999)

Element	Maximum Level Kuwait Bay	Lowest Effective Level ISQGs (mg/kg)	OPSGs
Cr	19.3	52.3	26
Fe	36.4	_	2%
Zn	19.5	124	120
Ni	12.9	_	16
Mn	4.4	_	460
As	1.2	7.24	6
Hg	0.36	0.13	0.3

3.5 Enrichment factor (EF) analysis

The elements content in Kuwait soils was determined by Al-Awadhi and Al-Shuaibi (2013) by analysing 184 top surface soil samples collected from different types of surface sediments. The results of the soil analysis are presented in Table 5 that shows the results of 5 toxic elements analysed in TSS samples. Their average concentrations are lower than the soil background values from the desert and coast of Kuwait by 1.6 to 22 times. Based on the finding of Al-Awadhi and AlShuaibi (2013), Mn is considered the baseline content of the reference element (B_{ref}) in Kuwait sediments. Accordingly, the results of the EFs for the elements in TSS in Kuwait Bay seawater are presented in Table 6, using Equation (1). Table 6 shows that most examined elements have EFs mean less than or equal to 20 with a decreasing order of their overall contamination degrees of TSS in the order of Cr>Zn>As>Ni>Co>. Table 7 presents five contamination categories recognized based on the EF values (Sutherland, 2000; Loska and Wiechuya, 2003). Thus, elements having maximum EF higher than 20, such as Cr (25.6) can be presented as a significant contamination. On the other hand, Co (1.6) represents minimal contamination, while Ni (4.9) and As (12.2) represent moderate and significant enrichments, respectively.

Table 5. Elemental contents in soil of Kuwait (mg/kg) compared to element contents in TSS collected in Kuwait Bay's seawater

Element	**Soil (N=184) mg/kg**	**TSS (N=24) mg/kg**	**Times lesser**
As	25.6	1.17	22
Co	3.7	0.2	18.5
Cr	25.6	15.63	1.6
Ni	22	3.7	6
Zn	18.4	5.3	3.4

Table 6. Results of the enrichment factor (EF) for different elements in the TSS samples

EF/Sample No.	As	Co	Cr	Ni	Zn
A6B6	8.8		27.8	6.2	2.0
B5C5	8.8	3.6	26.6	2.3	4.4
C4D4	8.9		26.5	1.3	25.1
C6D6	8.6		23.5	18.6	14.9
D5E5	9.1	1.7	27.9	0.0	10.9
E3F3	9.7	1.9	28.9	1.7	2.8
E4F4	12.7	0.5	25.1	0.9	21.1
E6F6	6.3	3.2	19.1	5.9	17.9
F5G5	10.4	0.2	29.4	0.0	18.8
G2H2	8.4	0.4	26.4	3.5	9.3
G4H4	10.8	0.0	27.2	1.7	19.1
G6H6	6.4	3.6	18.8	13.7	2.5
H3I3	7.4		25.9	1.6	14.6
H5I5	11.4		27.6	2.0	2.5
I2J2	9.6	1.1	25.2	4.1	13.1
I4J4	9.8	1.2	27.9	1.2	13.1
I6J6	10.8	0.4	27.2	20.0	11.5
I7J7	11.3		25.3	16.7	43.2
I8J8	12.8	2.2	26.9	0.0	10.1
J3K3	9.2		23.4	3.6	12.8
J5K5	9.6		27.6	1.2	3.0
K4L4	11.9	0.9	28.5	1.7	8.8
K6L6	7.0	4.2	19.7	4.3	1.6
K7L7	11.9	1.1	21.3	5.1	9.2
Average	9.6	1.6	25.6	4.9	12.2

Table 7. Contamination categories based on EF values (Sutherland, 2000)

Enrichment factor (EF)	Comment
EF < 2	Deficiency to minimal enrichment
EF = 2–5	Moderate enrichment
EF = 5–20	Significant enrichment
EF = 20–40	Very high enrichment
EF > 40	Extremely high enrichment

4. Discussion

Kuwait Bay is considered as one of the most important marine features in the Arabian Gulf. The location of the Bay is surrounded by residential areas, industries, harbours, and Jaber Causeway. Several sources of potential stress and pollution were identified around the Bay mainly from

sewage and Industrial effluent. The only polluted element detected in the seawater was Ba. The possible pathways by which Ba can enter an aquatic environment include atmospheric transport and deposition, sediment suspension and biological behavior. The emitted source of Ba could possibly be associated with lubricating oil additives, fuel synthesis, fuel combustion, phosphate fertilizers, and sewage sludge (Al-Ghadban and El-Sammak, 2005).

Large amounts of nutrients were recognized in seawater; namely nitrate (NO_3), ammonia (NH_3), nitrite (NO_2), and silicate (SiO_4) in Kuwait Bay. Major contributors to these nutrients are Shatt Al-Arab, sewage outlets, urban run-off, and particulates deposited by dust storms (Al-Yamani *et al*. 2004; El-Sammak *et.al.,* 2005). High concentrations of nutrients were found around emergency sewer outlets, where effluents and raw sewage discharges exist. This confirms the role of contributing anthropogenic activities, including wastewater from treatment plants, in increasing nutrients influx such as nitrites and ammonia in Kuwait Bay (Al-Abdulghani, *et al*.,2013). Generally, concentrations of these nutrients increase during winter and spring (Al-Yamani *et al.,* 2004).

The lower values of Dissolved Oxygen (DO) recorded in some areas in Kuwait Bay can also be associated with low mixing of the water column. Fluctuation of DO levels over the Bay may be due to many factors such as: high water temperature, sea plants, wave action and longshore currents direction, besides the amount of discharged organic matters such as sewage and industrial waste (Al-Yammani, *et al.,* 2004; Al-Shemmari, 2000). The mean concentration of DO in the Bay was calculated to be 6 mg/l, and according to Weiner (2000), the seawater with DO concentration between 4.5- and 6.5mg/l is classified as moderately polluted water. The DO reduction due to high temperature besides sewage waste impact can also minimize metabolic rates which produce dwarfed species and cause different types of deformations for marine species such as thin walled and less ornamentation in shells (Boltovasky, *et al.,* 1991; *Alve,* 1991).

The limited pH variation in surface water of Kuwait Bay can be linked to the following factors: sewage and waste brine discharges, and high productivity and decomposition rates (Al-Shemmari*, et al*., 2002; Al-Yamani, *et al*., 2004). However, the high mixing of seawater pH near the brine outfall will most likely affect the surrounding waters (El–Anbaawy, *et al.,* 2017). However, considerable spatial variations in temperature values (approximately 7 °C) were recorded across the Bay. Al-Rashidi *et al.* (2009) indicated that desalination and power plants contribute 13% of decadal increase in the seawater temperature in Kuwait Bay and the seawater temperature increases by 0.6 ºC per decade; i.e., about three times higher than the global average rate reported by the Intergovernmental Panel on Climate Change (IPCC) (Al-Mutairi *et al.,* 2014b). Also, the increase of seawater temperature directly affects the marine plants and fish and changes their life (Mann and Lazier, 2005). Therefore, high seawater temperature weakens the fish immune system and creates unstable conditions that may lead to massive Fish kill (Al-Marzouk, *et al*., 2005).

Temperature and salinity could affect directly the marine fauna and flora and alter marine ecosystem (Dawoud, 2012; Al-Dousari, *et al.,* 2012). Also, the increase of temperature and salinity will cause the concentration and saturation of oxygen to decrease, and may result in disorientation of marine life (Uddin, 2014). However, the salinity spatial distribution showed little variations throughout the Kuwait Bay. The lower salinity in Sulaibikhat Bay, for example, may be attributed

to the large amounts of sewage discharges (fresh water) in that area, while areas of Al-Doha and Shuwaikh power plants, where the hyper saline brine water is released, did not show significant salinity variation, indicating that the salinity of the brine discharged into the seawater has a limited spatial impact on the seawater salinity of the Bay. Generally, the mass influx of fresh water flowing from Iraq's rivers play a vital role in salinity variation in Kuwait Bay (Al-Abdulghani *et al*., 2013).

The turbidity values fluctuate over the seawater of Kuwait Bay, the highest turbidity level occurs in its center. This finding also concurs with the study of Al-Sahli (2009). Shatt Al-Arab discharge and dust storms may play an important role in increasing the turbidity of Kuwait Bay's waters (Al-Ghadban and A. El-Sammak, 2005), beside anthropogenic activities taking place around the Bay, such as the Subiya and Doha power plants (Al-Rashidi, *et al.,* 2009).

Furthermore, the distribution pattern and genesis of total suspended solids (TSS) indicate the possibility of tidal currents' effect and dust fallout's contribution (Al-Ghadban and El-Sammak, 2005) as well as, to a lesser extent, the effect of Shatt Al-Arab—especially in the northeastern part of Kuwait Bay. According to Al-Ghadban and El-Sammak (2005), the counter- clockwise eddy currents and the effect of the bottom currents are the main reasons of trapping the sediments in the water column.

The enrichment factor EF can be used to distinguish between metals produced from human activities and those from natural procedures, and to assess the level of anthropogenic influence. Cr shows maximum enrichment relative to the upper continental crustal component (Mn), while Zn, As, Ni and Co show lesser enrichment, respectively. Clear fluctuating range in the concentrations of hazard elements in Kuwait Bay could be attributed to different anthropogenic inputs like industrial. Locally, there are many sources of the anthropogenic activities surrounding Kuwait Bay including the desalination and power plants, rain and sewage discharges and recreational activities. These anthropogenic influences can affect the ecosystem of Kuwait Bay. For example, Bu-Olayan and Thomas (2008) have found out that the concentrated trace metal found in mullet fish reared in Kuwait Bay were higher than the mullets found in other coastal waters. According to Al-Ghadban *et al.* (2002), the desalination and power plants processes are responsible for 22% of total water pollution where the discharged sewage are responsible of 43% of total water pollution in Kuwait Bay.

5. Conclusions

In this study, the intensive anthropogenic activities along the coastline of Kuwait Bay have contributed in changing seawater quality in some areas of the bay. Since Kuwait has invested in many projects around the Kuwait Bay, the results of this study will be useful for the integrated and sustainable development for planning and implementation of new coastal projects. Thus, the spatial variations of seawater characteristics, carried out in this study, will be important parameters for assessing the probability and residual impacts on the marine environment. The present investigations did not show that the entire study area is polluted or quality-reduced except some parts close to nearshore waters of Kuwait Bay, where sources of the anthropogenic activities exist including the desalination and power plants, rain and sewage discharges and recreational activities.

TSS analysis showed moderate element pollution enrichment, on average, relative to the upper continental crustal component (Mn). Potential impacts of salinity and temperature at the vicinity of the power plants outlets were clearly recognized; found to be 3.7 ppt and 3^{o}C above mean salinity and temperature of seawater in Kuwait Bay, respectively. While DO reduction rate was recognized near in the vicinity of sewage water outlets and it was found to be 1.5 mg/l below mean DO value. The increase of Biological Oxygen Demand (BOD) will cause Fishkill in the areas where the salinity and temperature are high especially in summer times.

ACKNOWLEDGEMENTS

1- The National Unit for Environmental Research and Services – NUERS with Project No. SRUL01/13, Faculty of Science, Research Sector, Kuwait University.
2- The Environmental Public Authority – EPA for data source.

References

Al-Abdulghani, E., El-Sammak, A. & Al-Sarawi, M. (2013) Enviromental Assessment of Kuwait Bay: an Integrated Approch. **Coastal Conservation**, 3(**17**): 445-462.

Al-Awadhi, J. & Al-Shuaibi, A. (2013) Dust Fallout in Kuwait City: Deposition and Characterization. **Science of the total Enviroment**, 46(**2**): 139-148.

AL-Dousari, A., AL-Ghadban, A. N. & Sturchio, N. (2012) Marine Enviromental Impact of Power-desalination Plants in Kuwait. **Aquatic Ecosystem Health & Management**, 15(**1**): 50-55.

Al-Ghadban, A. (2004) Assessment Suspended Sediment in Kuwait Bay Using Landsat and Spot Images. **Kuwait Journal of Science and Engineering**, 31: 155-172.

Al-Ghadban, A., Al-Majed, N. & Al-Muzaini, S. (2002) The State of Marine Pollution in Kuwait: Northern Arabian Gulf. **Technology**, 8: 7-26.

Al-Ghadban, A. & El-Sammak, A. (2005) Sources, Distibution and Composition of the Suspended Sediment, Kuwait Bay, Northern Arabian Gulf. **Arid Enviroments**, 4(**60**): 647-661.

Al-Marzouk, A. et al. (2005) Fish Kill of Mullet Liza Klunzingeri in Kuwait Bay: The Role of Streprococcus Agalactiae and the Influence of Temperature**. Asian Aquaculture**, 143-153.

Al-Mussalam, F. (1999) Marine ecology and fisheries in Kuwait Bay with emphasis on the ecological impact of anthropogenic activities. Proceedings of the international conference on coastal zone management on development in the Gulf Region, Environmental Public Authority. Kuwait. 135–152.

Al-Mutairi, N., Abahussain, A. & Al-Battay, A. (2014a) Enviromental Assessment of Water Quality in Kuwait Bay. **Enviromental Science and Development**, 5(**6**): 527-532.

Al-Mutairi, N., Abahussain, A. & El-Battay, A. (2014b) Spatial and temporal characterizations of water quality in Kuwait Bay. **Marine pollution bulletin**, 83: 127-131.

Al-Rashidi, T., El-Gamily, H., Amos, C. & Rakha, K. (2009) Sea Surface Temperature Trends in Kuwait Bay, Arabian Gulf. **Natural Hazards**, 50(**1**): 73-82.

Al-Sahli, M. (2009) Characterizing surface temperature and clarity of Kuwait's Sea waters using remotely sensed measurement and GIS analyses, USA: Kansas Univ.

Al-Shemmari, H. (2000) Effects of Seasonal Variation on Trace Metal Concentration in the Sediments of Kuwait Bay, s.l.: **Kuwait Institue for Scientific Reasearch KISR**.

Al-Shemmari, H., Al-Senafi, M. & Al-Fayad, K. (2002) Effects of Seasonal Variation on the Water Quality in Kuwait Bay. Kuwait, EPA.

Alve, E. (1991) Benthic Foraminifera in Sediment Cores Reflecting Heavy Metal Pollution in Sorfjord, Western Norway. **Foraminifera Research**, 21: 1-19.

Al-Yamani, F., Bishop, J., Ramadan, E., Al-Husaini, M. & Al-Ghadban, A. (2004) Oceanography Atlas of Kuwait Bay, Kuwait: **Kuwait Institue for Scientific Research KSIR.**

Al-Yamani, Y. (2008) Importance of the Freshwater Influx from Shatt Al-Arab River on the Gulf Marine Enviroment. Basel, Birkhauser, 207-222.

Anderlini, V., Jacob, J. & Lee, J. (1982) Atlas of Physical and Chemical Oceanographic Characteristics of Kuwait Bay, Kuwait: **Kuwait Institue for Scientific Research KISR**.

Boltovasky, E., Scott, D. & Medioli, F. (1991) Morphological Variation of Benthic Foramina Feral Test in Response to Change in Ecological Parameters a Review. **Palentology**, 65: 175-185.

Bu-Olayan, A. & Thomas, B. (2008) Trace Metal Toxicity to the Body Structures of Mullet Fish Liza KlunZingeri. **International Journal of Enviromental Research**, 2(**3**): 249-254.

CCME, (1999) Canadian Sediment Quality Guidelines for the Protection of Aquatic Life. Canadian Environmental Quality Guidelines, s.l.: Canadian Council of Ministers for the Environment.

Dawoud, M. (2012). Enviromental Impacts of Sewater Desalination: Arabian Gulf Case Study. **International Journal of Enviromental and Sustainability**, 1(**3**): 22-37.

El-Anbaawy, M., Abdelhalim, A., Ndail, S. & Al-Sarawi, M. (2017) Environmental Impact of Effluents Generated from Al Subiya Power Plant on the Northern Kuwait Bay. **American Journal of Enviromental Protection**, 6(**5**): 120-139.

El-Sammak, A., Karam, Q. E., & Bu Shaiba, A. (2005) Preliminary assessment of the geological and water environments in Kuwait Bay: identification of hot-spot areas. **Kuwait Institute for Scientific Research**, Report No. KISR, 7665.

Loska, K. & Wiechula, D. (2003) Application of Principle Component Analysis for the Estimation of Source of Heavy Metal Contamination in Surface Sediments from the Rybnik Reservoir. **Chemosphere**, 51(**7**): 23-33.

MOOPA, (1999) Manual of Oceanographic Observations and Pollutant Analyses. 3 ed. Kuwait: Regional Organozation for the Protection of the Marine Enviroment.

Ontario, (2018) Ontario. [Online]Available at: https://www.ontario.ca/document/guidelines-identifying-assessing-and-managing-contaminated-sediments-ontario/identification-and-assessment#fna1 [Accessed 17 April 2018].

Pokavanich, T. & Al-Banaa, K. (2012) Role of water temperature variability to water circulation in an arid meso-tidal shallow bay in Kuwait. 8th International Confernce on Coastal and Port Engineering Developing Countries. Chennai, India.

Rakha, K., Al-Banaa, K. & Al-Hulail, F. (2010) Flushing characteristics of Kuwait Bay. **Kuwait Journal of Science and Engineering**, 37: 111-125.

ROPME, (1999) Manual of Oceanographic Observations and Pollutant Analyses Methods, ROPME, Kuwait: s.n.

Sutherland, R. (2000) Bed Sediments Associated Trace Metals in an Urban Stream, Oahu, Hawaii. **Environ Geol**, 39: 611-627.

Uddin, S. (2014) Environmental Impact of Desalination Activates in the Arabian Gulf. **International Journal of Enviromental Science and Development** , 5(**2**): 114-117.

USEPA, (1999) Compendium of methods for the determination of inorganic compounds in ambient air, NewYork: s.n.

Weiner, R. (2000) Enviromental Chemistry. Canada: Gutenberg Press.

Submitted: 20/09/2021
Revised: 03/01/2022
Accepted: 04/01/2022
DOI: 10.48129/kjs.16319

Kuwait J.Sci., Vol.50, No.(1A),January.2023,pp(49-70)

Facies analysis and depositional framework of Late Permian-Jurassic sedimentary successions, Western Salt Range, Pakistan: implications for sequence stratigraphic trends and paleogeography of the Neo-Tethys Sea

Abdul Basit[1], Muhammad Umar[2,*], Muhammad Jamil[3,4], Muhammad Qasim[4]

[1]*Geological Survey of Pakistan, Quetta, Pakistan*
[2]*Dept. of Earth Sciences, The University of Haripur KPK, Pakistan*
[3]*Dept. of Geosciences, Universiti Teknologi PETRONAS (UTP), Seri Iskandar, 32610 Perak, Malaysia*
[4]*Dept. of Earth Sciences COMSATS University Islamabad, Abbottabad campus, Pakistan*

*****Corresponding Author: umarkhan09@yahoo.com*

Abstract

Facies analysis and T-R sequence stratigraphic approach of Late Permian to Jurassic sedimentary units in Western Salt Range, Pakistan were accomplished to construe the depositional environments and basin evolution. The analysis affirms the rendition of sequence stratigraphic trends and paleogeography of first megasequence phase of Neo-Tethys Sea. Sedimentological contingents, T-R sequence stratigraphic framework and sea level curve of the strata argue active tectonic's effects on sedimentation. During Late Permian, the rift related magmatic activities deceased, which imparted to the onset of transgression and deposition of shelf carbonates with retrogradational (transgressive) parasequence sets in Wargal Formation. Respective rifting and tectonic uplift events induced the sea level fall ascertaining the onset of terrigenous shelves and deltaic successions in terminal Permian and Early-Mid Triassic with an enlighten switch from agradational to progradational parasequence sets (regressive parasequences) in Chhidru, Mianwali and Tredian formations. The closure of Paleo-Tethys and emergence of semi-arid hot tropical climate throughout Late-Triassic, led the onset of tidal-lagoonal environments and deposition of retrogradational (transgressive) parasequence sets in Kingriali Formation. During Early Jurassic, a well-known northward drift of Pangaea ensued in global cooling and increased humidity, which consequently stimulated clastic-carbonate sedimentation of Datta and Samana Suk formations with progradational and retrogradational parasequence sets respectively.

Keywords: Basin evolution; depositional environments; neo-tethys sea; sequence stratigraphic trends; western salt range.

1. Introduction

The evolution of sedimentary basins is ascertained by variety of factors e.g., fluctuation in sea level (sequence stratigraphic trends), tectonics, paleogeographic position, and sediment influx (clastic or carbonate factories). Well exposed complete Late Permian-Jurassic successions in Western Salt Range (WSR) provide an opportunity to empathize the paleoenvironments, paleogeographic

evolution and sequence stratigraphic trends such as transgressive – regressive cycles, associated systems tracts and maximum flooding surfaces. These changes have induced the closure of Paleo-Tethys and opening of Neo-Tethys (Wignall & Hallam, 1993). Salt Range intends a well-distinguished fold-and-thrust belt, evolved at the South of the Himalayan foothills in response of an ongoing collision between Eurasian and Indian Plates (Baker *et al*., 1988; Farooqui *et al*., 2019; Qureshi *et al*., 2019; Umar *et al*., 2020). The Salt Range is regarded as the youngest compressional feature of Himalayan Foreland owing to its southward propagation. The generalized stratigraphy and tectonic settings are shown in the Figure 1.

A variety of sedimentary rocks e.g., sandstone, shale, limestone, and dolomite formed in different sedimentary environments through geologic time, ranged from Late Permian to Miocene in WSR. The Late Permian- Jurassic successions of WSR display clastic, siliciclastic and carbonate depositional systems. Various stratigraphic formations of the successions are delineated as source and producing reservoirs (e.g., Nazir *et al*., 2020) in various wells of Salt Range and Potwar Plateau. Facies/microfacies analysis, depositional architecture and sea level fluctuations play significant role in petroleum play analysis (Catuneanu & Zecchin, 2010; Umar *et al.*, 2016). Moreover, global, local tectonics and sea level fluctuations directly affected the sedimentation (Umar *et al*., 2011; Farooqui *et al*., 2022). The present study is planned to apply lithofacies/microfacies analysis to interpret depositional environments, tectonic influence on sedimentation and sequence stratigraphic framework of Late Permian-Jurassic strata.

2. Lithofacies-Microfacies Analysis

Five microfacies have been encountered in Wargal Formation (Figure 2a), denoted by WMF. These are Bioclastic wackestone-packstone, Bioclastic peloidal mudstone, Mudstone-wackestone, Calcic mudstone and Dolomitic mudstone microfacies (Table 1, Figure 2b-f). Bioclasts of bryozoans, bivalves, foraminifera, brachiopods, crinoids, gastropods, undifferentiated and micritized bivalves with allochems such as, ooids, peloids, interclasts and lumps are characteristic features of identified microfacies. These microfacies refers various shelf environments i.e., restricted middle-outer shelf, open marine, low energy inner shelf below fair-weather wave base, deep marine low energy and restricted lagoonal conditions (e.g., Scholle & Ulmer-Scholle, 2003; Flügel, 2004; Tucker, 2006). The distinguished five microfacies and lithofacies (Table-1) in mixed carbonate-clastic Chhidru Formation (Figure 3a) are Interbedded sandy mudstone and shale, Calcareous massive sandstone, Thick bedded massive sandstone lithofacies, Sandy Mudstone-Wackestone and Sandy Wackestone-Packestone Microfacies. Wackestone-Packstone, Mudstone fabrics, associated fauna (fusulinids, bryozoans brachiopod, gastropods), detrital grains and bioturbation (Figure 3b-i) in sandstone exhibit low energy calm proximal, open marine, tropical-subtropical, distal middle and inner shelf environments (Scholle & Ulmer-Scholle, 2003).

Six lithofacies and microfacies are discerned in Mianwali Formation (Figure 4a) included Dolostone, Ceratite Wacke-Packstone, Bivalve Wackestone Microfacies, Shale, Parallel and Cross laminated sandstone facies (Figure 4b-i). The existence of dolomite rhombs, conodonts, ceratite, gastropods, pelecypods, quartz grains, bioclasts of ammonoids, echinoderms, few glauconite,

peloids, grain supported fabric and mottling denote the open shallow marine, restricted to storm dominated inner shelf, low energy deeper part of inner and middle shelf (Scholle & Ulmer-Scholle, 2003; Milsom & Rigby, 2010; Iqbal *et al.,* 2014).

Table 1. Brief characteristics of identified lithofacies and microfacies with their corresponding depositional environments in Late Permian-Jurassic succession, WSR.

Formation Name	Facies/Microfacies	Description	Depositional Environments
Samana Suk Formation (Jurassic)	Mudstone Microfacies (SSM-1)	Medium bedded, light grey limestone, allochem deficient (<10%), mud-supported fabric with undifferentiated bioclasts	Middle shelf
	Peloidal/Pelletal Wackestone Microfacies (SSM-2)	Thin to medium bedded, yellowish grey limestone, mud-supported (>10% allochems) fabric, peloids and pellets	Peritidal-lagoonal
	Bioclastic Mud-Wackestone Microfacies (SSM-3)	Thin to medium bedded, grey limestone, mud-supported (<10% to <40% allochems) fabric with undifferentiated bioclasts	Lagoonal
	Packstone Grainstone Microfacies SSM-4	Medium bedded, dark grey sandy limestone, matrix deficient, grain-supported fabric with bioclasts and detrital grains (quartz)	Proximal inner shelf
Unconformity			
Datta Formation (Jurassic)	Massive sandstone facies (DF-1)	Medium-coarse grained sandstone, beds tabular with sharp bases and bed thickness increases upward	Lower shoreface
	Planar cross bedded Sandstone facies (DF-2)	Medium to thick bedded, coarse grained (coarsening up trend), planar cross bedding and pebbly bases	Deltaic distributary channels
	Rippled Sandstone interbedded with shale facies (DF-3)	Medium to thick bedded and coarse-grained sandstone interbedded with shale, bioturbation and asymmetrical ripples and shale beds up to 15 cm thick	Deltaic flood plain
	Trough cross bedded Sandstone (DF-4)	Thick bedded, medium-coarse grained sandstone with large scale trough cross bedding, channel fills and coarsening upward trend	Deltaic flood plain
	Carbonaceous Shale and coal facies (DF-5)	Dark brown shale, organic matter (plant remains)	Inter distributary bays and swamps of delta

	Bioturbated Sandstone facies (DF-6)	Fine to medium grained, medium bedded, intensely burrowed sandstone and thin organic rich shale interbeds	Distal mouth bar (delta front)
	Laterite facies (DF-7)	30-70 cm thick reddish laterite layers, indicate soil horizon	Sub-aerial exposure
Unconformity			
Kingriali Formation (Triassic)	Brecciated Dolostone (KMF-1)	Medium-thick bedded brecciated dolostone, fine-coarse grained with xenotopic (anhedral) crystals of dolomite, iron staining and evaporitic mold	Supratidal
	Peloidal Dolostone (KMF-2)	Thick beds of dolostone, olomicritic matrix with rounded-oval peloids and stromatoporoids with tabular to irregular fenestrae	Inter-subtidal
	Micritized Fenestral Dolostone (KMF-3)	Subhedral to anhedral crystals of dolomite with spherical to irregular fenestrae, stylolite and pyrite frambroids	Peritidal
	Dolomudstone (KMF-4)	Subhedral to anhedral crystals of fine-grained dolomite with spherical fenestrae and coralline stromatoporoids	Inter-subtidal
	Dolomitized Ooidal Grainstone (KMF-5)	Dolomitized tangential and micritic ooids, spar cement amongst the ooids is dolomitized	Subtidal
	Micritic Dolostone (KMF-6)	Subhedral-anhedral mosaic crystals of dolomite with irregular fenestrae, molds and partially dolomitized micrite with the presence of pellets, some stromatoporoids along with tabulate corals	Restricted lagoon
Unconformity			
Tredian Formation (Triassic)	Parallel laminated Sandstone interbedded Shale facies (TDF-1)	Medium to coarse grained sandstone interbedded with shale and carbonaceous material, parallel laminated, bioturbated, thickening & coarsening upward trend	Distributary channel
	Slumped Sandstone facies (TDF-2)	Medium grained sandstone, convoluted bedding and slumped structures	Delta front
	Cross laminated Sandstone facies (TDF-3)	Medium to coarse grained sandstone with low angle cross lamination, thickening and coarsening upward trend	Proximal delta front
	Large scale tabular cross bedded Sandstone facies (TDF-4)	Thick bedded, coarse-grained sandstone, lenticular channelized beds, large scale planar tubular cross bedding and coarsening upward trend	Delta plain
	Dolostone facies (TDF-5)	Medium-thick bedded and yellowish grey dolomite	Restricted shelf

	Laterite facies (TDF-6)	Lateritic soil horizon (40-60 cm thick), terrestrial fossils traces e.g., burrows of soil modifying organism and fossilized roots	Terrestrial Subaerial
Mianwali Formation (Triassic)	Dolostone Microfacies (MWF-1)	Medium bedded and fossiliferous dolostone, grain supported fabric and equigranular zoned rhombs of dolomite	Middle shelf
	Ceratite Wacke-Packstone Microfacies (MWF-2)	Thin bedded, highly fossiliferous limestone, mud to grain supported fabric, fragments of bivalves, ammonoids and gastropods	Inner shelf
	Shale facies (MWF-3)	Medium bedded shale with thin bedded limestone, siltstone, ammonoids, gastropods and bivalves	Shallow inner shelf
	Bivalve Wackestone Microfacies (MWF-4)	Medium bedded, fossiliferous limestone, mud supported fabric with bioclasts of bivalves, ammonoids (*ceratites*), echinoderms, gastropods, crinoids, glauconite and peloids	Deep inner shelf
	Parallel laminated Sandstone interbedded shale facies (MWF-5)	Medium bedded, fine to medium grained sandstone interbedded with shale, parallel lamination and bioturbation	Shallow inner shelf
	Cross laminated Sandstone facies (MWF-6)	Medium to thick bedded, fine to medium grained sandstone, cross lamination, erosive bases, channel fills, bioturbation and thickening upward trend	Deltaic Distributary channel
P-T boundary			
Chhidru Formation (Late Permian)	Interbedded sandy mudstone and shale facies (CHF-1)	Medium bedded sandy limestone with shale, mud supported fabric, allochmes of micritized bioclasts of fusulinids, bryozoans brachiopod and gastropods	Distal Middle shelf
	Calcareous massive Sandstone facies (CHF-2)	Medium-thick bedded, medium-coarse grained calcareous sandstone with bioclasts of brachiopods and bryozoans.	Proximal inner shelf
	Sandy Mudstone-Wackestone Microfacies (CHF-3)	Medium bedded sandy limestone, mud supported fabric with allochems of bryozoans, fusulinids and brachiopods	Proximal middle shelf
	Sandy Wackestone-Packestone Microfacies (CHF-4)	Medium bedded sandy limestone, grain supported fabric with allochems of detrital grains and bioclasts of fusulinids, bryozoans, brachiopods	Proximal middle shelf

	Thick bedded massive Sandstone facies (CHF-5)	Medium-coarse grained, massive sandstone, tabular bedding with sharp bases	Inner shelf
Wargal Formation (Late Permian)	Bioclastic Wackestone-Packstone Microfacies (WMF-1)	Grain supported, allochems (40-70%) include bioclasts of bryozoans, brachiopods, crinoids and gastropods	Middle shelf
	Bioclastic Peloidal Mudstone Microfacies (WMF-2	Allochem deficient (<10%), mud supported, allochems includes ooids, peliods, fragments of bryozoans, crinoids, brachiopods and foraminifers	Restricted Inner shelf
	Mudstone-Wackestone Microfacies (WMF-3)	Allochem deficient, mud supported, allochems are bioclasts of brachiopods, bryozoans, bivalves, crinoids and gastropods	Inner shelf
	Calcic Mudstone Microfacies (WMF-4)	Allochem deficient (<10%), mud supported, undifferentiated micritized and reworked or fragmented bioclasts	Outer shelf
	Dolomitic Mudstone Microfacies (WMF-5)	Mud supported, pre mature dolomitization of mud, fauna absent, micritization and recrystallization	Middle lagoonal shelf

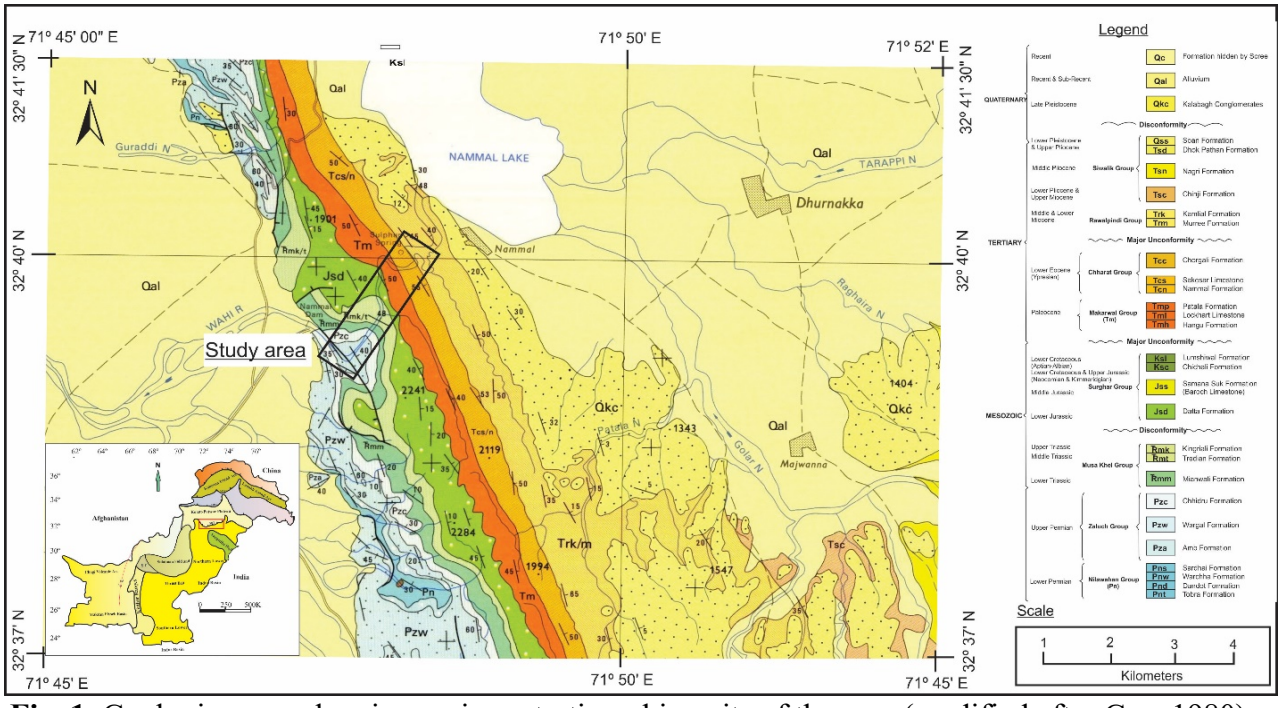

Fig. 1. Geologic maps showing various stratigraphic units of the area (modified after Gee, 1980).

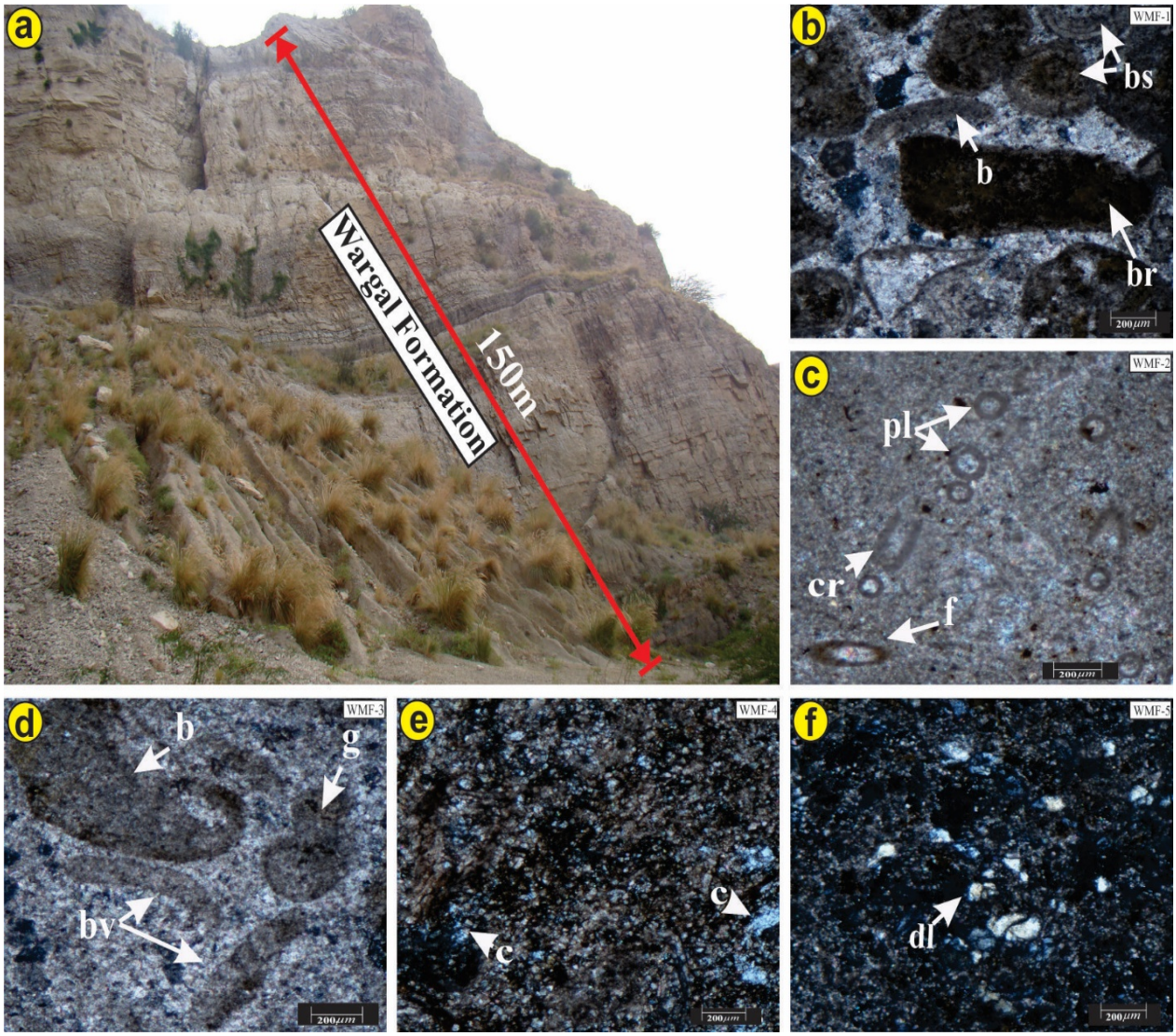

Fig. 2. (a) Field photograph showing general view of the Wargal Formation; (b) Photomicrograph of bioclastic wacke-packstone fabric of WMF-1, brachiopod spines (bs), brachiopod (b), bryozoans(br); (c) Photomicrograph indicates bioclastic peloidal mudstone microfacies (WMF-2), peloids (pl), crinoid (cr), foraminifera (f); (d) Photomicrograph of mudstone-wackestone microfacies (WMF-3) with bioclasts of bivalve (bv), gastropod (g), brachiopod (b); (e) Photomicrograph of calci mudstone fabric of WMF-4 and (f) Photomicrograph of dolomitic mudstone microfacies (WMF-5) dolomite crystals (dl).

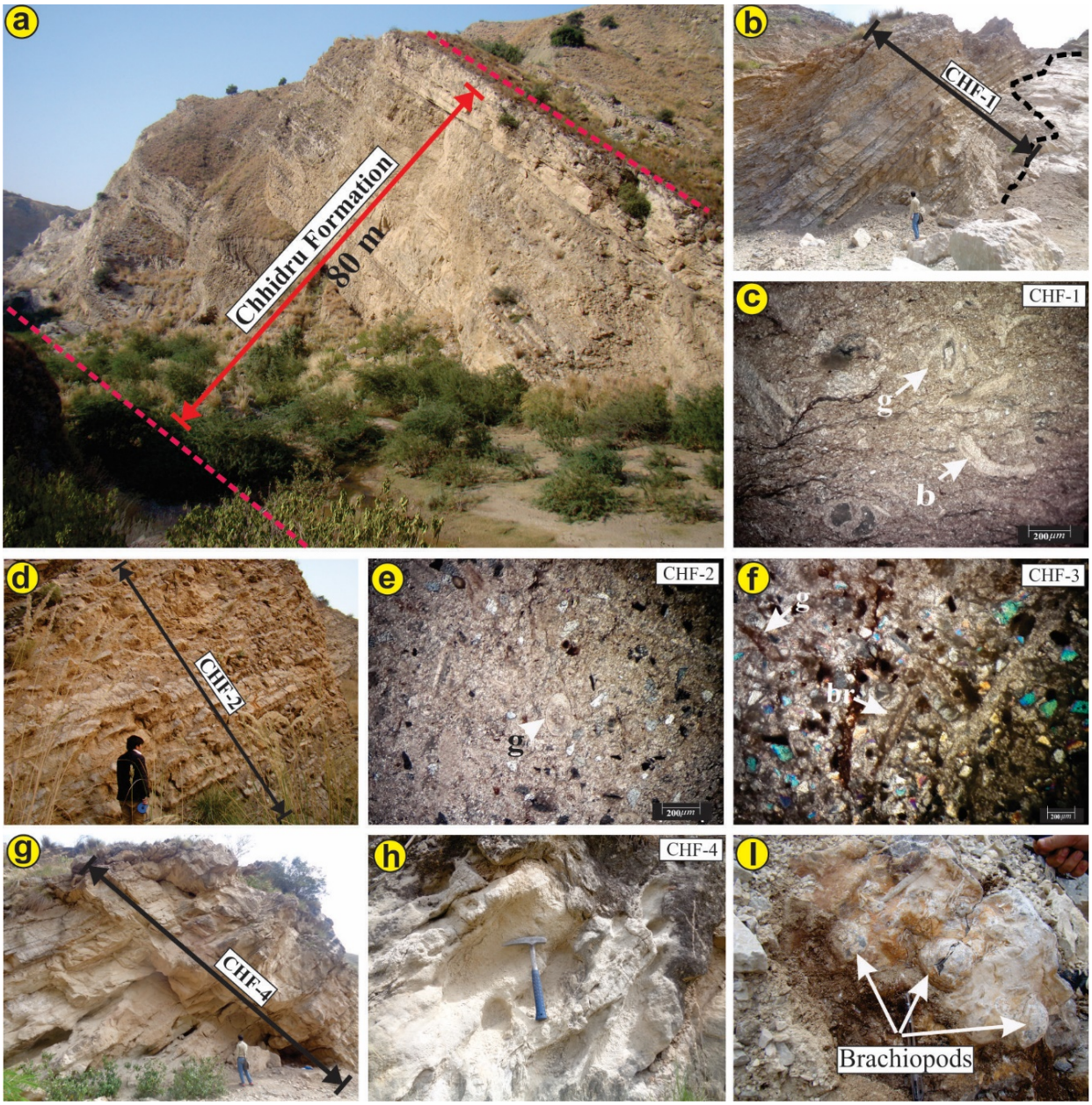

Fig. 3. (a) Field photograph showing exposure of Chhidru Formation; (b) Field photograph of interbedded fossiliferous mudstone facies (CHF-1) of Chhidru Formation; (c) Photomicrograph shows mud supported rock fabric with bioclasts of brachiopods (b), bryozoans (br), fusulinids (f) in CHF-1; (d) Field view of sandy mudstone-wackestone microfacies (CHF-2); (e) Photomicrograph exhibits sandy mudstone-wackestone fabric with gastropods fragments and undifferentiated bioclasts of CHF-2; (f) Photomicrograph of sandy wackestone-packstone fabric of CHF-3 with bioclasts of gastropods (g), bryozoans (br) and other undifferentiated bioclasts; (g) Field photograph of calcareous massive sandstone facies (CHF-4); (h) Field view of massive white colored sandstone of calcareous massive sandstone facies (CHF-4) and (i) Field view of shells of brachiopods in interbedded fossiliferous mudstone facies (CHF-1).

Laminated shale with thin limestone interbeds, parallel and cross laminated sandstones were formed in open marine, inner shelf and distributary channels of delta. Lithofacies recognized in Tredian Formation (Figure 5a), are parallel laminated sandstone interbedded with shale, slumped sandstone, cross laminated sandstone, large scale tabular cross bedded sandstone, dolomite and laterite facies (Oxisols) (Figure 5b-i). Sandstone of the formation is medium to thick bedded, parallel & cross laminated, cross stratified, lenticular, channelized, bioturbated exhibiting a coarsening/thickening upward trend. The sandstones were formed by wave & current actions, variation in flow velocities, suspension and traction processes in proximal delta front to continental delta plain. Slumped sandstone was reckoned owing to slope failure along steep channels and banks causing soft sediments deformation. Dolomite and laterite facies represent the restricted shelf and soil horizon respectively. Kingriali Formation (Figure 6a) is categorized into Brecciated dolostone**,** Peloidal dolostone, Micritized fenestral dolostone, Dolomudstone, Dolomitized ooidal grainstone and Micritic dolostone microfacies (Figure 6b-f). The significant features of recognized microfacies are brecciated dolomite, dolomitic limestone, two-phased dolomites, evaporitic molds, stromatoporoids, xenotopic, hypidiotopic, idiotopic crystals, jigsaw puzzle structures, rounded to oval peloids, spherical to irregular fenestrae fabric, pyrite frambroids, tangential & radial ooids, gastropods, pelecypods, tabulate corals and some intraclasts. Dolomites were primary and diagenetic in origin. The formation was deposited in supratidal, intertidal – subtidal, peridal, high energy inner shelf/ramp environments.

Terrigenous Datta Formation (Figure 7a) is characterized by Massive sandstone, Bioturbated sandstone, Planar cross bedded, Trough cross bedded sandstones, Rippled sandstone interbedded with shale, Carbonaceous shale and Laterite facies (Table 1; Figure 7b-i). The Formation depicts fine to medium grained, medium bedded, massive, intensely burrowed sandstone with few centimeters thick organic rich beds and were likely consociated with flood plain and proximal part of deltaic front settings. Coarse grained large scale planar cross bedded sandstone was produced by downstream movement of dune associated with unidirectional high velocity flow (Umar *et al*., 2011; 2016) in point bars and channel bars, topsets areas of deltaic system. Rippled sandstone interbedded with shale facies was formed by unidirectional flows associated with rivers and streams, longshore currents and backwash on beaches (Boggs, 2014). Trough cross bedded sandstone, channel fills and conglomeratic bases indicate migration of large dunes commonly associated with channel belt facies of deltaic plan environment (Boggs, 2014). Carbonaceous shale facies, interbeds of siltstone and organic matter in the form of plant remains and imprints of leaves were generally associated with low energy conditions of flood plains, swamps and inter-distributary bays of deltaic environments (e.g., Abbasi *et al*., 2012). Red color laterite, sandy and clayey soil were produced due to extensive weathering of bed-rock. The repeating trend of laterite beds attest various episodes of subaerial exposures (Kasi *et al*., 2018) and most probably associated with deltaic depositional settings. Carbonate rich Samana Suk Formation (Figure 8a) is dissevered into Mudstone, Peloidal/Pelletal wackestone, Bioclastic mud-wackestone and Wackestone-packstone microfacies (Figure 8b-f). Peliods and wackestone fabric refer low energy restricted peritidal-lagoonal environment (Scholle & Ulmer-Scholle, 2003; Khan *et al.*, 2021). Bioclastic Mud-Wackestone depositional fabric and fauna reveal low energy shallow

deposition of Kingriali Formation illustrated the Late Triassic transgressive phase of Haq *et al*. (1988).

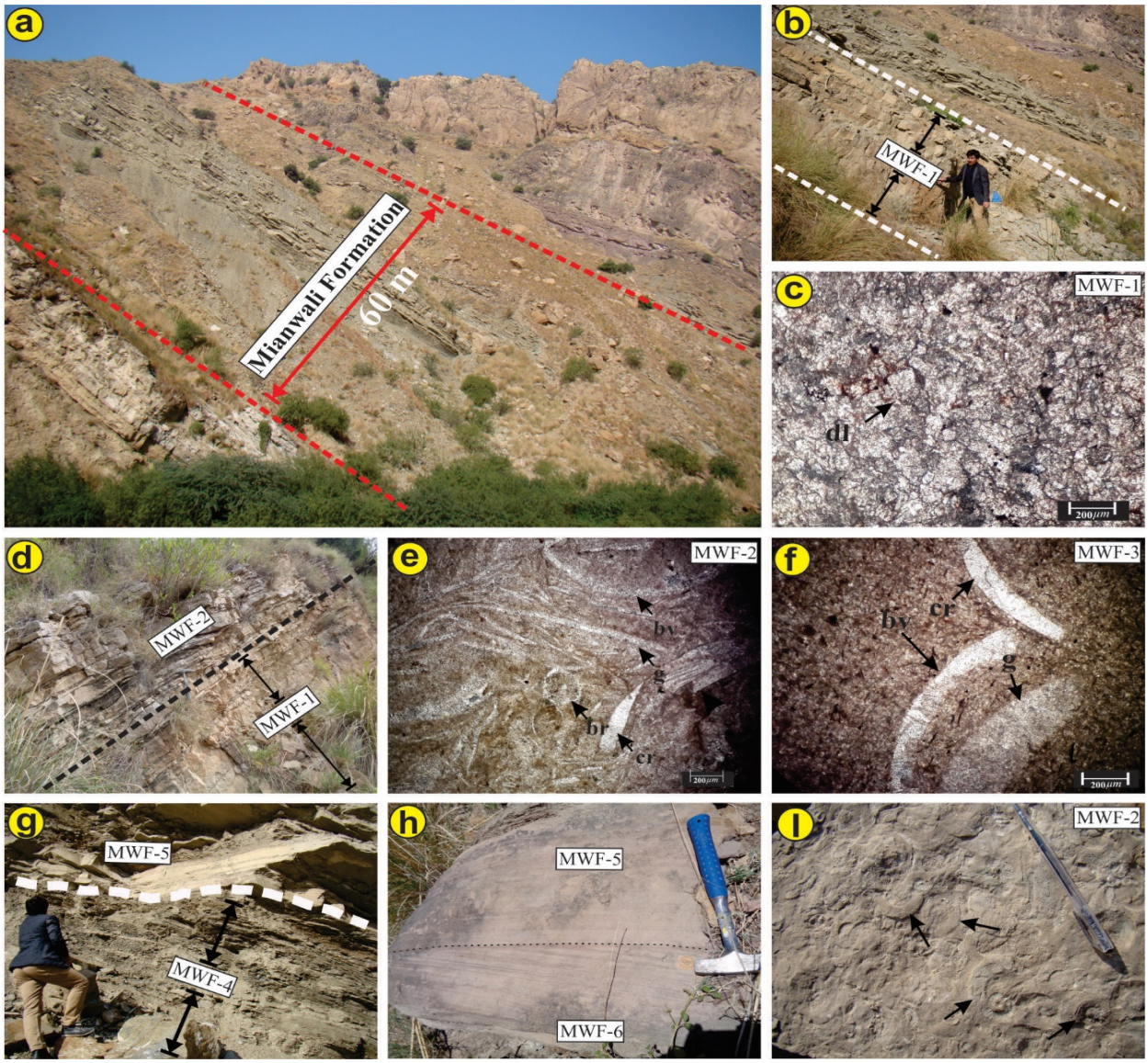

Fig. 4. (a) General view of Mianwali Formation; (b) Medium bedded dolomite of MWF-1; (c) Photomicrograph showing dolomite grains of MWF-1; (d) Field view thin bedded fossiliferous limestone of MWF-2; (e) Photomicrograph of bioclastic wackestone-packstone fabric of MWF-2, bioclasts of gastropods (g), bivalves (bv), brachiopods (br), crinoids (cr); (f) Photomicrograph of mud supported bioclastic wackestone fabric of MWF-3, bioclasts of bivalves (bv); (g) Field Photograph of shale (MWF-4) and overlying parallel laminated sandstone interbedded shale facies (MWF-5) (h) Field photograph showing cross laminated sandstone facies (MWF-6) overlain by (MWF-5); (i) Field view of fossiliferous bed of ceratite wacke-packstone microfacies (MWF-2).

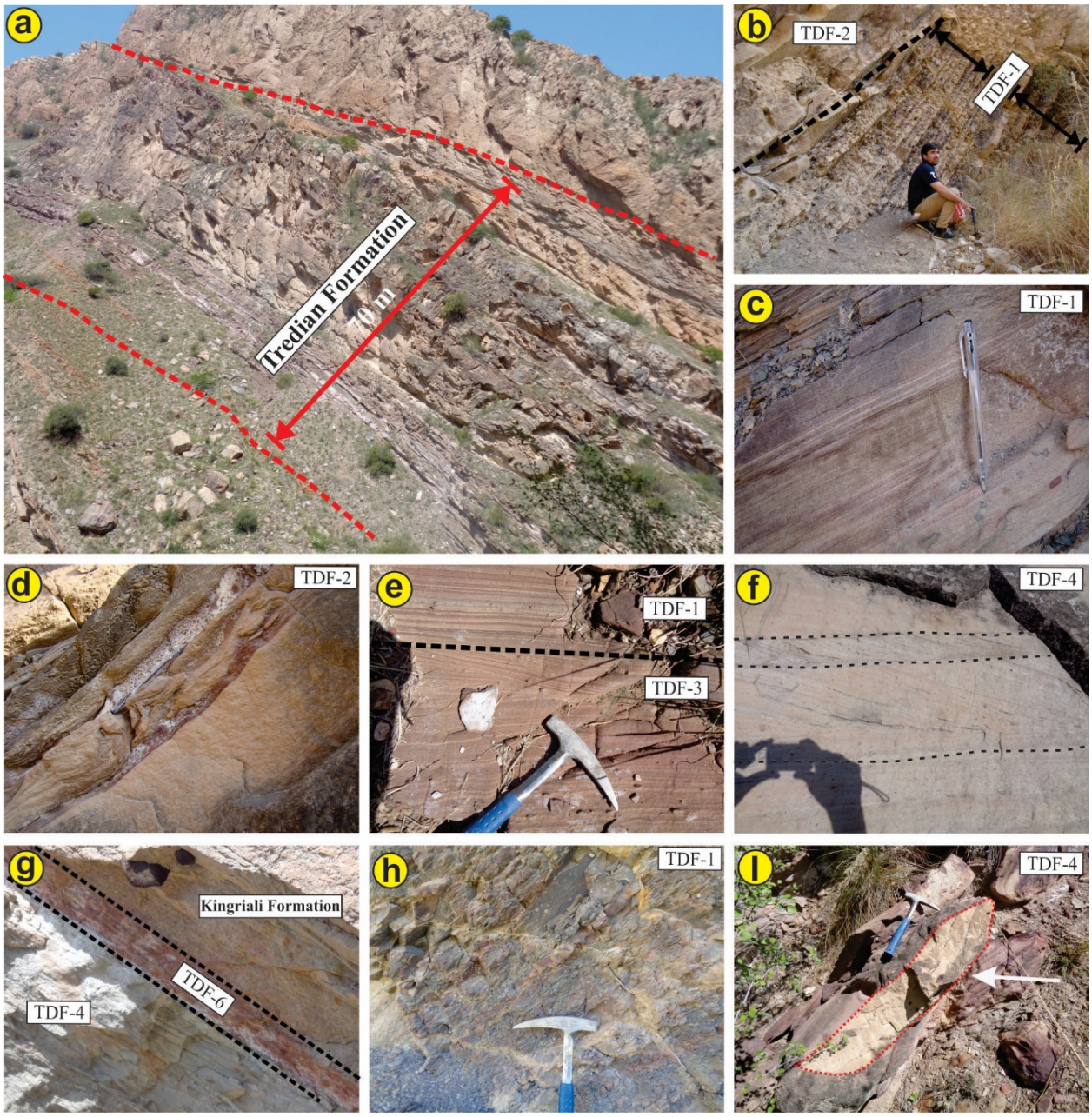

Fig. 5. (a) Field photographs of Tredian Formation; (b) Parallel laminated sandstone interbedded shale facies; (c) Parallel laminated sandstone of TDF-1; (d) Slumped sandstone facies (TDF-2); (e) Cross laminated sandstone of TDF-3; (f) Large scale tabular cross bedded sandstone facies (TDF-4); (g) soil horizon/laterite bed of TDF-6 at the top of Tredian Formation; (h) Carbonaceous material in shale of (TDF-1); (i) Channel structures in (TDF-4).

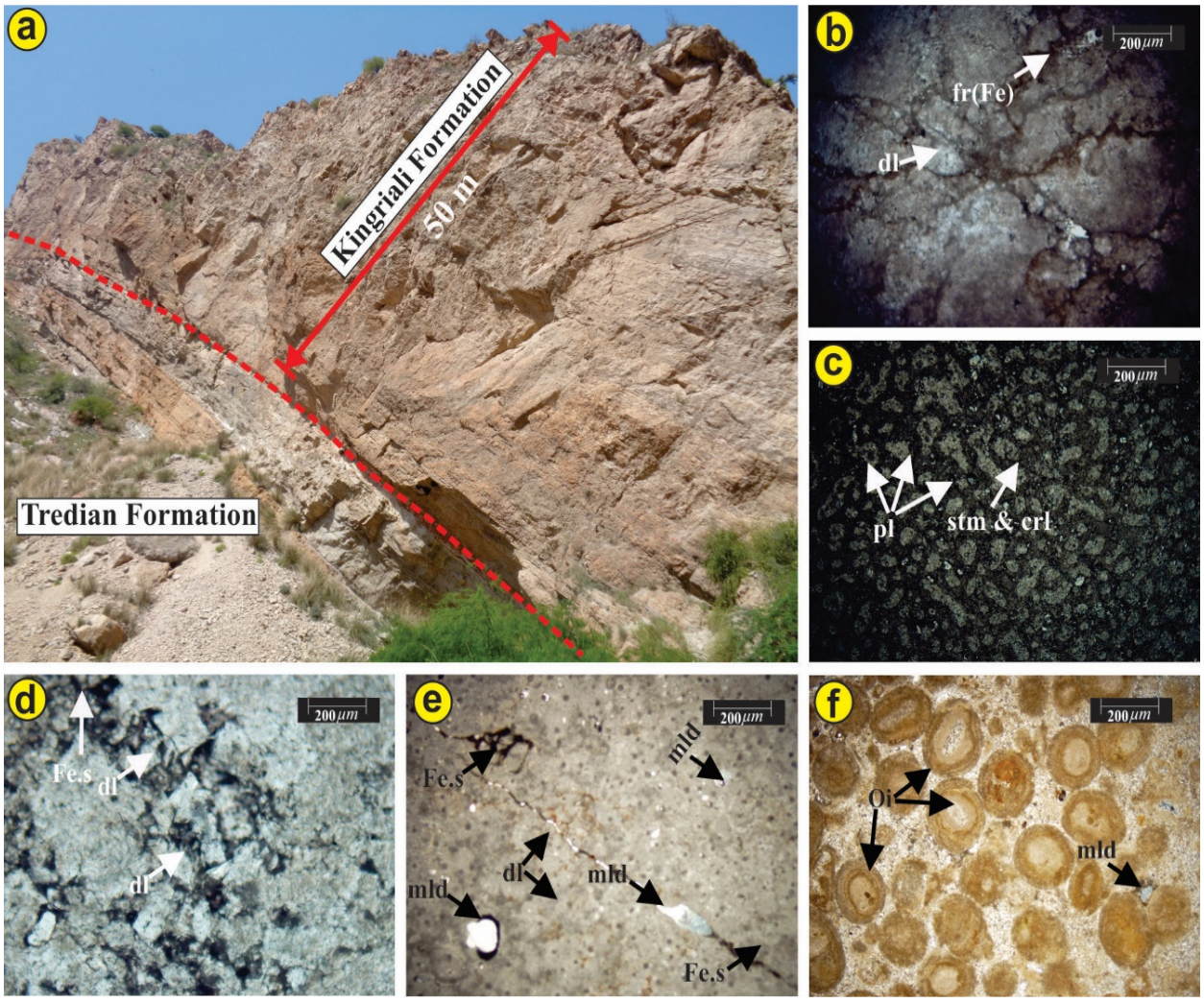

Fig. 6. (a) General view of the Kingriali Formation; (b) Photomicrographs of brecciated dolostone microfacies (KMF-1) with fine to coarse grained anhedral dolomite (dl) crystals with fractures (fr) and fractures filled with iron (Fe); (c) Peloidal dolostone microfacies (KMF-2) with pl; peloids with co-existence of stromatoporoids (stm) and corals (crl); (d) Micritized fenestral dolostone microfacies (KMF-3) with fine to coarse grained, subhedral to anhedral dolomite (dl) crystals with Iron staining (Fe.s); (e) Dolomudstone (KMF-4) with molds (mld) and iron staining (Fe.s); (f) Dolomitized ooidal grainstone microfacies (KMF-5) with tangential, radial and micritic ooids with bioclasts.

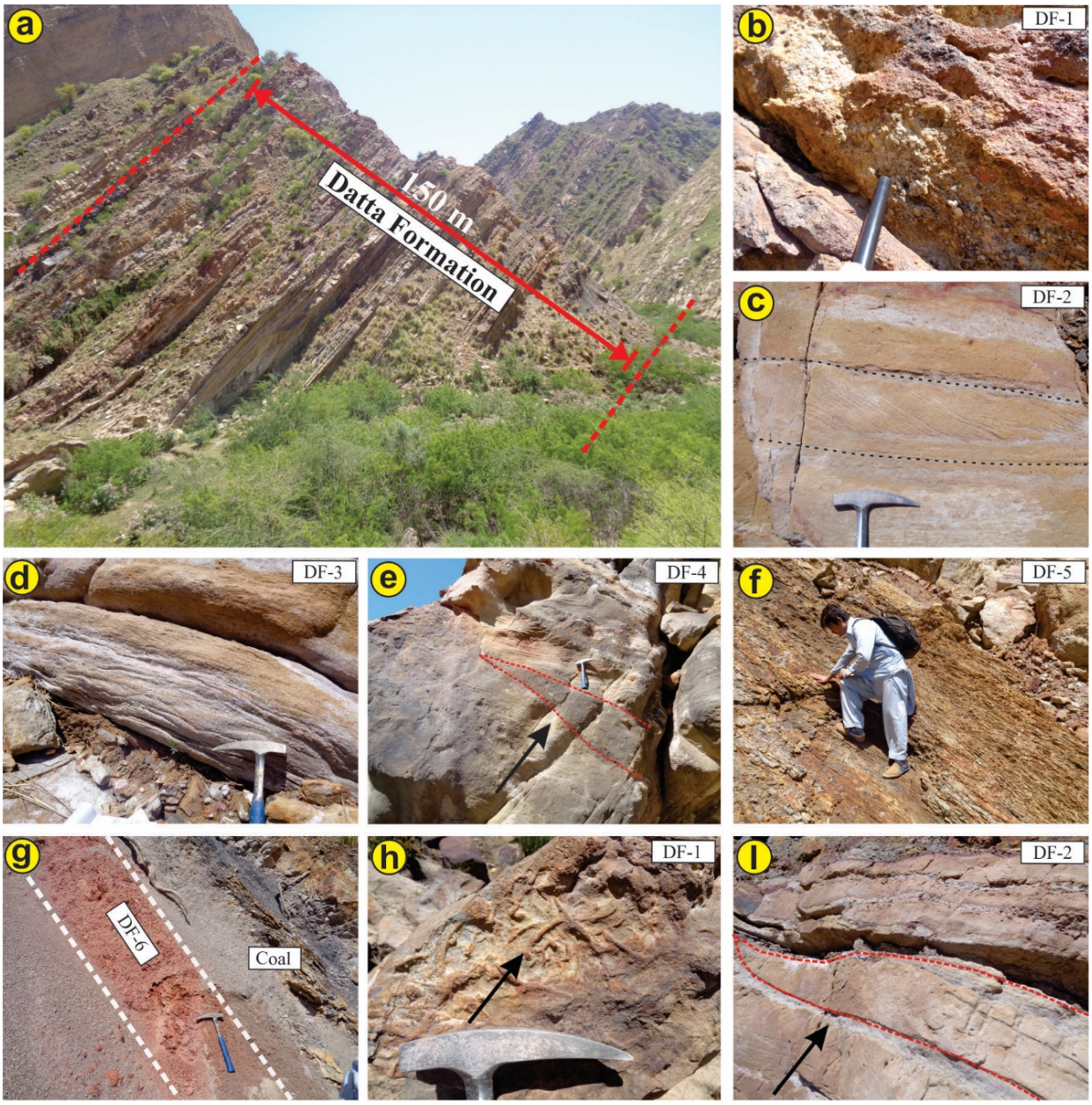

Fig. 7. (a) Field photograph showing outcrop exposure of Datta Formation; (b) View of massive sandstone facies (DF-1) with pebbly base; (c) Field photograph of planar cross bedded sandstone facies (DF-2); (d) Field photographs of rippled sandstone interbedded with shale facies (DF-3); (e) Trough cross bedded sandstone with channel structure (DF-4); (f) Shale of carbonaceous shale and coal facies (DF-5); (g) Laterite bed of laterite facies (DF-7); (h) Burrows in (TDF-1); (i) Channelized beds in (TDF-2).

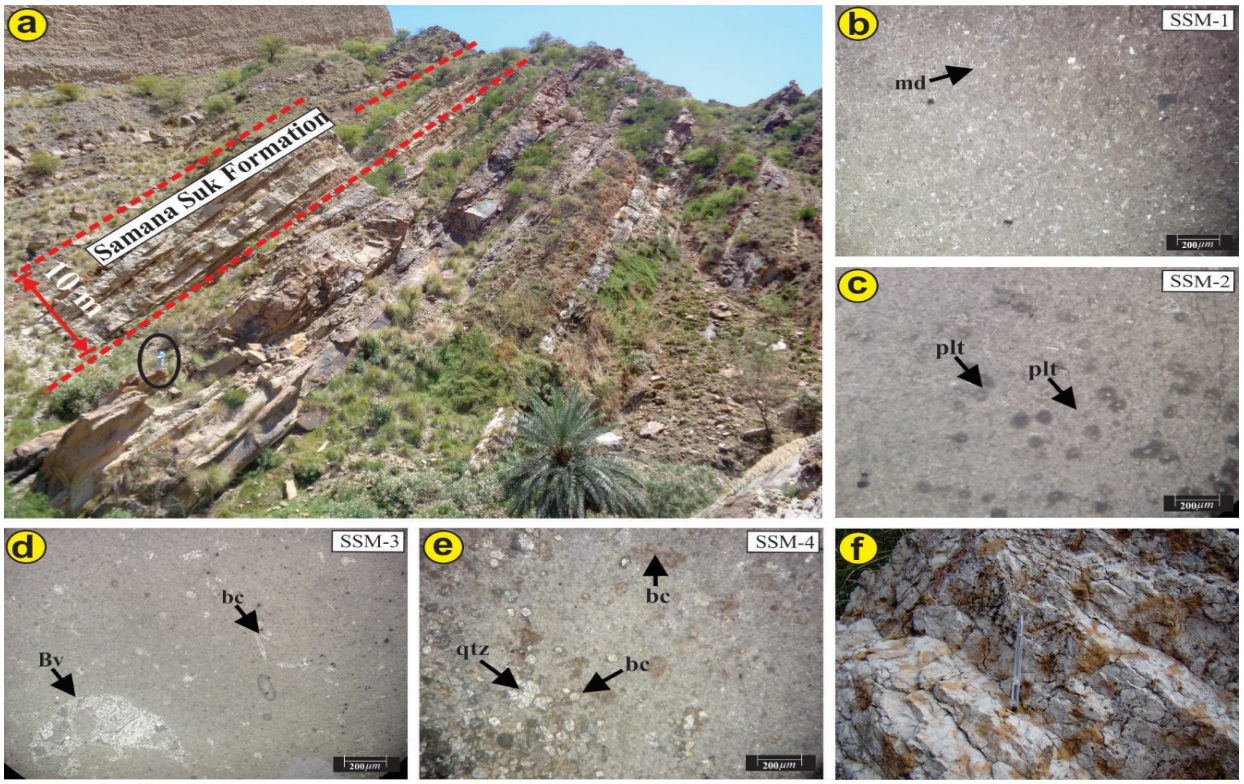

Fig. 8. (a) Field photograph shows exposure of Samana Suk Formation; (b) Photomicrograph of mud supported fabric of mudstone microfacies (SSM-1); (c) Mud supported and peloid and pellet containing fabric of peloidal/pelletal wackestone microfacies (SSM-2); (d) Bioclastic containing mud supported fabric of bioclastic mud-wackestone microfacies (SSM-3); (e) Wackestone-packstone microfacies (SSM-4); (f) Filed view of limestone of Samana Suk Formation

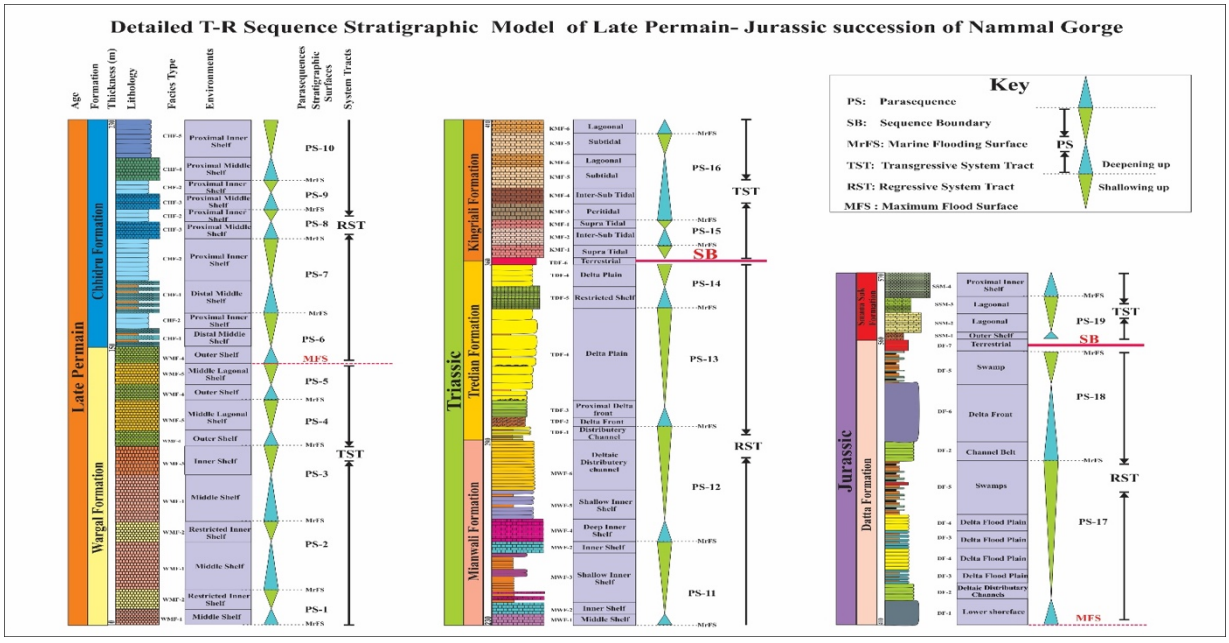

Fig. 9. Detailed Facies Architecture and T-R Sequence Stratigraphic Analysis.

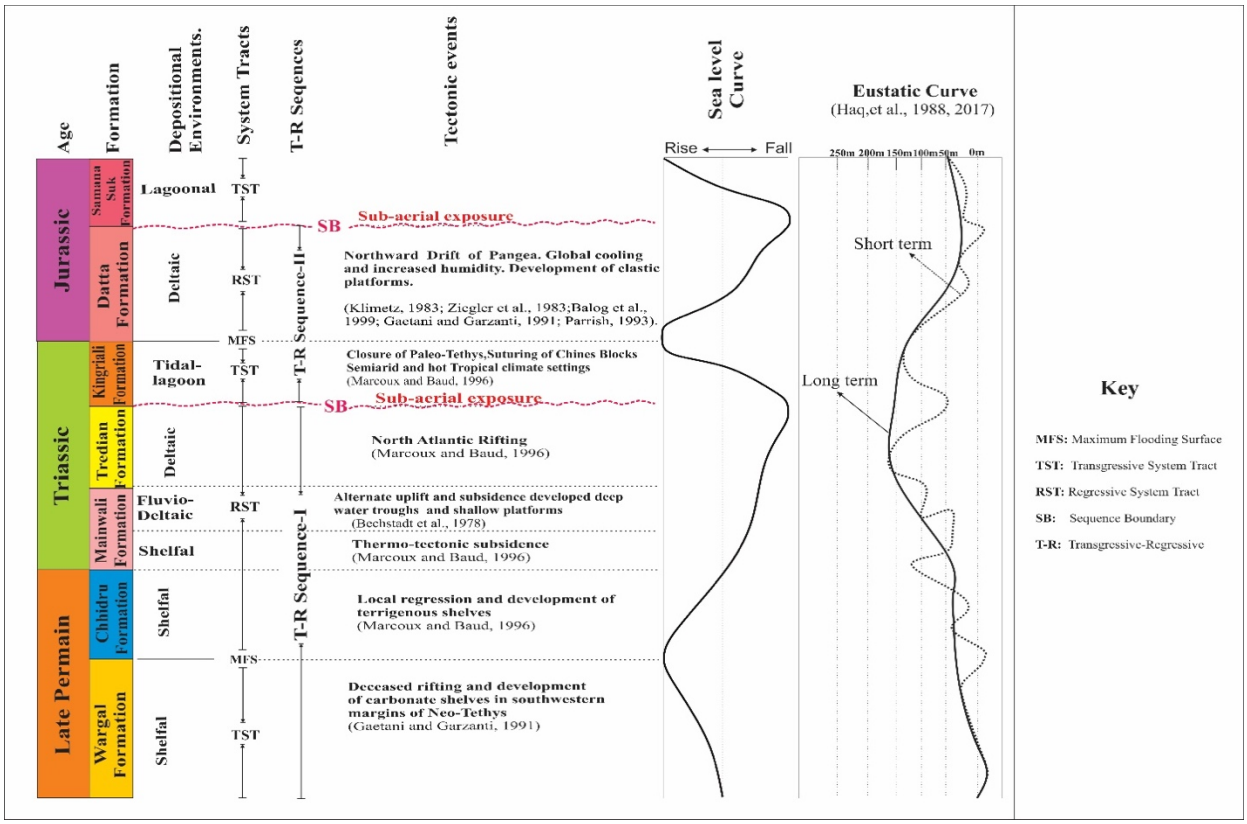

Fig. 10. T-R Sequence Stratigraphic Analysis and its relation to Tectonics and Sea Level Fluctuations of Late Permian-Jurassic rocks of studied area (modified after Haq *et al*., 1988, 2017).

The soil horizons in Datta Formation stigmatize cessation of Regression and Sequence Boundary of T-R Sequence-II. Global regression flux in Early Jurassic was manifested by regressive phase deposition of Datta Formation. Samana Suk Formation corresponded to transgressive phase of next T-R cycle.

3.2 Tectonic control on sedimentation

Stratigraphic succession exposed in various sedimentary basins, revealed the tectonic and depositional evolution of Indian Plate particularly during Permian-Jurassic time span in response to rifting of Gondwana, separation of Cimmerian Block and opening of Neo-Tethys Ocean. Terrigenous and carbonate sedimentation within sedimentary basins developed in response to episodic rifting of Gondwana super-continent through Carboniferous-Jurassic (Zeigler, 2015). The Gondwanian sedimentary rocks of Indian Plate were substantially correlated with terrains exposed in Madagascar, Eastern Africa, Seychelles, Arabian Peninsula and Indus Basin (including studied area) (Bhattacharya & Bhattacharya, 2015). Tectono-sedimentation in Carboniferous-Jurassic can be reconstructed e.g., western India was colligated with Madagascar, Africa, Arabia, and Seychelles Plates (Mukherjee, 2017), was moved towards North (near equator) in terminal Triassic (Torsvik & Cocks, 2013). North-South rifting induced crustal extension throughout Carboniferous – Permian and premised the breakup of Gondwana super-continent (Delvaux, 1991). Based on GIS

study, the linear disposition of Dwyka (South Africa), Al-Khalata, Gharif (Oman), Sakoa (Madagascar) and Nilawahan (Western Salt Range) formations, parallel faults trend to such lithostratigraphic units, persistence, resemblance of lithologies and structures exhibit the probable existence of Gondwana rift. The notion intends comparable tectono-sedimentary environments in South Africa, Oman, Madagascar, and Western Salt Range. Extension of such rift and separation of Cimmerian block were developed Neo-Tethys Ocean, North of India in Mid Permian–Early Triassic (Torsvik & Cocks, 2013). Basement ridges in Indus basin (Delhi-Lahore-Sargodha) were uplifted in Mid Permian (Asim *et al*., 2014).

Precambrian - Early Permian sedimentation on the Indian Plate, within Paleo-Tethys was shifted to Neo-Tethys in Late Permian due to final detachment of India from Gondwana and opening of Indian Ocean (Gaetani & Garzanti, 1991). The opening of Neo-Tethys was consorted with Early Permian extensional magmatic activity. The termination of magmatic activity succeeded to the deposition of transgressive parasequence sets of Wargal Formation in newly evolved Neo-Tethys shelf. In addition, shallow water carbonate platform was well established in Salt Range within Neo-Tethys between 30°N and 30°S. Terrigenous deposits of Chhidru Formation are comparable with clastic shelves of India and northwest Australia during Late-Permian due to local regressive cycle of T-R sequence (Marcoux & Baud, 1996). Thermo-tectonic subsidence and rift related submergence in Early Triassic (Gaetani & Garzanti, 1991; Marcoux & Baud, 1996) led to the deposition of MWF-1 and MWF-2 of Mianwali Formation in inner continental margin. Rapid shallowing upward conditions were acquired in Anisian and Ladinian (Mid-Triassic) owing to uplift, which ensued a complex pattern of deeper troughs and shallow water platforms (Bechstadt *et al*., 1978). On account of this composite pattern of deposition, a rigorous shift from under-fill to overfill basin (Lawa *et al*., 2013) is depicted in the form of shelf facies overlain by deltaic facies in Mianwali Formation with its regressive parasequence sets. North Atlantic rifting through Norian was inducted the clastic sedimentation in the Neo-Tethys (Marcoux & Baud, 1996) as marked in Tredian Formation and alike clastics in the other sedimentary basins of India (Gaetani & Garzanti, 1991). High sediments load and low accommodation space triggered the overfilling of basin up to subaerial exposure as exemplified by soil horizons (TDF-6) at the top of Tredian Formation and marks the end of regression. Furthermore, sub-aerial exposure (soil horizon) in WSR and Indian basin was recorded at Norian-Rhaetian Boundary. Late Triassic global tectonics demonstrate the commencing of Pangaea's breakup and occlusion of Paleo-Tethys (Fan *et al*., 2017) on account of northward drift of Cimmerian Plate, its convergence and suturing with Chinese Blocks led to the growth of large carbonate platform in Neo-Tethys margins (Ghosh *et al*., 2016; Sardar Abadi *et al*., 2019; Enayati-Bidgoli & Navidtalab, 2020). The subtidal/lagoonal dolomitization (Kingriali Formation), owing to semiarid and hot tropical climate conditions in transgressive parasequence sets was resulted by such tectonostratigraphic event. Late Triassic Dolostone units were deposited in Central Asia (Fan *et al*., 2017; Borrelli *et al*., 2019; Enayati-Bidgoli & Navidtalab, 2020) is comparable with Kingriali Formation. Global cooling and humidity increase owing to well-documented northward movement of Pangea, the dolomitization abruptly quitted at the end of Triassic (Gaetani & Garzanti, 1991). The similar cessation of dolomite was observed at the top of Triassic Kingriali Formation in WSR. Sedimentation in Early Jurassic depicts shift from tidal-

lagoonal to deltaic facies of Datta Formation. The condensed black shale at the base of Datta formations signs the maximum flooding surface across which the change from transgressive to regressive parasequence sets is obviously manifest (Omar *et al*., 2015). In Early Jurassic till Late Callovian, high sediments supply but low accommodation space stimulated sub-aerial exposure and development of laterite beds. Such subaerial exposure is distinguished by existence laterite beds (DF-7) at the top of Datta Formation correspond to referred episode of sedimentation in Neo-Tethys. A Transgressive episode was commenced in terminal Callovian and shelf carbonate platforms ensued to form in Late Jurassic. Samana Suk Formation was accumulated during such episode of sedimentation (Khan *et al*., 2021) in Neo-Tethys Ocean.

4. Conclusions

1. Lithofacies, microfacies, sequence stratigraphic framework and sea level curve of Late Permian to Jurassic strata Western Salt Range, contend the tectonic consequence on sedimentation.

2. The Wargal Formation dominantly compiled the mudstone, mud-wackestone, wackestone-packstone and dolomitic mudstone depositional fabrics corresponding to lagoonal and restricted inner to outer shelf environments. The microfacies of the formation exhibit retrogradational depositional architecture inducing TST of T-R Sequence-I. Mixed clastic – carbonate sedimentation in the Chiddru Formation constitutes regressive phase sequence throughout Late Permian period.

3. Early Triassic Mianwali Formation typifies RST with progradational depositional architecture in clastic-carbonate mixed succession. Terrigenous-rich Tredian Formation was accumulated in fluvio-deltaic environments as attested by defined lithofacies e.g., large-scale cross bedded, cross laminated, parallel laminated sandstones interbedded with shale and slumped sandstone facies. The soil horizons signal sub-aerial exposure and set the sequence boundary. Tidal – lagoon settings were acquired due to closure of Paleo-Tethys, suturing of Chines Blocks and development of semi-arid hot tropical climate in Late Triassic time. Dolomite-rich Kingriali Formation was deposited in the same environments. The boundary between Tredian and Kingriali formations signs the sequence boundary and initiate transgressive episode of next T-R Sequence-II.

4. Global cooling and humidity enhancement owing to northward drift of Pangea and led to development of clastic-carbonate successions in Early Jurassic. The distinguished lithofacies of Datta Formation display fluvio-deltaic environments. The formation corresponds to RST of T-R Sequence-II, whereas the laterite beds represent sub-aerial exposure and marked the sequence boundary. Samana Suk Formation represents the transgressive phase of succeeding cycle.

5. Sedimentation of Late Permian - Jurassic strata, WSR was tempted by active tectonic and most probably correspond to rifting of Gondwana, separation of Cimmerian block, opening of Neo-Tethys Ocean, northward drift of Pangea and suturing of Chinese Blocks.

References

Abbasi, I.A., Haneef, M., Obaid, S., Daud, F., & **Qureshi, A.W. (2012)** Mesozoic deltaic system along the western margin of the Indian Plate: lithofacies and depositional setting of Datta Formation, North Pakistan. Arabian Journal of Geosciences, 5(**3**), 471-480.

Asim, S., Qureshi, S.N., & **Khan, N. (2014)** Study of an uplift of Sargodha High by stratigraphical and structural interpretation of an east-west seismic profile in Central Indus Basin, Pakistan. International Journal of Geoscience, 5(**9**), 1027.

Baker, D.M., Lillie, R.J., Yeats, R.S., Johnson, G.D., Yousuf, M., & **Zamin, A.S.H. (1988)** Development of the Himalayan frontal thrust zone: Salt Range, Pakistan. Geology, 16(**1**), 3-7.

Bechstadt, T., Brandner, R., Mostler, H. & **Schmidt, K. (1978)** Aborted rifting in the Triassic of the Eastern and Southern Alps, Neues Jabrbuch fur Geologie und Palaontologie Abhandlungen, 156, 157-178.

Bhattacharya, H.N., & **Bhattacharya, B. (2015**) Lithofacies architecture and paleogeography of the Late Paleozoic glaciomarine Talchir Formation, Raniganj Basin, India. Journal of Paleogeography, 4(**3**), 269-283.

Boggs, S. (2014) Principles of Sedimentology and Stratigraphy, 5th Edition. Pearson Publisher, 598.

Borrelli, M., Campilongo, G., Critelli, S., Perrotta, I.D., & **Perri, E. (2019)** 3D nanopores modeling using TEM-tomography (dolostones-Upper Triassic). Marine and Petroleum Geology, 99, 443-452.

Catuneanu, O., & **Zecchin, M. (2010)** High resolution sequence stratigraphy of clastic shelves III: Application to reservoir geology. Marine and Petroleum Geology, 62, 161-175.

Delvaux, D. (1991) The Karoo to Recent rifting in the western branch of the East-African Rift System: A bibliographical synthesis. Rapport Annuel 1989-1990, de Geologie et Mineraloqie, Musee Royale de I'Afrique Centrale, Tervuren, Belgium, B-3080, 63-83.

Embry, A.F., & **Johannessen, E.P. (1992)** T-R sequence stratigraphy, facies analysis and reservoir distribution in the uppermost Triassic-Lower Jurassic succession, western Sverdrup Basin, Arctic Canada. In: Vorren, T. O., Berg - Sager, E., Dahl-Stamnes, O. A., Holter, E., Johansen, B., Lie, E., Lund, T. B. (Eds.), Arctic Geology and Petroleum Potential. Norwegian Petroleum Society (NPF) Special Publication, 2: 121–146.

Enayati-Bidgoli, A., & **Navidtalab, A. (2020)** Effects of progressive dolomitization on reservoir evolution: A case from the Permian–Triassic gas reservoirs of the Persian Gulf, offshore Iran. Marine and Petroleum Geology, 119, 104480.

Fan, J.J., Li, C., Xie, C.M., Liu, Y.M., Xu, J.X., & **Chen, J.W. (2017)** Remnants of Late Permian–Middle Triassic Ocean islands in northern Tibet: implications for the late-stage evolution of the Paleo-Tethys Ocean. Gondwana Research, 44, 7-21.

Farooqui, M.A., Umar, M., Sabir, M.A., Pervez, R. & **Jalees, T. (2019)** Geochemical attributes of late Neoproterozoic Salt Range Formation, Pakistan: constraints on provenance, paleoclimate, depositional and tectonic settings. Geosciences Journal, 34(**2**): 201218.

Farooqui, M.A., Rehman, K.,Yaseen, A., Roohi, G., & **Umar, M. (2022)** Petrography, geochemistry and depositional model of Ispikan Conglomerate, Makran Accretionary Prism, Southwest Pakistan. Kuwait Journal of Science, 49 (**1**),1-25.

Flügel, E. (2004) Microfacies of carbonate rocks: analysis, interpretation and application. Springer, New York, 976.

Gaetani, M., & **Garzanti, E. (1991)** Multicyclic history of the northern India continental margin (northwestern Himalaya). Bulletin of American Association of Petroleum Geologists, 75(**9**), 1427-1446.

Gee, E.R. (1980) Pakistan Geological Salt Range Series: Directorate of Overseas Surveys, United Kingdom, for the Government of Pakistan, and Geological Survey of Pakistan, 6 sheets, scale 1:50,000.

Ghosh, N., Basu, A.R., Bhargava, O.N., Shukla, U.K., Ghatak, A., Garzione, C.N., & **Ahluwalia, A.D. (2016)** Catastrophic environmental transition at the Permian-Triassic Neo-Tethyan margin of Gondwanaland: Geochemical, isotopic and sedimentological evidence in the Spiti Valley, India. Gondwana Research, 34, 324-345.

Haq, B.U., Hardenbol, J., & **Vail, P.R. (1988)** Mesozoic and Cenozoic chronostratigraphy and cycles of sea-level change. In: Wilgus, C.K., Hastings, B.S., Kendall, C.G. St. C., Posamentier, H.W., Ross, C.A., Van Wagoner, J.C. (eds.) Sea-Level Changes: An Integrated Approach. Special Publication, No. 42. Society of Economic Paleontologists and Mineralogists, Tulsa. 71–108.

Haq, B.U., & **Huber, B.T. (2017)** Anatomy of a eustatic event during the Turonian (Late Cretaceous) hot greenhouse climate. Science China Earth Sciences, 60(**1**), 20-29.

Iqbal, S., Jan, I.U., & **Hanif, M. (2014**) The Mianwali and Tredian formations: An example of the Triassic progradational deltaic system in the low-latitude western Salt Range, Pakistan. Arabian Journal for Science and Engineering, 39(**7**), 5489-5507.

Kasi, A.K., Kassi, A.M., Umar, M., Friis, H., Mohibullah, M., & **Mannan, A.R. (2018)** A Paleogeographic and Depositional Model for the Neogene Fluvial Succession, Pishin Belt, Northwest Pakistan: Effect of Post Collisional Tectonics on Sedimentation in a Peripheral Foreland Setting. Acta Geol Sinica, 92(**2**), 499-518.

Khan, M.M.S.S., Jadoon, Q.A., Umar, M. & **Khan, A.A. (2021)** Microfacies, diagenesis and hydrocarbon Potential of Eocene carbonate strata Pakistan. Carbonates and evaporates, 36(**48**), 1-21.

Lawa, F.A., Koyi, H., & **Ibrahim, A.O. (2013)** Tectono-stratigraphic evolution of the NW segment of the Zagros fold belt, Kurdistan Region. Journal of Petrol Geology, Oxford Blackwell publishing, 36 (**1**), 75-69.

Marcoux, J., & Baud, A. (1996) Late Permian to Late Triassic Paleo-environments. Three snapshots: Late Murgabian, Late Anisian, Late Norian. The Tethys Ocean, Plenum Press, New York, 153-190.

Milsom, C., & **Rigby, S. (2010)** Fossils at a glance: John Wiley & Sons, 170.

Mukherjee, S. (2017) Shear heating by translational brittle reverse faulting along a single, sharp and straight fault plane. Journal Earth System Science, 126(**2**), 1-5.

Nazir, J., Ali, M., Sana, E., Ahmad, Q.A., Ghaffari, A., Basit, A., Javed, S., Ahmad, R., Ali, B., & **Rehman, N.U. (2020)** AVO analysis of Post-Stack Seismic data of Cretaceous Lumshiwal Formation in Kabirwala Block, Central Indus Basin Pakistan. Journal of Himalayan Earth Sciences, 53(**2**), 70-77.

Omar, A.A., Lawa, F.A., & **Sulaiman, S.H. (2015)** Tectonostratigraphic and structural imprints from balanced sections across the north-western Zagros fold-thrust belt, Kurdistan region, NE Iraq. Arabian Journal of Geosciences, 8(**10**), 8107-8129.

Qureshi, K., Shah, M.R., Meerani, I.A., Basit, A., Fahad, S., Shah, A.A., & **Hussain, H. (2019)** Hydrocarbon source and reservoir rock potential of Paleocene Hangu Formation in the Himalayan Foreland Basin, North West Pakistan: insight from geochemical and diagenetic study. Pakistan Journal of Scientific & Industrial Research, 62A (**3**), 157-166.

Sardar A.M., Soreghan, G.S., Heavens, N.G., Voeten, D.F.A.E., & **Ivanova, R.M. (2019**) Warm-water carbonates in proximity to Gondwanan ice–sheets: A record from the Upper Paleozoic of Iran. Palaeogeography Palaeoclimatology Palaeoecology, 531, 108914.

Scholle, P.A., & **Ulmer-Scholle, D.S. (2003)** A color guide to the petrography of carbonate rocks: grains, textures, porosity, diagenesis. American Association of Petroleum Geologists Memoir, 77.

Torsvik, T.H., & **Cocks, L.R.M. (2013)** Gondwana from top to base in space and time. Gondwana Research, 24(**3-4**), 999-1030.

Tucker, M.E., Wright, V.P., & **Dickson, J.A.D. (2006)** Carbonate sedimentology: John Wiley & Sons, 496.

Umar, M., Khan, A.S., Kelling, G., & **Kassi, A.M. (2011)** Depositional environments of Campanian–Maastrichtian successions in the Kirthar Fold Belt, southwest Pakistan: Tectonic influences on Late Cretaceous sedimentation across the Indian passive margin. Sedimentary Geology, 237(**1-2**), 30-45.

Umar, M., Khan, A.S., Kelling, G., Friis., H., & **Kassi, A.M. (2016)** Reservoir attributes of a hydrocarbon-prone sandstone complex: case of the Pab Formation (Late Cretaceous) of southwest Pakistan. Arabian Journal of Geosciences, 9(**1**), 74-89.

Umar, M., Khan, A.A., Qasim, M., Sabir, M., Jadoon, I.A.K., Farooq, M., & **Jamil, M. (2020)** Sedimentology of Galdanian Formation Hazara Basin Lesser Himalaya Pakistan: The signatures of Cambrian-Ordovician Pan-African Orogeny. Himalayan Geology, 41, 93-104.

Wignall, P.B., & **Hallam, A. (1993)** Griesbachian (Earliest Triassic) palaeoenvironmental changes in the Salt Range, Pakistan and southeast China and their bearing on the Permo-Triassic mass extinction. Palaeogeography Palaeoclimatology, Palaeoecology, 102(**3-4**), 215-237.

Zeigler, P.A. (2015) Post-Hercynian plate reorganization in the Tethys and Arctic-North Atlantic domains, Triassic Jurassic Rifting: Continental Breakup and the Origin of the Atlantic Ocean and Passive Margins (ed.) Manspeizer W, Elsevier, 711–756.

Submitted: 21/08/2021
Revised: 03/02/2022
Accepted: 07/02/2022
DOI: 10.48129/kjs.16575

Forecasting seasonal mean temperature over Rangpur, Bangladesh

Zakaria Hossain

Dept. of Mathematics, Bangladesh University, Dhaka-1207, Bangladesh

*Corresponding author: zakariaru001@gmail.com

Abstract

The study was conducted by Climate Predictability Tools (CPT) to forecast (short-range forecast) the seasonal mean temperature over Rangpur for six Bengali seasons in Bangladesh. In this study, the sea surface temperature (SST) for the period of 1975 to the previous month of each season of 2008 was used as the predictor. This study also evaluated the difference between forecasted seasonal mean temperature and observed seasonal mean temperature for six seasons. To find the SST that is similar to the temperature in Rangpur, a correlation between the temperature of Rangpur and the sea surface temperature of various parts of the earth was performed through CPT using both data of 1975- 2008 years. The obtained SST through correlation that is more or less similar to the temperature in Rangpur was used as a predictor to forecast seasonal mean temperature of the year 2009. Statistical and mathematical methods were applied by CPT in this research which included canonical correlation analysis, covariance matrix, and eigenvalues equations.The study found that the forecasted seasonal mean temperature was higher in rainy and winter seasons than the temperature observed and was lower in summer, autumn, late autumn, and spring season than the observed temperature at Rangpur. The maximum overestimated temperature was found to be 0.52^{o}C/day in winter and the maximum underestimated temperature was found to be 0.54^{o}C/day in autumn. On the other hand, the minimum overestimated temperature was found during the rainy season having the value of 0.34^{o}C/day and the minimum underestimated temperature was obtained during the summer season having the value of 0.25^{o}C/day, which was the best-forecasted temperature.

Therefore, the forecasted values of temperature in the summer and rainy seasons were found closer to the observed temperature during 2009. So, it can be said that it is possible to obtain good forecasting of temperature through CPT.

Keywords: Air temperature; climate predictability tool; forecasting; seasons of Bangladesh; sea surface temperature.

1. Introduction

The climate change process, in particular the change of temperature is a vital issue in the world at present. The pattern of temperature and rainfall is getting changed due to global climate change which is also getting seen in Bangladesh at present. The report of the Intergovernmental Panel on Climate Change revealed the amount of global climate change was between 0.3 to 0.6 degrees Celsius from 1900 to 1995 (IPCC, 2001). It is extensively believed that Bangladesh will be more

severely affected than developing countries in the world's tropics because of its disadvantageous geographic location as well as climate changes. (Machiwal & Jha, 2006; Shamsnia *et al.,* 2011). On the other hand, the temperature has been identified as one of the main factors of climate change in the last two decades (Oyamakin, *et al.,* 2010) and The Reinsurance industry revealed that the number of climate-related disasters significantly increased in the 1930s (Cheema *et al.,* 2011). That's why the climate forecast has been essential to protect the agricultural sector of Rangpur in Bangladesh at present. So that, three to six months before a perfect climate forecast, probable growers and others in the agricultural sector may decide to abate the unexpected impact. So some forecasting-related studies were completed for this study. Such as Khan *et al.* (2020) applied a Long Short-Term Memory (LSTM) model in their study to predict monthly temperatures and precipitation by analyzing weather data of Bangladesh from 1901-2015. The LSTM model has shown -0.38 degree centigrade mean error in the case of predicting month-based temperatures of 2 years and -17.64 mm in the case of rainfall predicting. This prophecy model can help understand the changing pattern of weather in addition to studying Bangladesh's seasonal diseases whose prevalence depends on regional temperature and/or rainfall.

Karna *et al.* (2021) conducted a study and used in their study Statistical Linear Regression and Linear Regression including elastic nets and hyper parameters, and it is stated in the outcomes of the analysis that the regression based highest temperature long-term prediction models provide more accuracy with the RMSE (root mean square error) and MAE (mean absolute error). According to both Hydrology and Meteorology Department (HM D), only 284 weather centers are currently operating in Nepal. Though empirical predicting models are extensively analyzed as well as evaluated, the performance of these models is seen to vary following local climate and geographical location (Fan *et al*., 2018). Using Cluster Analysis (CA) and Principal Component Analysis (PCA)), the selected stations were clustered in well-defined groupings, and afterward one individual NN (neural network) was used in every group of stations. On the other hand, another NN (neural network) model was also created to measure the accuracy of the model proposed and was used in all the stations. Statistical outcomes exhibited that the 1st model generated better-predicted outcomes than the 2nd model (Arab Amiri *et al*., 2018). Portugal's annual temperatures were predicted using the autoregressive model, and research has shown that annual temperatures change from decade to decade. In other words, it was found fluctuations in the annual and decade temperature (Leite & Peixoto, 1996).

Using the seasonal ARIMA model Nury *et al*. (2013) forecasted the minimum and maximum temperatures of Moulvibazar and Sylhet districts and it suggested that this method would work better to forecast the time series data. A significant relationship between mortality and temperature was found in several cities around the world, where the direct temperature is responsible for maximum deaths for example the reason for cardio-respiratory disease may be the temperature rising of human body or vessels' weak functioning to transfer blood and nutrients in the human body (Kalkstein, 1991; Martens, 1998). Using artificial neural networks Jain (2003) conducted research on weather data, especially temperature for forecasting the next one to twelve hours in South Georgia. Rehman & Mohandas (2008) exhibits in their research that the neural

network can predict Saudi Arabia's solar radiation by temperature and relative humidity from 1999 to 2000. A flexible and powerful tool was developed by researchers (Sharma & Bose, 2014) as an intelligent method for seeking ways to forecast weather parameters beyond the general method. ANN (Artificial neural network) is one of the intelligent methods capable of calculating logical functions and arithmetic. Forecasting of temperature is very important in agriculture and other sectors because Bangladesh is a major agricultural country. The output of this research will help the Agricultural Officials and National planners to take possible mitigation measures for protecting the crops from the adverse consequences of global climate change. The necessity of simulating or forecasting climate parameters in recent decades has become much more important because of climate change and global warming. So this study forecasted Rangpur temperature for six seasons in Bangladesh using the CPT model. Because Bangladesh is a country with six seasons (BBS, 2020).

This is a new field of study. Although some studies have been reported on temperature and rainfall, no specific study has been found on the forecast of seasonal temperature for Bengali seasons in Bangladesh. So, this study will fill up the research gap. Thus, to achieve the goal, the objectives are : (i) To forecast the seasonal mean temperature of six Bengali seasons: summer (14 April to 14 June), rainy season (15 June to 15 August), autumn (16 August to 15 October), late-autumn (16 October to 14 December), winter (15 December to 12 February), and spring (13 February to 13 April), by CPT using sea surface temperature for the period of 1975 to till the previous month of each season of 2008 as the predictor and (ii) To determine the differences between temperatures forecasted by CPT and observed temperatures.

2. Data and methods

2.1 Study area

Rangpur is 29 meters above sea level and located in a geographic position between 25°18' and 25°57' N latitudes and between 88°56' and 89°32' E longitudes. Rangpur lies in the northwestern part of Bangladesh. Rangpur district (Figure 1), covering a place of about 2,401 km². There are five major rivers in the Rangpur region–Dharla, Teesta, Brahmaputra, Dudhkumar, and Saniajan flow over the danger level because of the onrush of water from upstream and heavy rain. Geologically, the study area lies in the north-northwestern part of the Bengal Basin. The composition of the soil is predominantly Teesta River basin's alluvial soil which is 80%, and the residual is barind soil. The climate of Rangpur is categorized as temperate and warm. In accordance with Köppen and Geiger, this climate is classified as Cwa **(**Monsoon-influenced humid subtropical climate). There exists a humid subtropical climate at Rangpur. The temperature range is 32ºC to 11ºC. In winter, the night temperature can drop below 11.7 degrees Celsius whereas, the daytime temperature is around 23.6 degrees Celsius. Annual averages rainfall is 2931 mm**;** almost all of them fall from June to September, although there is very little rainfall from November to March, but a small amount of rainfall due to western disturbances coming from the Mediterranean Sea. Snow and frost have never been recorded in Rangpur. Around 2802.78 hours

of sunshine are counted in Rangpur throughout the year. On average there are 92.24 hours of sunshine per month. The month of maximum relative humidity is September (86.88%).The month of minimum relative humidity is March (50.41 %). Jun of the year is the windiest month in Rangpur with an average speed of 12.6 kilometers per hour. December of the year is the quietest month in Rangpur with an average speed of 6.0 kilometers per hour (Rangpur climate, 2021).

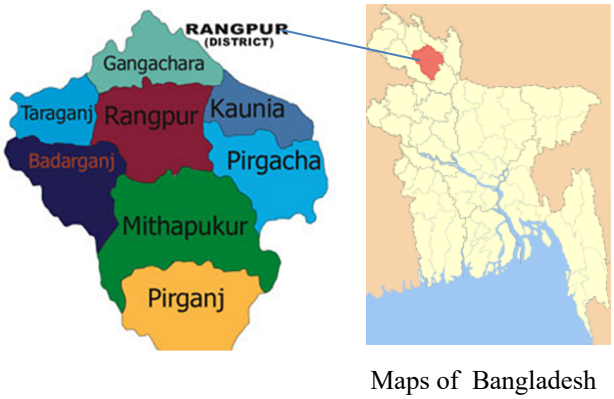

Fig. 1. Study Area (Rangpur District)

2.2 Data collection

Sea surface temperature (The multimodel ensemble global product of APCC data) was considered as a predictor to forecast seasonal mean temperature (Basnayake *et al.,* 2010) for the six Bengali seasons in Bangladesh in this study. This data was obtained from the DODS server of ICTP (International Center for Theoretical Physics). The data downloading from the mentioned site was binary data that is converted to the ASCII format by FORTRAN code next. Daily observed temperature data of Rangpur station in Bangladesh was taken up from Bangladesh Meteorological Department. This observed data was processed to get the seasonal mean temperature as the predictands for the CPT. The temperature at Rangpur station was calculated for six Bengali seasons and converted to a format (text) suitable for the CPT software.

2.3. Methods

In this study statistical and mathematical methods were applied by CPT which included canonical correlation analysis, covariance matrix and eigenvalues equations. Canonical correlation analysis is used to find two sets of basis vectors which are one for u and the other for v, as a result onto these basis vectors the correlations between the estimates of the variables are reciprocally maximal. There is such a case where solely one pair basis vectors is required, as for instance, the ones related with maximal canonical correlation: considering $u = u^T \hat{z}_u$ and $v = v^T \hat{z}_v$ as linear combinations for two variables respectively. It's meaning that the maximal function is

$$\rho = \frac{E[uv]}{\sqrt{E[u^2]E[v^2]}} = \frac{E\left[\hat{z}_u{}^T uv^T \hat{z}_v\right]}{\sqrt{E\left[\hat{z}_u{}^T uu^T \hat{z}_u\right]E\left[z_v{}^T vv^T \hat{z}_v\right]}} = \frac{z_u{}^T C_{uv} z_v}{\sqrt{z_u{}^T C_{uu} z_u z_v{}^T C_{vv} z_v}} \quad (1)$$

The largest of ρ in respect of z_u and z_v is highest canonical correlation. The posterior canonical correlations are not correlated on account of various solutions, i.e.

$$\begin{cases} E[u_i u_j] = E\left[z_{ui}{}^T uu^T zuj\right] = z_{ui}{}^T C_{uu} z_{uj} = 0 \\ E[v_i v_j] = E\left[z_{vj}{}^T yy^T z_{yj}\right] = z_{vi}{}^T C_{vv} z_{vj} = 0 \quad \text{for } i \neq j. \\ E[u_i v_j] = E\left[z_{ui}{}^T xy^T z_{yj}\right] = z_{ui}{}^T C_{uv} z_{vj} = 0 \end{cases} \quad (2)$$

Calculating canonical correlations: Consider u and v are two variables with zero mean. The total covariance matrix

$$C = \begin{bmatrix} C_u & C_{uv} \\ C_{vu} & C_{vv} \end{bmatrix} = E\left[\begin{pmatrix} u \\ v \end{pmatrix} \quad \begin{pmatrix} u \\ v \end{pmatrix}^T \right] \quad (3)$$

For u and v the within-sets covariance matrix are C_{uu} and C_{vv} respectively, and $C_{uv} = C^T{}_{vu}$ is the covariance matrix between-sets. Between u and v we can get canonical correlations by solving the eigenvalues equations

$$\begin{cases} C^{-1}{}_{uu} C_{uv} C^{-1}{}_{vv} C_{vu} \hat{z}_u = \rho^2 \hat{z}_u \\ C^{-1}{}_{vv} C_{vu} C^{-1}{}_{uu} C_{uv} \hat{z}_v = \rho^2 \hat{z}_v \end{cases} \quad (4)$$

Where ρ^2 indicate eigenvalues, which are squared canonical correlations. On the other hand, $\hat{z}_u$ and $\hat{z}_v$ indicate eigenvectors which are normalized canonical correlation of basis vectors. Non zero solutions of these equations are limited to the lowest dimensionality of u and v. E.g. if 8 and 5 are the dimension of u and v respectively, the highest number of canonical correlations will be 5.Only one among the eigenvalue equations needs to be resolved because the solutions are related by

$$\begin{cases} C_{uv} \hat{z}_v = \rho \lambda_u C_{uu} \hat{z}_u \\ C_{vu} \hat{z}_u = \rho \lambda_v C_{vv} \hat{z}_v \end{cases} \quad (5)$$

$$\text{Where } \lambda_u = \lambda_v{}^{-1} = \sqrt{\frac{\hat{z}_v{}^T C_{vv} \hat{z}_v}{\hat{z}_u{}^T C_{uu} \hat{z}_u}} \quad (6)$$

2.4 Climate predictability tool as software

The Climate predictability Tool was used as mathematical software for forecasting seasonal mean temperature using sea-surface temperatures as predictors and observed temperatures as predictands. It can be used in any area for diagnostic research and forecasting. In this study canonical correlation analysis on a pair of data sets was performed by CPT.

3. Results and discussion

3.1 Forecasting of seasonal mean temperature

CPT was employed to forecast seasonal mean temperature for six Bengali seasons over Rangpur and the sea surface temperature (SST) for the period of 1975 to till the previous month of each season of 2008 was used as the predictor. In this study, some skill scores exempli gratia Hit Score (HS), Mean Absolute Error (MAE), Bias, and Root Mean Square Error (RMSE) were calculated to understand the exactness of forecasting results. RMSE is the metering of the distinction between the value observed and the value calculated by the CPT which helped to determine accuracy. Bias is an estimation of the value produced by the model compared to the observed value and it can be anyone positive or negative depending on the value produced by the model. The Hit Score is taken into consideration as the value of percentage (%) of the proportion of value calculated by the CPT model with the accurate value of observed data. Hence, if the forecasted value would be the same as the observed value, the Hit score should have been 100%. MAE is a type of measure by which we can easily understand how much the forecasted value is closer to the actual value.

3.2 Forecasting of seasonal mean temperature over Rangpur for six Bengali seasons in Bangladesh using sea surface temperature for the period of 1975 to till the previous month of each season of 2008 as the predictor.

To find the sea surface temperature (SST) that is similar to the temperature in Rangpur, a correlation between the temperature of Rangpur and the sea surface temperature of various parts of the earth was performed with the help of the CPT using both data from 1975- 2008 years. The obtained SST that is more or less similar to the temperature in Rangpur through correlation was used as the predictor to forecast the seasonal mean temperature of the year 2009. The maximal goodness index in this study was found by altering the X domain for Cross-Validated window. On the other hand, SST was obtained by using the correlation method of Pearson's and Spearman. Besides this was obtained the value of Pearson correlation coefficients and Spearman correlation coefficients along with the value of the forecasted seasonal mean temperature of six Bengali seasons for the year 2009. In Table 1, the obtained outcomes are presented.

Table 1. The obtained outcomes of correlation coefficients, GI, CVW, and forecasted temperature in various x-domains during the period 1975-2008 using sea surface temperature for the period of 1975 to till the previous month of each season of 2008 as the predictor.

		GI		CVW	Correlation coefficients		Forecasted temperature
seasons	*x*-domain	Pearson	Spearman		Pearson	Spearman	(° C/day) in 2009
Summer	2S-8N 2-48E	0.274	0.974	27	0.274	0.483	27.76
Rainy season	8S-8N 2-35E	-0.434	0.984	5	-0.434	-0.408	28.54
Autumn	44S-19N 4-50E	-0.312	0.992	11	-0.312	-0.25	28.06
Late Autumn	40S-20N 10-200E	0.258	0.998	1	0.25	0.357	22.45
Winter	10S-60N 10-80E	-0.311	0.994	5	-0.311	-0.288	16.8
Spring	12S-30N 2-58E	0.279	0.992	25	0.28	0.331	23.23

The following (Figures 2-7) showing X Domain of SST for six seasons in Bangladesh.

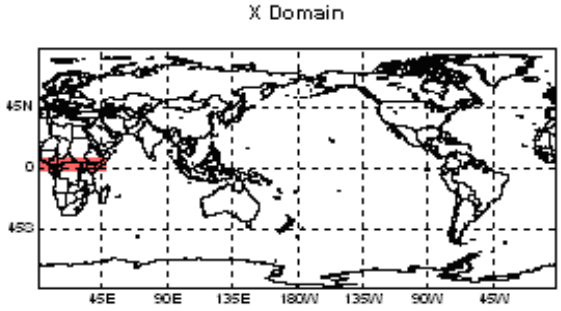

Fig.2. X Domain of global sea surface temperature in the summer for forecasting of temperature over Rangpur

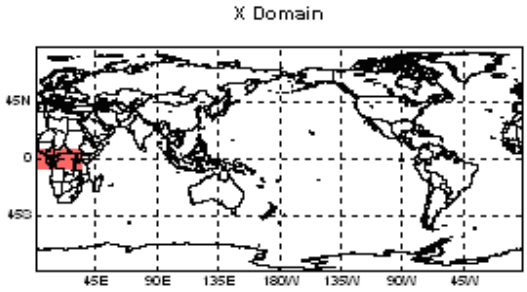

Fig. 3. X Domain of global sea surface temperature in the rainy season for forecasting of temperature over Rangpur.

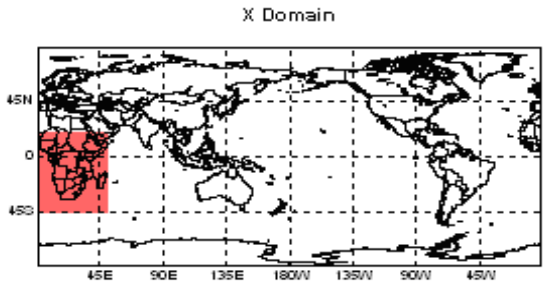

Fig. 4. X Domain of global sea surface temperature in the autumn for forecasting of temperature over Rangpur

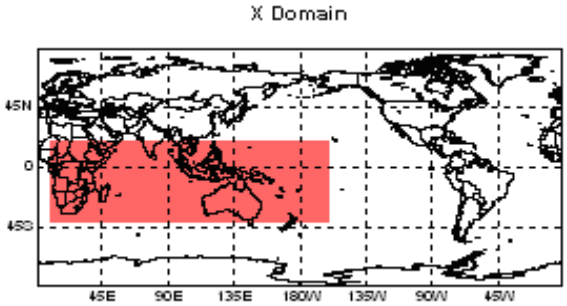

Fig. 5. X Domain of global sea surface Temperature in late autumn for forecasting of temperature over Rangpur

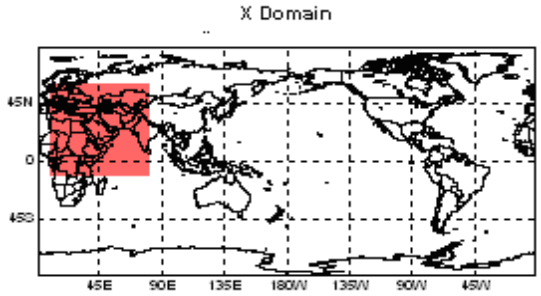

Fig. 6. X Domain of global sea surface temperature in the winter season for forecasting of temperature over Rangpur

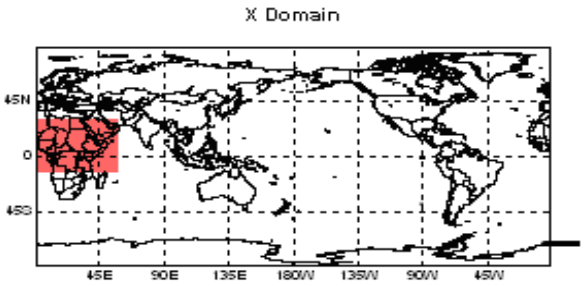

Fig.7. X Domain of global sea surface temperature in the spring season for forecasting of temperature over Rangpur

From Table 1 and (Figures 2-7) it is said that maximal goodness index (GI) was not found for all x domain. This means that a different x-domain was found for one season to another season in case of getting maximum correlation coefficient and maximum GI. From Table 1 the positive correlation coefficients were obtained only in summer, late autumn, and spring seasons for the both Pearson and Spearman processes. The value of the forecasted temperature for the year 2009 was found to be nearby to the observed temperature, shown in Table 3. In Table 2, the skill scores for forecasting seasonal mean temperature over Rangpur are presented.

Table 2. Efficiency scores of forecasting seasonal temperature over Rangpur

Name of Seasons	RMSE (°C/day)	HS (%)	Bias	MAE (°C/day)
Summer	2.24	58.82	0.31	1.28
Rainy season	1.73	35.29	0.00	0.93
Autumn	1.26	29.41	-0.05	0.74
Late autumn	0.65	52.94	-0.01	0.47
Winter	1.09	38.24	-0.05	0.78
Spring	1.24	52.94	0.19	0.82

From the above Table 2, it is seen that the values of root mean square error (RMSE) were logically less in all the seasons except summer. The mean absolute errors (MAE) were lower in the rainy season, autumn, late autumn, winter, and spring and relatively higher in the summer season only. On the other hand, the bias was very lower in the rainy season, autumn, late autumn and winter than in summer and spring. The range of hit scores was 29.41 to 58.82 which is relatively lower. The forecasted temperatures were not near to the observed temperature as much could be seen in Figures 8 to 13. It may be occurred because of a lower hit score (HS). But the figures for actual and forecasted temperature exhibit more or less equivalent patterns of variation which is very much encouraging. It is seen that the values of root mean square error (RMSE) were logically less.

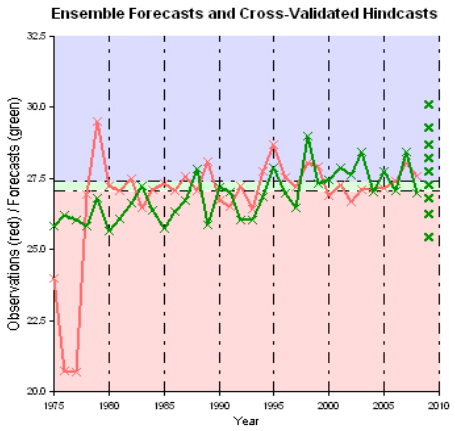

Fig. 8. Ensemble forecast temperature & Cross-Validated Hindcasts during summer over Rangpur.

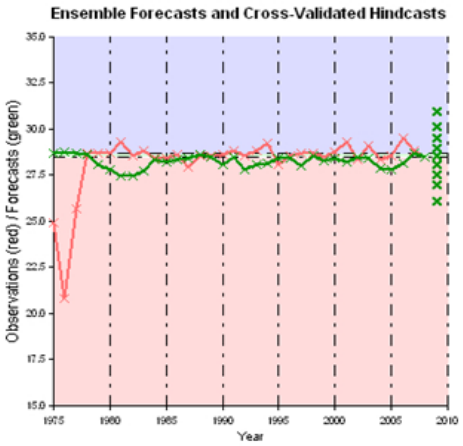

Fig. 9. Ensemble forecast temperature & Cross-Validated Hindcasts during the season of rainy over Rangpur.

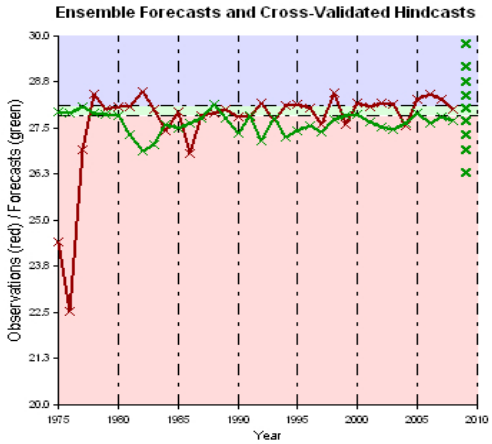

Fig. 10. Ensemble forecast temperature & Cross-Validated Hindcasts during autumn season over Rangpur.

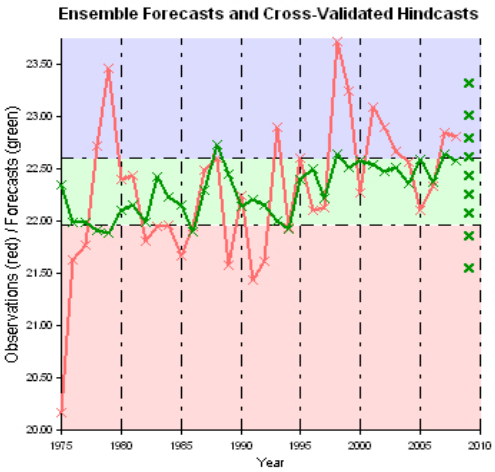

Fig. 11. Ensemble forecast temperature & Cross-Validated Hindcasts during late autumn over Rangpur.

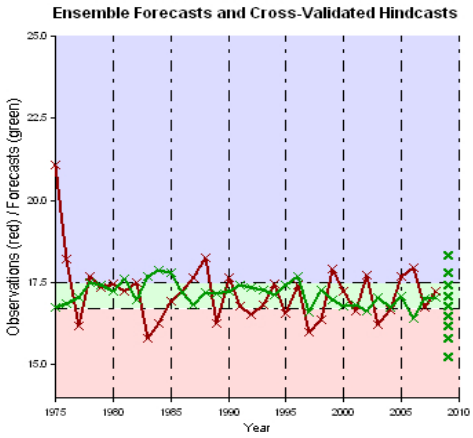

Fig. 12. Ensemble forecast temperature & Cross-Validated Hindcasts during winter over Rangpur.

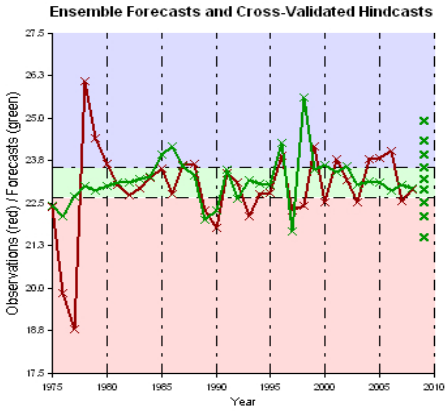

Fig.13. Ensemble forecast temperature & Cross-Validated Hindcasts during spring over Rangpur.

Table 3. Observed temperature, forecasted temperature and deviation of forecasted temperature from observed temperature of the year 2009.

Seasons	Observed temperature (º C/day)	Forecasted temperature (º C/day)	Deviation
Summer	28.01	27.76	0.25
Rainy-season	28.20	28.41	-0.21
Autumn	28.60	28.06	0.54
Late-autumn	22.85	22.45	0.40
Winter	16.28	16.80	-0.52
Spring	23.61	23.23	0.38

From Table 3, the value of the forecasted seasonal mean temperature was more as compared to the actual (observed) temperature during the rainy and winter seasons at Rangpur. Syeda (2012) found in his study a decreasing trend in temperature simulated by the ARIMA model over Rajshahi and Barisal and an increasing trend over other divisions of Bangladesh with Rangpur. On the other hand, the value of the forecasted seasonal mean temperature was low as compared to the actual temperature during summer, autumn, late autumn, and spring seasons at Rangpur. The annual average temperature of Dinajpur, Rajshahi, and Rangpur was decreased at the rate of 0.01180^{o}C/year, 0.01340^{o}C/year, and 0.02620^{o}C/year respectively, which is reported by Ferdous & Baten **(**2011). The forecasted temperature deviation from the observed temperature was minimally positive that is 0.25^{o}C/ day during the summer and maximally positive that is 0.54 ^{o}C/day during the autumn. On the other hand, the minimum negative value of -0.21^{o}C/day during the rainy season and the maximum negative value of -0.52^{o}C/day during the winter season was found at Rangpur. From above discussion it is seen overestimated forecasted temperature during some seasons and underestimated forecasted temperature during some seasons. It may be occurred due to variations of hit score (HS) or Goodness index (GI). However, it can be said that the Climate Predictability Tool (CPT) skillfully forecasted the seasonal mean temperature over Rangpur region. It can be undoubtedly said that forecasting temperature is one of the most important ways through which it is possible to enlarge both the quality and quantity of production in the agricultural sector having diminished temperature-related risk. As a result, the people of Rangpur will be able to recover in advanced social and economic management products in livestock and agriculture by using reliable and up-to-date seasonal temperature forecasts.

6. Conclusion

A seasonal climate forecast is very useful for agricultural activity planning due to climate change. So in this research, an attempt was made to forecast seasonal mean temperature for six Bengali seasons of Bangladesh in the year 2009 using Climate Predictability Tool (CPT). From this study, it was found that sea surface temperature for the period of 1975 to till the previous month of each season of 2008 was more or less appropriate for CPT as the predictor. So, it can be said without a doubt that CPT exhibited a lot of skill in the forecasting of seasonal mean temperature over the Rangpur division during some selected seasons: The Summer and Rainy seasons of Bangladesh. Finally, it can be concluded that Climate Predictability Tool (CPT) is a powerful model to forecast seasonal mean temperature.

ACKNOWLEDGEMENTS

This study was performed by CPT which was made by the International Research Institute at Columbia University in the United States. Support of Climate Predictability Tools (CPT) is gratefully acknowledged. The author greatly appreciates the support from Bangladesh Meteorological Department (BMD) and the International Center for Theoretical Physics, DODS server. On the other hand, the author is a lot grateful to the referees for their valuable advice.

References

Arab Amiri, M., Conoscenti, C. & Mesgari, M.S. (2018). Improving the accuracy of rainfall prediction using a regionalization approach and neural networks. Kuwait J. Sci. **45 (4):** 66 -75.

Basnayake, B.R.S.B., Nesssa, F.F. & Mannan, M.A. (2010). Seasonal weather forecasting in Bangladesh using Climate Predictability Tool (CPT). SMRC Report No. **34**: SAARC Meteorol. Res.Cen.(SMRC), Dhaka, Bangladesh.

BBS (Bangladesh Bureau of Statistics) (2020). Bangladesh Statistics 2020, Statistics and Informatics Division (SID), Ministry of Planning, Government of the People's Republic of Bangladesh, page 2.

Cheema, S.B., Rasul, G., Ali, G. & Kazmi, D.H. (2011). A comparison of minimum temperature trends with model projections. Pakistan Journal of Meteorology, **8**: 39-52.

Fan, J., Chen, B., Wu, L., Zhang, F., Lu, X. & Xiang, Y. (2018). Evaluation and development of temperature-based empirical models for estimating daily global solar radiation in humid regions. Energy,**144:** 903–914.

Ferdous, M.G. & Baten, M.A. (2011). Climatic Variables of 50 Years and their Trends over Rajshahi and Rangpur Division. Journal of Environmental Science and Natural Resources, **4**: 147-150.

Intergovernmental Panel on Climate Change (IPCC), (2001). Climate change 2001: impacts, adaptation and vulnerability. Cambridge University Press, Cambridge, UK.

Jain, A. (2003). Predicting air temperature for frost warning using artificial neural network. A Thesis Submitted to the Graduate Faculty of the University of Georgia in Partial Fulfillment of the Requirements for the Degree Master of Science, Athens, Georgia, 92 pages.

Khan, M.M.R., Siddique, M.A.B., Sakib, S., Aziz, A., Tasawar, I.K. & Hossain, Z. (2020) Prediction of Temperature and Rainfall in Bangladesh using Long Short-Term Memory Recurrent Neural Networks. 4th International Symposium on Multidisciplinary Studies and Innovative Technologies, IEEE, TURKEY, 22-24.

Karna, N., Roy, P. C. & Shakya, S. (2021). Long Term Temperature Forecasting using Regression Model. International Journal of Advanced Engineering, **4(2):** 73-92.

Kalkstein, L.S. (1991). A new approach to evaluate the impact of climate on human mortality. Environmental Health Perspectives, **96**: 145–150.

Leite, S.M. & Peixoto, J.P. (1996). The autoregressive model of climatological time series: an application to the longest time series in Portugal. International Journal of Climatology, **16**: 1165-1173.

Martens, W.J.M. (1998). Climate change, thermal stress and mortality changes. Social science & medicine, **46:** 331–344.

Machiwal, D. & Jha, M.K. (2006). Time Series Analysis of Hydrologic Data for Water Resources Planning and Management: A Review. J. Hydrol. Hydromech., **54**: 237–257.

Nury, A.H., Koch, M. & Alam, M.J.B. (2013). Time Series Analysis and Forecasting of Temperatures in the Sylhet Division of Bangladesh. In: 4th International Conference on Environmental Aspects of Bangladesh (ICEAB), 65-68.

Oyamakin, O., Adebayo, J., Ayoola, F. J. & Oyeleye, B. (2010). Time Series Analysis of Rainfall and Temperature in South West Nigeria. The Pacific J. of Sci. and Techno., **11**: 552-564.

Rehman, S. & Mohandes, M. (2008). Artificial neural network estimation of global solar radiation using air temperature and relative humidity. Energy Policy, **36**: 571–576.

Rangpur climate (2021). Average Temperature, weather by month, Rangpur weather averages - Climate-Data.org. en.climate-data.org. Retrieved 1.

Sharma, A. & Bose, M. (2014). Rainfall prediction using k-NN based similarity measure. Recent advances in information technology, Advances in Intelligent Systems and Computing, **266**:125-132.

Syeda, J. A. (2012). Trend and Variability Analysis for Forecasting of Temperature in Bangladesh. Journal of Environmental Science and Natural Resources, **5**: 243-252.

Shamsnia, S.A., Shahidi, N., Liaghat, A., Sarraf, A. & Vahdat, S.F. (2011). Modeling Of Weather Parameters (Temperature, Rainfall and Humidity) Using Stochastic Methods. International Conference on Environment and Industrial Innovation IPCBEE, IACSIT Press, Singapore, **12**: 282-285.

Submitted: 13/02/2022
Revised: 10/05/2022
Accepted: 31/05/2022
DOI: 10.48129/kjs.18877

Kuwait J.Sci., Vol.50, No.(1A),January.2023,pp(85-106)

Identifying potential sites for artificial groundwater recharge using GIS and AHP techniques: A case study of Erbil basin, Iraq

Omeed H. Al-Kakey[1,*], Arsalan A. Othman[2,3], Broder J. Merkel[1]

[1] *Institute of Geology, TU Bergakademie Freiberg, 09599 Freiberg, Germany*

[2] *Iraq Geological Survey, Al-Andalus Square, 10068 Baghdad, Iraq*

[3] *Dept. of Petroleum Engineering, Komar University of Science and Technology, 46001 Sulaymaniyah, Iraq*

* *Corresponding author: omeed.alkakey@gmx.de*

Abstract

Excessive extraction, uncontrolled withdrawal of groundwater, and unregulated practices have caused severe depletion of groundwater resources in the Erbil basin, Iraq. This situation has had a number of negative consequences on human settlement, agricultural activities, clean water supply, and the environment. Runoff harvesting and artificial groundwater recharge play a significant role in the sustainable management of water resources, particularly in arid and semi-arid regions. This study aims to: (1) delineate groundwater recharge zones using multiple thematic layers that control the groundwater recharge process, and (2) identify prospective sites and structures to perform artificial groundwater recharge. In order to generate a potential map for groundwater recharge zones, seven thematic layers are considered in this study, namely, topographic position index, geomorphology, lithology, land cover, slope, drainage-length density, and lineament-length density. After that, the analytic hierarchy process was applied to weight, rank, and reclassify these seven thematic layers. All maps are then integrated within the ArcGIS environment for delineating groundwater recharge zones. Accordingly, the resulting map categorizes the study area into five zones: extremely high, high, moderate, low, and extremely low potential for groundwater recharge. As expected, areas along the Greater Zab river show the highest possibility for groundwater recharge. Likewise, rugged eastern hills demonstrate an encouraging capacity for artificial aquifer recharge, whereas the least effective area is represented by built-up land. Based on the generated map, two dams are proposed as promising artificial recharge structures for harvesting runoff water east of Erbil city. Lastly, the resulting map of the potential groundwater recharge zones is verified using static water level data, where the coefficient of determination (R^2) achieved a satisfactory result (0.73). These findings provide crucial evidence for implementing a sustainable management plan for surface and groundwater resources. The applied method is eventually valid for regions where appropriate and adequate field data availability is a serious issue.

Keywords: Artificial recharge; groundwater; runoff harvesting; GIS; Iraq.

1. Introduction

Groundwater is one of the most extensively exploited natural resources in many parts of the world. In the past decades, groundwater extraction has immensely increased due to the development of new and affordable drilling and pumping techniques (Barbier, 2019). As groundwater resources are dynamic and interdisciplinary, they are influenced by different human activities, including urbanization, expansion of cultivated and irrigated areas, industrialization, and also by natural features such as geological structures of different compositions (Nalbantcilar & Guzel, 2006; Thangarajan, 2007; Kavaf & Nalbantcilar, 2007; Nalbantcilar & Pinarkara, 2015; Nalbantcilar & Pinarkara, 2016). According to Ahmed *et al.* (2008), over-exploitation of groundwater resources causes regional imbalances in both water demand and supply. Therefore, it has become critical to implement sustainable management plans to avoid groundwater depletion due to insufficient natural recharge.

The water resources in Iraq have considerably reduced due to the dam construction strategy in the upstream countries (Turkey, Iran, and Syria), chiefly including the Southeastern Anatolia Project (GAP) that Turkey has accomplished. The GAP project involves constructing 22 massive dams on the Tigris and Euphrates rivers to control surface water flow. After completing the GAP project, water stress dramatically increased in Iraq (Al-Muqdadi, 2019). The expansion of agricultural and industrial projects and drought conditions intensely depleted water resources in the Iraqi Kurdistan Region. Accordingly, a substantial reduction in groundwater levels has been observed in many parts of the Erbil basin. Replenishing groundwater through artificial recharge has been carried out in different parts of the world (Bowen, 1986) and some parts of Iraq (Salar *et al.,* 2018; Al-Manmi *et al*., 2021). Although precipitation is the primary source of natural recharge, it forms a small percentage, especially in dry countries (Boyko *et al.,* 2021). Hence, runoff harvesting and artificial recharge represent alternative techniques for the longevity of freshwater resources (Chowdhury *et al*., 2009). The procedure involves collecting and storing the runoff water in the subsurface to meet future water demands (Kumar *et al*., 2016).

Many scientific reports have been published worldwide on utilizing remote sensing (RS) and geographic information system (GIS) to investigate water resources. Researchers in watershed engineering and other fields have recently become increasingly interested in using GIS to fulfill site selection for artificial groundwater recharge (Rahimi *et al.*, 2014). In the study area, wars and internal conflicts have prevailed for the past decades. Thus, only a few water resources studies have been carried out using GIS and RS data. Hameed (2013) applied RS and GIS techniques to detect suitable water harvesting sites in the Erbil Governorate. In another study, Mulder *et al*. (2015) used GRACE satellite data to identify water mass variation in northern Iraq. Another study from Hameed (2017) estimated the consequences of urban growth and land-use changes on annual runoff in the Erbil subbasin using the GIS technique.

Since the region of interest is severely afflicted with water scarcity challenges, aquifer replenishment through artificial recharge is necessary to sustain the groundwater resources on a long-term basis. Due to the inadequacy of essential hydrogeological data for the entire study area, the present study is mainly built on surface parameters that control groundwater recharge. In this

paper, the normalized weights of seven thematic layers are calculated using the analytic hierarchy process (AHP) and then integrated within ArcGIS 10.1. Up till now, the AHP method has represented a practical approach to identifying groundwater potential recharge zones (Akbari *et al*., 2021; Das *et al.*, 2021; Vishwakarma *et al*., 2021). The present study was designed to delineate potential zones and identify suitable sites and structures for artificial groundwater recharge in the Erbil basin based on AHP and GIS. The resulting map of potential recharge zones was visually and statistically compared with the static water level map to check the accuracy of the proposed model. Consequently, the findings provide decision-makers with a scientific basis for further assessing and sustainably managing water resources. To date, no such research has been reported in the study area.

2. Study area

The study area is mainly located within the Erbil Governorate, north of Iraq. The region of investigation lies between longitude 43°30'E - 44°17'E and latitude 35°52'N - 36°29'N. It covers about 3000 km^2, forming 20% of the Erbil Governorate's total area (Figure 1). The study area has semi-arid climate conditions with cold winter and dry-hot summer. Rainfall occurs mainly between October and May, where the average annual rainfall is approximately 400 mm (Hameed, 2013). The primary water resources in the Erbil basin include rain, groundwater, and surface water, the latter represented by the Greater Zab River (GZR). The GZR crosses the study area from the northwest, a significant source of groundwater recharge. Bastora valley surrounds the north-northeast area, in which valley flow discharges into the GZR. Recent alluvial deposits and Miocene-Pliocene formations form the primary aquifer system in the study area. This intergranular aquifer system is usually highly productive, and the discharge of many wells exceeds 30 l/s (Stevanovic & Iurkiewicz, 2009). Most croplands are irrigated by rainfall and groundwater, while surface water is frequently used for drinking and domestic purposes.

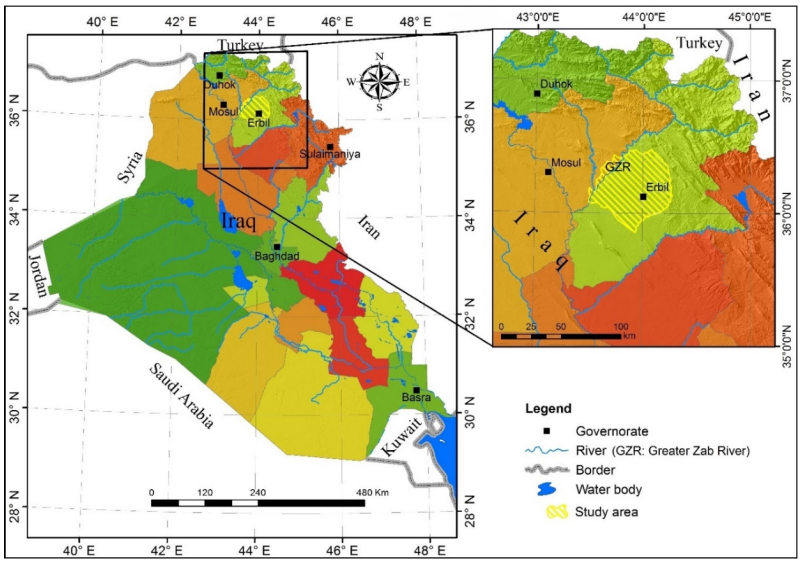

Fig. 1. Location map of the study area.

3. Geological setting

The collision of Arabian and Eurasian plates shaped Iraq's modern tectonic features (Salar *et al*., 2018). Iraq territory is divided into three main tectonic zones: (1) Stable Shelf, (2) Unstable Shelf (US), and (3) Zagros Suture Zone. The US involves the Mesopotamia Foredeep, the Foothill Zone (FZ), the High Folded Zone, and the Imbricated Zone. Furthermore, each of these zones has its characteristics; age, rock type, thickness, and structural evolution. Surface folds are an essential characteristic feature of the US. Besides, the rocks of the US were affected by Alpine orogeny during the Mesozoic Era. The study area is a part of the FZ, which comprises long-narrow anticlines (trending NW-SE) of different amplitude and broad synclines containing thick Miocene-Quaternary molasse (Jassim & Goff, 2006; Othman *et al*., 2018).

Five geological formations crop out in the study area: Pila Spi, Fatha, Injana, Mukdadiya, and Bai Hassan. Pila Spi Formation belongs to the Middle-Upper Eocene age and consists of well-bedded, porous, chalky, bituminous, poorly fossiliferous limestone (Jassim & Goff, 2006). Fatha Formation of the Middle Miocene age is divided into two parts; the lower portion comprises thick reddish and greenish silty claystone, thin-bedded limestone, and grayish sandstone. In comparison, the upper part is composed of alternating beds of gypsum, anhydrite, and salt, interbedded with limestone, marl, and reddish-brown clastics. Injana Formation (Late Miocene age) consists of coarsening-upward cycles of brown, red, grey claystone, siltstone, and sandstone, with thin limestone gypsum horizons. Mukdadiya Formation of Late Miocene–Pliocene age comprises alternating layers of pebbly sandstone, coarse sandstone, claystone, and siltstone. Bai Hassan Formation, which belongs to the Pliocene-Pleistocene age, mainly consists of coarse and thick fluviatile conglomerate, sandstone, and claystone. At the same time, the Quaternary deposits of the Pleistocene-Holocene age cover a considerable part of the investigation area, such as sediments of slope and floodplain, river terraces, and polygenetic. Coarse clastics characterize the sediments of Quaternary deposits, a mixture of conglomerate and gravel intermixed with clay and sand (Sissakian & Al-Jiburi, 2012).

4. Materials and methods

4.1 Data acquisition

GIS-AHP-based model and multi-parametric data sets were applied in this study to determine potential recharge zones and find suitable sites for artificial groundwater recharge in the Erbil basin. Hence, seven frequently used factors were identified that control groundwater recharge. These factors include topographic position index (TPI), geomorphology, lithology, land cover, slope, drainage-length density (DD), and lineament-length density (LD). The Iraq geological survey (GEOSURV) provided pre-existing maps of four layers with a scale of 1:250,000 (geomorphology, lithology, land cover, and lineament). Because these four maps were in paper format, they were first scanned and georeferenced to the UTM coordinate system in zone 38 north. After that, the four maps were digitized in ArcGIS 10.1.

The ASTER Global Digital Elevation Model (ASTER GDEM) at 30 m resolution was obtained from the United States Geological Survey (USGS). Moreover, the slope, TPI, and drainage map were derived from the ASTER GDEM. The static water level data from 101 randomly distributed monitoring wells over the entire study area were gathered from the GEOSURV. These collected data were utilized to generate a thematic map for each of the seven factors and validate the results. Thus, the weights of different themes and their corresponding features were assigned using the integrated GIS and the AHP method. Afterward, the seven generated thematic maps were overlayed by raster calculation for mapping and identifying potential recharge zones. Later, based on runoff availability, ASTER GDEM, TPI class, and drainage network map, two basins were chosen to implement artificial groundwater recharge. Lastly, the generated map was compared with the static water level map to validate the proposed methodology.

4.2 Preparation of thematic layers

4.2.1 Elevation

The elevation represents an essential factor that plays a vital role in deriving TPI, drainage networks, watershed delineation, and slope maps. According to Salar et al. (2018), elevation has an inverse relationship with groundwater recharge; the lower the height, the higher the possibility of surface water accumulation and infiltration, where surface water tends to flow towards lower elevations. ASTER GDEM is nominally the most detailed GIS layer with public access (Hengl & Reuter, 2011). The elevation map is derived from the ASTER GDEM. The study area elevation ranges from 176 to 1182 m above sea level (Figure 2a).

4.2.2 Watershed delineation

Watershed delineation is the process of defining an area that contributes surface water flow to a single outlet point. Amid technical development in geospatial software, GIS became a widely used hydrologist tool for delineating the watershed boundary (Castronova & Goodall, 2014). ArcGIS calculates diverse terrain processing components for watershed delineation, including determining flow direction, flow accumulation, depression filling, extracting stream network, and outlets. In the present study, the watershed was delineated and derived from the ASTER GDEM as input data using the watershed tools in ArcGIS 10.1. The study area comprises 13 watersheds, generally elongated in the NE-SW direction (Figure 2b).

4.2.3 Topographic position index (TPI)

TPI is the difference in elevation between the central cell and the average elevation of neighboring cells with a predetermined radius (Wilson & Gallant, 2000). Further, TPI is widely used in hydrology, geomorphology, agriculture, geology, aquifer recharge, hydrogeology, forest management, climatology, behavioral ecology, bathymetry, archaeology, risk management, and wildlife management (De Reu *et al.*, 2013; Nalbantcilar *et al.*, 2009). In the current study, the TPI

layer was derived from the ASTER GDEM using the open-source SAGA GIS software. The search radius of the kernel was set to 6000 m with a 30 m output cell size. The TPI is calculated based on the following equation (Othman *et al.*, 2018):

$$TPI = Ec - Ea \quad (1)$$

$$Ea = \frac{1}{n_M}\sum_{i\in m} E_i \quad (2)$$

where Ec is the elevation of the central cell, Ea is the average elevation of surrounding cells, and Ei is the elevation of the cell (i) within the kernel-matrix (M), which includes (n) cells. A positive TPI value suggests the cell is near the top of a ridge or hill, and a negative value proposes the cell is close to the bottom of a valley. Zero value could mean either a mid-slope area or flat terrain (Tagil & Jenness, 2008). TPI map is classified in this study into five classes (Figure 3a).

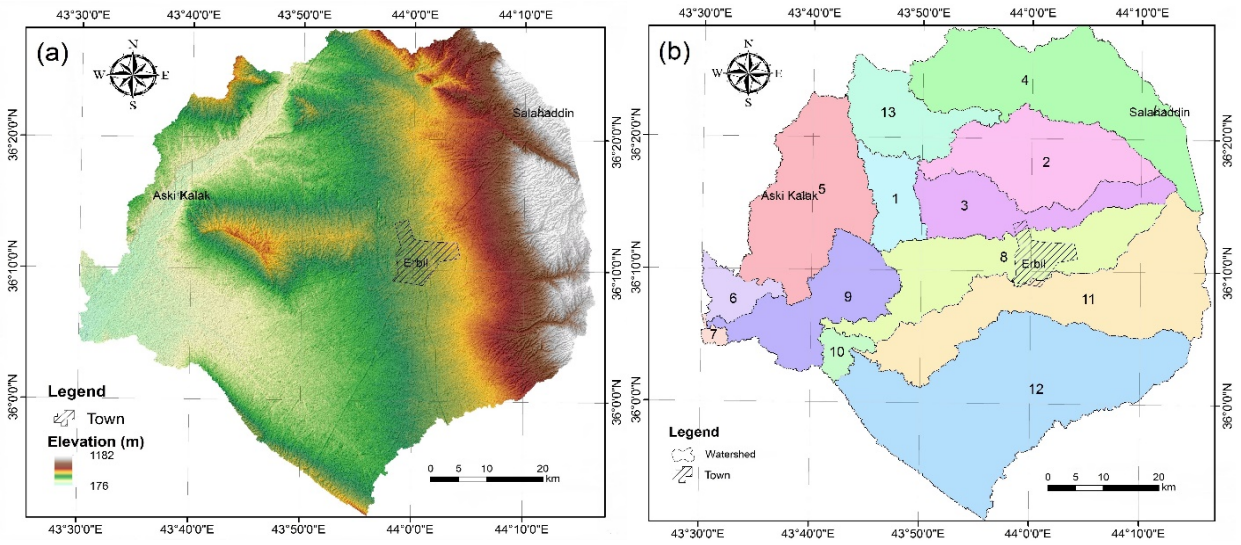

Fig. 2. Maps of (a) elevation and (b) watershed delineation of the study area.

4.2.4 Slope

The slope is the incline of a terrain's ground surface measured in degrees from 0 to 90. Besides, it is the steepest slope of a plane defined by the cell and its eight surrounding cells (Bajjali, 2018). According to Aluko & Igwe (2017), the slope represents another factor that plays an essential role in predicting water flow direction; it controls groundwater recharge and discharge processes. The flat plains tend to hold more rainwater and consequently facilitate the recharge process. In contrast, mountainous areas with high slope degrees have a high potential for runoff and low infiltration capability (Singh *et al.*, 2013). The spatial distribution of the slope demonstrates noticeable variations from the northeastern part to the southwestern area of the investigated basin (Figure 3b).

The slope layer was generated from the ASTER GDEM using ArcGIS, and it is grouped into five classes.

4.2.5 Lithology

The lithological character of exposed rocks and sediments significantly governs groundwater recharge (Shaban *et al*., 2005). Two lithological units exist in the study area, Tertiary formations and Quaternary sediments. Tertiary formations occupy the higher elevation areas, namely Pila Spi, Fatha, Injana, Mukdadiya, and Bai Hassan. In comparison, lowlands within the study area belong to the Quaternary sediments. Pila Spi Formation is represented by well-bedded and highly fractured limestone (Sissakian & Al-Jiburi, 2012). The fissured aquifer of Pila Spi is a substantial source of groundwater; in some cases, well productivity might achieve 40 l/s. The heterogeneous facies of Fatha and Injana formations comprise sandstones, marls, gypsum, anhydrite, sand, clays, and conglomerates. Groundwater in both formations is generally brackish with relatively more fresh water in Injana Formation. Since Fatha and Injana formations have repetitive cycles of impermeable rocks, the groundwater resources are insignificant and could solve only local water needs (Stevanovic & Iurkiewicz, 2009).

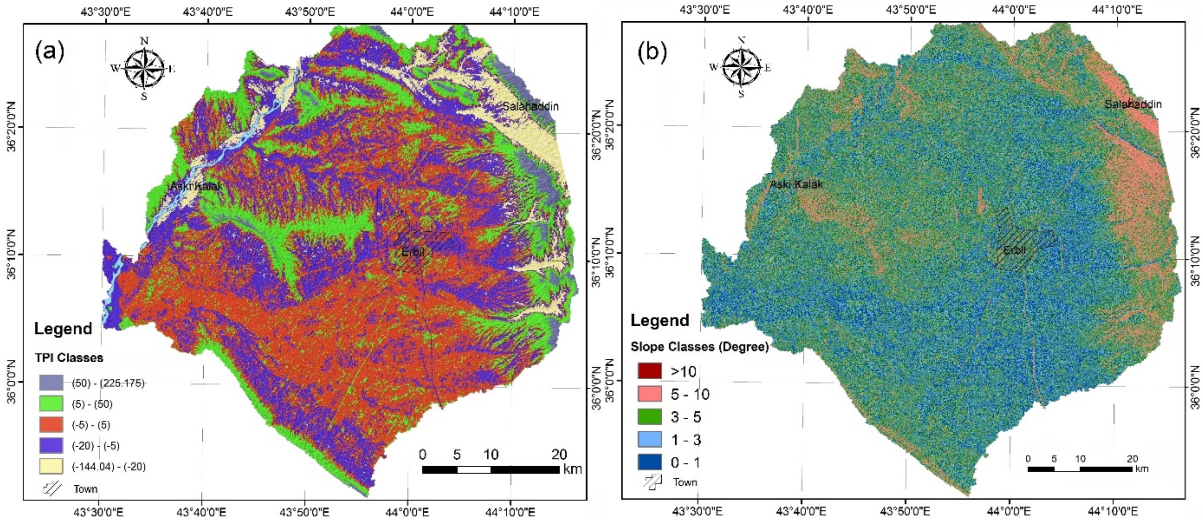

Fig. 3. Maps of (a) topographic position index (TPI) and (b) slope of the study area.

The heterogeneous lithology of Mukdadiya and Bai Hassan formations covers a large surface in the study area. With a massive thickness, it consists of a successive repetition of pebbly sandstone, sandstone, claystone, siltstone, and conglomerate (Sissakian & Al-Jiburi, 2012). These repetitive cycles of fine, medium, and coarse-grained textures are typical characteristics of this aquifer system. Several deep wells were drilled in the Mukdadiya-Bai Hassan aquifer with relatively high discharge; some wells exceeded 30 l/s (Stevanovic & Iurkiewicz, 2009). The unconsolidated Quaternary sediments cover large areas in the investigation region, mainly four types: river terraces, floodplains, slopes, and polygenetic sediments, forming the study area's

central aquifer system (Sissakian & Al-Jiburi, 2012). In the present study, the lithological map was obtained from the GEOSURV. The geological formations and Quaternary deposits are classified into nine classes according to their impact on groundwater recharge (Figure 4a).

4.2.6 Land cover

The land cover represents a fundamental indicator for selecting suitable sites for artificial groundwater recharge (Singh *et al.*, 2013). It includes the distribution of residential areas, soil type, and vegetation cover. The vegetation cover plays a vital role in the infiltration capacity, where the root system of plants increases soil porosity. Accordingly, it raises water infiltration into the subsurface (Shaban *et al*., 2005). The runoff, infiltration, and evapotranspiration vary based on the type of land cover. Croplands comprises increased infiltration rates and decreased runoff components, whereas bare and built-up lands tend to have high runoff and low infiltration and recharge (Anbazhagan *et al*., 2005). The land cover map was gathered from the GEOSURV and classified into seven classes: agricultural land, bare land, field, mixed-barren land, waterbody, irrigated land, and the built-up parts (Figure 4b).

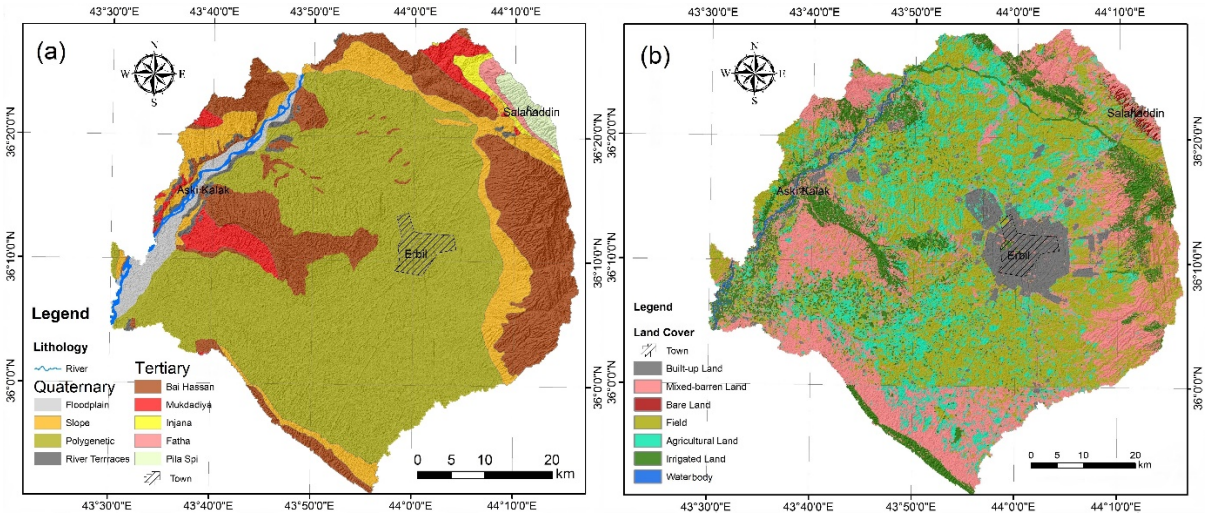

Fig. 4. Maps of (a) lithology and (b) land cover of the study area.

4.2.7 Geomorphology

Geomorphology refers to studying the earth's physical land-surface features such as hills, plains, and beaches. It investigates landforms and the processes that fashion them. Further, the water and rock cycles are crucial for understanding landform evolution (Huggett, 2011). Aluko & Igwe (2017) stated that geomorphology is one of the controlling factors for assessing potential groundwater recharge sites. Different structural features and landforms are significantly helpful for identifying prospective areas of groundwater occurrence. Broad plains with moderate slopes, alluvial fans, and pediments are considered favored locations for developing artificial groundwater

recharge projects (Rahimi *et al.*, 2014). In this study, the geomorphological map was obtained from the GEOSURV. The study area includes eight geomorphological units of floodplain and island, terraces, badland, depositional glacis, cuestas and hogbacks, erosional glacis, infill valley, and structural ridge. Each geomorphological feature shows a typical influence on aquifer recharge (Figure 5a).

4.2.8 Drainage-length Density (DD)

The DD is expressed as the total length of all channels per the drainage basin's total area (km/km^2), which describes the closeness of channel spacing (Singh *et al*., 2013). Numerous factors control the formation of a drainage system, like lithology, geological structure, soil properties, slope angle, infiltration rate, and vegetation cover (Salar *et al.*, 2018). According to Chowdhury *et al*. (2009), an inverse relationship exists between permeability and drainage density. The higher the drainage density, the lower the infiltration of rainwater, and vice versa. DD may indicate a channel system's development, surface runoff, rock permeability, and infiltration rate. Thus, it can be considered an indirect indicator of an area's suitability for artificial aquifer recharge. The DD value is computed from the following equation (Yeh *et al.*, 2009):

$$DD = \frac{\sum_{I=1}^{i=n} Si}{A} \tag{3}$$

where Si denotes the total length of drainage in km, and A is the area in km^2. In this study, the DD map was derived from the ASTER GDEM with a search kernel radius of 6000 m using ArcGIS 10.1. Strahler classification was used to assign a numeric order to link the drainage networks. The DD map is grouped into four classes based on its significance for identifying suitable sites for groundwater recharge (Figure 5b).

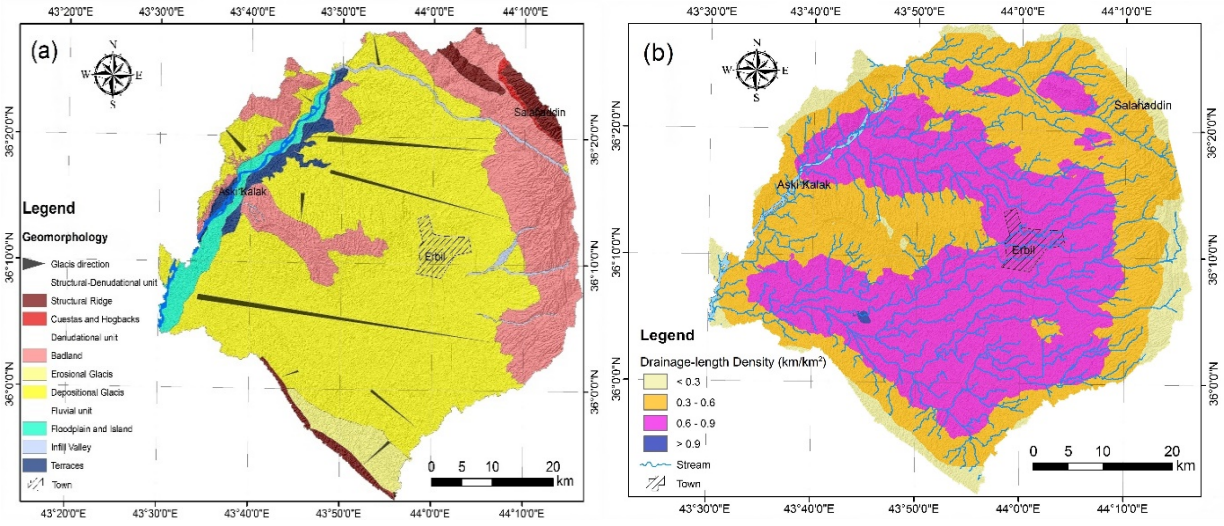

Fig. 5. Maps of (a) geomorphology and (b) drainage-length density of the study area.

4.2.9 Lineament-length Density (LD)

Lineament is a visible straight or curved linear feature on the ground surface. It can be human-made structures like canals and roads or geological structures such as fractures, cleavages, stream networks, faults, folds, and various discontinuity surfaces. Besides, lineaments can be mapped either in field surveys or by using remotely sensed data (Yeh *et al.*, 2009). Lineaments are an indispensable guide for groundwater exploration, where many successful groundwater investigations for determining drilling sites were based on the lineaments map (Teeuw, 1995). Jhariya *et al*. (2016) stated that the intersection of lineaments defines a potential groundwater recharge zone.

The lineaments map of the study area was obtained from the GEOSURV. This map was extracted by visual interpretation from LANDSAT MSS images. LANDSAT images' interpretation was primarily based on the lineaments and folds delineation in Iraq (Al-Amiri, 1982). The lineaments map was scanned with 300 dpi and georeferenced to the UTM coordinate system in Zone 38 north, then digitized in ArcGIS 10.1. The LD is defined as the total length of lineaments per unit area (km/km^2) and calculated through the following formula (Yeh *et al*., 2009):

$$LD = \frac{\sum_{I=1}^{i=n} Li}{A} \tag{4}$$

where Li is the total length of lineaments in km, and A is the area in km^2. An area with high LD indicates high secondary porosity, consequently, a high potential for groundwater recharge (Yeh *et al*., 2009). The LD map is classified into three classes (Figure 6).

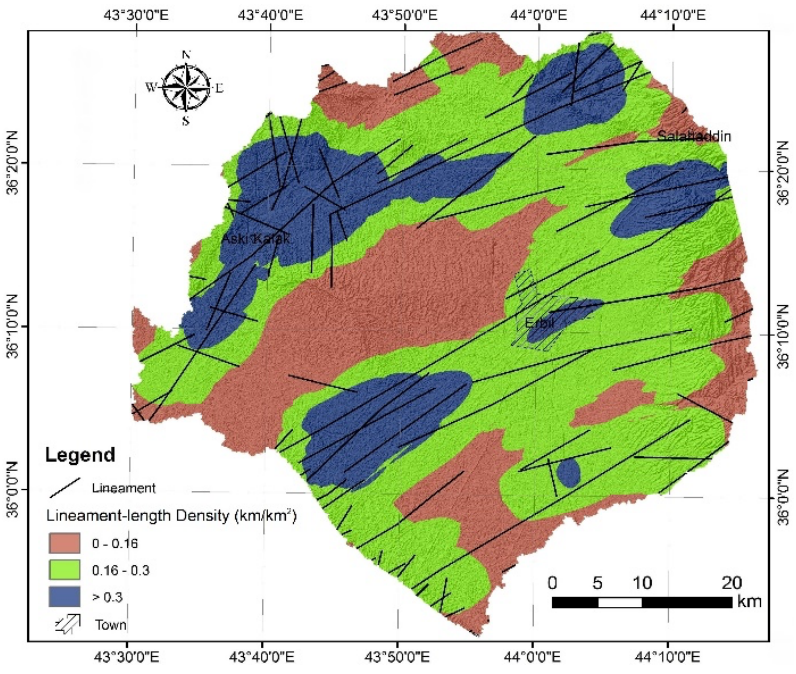

Fig. 6. Lineament-length density map of the study area.

4.3 Analytic Hierarchy Process (AHP)

This method was initially developed by Saaty (1990) as a verbal scale that enables decision-makers to incorporate subjective knowledge and experience naturally and intuitively (Saaty & Vargas, 2012). AHP is a mathematical method for organizing and analyzing complex decisions with multiple attributes (Al-Abadi & Al-Shamma'a, 2014). It decomposes a complex multi-criteria decision problem into a multi-dimensional hierarchical structure of criteria, objectives, and alternatives (Stojanovic *et al*., 2015). In other words, AHP formulates a decision problem in the form of a hierarchy structure, where a hierarchy is an efficient approach for organizing complex systems. In a typical hierarchy, the top levels indicate the overall objective of the decision problem. The elements influencing the decision are signified at an intermediate level. The lowest level comprises the decision options. After a hierarchy is built, the decision-maker starts a prioritization procedure to determine the relative importance of elements in each hierarchy level, where the elements in each level are compared as pairs with respect to their importance in making a decision (Al-Abadi & Al-Shamma'a, 2014). In the present study, the layers are reclassified and mapped using the AHP method in the ArcGIS environment to delineate potential groundwater recharge zones. Table 1 illustrates ratings on a nine-point continuous scale (Saaty & Vargas, 2012).

The AHP method is used for weighting and rating the input parameters for delineating prospective recharge zones. This was based on a previous literature review that applied these controlling factors for mapping aquifer recharge zones (Jhariya *et al*., 2016; Aluko & Igwe, 2017; Salar *et al.*, 2018). The utilized themes are TPI, geomorphology, lithology, land cover, slope, DD, and LD. Based on the reviewed literature, these themes and their features were weighted, ranked, and reclassified using the AHP method. The weights of different themes were assigned on a scale of 2-9 based on their relative importance for the recharge process. Likewise, the weight of each feature class of a particular theme was assigned on a scale of 1-7 (Table 2). Thus, the feature classes of each theme were quantitatively weighted as very good (weight 6-7), good (weight 5-6), moderate (weight 3-5), poor (weight 2-3), and very poor (weight = 1-2).

Table 1. The fundamental scale of AHP.

Rank	Definition
1	Equal importance
2	Equal to moderate importance
3	Moderate importance
4	Moderate to strong importance
5	Strong importance
6	Strong to very strong importance
7	Very strong importance
8	Very to extremely strong importance
9	Extremely importance

4.4 Integration of thematic layers and validation

Integration of thematic layers is an analytical technique for multiple attribute considerations like site selection or suitability modeling (Salar *et al.*, 2018). Groundwater potential refers to the possibility of groundwater occurrence in a particular area. It is a function of several hydrologic and hydrogeological parameters (Jha *et al.*, 2010). Further, an appropriate assessment of groundwater potential can serve as a valuable tool for sustainably managing an aquifer system (Al-Abadi & Al-Shamma'a, 2014). In this study, the delineation and identification of prospective groundwater recharge sites are implemented through weighted overlay processes and combinations of the seven thematic layers in the ArcGIS environment. Salar *et al*. (2018) stated that the weighted linear combination represents the most frequently used technique for multi-criteria evaluation. The assigned weights of these seven themes are shown in Table 2. The map of potential groundwater recharge zones (PGWRZ) in the Erbil basin is calculated by the raster overlay algorithm using the following equation (Salar *et al*., 2018):

$$PGWRZ = \sum_{i=1}^{n} xiwi \quad (5)$$

where *xi* is the weight of theme *i, wi* is the weight of feature *i,* and *n* is the number of themes (Table 2). Values of the different factors were normalized to obtain a unified scale so that all thematic layers would be positively correlated. The resulting map determined five potential zones for groundwater recharge.

For the validation, we used static water level data that was obtained from the GEOSURV. These data comprise 101 monitoring wells dug in the study area. In addition to the visual interpretation between the PGWRZ and the interpolation map of the static water level, the R^2 was used to verify the accuracy of the applied model to identify suitable sites for artificial aquifer recharge.

Table 2. Assignment of weight for the themes and their corresponding features.

Theme	Weight	Feature	Ranking
Topographic position index	9	(-144) - (-20)	7
		(-20) - (-5)	6
		(-5) - (5)	4
		(5) - (50)	2
		(50) - (225)	1
Geomorphology	8	Floodplain and Island	7
		Terraces	7
		Infill Valley	6
		Depositional Glacis	5
		Badland	4
		Cuestas and Hogbacks	3
		Erosional Glacis	3
		Structural Ridge	1

Lithology	7	Pila Spi Formation	7
		Bai Hassan Formation	7
		Mukdadiya Formation	7
		River terraces	6
		Floodplain	5
		Injana Formation	4
		Polygenetic	4
		Slope	3
		Fatha Formation	2
Land cover	6	Water Body	7
		Irrigated Land	7
		Agricultural Land	6
		Field	5
		Bare Land	5
		Mixed-Barren Land	4
		built-up	1
Slope (degree)	5	0 - 1.0	7
		1.0 - 3.0	6
		3.0- 5.0	4
		5.0 - 10	3
		> 10	1
Drainage-length density (km/km^2)	3	0 - 0.30	5
		0.30 - 0.60	4
		0.60 - 0.90	3
		> 0.90	2
Lineament-length density (km/km^2)	2	0.30 - 0.60	4
		0.16 - 0.30	3
		0 - 0.16	1

5. Results

This study generated a potential map for the groundwater recharge zones using weighted overlay processes of seven parameters: TPI, geomorphology, lithology, land cover, slope, DD, and LD in the ArcGIS environment. The resulting map is classified into five categories: extremely low, low, moderate, high, and extremely high (Figure 7). The findings indicate that sites with high and extremely high recharge classes are located in the rugged eastern hills, areas along the GZR, and northern parts of the study area and occur in the lower reaches of the valleys, lowlands, and coarse-grained rock units of Mukdadiya and Bai Hassan formations. These high and extremely high classes also involve Quaternary sediments like floodplains and river terraces. Several geomorphological features and land cover classes are dominated in high and extremely high recharge zones, such as floodplain and island, badland, infill valley, mixed-barren land, and irrigated land, where this area provides appropriate conditions for percolating rainwater to recharge the subsurface aquifers.

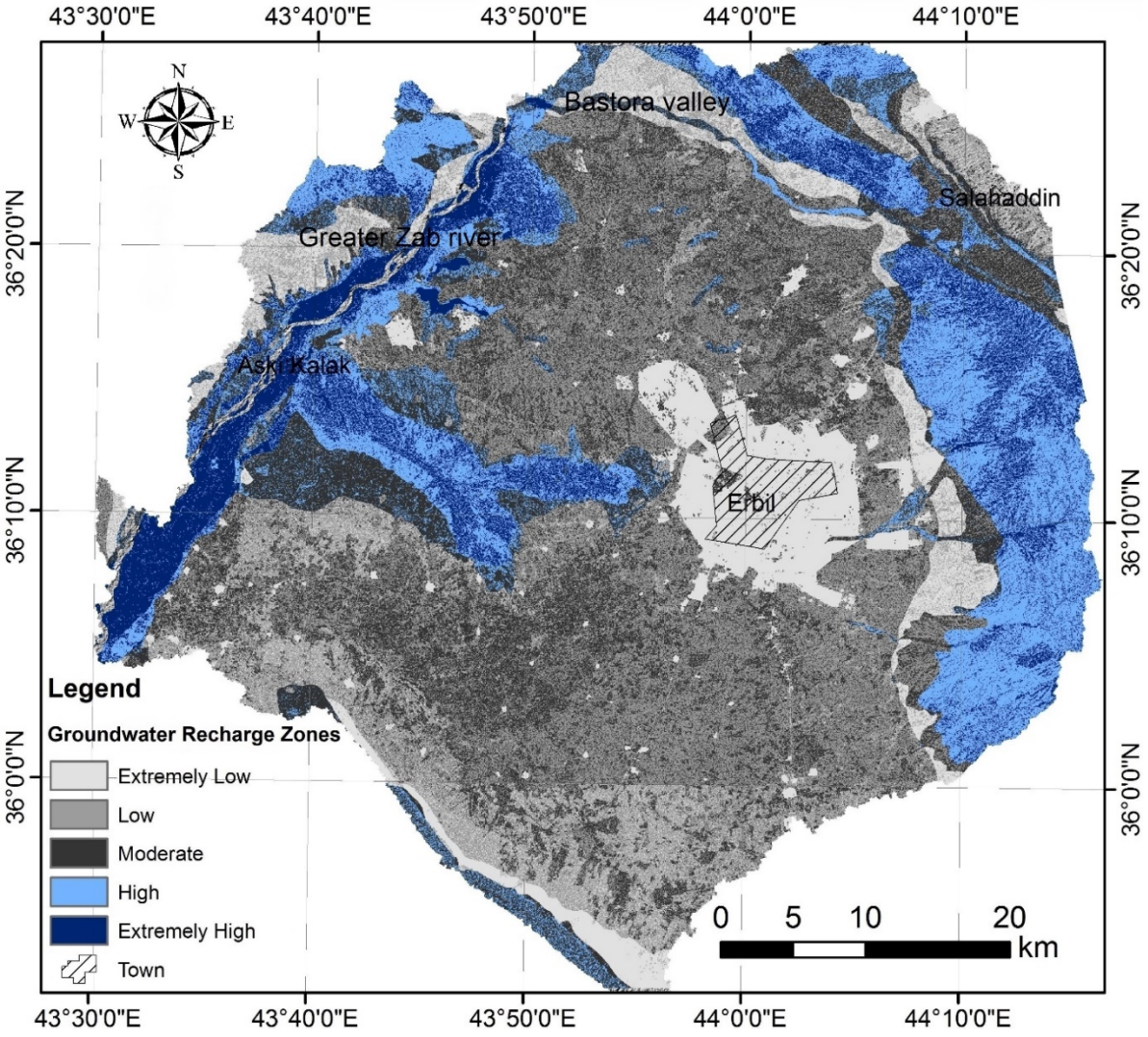

Fig. 7. Map of potential groundwater recharge zones (PGWRZ) in the study area.

Considerable areas with extremely low, low, and moderate recharge classes are situated in the Salahaddin district, the majority of Bastora valley, southwestern, and most central part of the study area consisting of fine-grained rock units of Injana, Fatha, and Pila Spi formations. Moreover, these three classes contain polygenetic and slope Quaternary sediments. Geomorphologically, erosional glacis, depositional glacis, cuestas and hogbacks, and structural ridges are the dominant features. While prevailing land cover classes are bare land, built-up land, field, agricultural land, and mixed-barren land. Overall, these conditions caused an extremely low to moderate possibility for groundwater recharge to occur. The total area of high and tremendously high groundwater recharge classes equals 25.6% of the Erbil basin. The remaining 74.4% of the study area is categorized under extremely low to moderate potential for aquifer recharge (Table 3).

Table 3. Classes of PGWRZ in the Erbil basin.

PGWRZ Class	Area (%)	Area (km^2)
Extremely high	9.8	294
High	15.8	474
Moderate	28.2	846
Low	32.8	984
Extremely low	13.4	402

The eastern part is primarily hilly with a deep-narrow drainage network compared to the study area's southern and western portions. Although this area demonstrates excellent lithological conditions for groundwater recharge, the steep slopes impede runoff accumulation and, consequently, its infiltration into the underground. As a result, the ASTER GDEM, TPI layer, and drainage network map were used to propose two basins for dam construction as promising artificial recharge structures east of Erbil city (Figure 8 a-b).

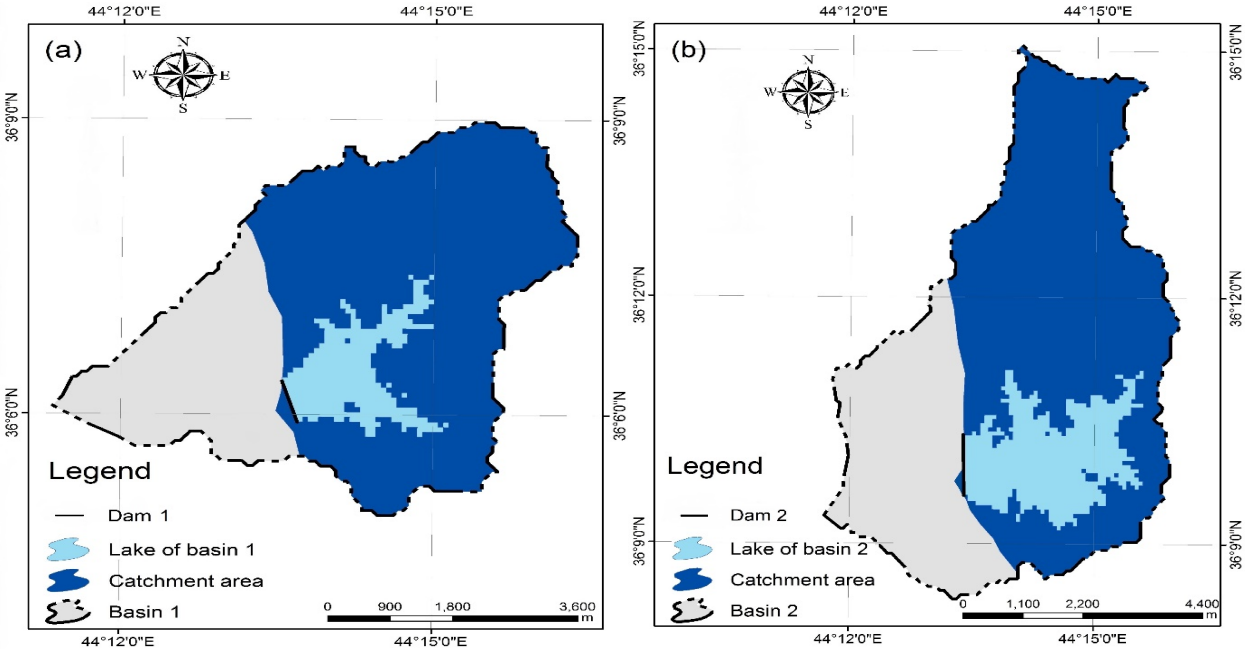

Fig. 8. Maps of two proposed basins for artificial groundwater recharge in the study area.

Two factors controlled the site selection of the suggested dams. Foremost, the availability of surface runoff that could be stored in the reservoirs during the wet season. The highest concave TPI class was the second crucial factor for accumulating surface water in the proposed basins. Besides that, other factors for good runoff accumulation conditions are vital, such as soil type, land use, and antecedent soil water content (Gabriels *et al.,* 2022). Table 4 demonstrates the properties

of the proposed dams using ArcGIS tools. These findings are generated based on the utilization of surface parameters only. Therefore, the results need to be interpreted with caution.

Table 4. Properties of the proposed dams east of Erbil city.

Proposed dam	Elevation (m) above sea level	Dam height (m)	Dam length (m)	Storage capacity (km^3)
Dam 1	848	46	850	1.935
Dam 2	1060	69	1085	4.542

6. Discussion

As the first study in its field in the Erbil basin, AHP identified the most suitable sites for the application of artificial aquifer recharge using multiple criteria within the ArcGIS environment. It is interesting to note that 25.6% of the study area showed an encouraging capability to perform artificial groundwater recharge. However, 74.4% of the investigated region revealed extremely low to moderate potency for aquifer recharge. The spatial distribution of the promising classes is concentrated along the main river channel, Bastora valley, and the eastern hills of the study area. Coarse-grained rock units occupy these zones with a substantial percentage of Quaternary sediments.

Excessive groundwater extraction for agricultural purposes and a low natural recharge rate in the Erbil basin led to a sharp decline in groundwater levels. Rainfall occurs mainly from October to May and frequently reaches 400 mm/year in the study area. Therefore, runoff harvesting and artificial groundwater recharge represent alternative methods to replenish groundwater storage. The slope in both proposed basins (Figure 8) is steep, which subsequently drains available rainwater into a seasonal canal south of Erbil city. Thus, the objective is to construct two dams in the proposed basins to collect surface runoff during the rainy season and recharge the underlying aquifer. Besides, check dams are recommended recharge structures in Bastora valley to harvest rainwater and recharge the subsurface aquifer. Simultaneously, flooding and injection well methods are applicable in the surrounding areas of the GZR. Consequently, these water conservation structures influence the natural regime and regulate aquifer exploitation within the management frame.

Essentially, the resulting map of PGWRZ was visually compared with the static water level map to check the applicability of the proposed sites for implementing artificial groundwater recharge (Figure 9 a-b). Results show that both suggested basins are located within the high to extremely high suitability classes for groundwater recharge. From the standpoint of runoff harvesting, high to extremely high recharge areas are suitable for surface water harvesting due to their deep-narrow drainage network. The formations that crop out in the northeastern and northwestern parts of the study area are highly porous (Mukdadiya and Bai Hassan). These formations represent encouraging recharge zones for the underlying aquifers. Most of the Quaternary sediments, except river terrace sediments located in the central part of the study area,

are poorly permeable due to their high clay contents (Sissakian & Al-Jiburi, 2012). Stevanovic & Iurkiewicz (2009) performed two artificial aquifer recharge tests in the vicinity of Erbil; the first test relied on gravitational recharge, while the second one consisted of the injection of water under pressure. It was concluded that water injection is more effective than the gravitational recharge method, where under a pressure of 8 bar, it was possible to inject a maximum of 6 l/s continuously. At the same time, the natural infiltration rate did not exceed 0.125 l/s. Accordingly, the stored surface runoff in the two proposed basins could be injected under pressure through injection wells to recharge the aquifers artificially. Also, stored water might irrigate neighboring croplands or be transferred to the city of Erbil by a drainage network. Figure 10 illustrates the correlation analysis between the static water level and the PGWRZ, which shows a substantial result ($R^2 = 0.73$).

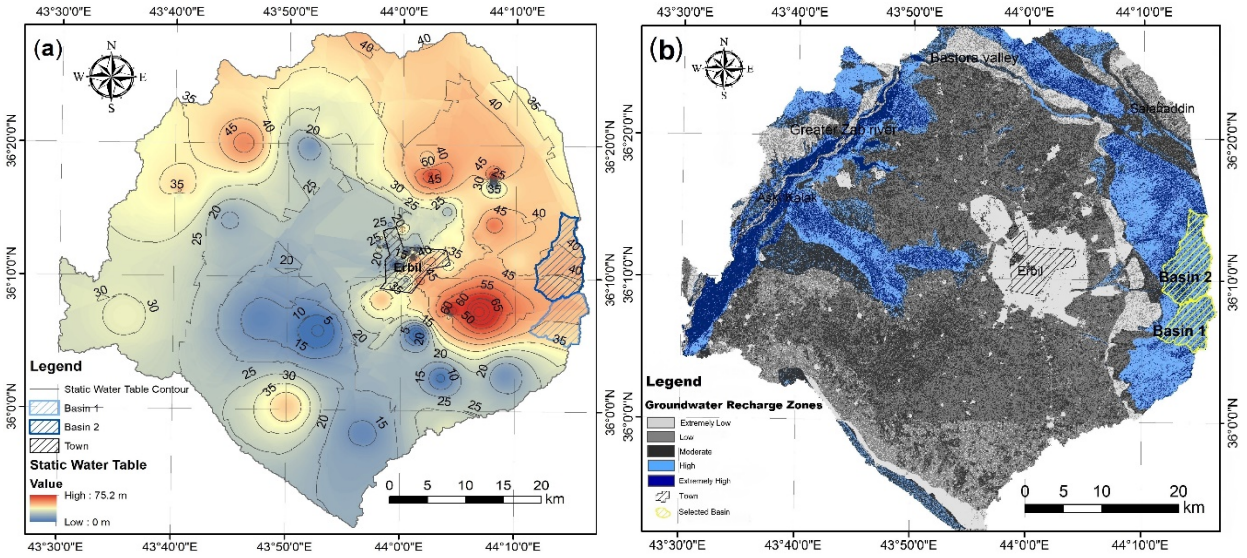

Fig. 9. Maps of (a) static water level and (b) PGWRZ in the study area.

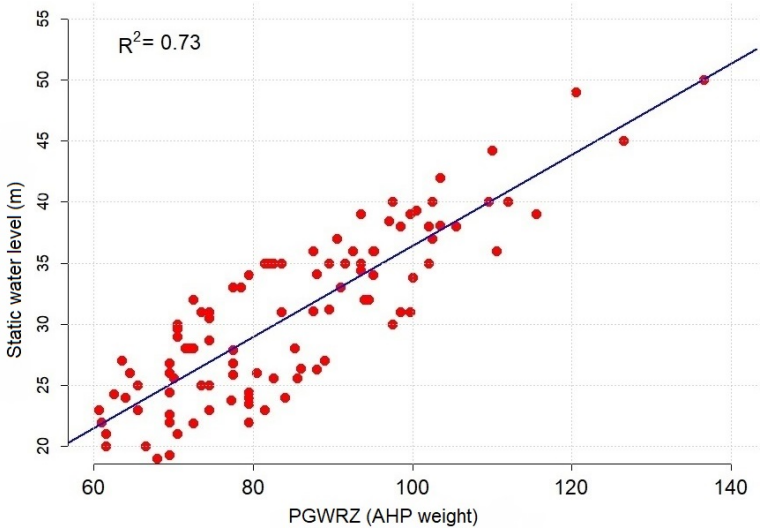

Fig. 10. Scatter plot of the static water level and the PGWRZ.

Further, the direct and reasonable relationship verified that the AHP model suggested in this study is acceptable. This finding has significant implications for developing a sustainable plan to replenish depleted groundwater in the Erbil basin through artificial recharge. Further research with more focus on groundwater flow modeling is therefore recommended. To develop a full picture of groundwater recharge, additional studies will be needed to investigate surface water quality in terms of particles and chemical components, where both are critical for artificial recharge.

7. Conclusions

For the first time, this study delineated the potential groundwater recharge zones in the Erbil basin and identified two prospective sites for performing artificial aquifer recharge using a multi-criteria approach. The statistical validation shows that the GIS and AHP techniques provide a powerful integrated tool for evaluating water resources condition in areas with different scales. Based on visual and statistical comparisons, multiple parameters demonstrated a substantial impact on groundwater recharge in the study area, namely slope, lithology, DD, TPI, land cover, geomorphology, and LD. The resulting PGWRZ map in the investigated basin is classified into five recharge classes: extremely low, low, moderate, high, and extremely high. The eastern hills, Bastora valley, and areas along the GZR are located within the high to extremely high recharge zones.

The high to extremely high recharge zones are characterized by variable units of conglomerate, gravel, sandstone, and clay, which are mainly advantageous for groundwater recharge due to their high hydraulic conductivity. These promising recharge zones cover 25.6% of the Erbil basin. In contrast, extremely low to moderate recharge classes include most central, northern, southern, and southwestern parts, making 74.4% of the entire watershed. The most prominent finding to emerge from this study is that eastern hills demonstrated encouraging suitability for rainwater harvesting and artificial groundwater recharge. Consequently, two basins are proposed for collecting valley flow and storing it in the underlying aquifer. This investigation establishes a preliminary basis to formulate a long-term plan for managing water resources in the Erbil basin. Since the study was mostly limited to surface data, it is recommended to perform further hydrogeological analysis to evaluate the aquifers' properties. Despite its exploratory nature, this study offers insight into sustainable aquifer management in arid and semi-arid regions.

ACKNOWLEDGMENTS

We are grateful to the Deutscher Akademischer Austauschdienst (DAAD) and the Ministry of Higher Education and Scientific Research - Kurdistan Region of Iraq for the financial support. Special thanks go to the Iraq Geological Survey and the United States Geological Survey for providing the necessary datasets for this research.

References

Ahmed, S., Jayakumar, R. & Salih, A. (2008) Groundwater Dynamics in Hard Rock Aquifers. Springer Netherlands, Dordrecht. Pp. 252.

Akbari, M., Meshram, S.G., Krishna, R.S., Pradhan, B. & Shadeed, S. et al. (2021) Identification of the Groundwater Potential Recharge Zones Using MCDM Models: Full Consistency Method (FUCOM), Best Worst Method (BWM) and Analytic Hierarchy Process (AHP). Water Resources Management, 35 (14):4727-4745.

Al-Abadi, A. & Al-Shamma'a, A. (2014) Groundwater Potential Mapping of the Major Aquifer in Northeastern Missan Governorate, South of Iraq by Using Analytical Hierarchy Process and GIS. Journal of Environment and Earth Science, 4(10):125–150.

Al-Amiri, H.M. (1982) Structural Interpretation of Landsat Satellite Images for the Republic of Iraq, scale 1:250000. The Iraq Geological Survey, Baghdad, Iraq.

Al-Manmi, D.A., Mohammed, S.H. & Szűcs, P. (2021) Integrated remote sensing and GIS techniques to delineate groundwater potential area of Chamchamal basin, Sulaymaniyah, NE Iraq. Kuwait Journal of Science, 48(3):1–16.

Al-Muqdadi, S.W.H. (2019) Developing Strategy for Water Conflict Management and Transformation at Euphrates-Tigris Basin. Water 2019, 11(10):2037.

Aluko, O.E. & Igwe, O. (2017) An integrated geomatics approach to groundwater potential delineation in the Akoko-Edo Area, Nigeria. Environmental Earth Sciences, 76(6):1–14.

Anbazhagan, S., Ramasamy, S.M. & Das Gupta, S. (2005) Remote sensing and GIS for artificial recharge study, runoff estimation and planning in Ayyar basin, Tamil Nadu, India. Environmental Geology, 48(2):158–170.

Bajjali, W. (2018) ArcGIS for Environmental and Water Issues. Springer International Publishing AG, Basel. Pp. 353.

Barbier, E. (2019) The Water Paradox: Overcoming the Global Crisis in Water Management. Yale University Press, New Haven . Pp. 281.

Bowen, R. (1986) Groundwater. Elsevier applied science publishers, London and New York. Pp. 428.

Boyko, K., Fernald, A.G. & Bawazir, A.S. (2021) Improving groundwater recharge estimates in alfalfa fields of New Mexico with actual evapotranspiration measurements. Agricultural Water Management 2021, 244:106532.

Castronova, A.M. & Goodall, J.L. (2014) A hierarchical network-based algorithm for multi-scale watershed delineation. Computers and Geosciences, 72:156–166.

Chowdhury, A., Jha, M.K. & Chowdary, V.M. (2009) Delineation of groundwater recharge zones and identification of artificial recharge sites in West Medinipur district, West Bengal, using RS, GIS and MCDM techniques. Environmental Earth Sciences, 59:1209–1222.

Das, M., Parveen, T., Ghosh, D. & Alam, J. (2021) Assessing groundwater status and human perception in drought-prone areas: a case of Bankura-I and Bankura-II blocks, West Bengal (India). Environmental Earth Sciences, 80 (18), art. no. 636.

De Reu, J., Bourgeois, J., Bats, M., Zwertvaegher, A. & Gelorini, V. et al. (2013) Application of the topographic position index to heterogeneous landscapes. Geomorphology 2013, 186:39–49.

Gabriels, K., Willems, P. & Van orshoven, J. (2022) An iterative runoff propagation approach to identify priority locations for land cover change minimizing downstream river flood hazard. Landscape and Urban Planning, 218: 104262.

Hameed, H.M. (2013) Water harvesting in Erbil Governorate, Kurdistan region, Iraq: Detection of suitable sites using Geographic Information System and Remote Sensing. M.Sc. thesis, Department of Physical Geography and Ecosystems Science, Lund University, Lund, Sweden.

Hameed, H.M. (2017) Estimating the Effect of Urban Growth on Annual Runoff Volume Using GIS in the Erbil Sub-Basin of the Kurdistan Region of Iraq. Hydrology 2017, 4(1), 12.

Hengl, T. & Reuter, H. (2011) How accurate and usable is GDEM? A statistical assessment of GDEM using LiDAR data. Geomorphometry 2011 conference, Redlands, California, USA.

Huggett, R.J. (2011) Fundamentals of Geomorphology. Routledge-Taylor and Francis Group, Oxford. Pp. 516.

Jassim, S.Z. & Goff, J.C. (2006) Geology of Iraq. Dolin, Prague and Moravian Museum, Brno. Pp. 431.

Jha, M.K., Chowdary, V.M. & Chowdhury, A. (2010) Groundwater assessment in Salboni Block, West Bengal (India) using remote sensing, geographical information system and multi-criteria decision analysis techniques. Hydrogeology Journal, 18(7):1713–1728.

Jhariya, D.C., Kumar, T., Gobinath, M., Diwan, P. & Kishore, N. (2016) Assessment of groundwater potential zone using remote sensing, GIS and multi criteria decision analysis techniques. Journal of the Geological Society of India, 88(4):481–492.

Kavaf, N. & Nalbantcilar, M.T. (2007) Assessment of Contamination Characteristics in Waters of the Kütahya Plain Turkey. CLEAN-Soil, Air, Water, 35(6), 585-593.

Kumar, T., Gautam, A.K. & Jhariya, D.C. (2016) Multi-criteria decision analysis for planning and management. Environmental Earth Sciences, 75, 649:1–16.

Mulder, G., Olsthoorn, T.N., Al-Manmi, D.A.M.A., Schrama, E.J.O. & Smidt E.H. (2015) Identifying water mass depletion in northern Iraq observed by GRACE. Hydrology and Earth System Sciences, 19:1487–1500.

Nalbantcilar, M.T. & Guzel, A. (2006) Trace element pollution of drinking water supply of Konya Turkey. Journal Geological Society of India (68), 1087-1092.

Nalbantcilar, M.T., Guzel, A. & Durduran, S.S. (2009) Assessing of Groundwater Vulnerability Contamination Potential of Konya Turkey Using Hydrogeological Specifications and GIS. Asian Journal of Chemistry, 4(21), 2925-2934.

Nalbantcilar, M.T. & Pinarkara, D. (2015) Impact of Industry on Ground water Contamination A Case Study in Konya City Turkey. Global NEST Journal, 17(4), 796-815.

Nalbantcilar, M.T. & Pinarkara, S.Y. (2016) Public health risk assessment of groundwater contamination in Batman Turkey. Journal of Water and Health, 14(4), 650-661.

Othman, A.A., Gloaguen, R., Andreani, L. & Rahnama, M. (2018) Improving landslide susceptibility mapping using morphometric features in the Mawat area, Kurdistan Region, NE Iraq: Comparison of different statistical models. Geomorphology 2018, 319:147–160.

Rahimi, S., Roodposhti, M.S. & Abbaspour, R.A. (2014) Using combined AHP-genetic algorithm in artificial groundwater recharge site selection of Gareh Bygone Plain, Iran. Environmental Earth Sciences, 72(6):1979–1992.

Saaty, T.L. (1990) The analytic hierarchy process in conflict management. International Journal of Conflict Management, 1(1):47–68.

Saaty, T.L. & Vargas, L.G. (2012) Models, Methods, Concepts & Applications of the Analytic Hierarchy Process. Springer US, Boston. Pp. 346.

Salar, S.G., Othman, A.A. & Hasan, S.E. (2018) Identification of suitable sites for groundwater recharge in Awaspi watershed using GIS and remote sensing techniques. Environmental Earth Sciences, 77(19):1–15.

Shaban, A., Khawlie, M. & Abdallah, C. (2005) Use of remote sensing and GIS to determine recharge potential zones: The case of Occidental Lebanon. Hydrogeology Journal, 14(4):433–443.

Singh, A., Panda, S.N., Kumar, K.S., & Sharma, C.S. (2013) Artificial groundwater recharge zones mapping using remote sensing and gis: A case study in Indian Punjab. Environmental Management, 52(1):61–71.

Sissakian, V.K. & Al-Jiburi, B.S.M. (2012) Stratigraphy of the Low Folded Zone. Iraqi Bulletin of Geology and Mining, Special Issue (5):63–132.

Stevanovic, Z. & Iurkiewicz, A. (2009) Groundwater management in northern Iraq. Hydrogeology Journal, 17(2):367–378.

Stojanovic, C., Bogdanovic, D. & Urosevic, S. (2015) Selection of the optimal technology for surface mining by multi-criteria analysis. Kuwait Journal of Science, 42(3):170–190.

Tagil, S. & Jenness, J. (2008) GIS-based automated landform classification and topographic, landcover and geologic attributes of landforms around the Yazoren Polje, Turkey. Journal of Applied Sciences, 8(6):910–921.

Teeuw, R.M. (1995) Groundwater Exploration Using Remote Sensing And A Low-Cost Geographical Information System. Hydrogeology Journal, 3(3):21–30.

Thangarajan, M. (2007) Groundwater Resource Evaluation, Augmentation, Contamination, Restoration, Modeling and Management. Springer Netherlands, Dordrecht. Pp. 362.

Vishwakarma, A., Goswami, A. & Pradhan, B. (2021) Prioritization of sites for Managed Aquifer Recharge in a semi-arid environment in western India using GIS-Based multicriteria evaluation strategy. Groundwater for Sustainable Development, 12, art. no. 100501.

Wilson, J.P. & Gallant J.C. (2000) Terrain analysis: principles and applications. Wiley, New York. Pp. 520.

Yeh, H.F., Lee, C.H., Hsu, K.C. & Chang, P.H. (2009) GIS for the assessment of the groundwater recharge potential zone. Environmental Geology, 58(1):185–195.

Submitted: 18/01/2021
Revised: 21/11/2021
Accepted: 03/01/2022
DOI: 10.48129/kjs.11917

Local Site effects for ground motion acceleration and amplification at Bahrah, Saudi Arabia.

Faisal Rehman[1], Abdullah M. Alamri[2], Sherif M. El-Hady[3], Hussein M. Harbi [4], Faisal Rehman[5, *], Muhammad Fahad Ullah[1], Saif Ur Rehman[6]

[1]Dept. of Earth Science, University of Sargodha, Sargodha, Pakistan.
[2]Dept. of Geology & Geophysics, King Saud University, Riyadh, 11451, Saudi Arabia.
[3]Seismology Department, National research institute of Astronomy and Geophysics (NRIAG).
[4]Dept. of Geophysics, Faculty of Earth Sciences, King Abdulaziz University, Jeddah, Saudi Arabia.
[5]Dept. of Earth Sciences, Quaid-i-Azam University, Islamabad, Pakistan.
[6]Institute of Geology, University of the Punjab, Lahore, Pakistan.

[*] Corresponding author: frehman@qau.edu.pk.

Abstract

The soil conditions variability at site strongly influence ground motions during earthquakes. The disastrous earthquakes have shown that the local site conditions are the essential factors that impact surficial ground motions. In present study, local site effects are evaluated for ground motion acceleration and amplification at Bahrah. The town is situated on quaternary alluvial wadi deposits. The ground motion time series are obtained through Spectral matching technique.. The ground motion time series and shallow Geophysical data are utilized to carry out One-dimensional simulation for equivalent linear seismic response analyses for soil layers. Results of One-dimensional site response analysis are interpolated to generate maps that account for ground motion accelerations and amplifications at top of the soil for selected spectral periods (PGA, 0.1, 0.2 and 2) for 475 years return period. The maximum value of amplification ranges upto 3.46 and acceleration upto 0.86 g. The undulation of bed rock topography and existence of deep soft sediments are reflected considerably on the results of the study area.

Keywords: Ground acceleration; ground amplification; local site effect; spectral matching; site response analysis.

1. Introduction

Natural Hazards and Disasters have asserted huge number of lives and damage to infrastructure (Rehman & Harbi, 2018). Local site characterization is inevitable procedure for sustainability against the natural disasters which results in huge number of mortalities and infrastructure destruction. Site characterization can be achieved systematically by evaluating the response of soil layers to earthquake vibrations (Nejad *et al.,* 2018; Tempa *et al.,* 2020). Soil layers under the effect of dynamic forces can act quite contrarily as compared to static conditions. Earthquake vibrations are affected by soil layers as they pass through them (Akkaya & Özvan, 2019). Local site effects are caused by local unconsolidated sediments

which result in significant enlargement of the amplitudes earthquake ground motions (Kuo *et al.,* 2018; Rezaei & Choobbasti, 2018; Touhami *et al.,* 2020; Sadiq *et al.,* 2021). The thickness and degree of stiffness of soil deposits are two major geological characteristic that control the earthquake shaking. In order to evaluate the soil layers behavior for derivation of 1-D layered ground models, surface wave dispersion curves and elastic properties of the soils has been extensively used. (Navarro *et al.,* 2014; Hassan *et al.,* 2020). The severity of damage to buildings can vary dramatically at shorter distances across a city due to variation in the spatial distribution of earthquake response which is controlled by local site characteristic (Ding *et al.,* 2004; Kamalian *et al.,* 2008; Lee *et al.,* 2012; Talhaoui *et al.,* 2004). On the other hand, subsoil structures drive the damage to buildings and ground motion over relatively short distances (Anastasiadis *et al.,* 2001). The few of subsoil controlled most horrible examples include the Michoacan, Mexico 1985 event, the Spitak Armenia 1988 event, the Loma Prieta 1989 earthquake and the Dinar, Turkey earthquake (Ansal *et al.,* 2001; Kanlı, 2006).

The fundamental approach in evaluation of local site effects actually comprises of three steps; probabilistic seismic hazard assessment (PSHA), local soil dynamic properties evaluation, and site response analysis. The PSHA provides unified hazard spectrum for a specific return period (Rehman *et al.,* 2019b). The local soil properties enable the illustration of soil dynamic behavior by site response analysis. The results of site response analysis provide the soil amplification and acceleration at various spectral periods (Rehman *et al.,* 2016a; Rehman *et al.,* 2017). Besides spectral matching, geotechnical and geophysical techniques are employed to incorporate local soil effect (Rehman *et al.,* 2016a). Multichannel analysis of surface wave is mainly used geophysical technique. (Anukwu *et al.,* 2018; Karslı *et al.,* 2017; Rehman *et al.,* 2018a). The shear wave velocity and density information for first 30 meters are obtained by surface wave surveying (Ezzelarab *et al.,* 2018; Rehman *et al.,* 2016b). Spectral matching results, subsurface shear wave velocity and density information in addition to lithological data are utilized to carry out site response analysis. Site response analysis provides surface ground motion parameters. These parameters include spectral acceleration and ground amplifications at various spectral periods (Anbazhagan *et al.,* 2013; Rehman *et al.,* 2016a).

Rapid urbanization presents challenges for governments and stake holders. The one of challenging issue is Aseismic structures including residential as well as commercial centers. The site response analysis is fundamental component in earthquake risk assessment or hazard mapping. In the current study, local site effects are evaluated for Bahrah, a rapidly growing town located in western Saudi Arabia mid-way between Makkah and Jeddah City (Figure. 1). Jeddah is one of the major urban center of the central western coast of Saudi Arabia (Rehman & El-Hady, 2017; Rehman *et al.,* 2019a). Bahrah is located in close proximity to the Red Sea active tectonics controlling seismic hazard to whole area. The town is situated on quaternary alluvial wadi deposits. Undesired dangerous amplification of earthquake shaking had been noticed for most of sites characterized by this type of sediments (El-Hady *et al.,* 2012).

2. Methodology

2.1 PSHA and Deaggregation:

PSHA provides the ground motion characteristics which is carried out by this scheme, is mainly based on the historical and recorded seismicity, and earthquake motion data (Anbazhagan *et al.,* 2009; Mihalić *et al.,* 2011; Muço, 2012).

Deaggregation technique has been proved significantly essential approach to understand seismic hazard. This process helps to precisely identify the controlling earthquake magnitude size and distance range that stems to site hazard (Bazzurro & Cornell, 2004; Halchuk & Adams, 2004; McGuire, 1995).

This process enables the identification of seismicity attributes, i.e., distance to site and magnitude, accountable for seismic hazard (Fauzi & Fauzi 2013; Goda & Atkinson, 2009; Sosson *et al.,* 2010). Normally, PSHA is deaggregated in provisions of two variables: source to site distance and magnitude (El-Hussain *et al.,* 2012).

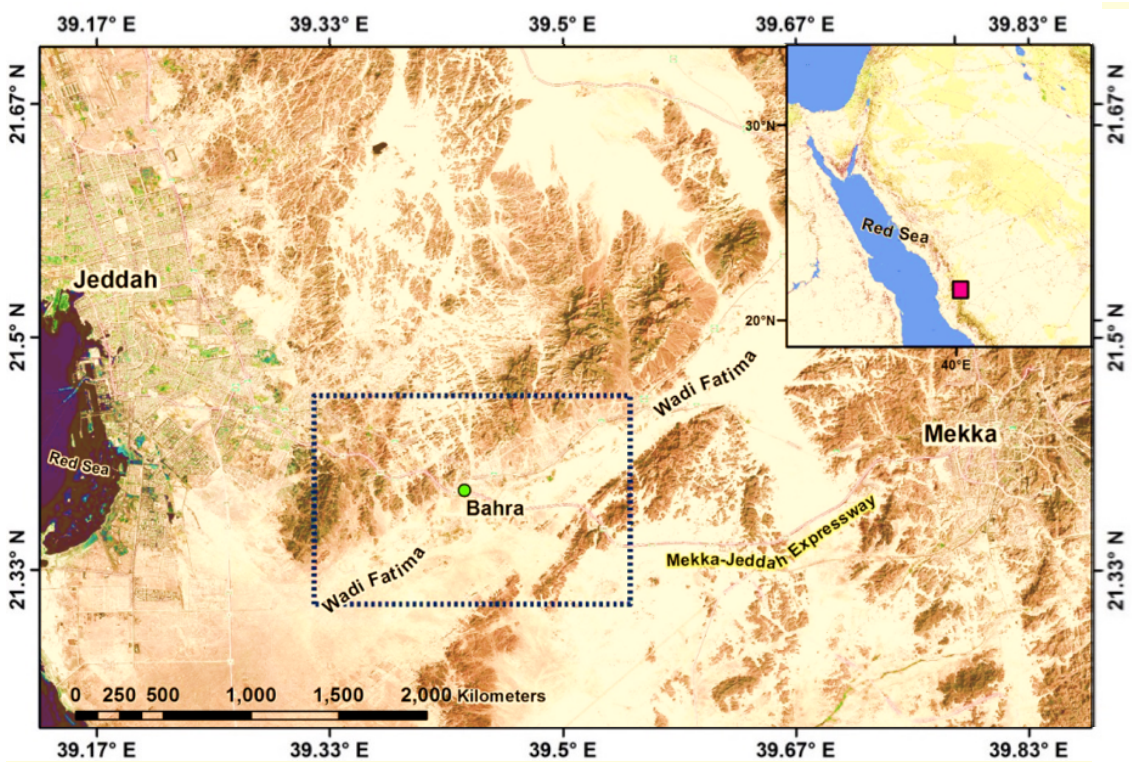

Fig. 1. Location map of the study area.

In the current study deaggregation is carried out to select an appropriate earthquake scenario with specific distance to site and magnitude. Deaggregation is carried out for PSHA result of Rehman et al. (2018b) for return periods of 475 years at selected spectral periods PGA and 0.1s, 0.2s and 2s. Deaggregation results assist the selection of controlling earthquake scenario in terms of magnitude and distance from the site (Figure. 2).

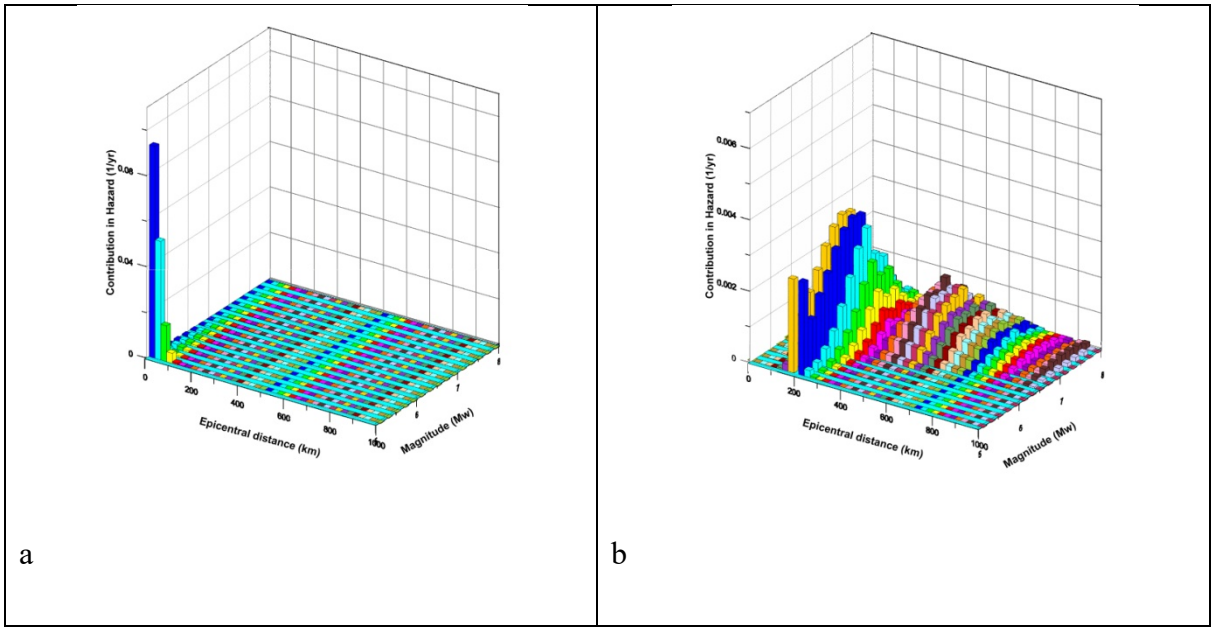

Fig. 2. Deaggregation results. a) PGA , b) Spectral Period 2 sec

2.2 Spectral Matching:

Spectral Matching is the process to generate synthetic/artificial ground motion acceleration time histories having shapes virtually indistinguishable to the predetermined target spectrum (Fahjan and Ozdemir, 2008). This technique is used to estimate nonlinear structural response. It is generally accepted that lower dispersion is present in spectral matching results in most of the cases (Kang *et al.,* 2014). The generation of artificial time histories can be done iteratively in two major domains: Frequency-Domain-based (FD) and Time-Domain-based (TD) matching (Carballo and Cornell, 2000).

In this study, spectral matching is carried on the basis of deaggregation results. The standard search parameters selected for near field effects are 20 seconds duration and for far field are 80 seconds duration. The magnitude is set to of 5.5, while the distance is set to around 25 km from the site for short period duration earthquake. However the long duration far field search parameters for spectral matching involve a distance to site of more than 175 km and a magnitude of 7.5 earthquake (Figure. 2).

Ez-Frisk software ver.7.52 is used for database search and for spectral matching procedure. The available database of strong motions record includes PEER NGA7.3 and USNRC CEUS. The Ez-Frisk software is utilized to search target ground motion record for the study area. The input time histories are matched with unified hazard spectra of Bahrah for the 475 and 2475 years return periods for near and far field effect.

The RspMatch algorithm, developed by Al Atik and Abrahamson (2010) for spectral matching, is applied for preservation of non-stationary frequency content of selected ground motion record. The response spectrum for site response analysis achieved by spectral matching is shown in Figure. 3 for 475 years return period.

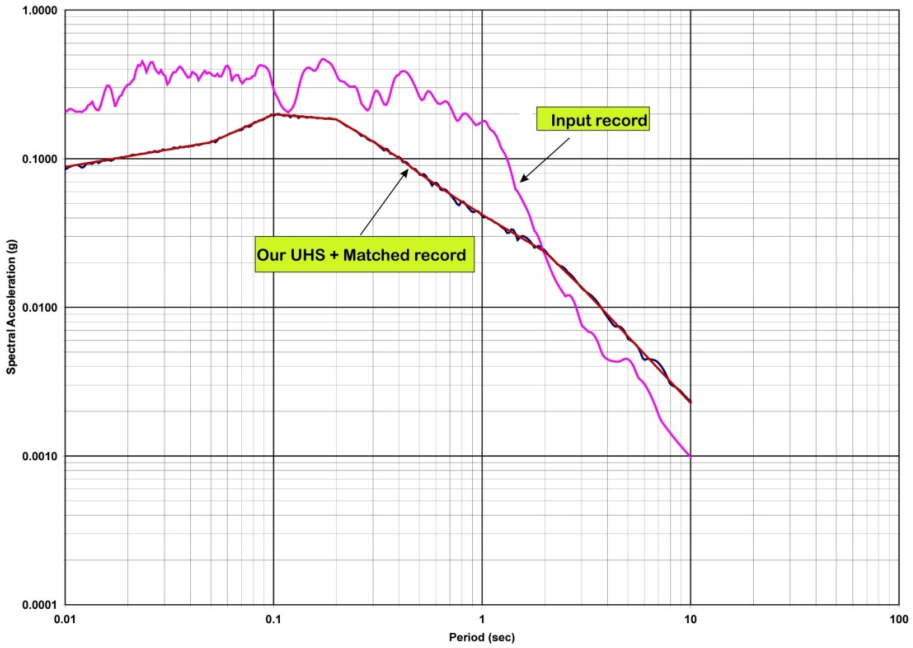

Fig. 3. Response spectrum achieved by spectral matching for 475 years.

2.3 Shallow Geophysical Survey:

The shallow geophysical techniques are most commonly used for near surface investigations (Adesola *et al.,* 2017; LI *et al.,* 2020). The geophysical techniques are cost-effective and rapid the way to obtain sub soil properties (Karslı *et al.,* 2017; Rehman *et al.,* 2016a: Olasunkanmi *et al.,* 2020). Shallow geophysical techniques are usually applied to investigate the Depth, thicknesses, composition and dynamic behavior of subsurface sediments and soils. Multichannel analysis of surface waves (MASW) is a geophysical technique for shallow subsurface exploration that has been effectually utilized for local site effects evaluation (Anbazhagan *et al.,* 2013; Kanlı *et al.,* 2006; Mahajan *et al.,* 2007; Miller *et al.,* 1999a; Miller *et al.,* 1999b; Rehman *et al.,* 2016b; Rehman *et al.,* 2018a; Xia *et al.,* 2000 ; Anukwu *et al.,* 2018; Liu *et al.,* 2020; Mogren, 2020; Tap *et al.,* 2020).Recent advancements in data processing especially application of genetic algorithm has enhanced the subsurface visualization.

In the current study, 13 seismic refraction and 66 MASW profiles acquired in study area are utilized (Figure. 4a). The refraction profiles are acquired at different locations in the study area. The refraction profile total length is 115 meters with five shots for each profile. The major goal of the MASW survey is to calculate the one-dimensional (ID) shear wave velocity of soil layers and density information. The MASW data is acquired using 4.5 Hz geophones with help of sledge hammer as source. The 24 channel Geometrics system (StrataVisor seismograph) is employed for data recording. The geophone spacing is kept one meter and the length of each MASW profile is 63 meters. The dispersion curves are generated and inverted to obtain one dimensional shear waves profile for subsurface. One dimensional shear wave velocity profiles are generated to be used for site response analysis (Figure. 4b & 4c).

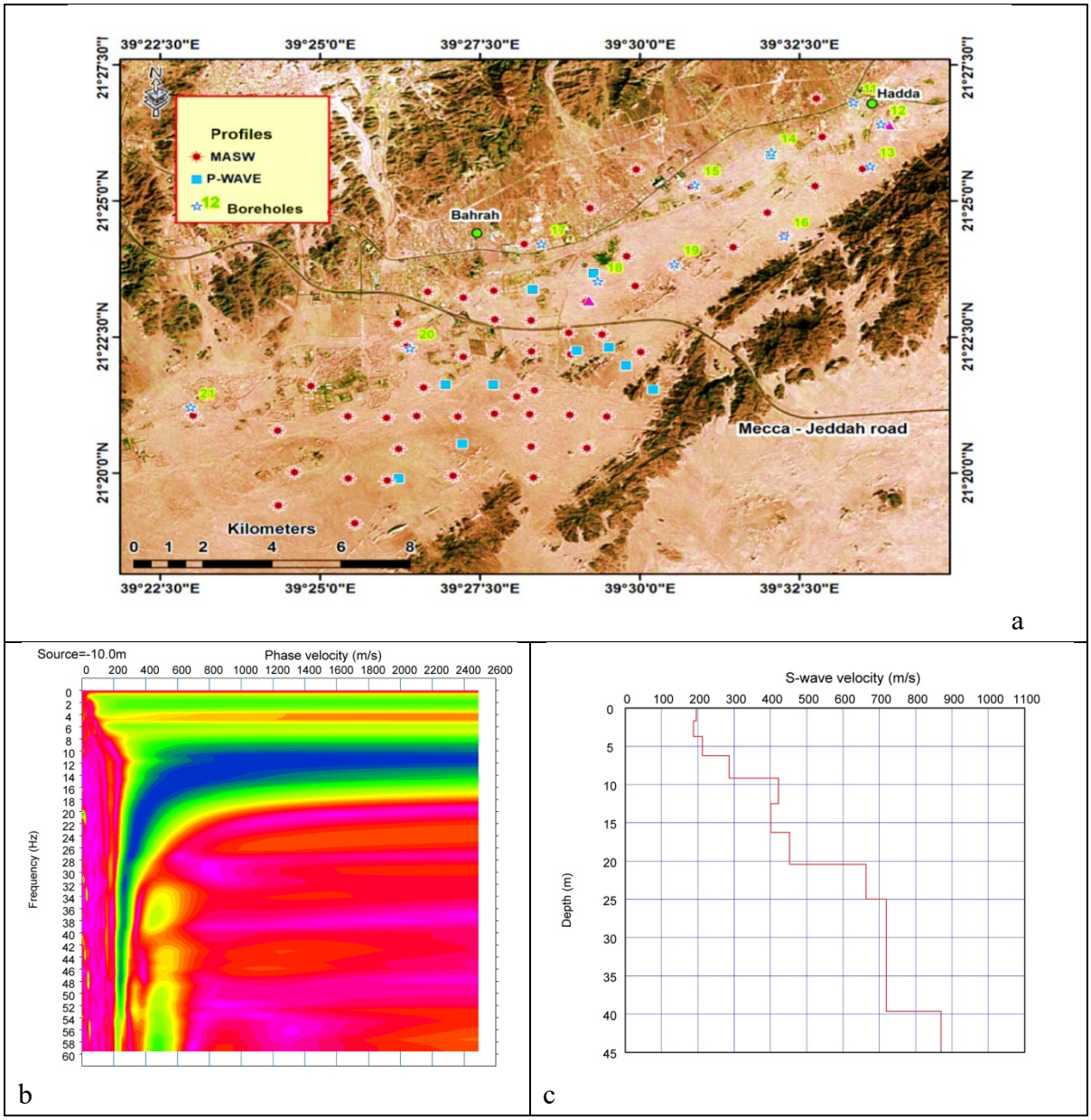

Fig. 4. a) Location map of shallow geophysical survey, b) Dispersion curve for acquired MASW Profile, c) 1D shear wave velocity profile

2.4 Site Response Analysis:

Site response analysis is one of the important steps in evaluating soil conditions under earthquake excitation. It yields site based ground vibration characteristics resulting from earthquake excitation. The site response analysis is mainly conducted for estimation of the site's ground amplification factor, peak ground velocity (PGV), and peak ground acceleration (PGA), or spectral accelerations (SA) (Anastasiadis *et al.,* 2001; Ding *et al.,* 2004; Pitilakis *et al.,* 2004).

The input of site response analysis include, strong motion earthquake data, surface and subsurface lithological information, thickness of subsurface lithologies, shear waves velocity, density information of subsurface lithologies and depth to bedrock at the site. Unfortunately,

for Bahrah area, there is a lack of strong motion data records. This problem was solved through deaggregation and spectral matching for PSHA result of Rehman *et al.,* (2018b) . The results obtained from the spectral matching serve as input parameter for site response analysis.

The other input parameters are 1D shear wave velocity profiles (MASW results), subsurface density information (seismic refraction profiling), and lithological information.

Results from spectral matching, 1D shear wave velocity, density information from MASW, and lithological information from available borehole data are integrated to run site response analysis in Shake 91+ code, available in the Ez-Frisk 7.52 software. The site response results are used to generate soil maps in terms of amplification and ground acceleration at top soil (Figure. 5 a & b).

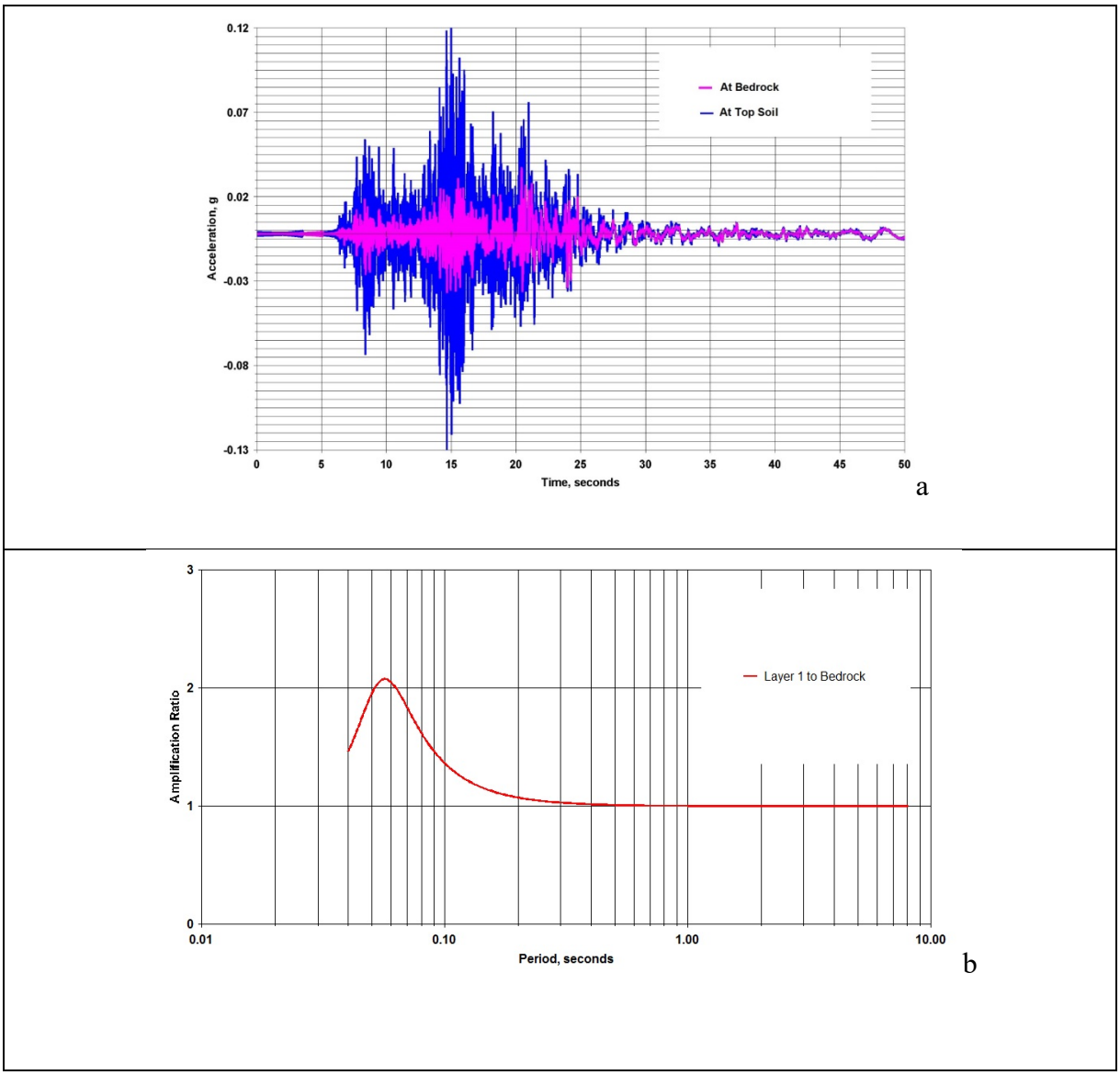

Fig.5. a) Result of site response analysis for ground motion acceleration in a site near borehole, b) resultant site amplification at top of soil for same location

3. Results and Discussion

The site response analysis is carried out for 475 years return periods. The final output for amplification and acceleration is obtained by averaging the near and far field effect calculations for 475 years return period. This task is achieved by making two runs for each site point for 475 years return periods for PGA, 0.1s, 0.2s and 2s seconds. The site response analysis provided ground accelerations and site amplifications at selected spectral periods. The results of site response analysis are interpolated to generate maps in terms of ground acceleration and ground amplification at top soil for various spectral periods.

The site response analysis requires strong motion records at the site. The study area lacks strong motion records. In order to obtain strong motion record compatible with PSHA results, spectral matching is carried out. Spectral matching requires a controlling earthquake scenario which stems hazard to the site. The deaggregation is applied to PSHA results to obtain the controlling earthquake scenario. Spectral matching in the current study is conducted using the Ez-Frisk 7.52 software. The spectral matching results, 1D Vs profiles from geophysical survey, and subsurface lithological information are used as inputs in the SHAKE91+ code to obtain the soil effect. The site response outcome is site amplifications and ground motion accelerations at soil surface with a critical value of 5% damping.

Most of the amplification factors calculated for 475 years return period at PGA (Figure. 6) ranges from 1.0 to 2.7 and spectral period 0.1 second (Figure. 7) ranges from 1.0 to 3.46. Higher amplifications are noticed along the valley trend at spectral period 0.2 second and spectral period 0.3 second. The soil amplifications factor at spectral period 0.2s (Figure. 8) ranges from 1.0 to 3.4, and 0.3s (Figure. 9) ranges from 1.0 to 3.2.

The ground response spectra with a critical value of 5% damping are also calculated by site response analysis in SHAKE 91+ beside amplification factors. The ground acceleration at PGA (Figure. 10) for 475 years returns period ranges from 0.09 to 0.22g. The soil accelerations (acceleration at the surface of the soil) for spectral period 0.1 second (Figure. 11) ranges from 0.20 to 0.66g. The ground acceleration for the top soil at 0.2 second (Figure. 12) and 0.3 second (Figure. 13) for 475 years return period nearly adopts the trend of PGA. The acceleration ranges from 0.18 to 0.5g for 0.2 second and 0.33 to 0.86 g for 0.3 second. The higher accelerations are observed northeast to southwest.

Rehman et al. (2016b) carried out site characterization for study area (Figure. 14). Soil classification maps are correlated with our results of site response analysis. The amplification character varies throughout the site area. The high amplification character can be attributed to D class sites and the lower limit of C class for the majority of the investigated site points at nearly all spectral periods. Significantly higher amplifications are present in the southern part of the valley. These higher amplifications at this spectral period are attributed to deep bedrock and a possible site belongs to lower limit of C class. However few sites at the upstream of the valley, northeast direction indicate high amplifications. The trend for higher acceleration is nearly aligned along the main valley trend. This affinity is linked with deep sediments and lower range of C class.

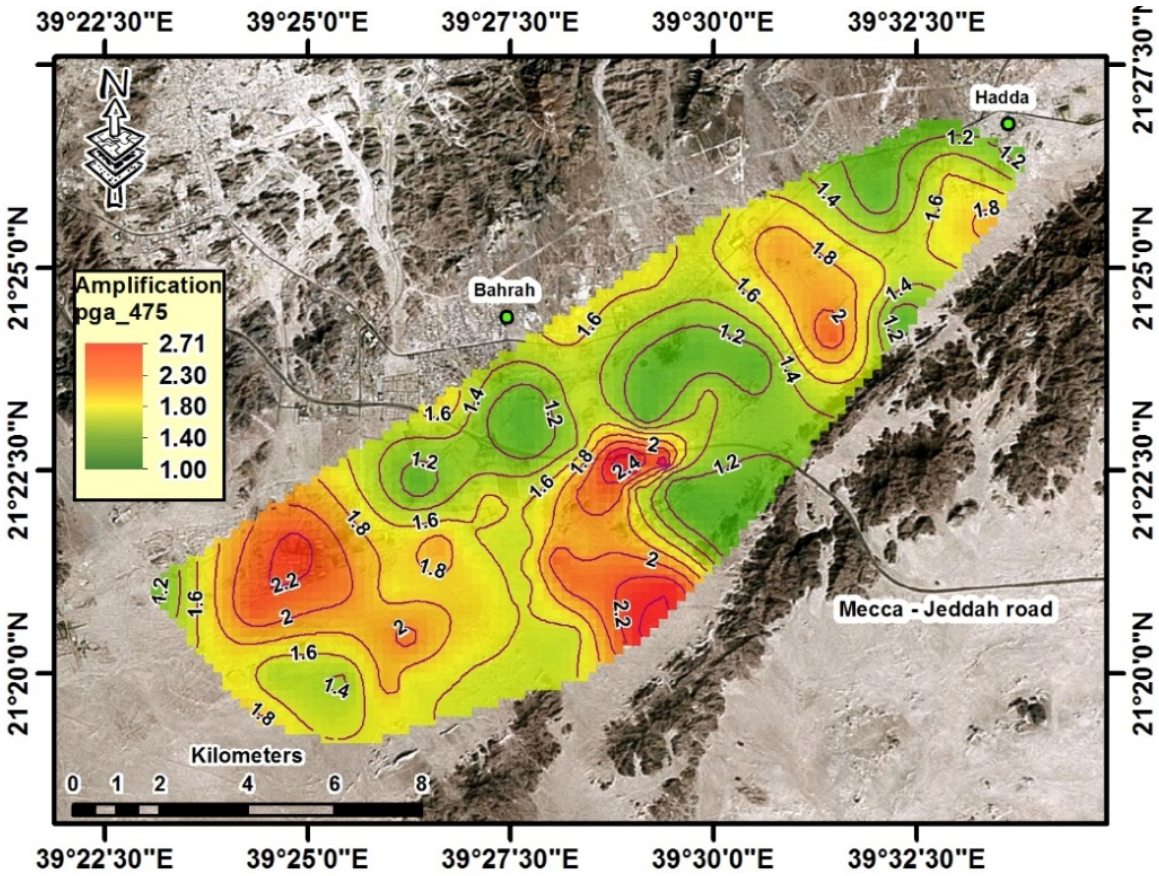

Fig. 6. Soil amplification map at PGA for 475 years return period.

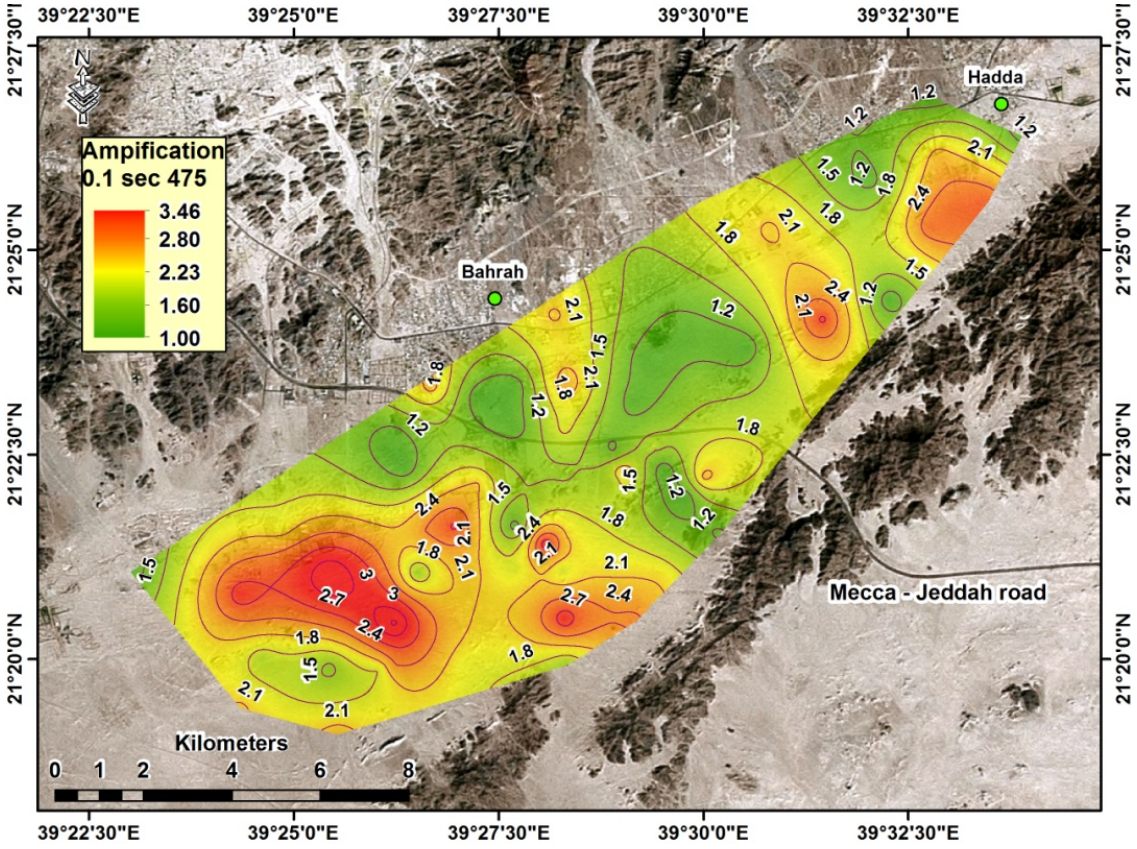

Fig. 7. Soil amplification map at 0.1s for 475 years return period.

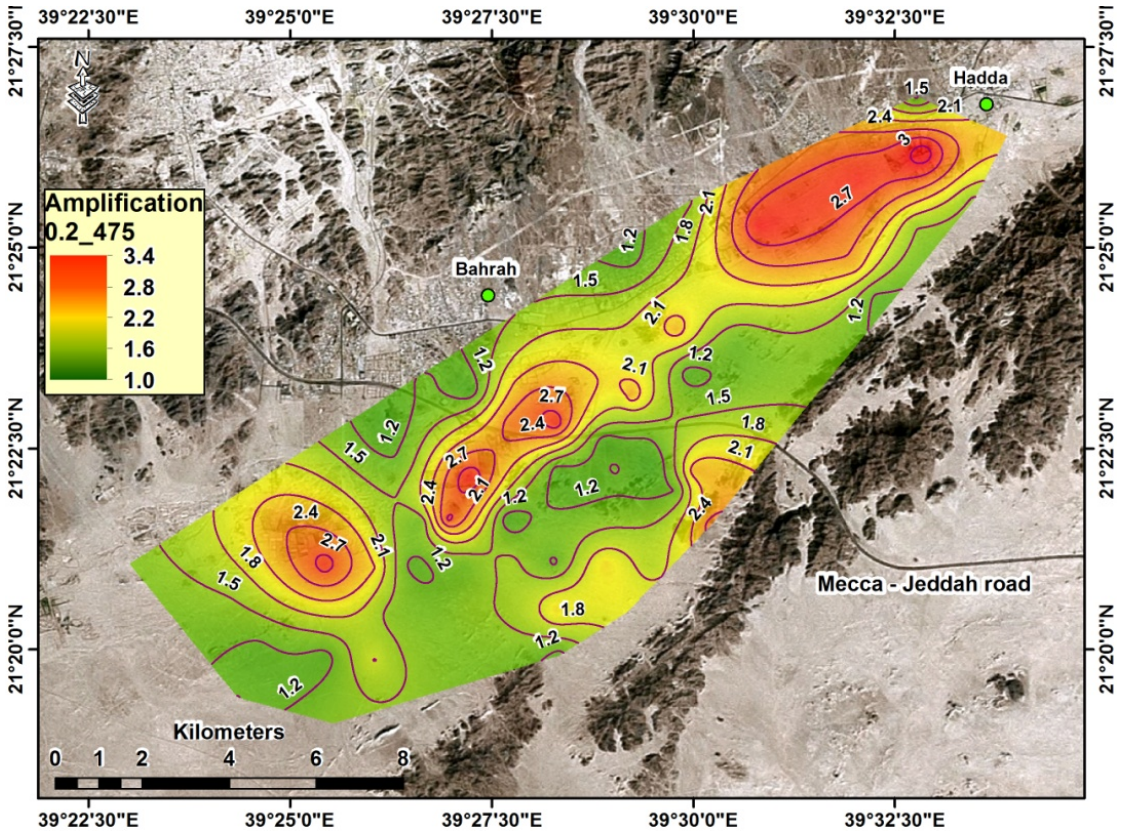

Fig. 8. Soil amplification map at 0.2s for 475 years return period.

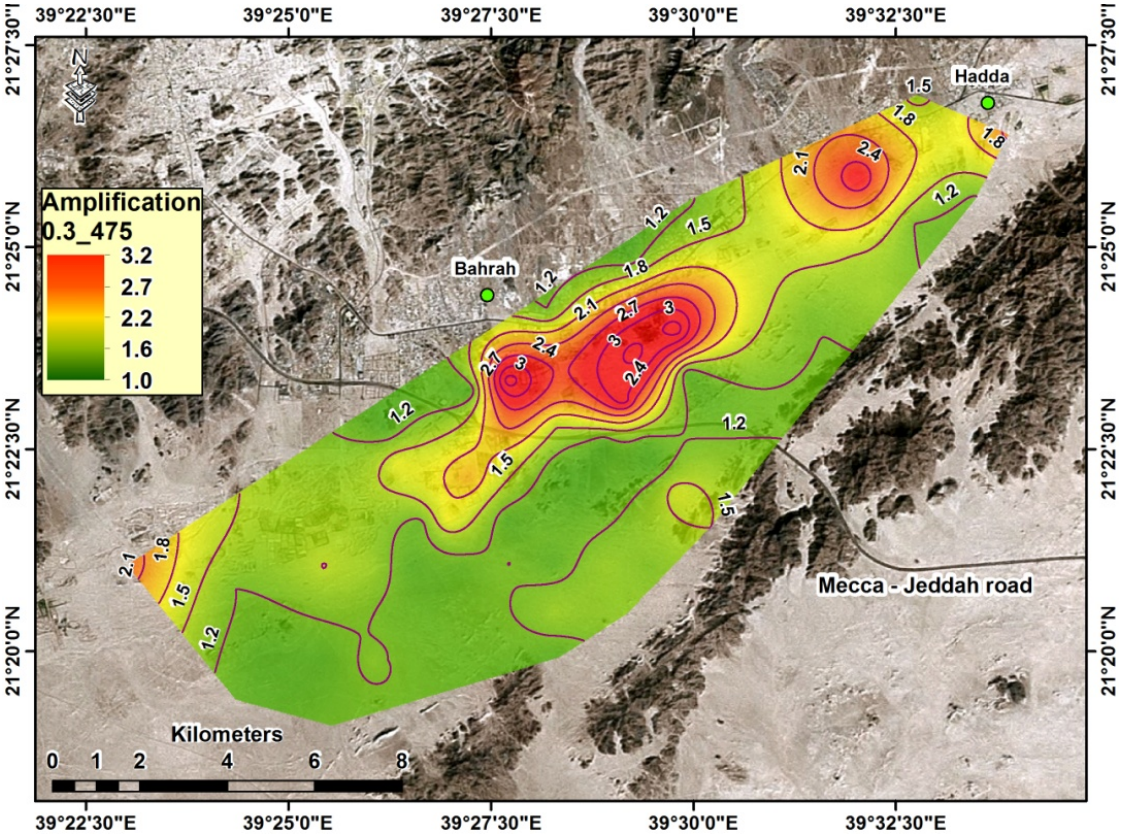

Fig. 9. Amplification map at 0.3s for 475 years return period.

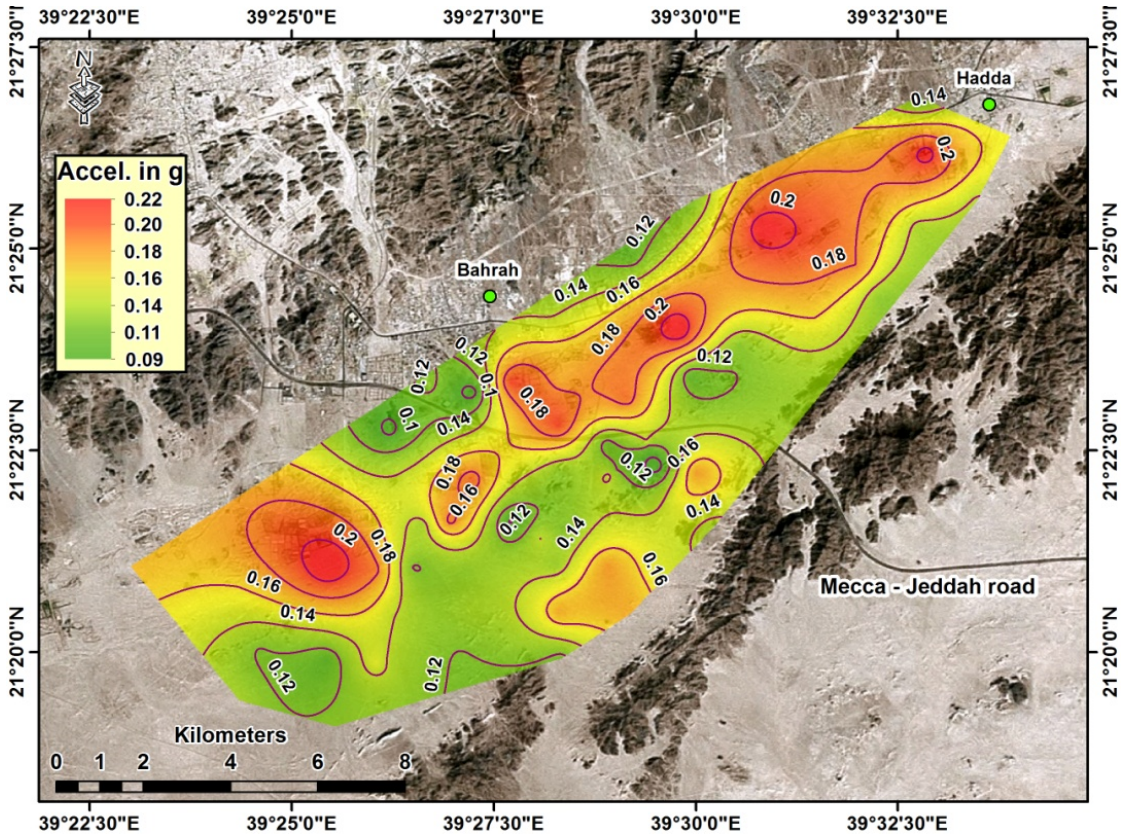

Fig. 10. Ground acceleration map at PGA for 475 years return period.

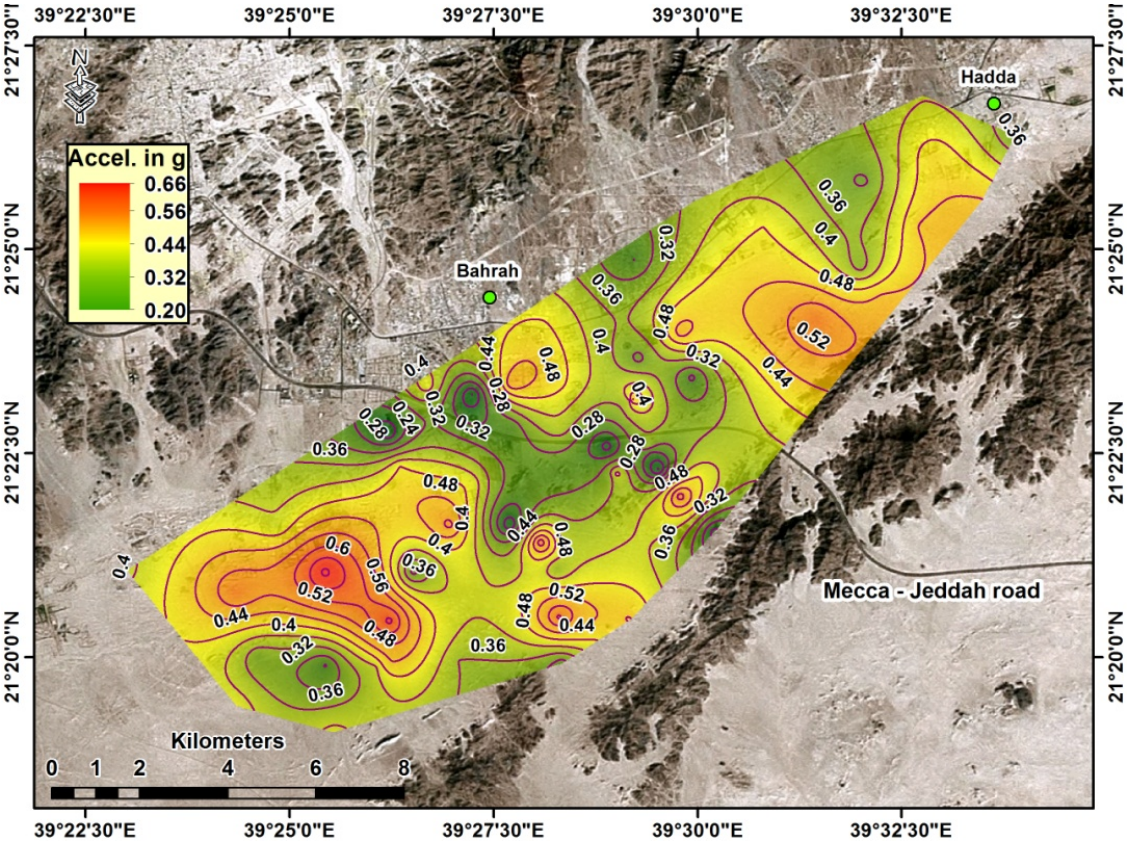

Fig. 11. Ground acceleration map at 0.1s for 475 years return period.

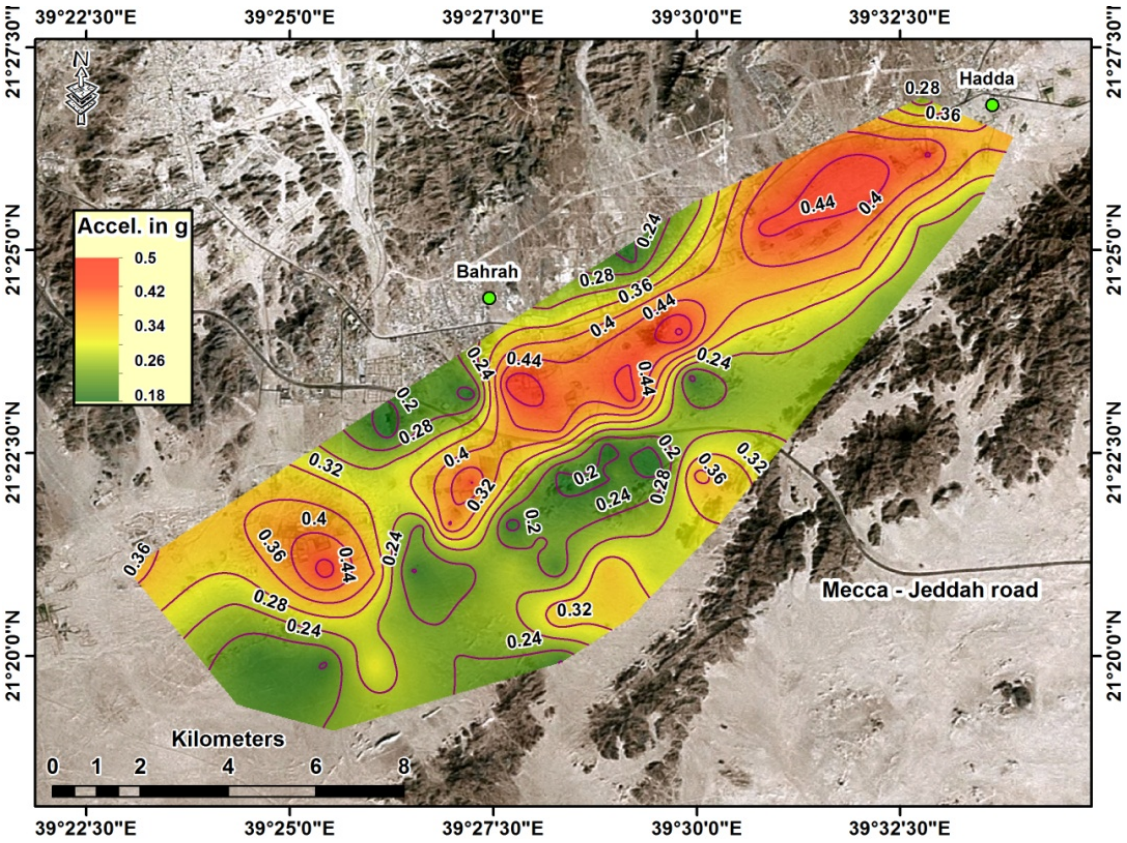

Fig. 12. Ground acceleration map at 0.2s for 475 years return period.

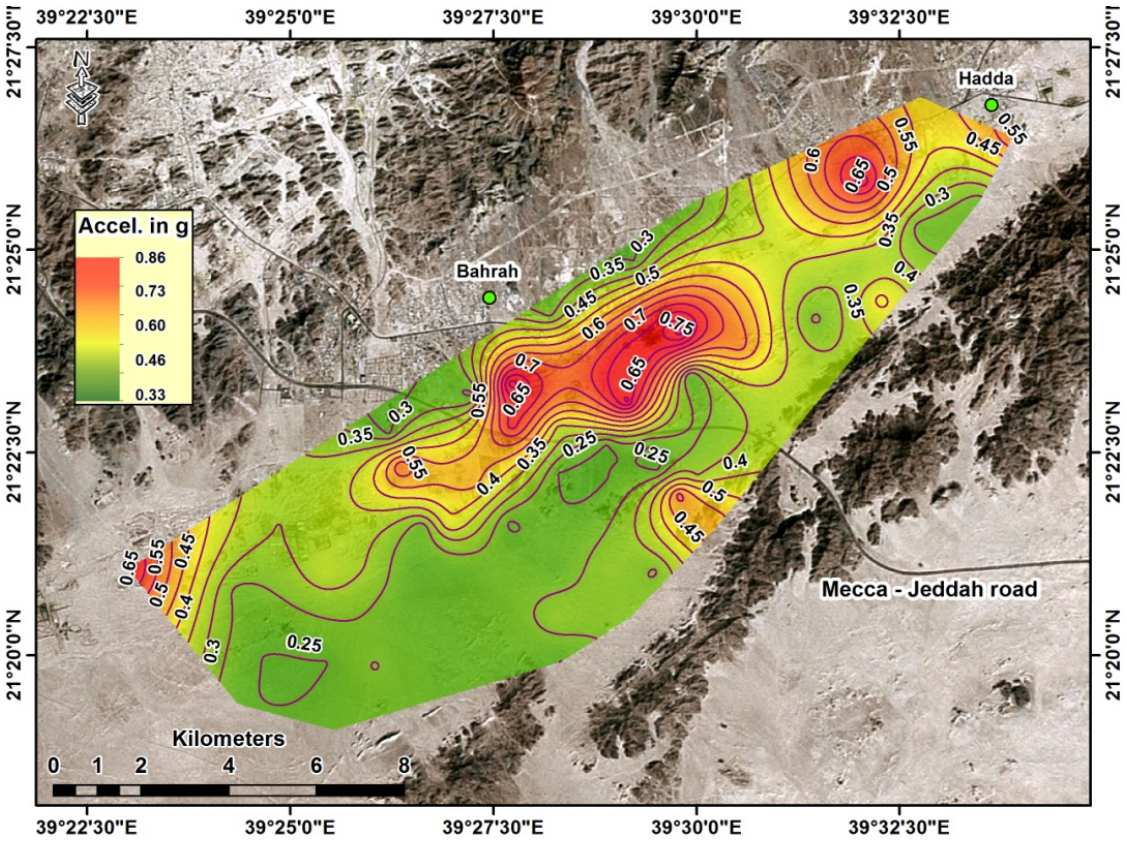

Fig. 13. Ground acceleration map at 0.3s for 475 years return period.

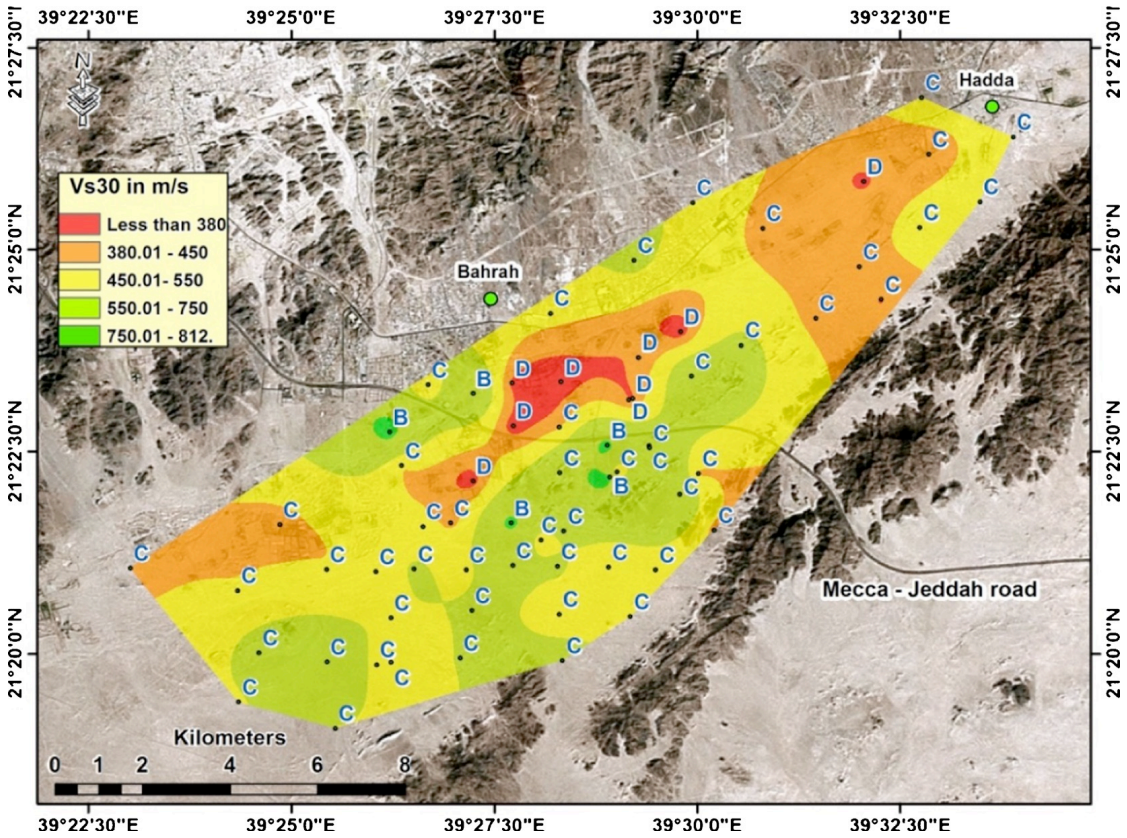

Fig. 14. Soil Classification map for study area [Rehman *et al.,* 2016b]

4. Conclusions

This study provides local site effects in terms of amplification factor and ground surface acceleration maps in Bahrah, western Saudi Arabia. The Bahrah town is approximately located at mid-way between Jeddah and Makkah City. This rapidly growing town in near future can key strategic location for transportation network and urban development. The site response analysis is carried out using the results from spectral matching, 1D Vs profiles, and available borehole data. The SHAKE-91 analysis provides soil amplification character and ground motion acceleration at soil top. Amplification factor for ground vibrations ranges up to 3.5. The maximum surface ground motion values are associated with the 5% damped horizontal spectral acceleration with a period of 0.3 second for 475 years return periods. The amplification character varies throughout the site area. The high amplification character can be attributed to presence of deep sediments for the majority of the investigated site points at nearly all spectral periods. The higher acceleration at different spectral periods is attributed to existence of thick sediment cover and deep bedrock. Significantly higher amplifications are present in the southern part of the valley. However few sites at the upstream of the valley, northeast direction indicate high amplifications.

The study area is uninhabited, which is one of the most important features of this area and has a potential to grow in near future. This study can provide assistance to any civil work opportunity to be carried out in future. These maps will assist in the structural designing of the critical buildings. These maps will assist a better understanding of the potential spatial distribution of seismic risk. These efforts will provide a cogent basis for policy making and

planning regarding mitigation of earthquake hazards. These maps produced through this research study can serve as an essential tool for urban planning and to build earthquake crisis rescue plans. The organizations including government sector, private industry, transportation networks, hazardous goods transportations, and storage department, community planners and utility operators can benefit from this information.

References

Adesola, A. M., Ayokunle, A. A., & Adebowale, A. O. (2017). Integrated geophysical investigation for pavement failure along a dual carriage way, Southwestern Nigeria: a case study. Kuwait Journal of Science, 44(4).

Akkaya, İ., and Özvan, A., (2019) Site characterization in the Van settlement (Eastern Turkey) using surface waves and HVSR microtremor methods: *Journal of Applied Geophysics*, v. 160, p. 157-170.

Al Atik, L., and Abrahamson, N., (2010) An improved method for nonstationary spectral matching: *Earthquake Spectra*, v. 26, no. 3, p. 601-617.

Anastasiadis, A., Raptakis, D., and Pitilakis, K., (2001) Thessaloniki's Detailed Microzoning: Subsurface Structure as Basis for Site Response Analysis: *pure and applied geophysics*, v. 158, no. 12, p. 2597-2633.

Anbazhagan, P., Kumar, A., and Sitharam, T., (2013) Seismic site classification and correlation between standard penetration test N value and shear wave velocity for Lucknow city in Indo-Gangetic Basin: *Pure and Applied Geophysics,* v. 170, no. 3, p. 299-318.

Anbazhagan, P., Vinod, J. S., and Sitharam, T. G., (2009) Probabilistic seismic hazard analysis for Bangalore: *Natural Hazards*, v. 48, no. 2, p. 145-166.

Anukwu, G. C., Khalil, A. E., & Abdullah, K. B. (2018, April) Evaluating the effectiveness of the MASW technique in a geologically complex terrain. In Journal of Physics: Conference Series (Vol. 995, No. 1, p. 012059). IOP Publishing.

Anukwu, G., Khalil, A., and Abdullah, K., (2018) Evaluating the effectiveness of the MASW technique in a geologically complex terrain, *in* Proceedings Journal of Physics: Conference Series, Volume 995, IOP Publishing, p. 012059.

Bazzurro, P., and Cornell, C. A., (2004) Nonlinear soil-site effects in probabilistic seismic-hazard analysis: *Bulletin of the Seismological Society of America*, v. 94, no. 6, p. 2110-2123.
Carballo, J. E., and Cornell, C. A., (2000) Probabilistic seismic demand analysis: spectrum matching and design, Reliability of Marine Structures Program, Department of Civil Engineering.

Ding, Z., Chen, Y. T., and Panza, G. F., (2004) Estimation of Site Effects in Beijing City: *Pure and Applied Geophysics*, v. 161, no. 5-6, p. 1107-1123.

El-Hussain, I., Deif, A., Al-Jabri, K., Toksoz, N., El-Hady, S., Al-Hashmi, S., Al-Toubi, K., Al-Shijbi, Y., Al-Saifi, M., and Kuleli, S., (2012) Probabilistic seismic hazard maps for the sultanate of Oman: *Natural Hazards,* v. 64, no. 1, p. 173-210.

Ezzelarab, M., El-Hussain, I., Mohamed, A. M., and Deif, A., (2018) Site-specific earthquake ground motion parameters at the Southeastern part of Muscat, Sultanate of Oman: *Journal of African Earth Sciences*.

Fahjan, Y., and Ozdemir, Z., (2008) Scaling of earthquake accelerograms for non-linear dynamic analysis to match the earthquake design spectra, *in* Proceedings The 14th World Conference on Earthquake Engineering, Beijing, China.

Fauzi, A., & Fauzi, U. J. (2013) Deaggregation of new national seismic hazard maps for Indonesia. In proceedings of 10 International Conference on Urban Earthquake Engineering, Tokyo, Japan**.**

Goda, K., and Atkinson, G. M. (2009) Probabilistic characterization of spatially correlated response spectra for earthquakes in Japan: *Bulletin of the Seismological Society of America*, v. 99, no. 5, p. 3003-3020.

Halchuk, S., and Adams, J. (2004) Deaggregation of seismic hazard for selected Canadian cities, *in* Proceedings Proceedings of the 13th World Conference on Earthquake Engineering, Vancouver, Canada.

Hassan, H. M., Fasan, M., Sayed, M. A., Romanelli, F., ElGabry, M. N., Vaccari, F., & Hamed, A. (2020) Site-specific ground motion modeling for a historical Cairo site as a step towards computation of seismic input at cultural heritage sites. Engineering Geology, 268, 105524.

Kang, P., Wang, Z.-w., and Sun, J.-j. (2014) Generation of artificial earthquakes for matching target response unsmooth spectrum via wavelet package transform: *Transactions of Nonferrous Metals Society of China*, v. 24, no. 8, p. 2612-2617.

Kamalian, M., Jafari, M. K., Sohrabi-Bidar, A., & Razmkhah, A. (2008). Seismic response of 2-D semi-sine shaped hills to vertically propagating incident waves: amplification patterns and engineering applications. Earthquake Spectra, 24(2), 405-430.

Kanlı, A. I., Tildy, P., Prónay, Z., Pınar, A., and Hermann, L. (2006) VS30 mapping and soil classification for seismic site effect evaluation in Dinar region, SW Turkey: *Geophysical Journal International*, v. 165, no. 1, p. 223-235

.

Karslı, H., Şenkaya, G. V., Şenkaya, M., and Güney, R., (2017) Investigation of soil structure in Uzungöl settlement area by Shallow Seismic Methods: *Eurasian Journal of Soil Science*, v. 6, no. 2, p. 134-143.

Kuo, C.-H., Wen, K.-L., Lin, C.-M., Hsiao, N.-C., and Chen, D.-Y. (2018) Site amplifications and the effect on local magnitude determination at stations of the surface–downhole network in Taiwan: *Soil Dynamics and Earthquake Engineering*, v. 104, p. 106-116.

Lee, S. H., Sun, C. G., Yoon, J. K., and Kim, D. S. (2012) Development and verification of a new site classification system and site coefficients for regions of shallow bedrock in Korea, Journal of Earthquake Engineering 16(6), 795–819.

LI, Z. T., LI, Q. M., & ZHANG, H. (2020) Integrated physical detection technology in complicated surface subsidence area of mining area. Kuwait Journal of Science, 47(1).

Liu, H., Maghoul, P., Shalaby, A., Bahari, A., & Moradi, F. (2020) Integrated approach for the MASW dispersion analysis using the spectral element technique and trust region reflective method. Computers and Geotechnics, 125, 103689.

Mahajan, A., Slob, S., Ranjan, R., Sporry, R., and van Westen, C. J. (2007) Seismic microzonation of Dehradun City using geophysical and geotechnical characteristics in the upper 30 m of soil column: *Journal of seismology*, v. 11, no. 4, p. 355-370.

McGuire, R. K., (1995) Probabilistic seismic hazard analysis and design earthquakes: closing the loop: *Bulletin of the Seismological Society of America*, v. 85, no. 5, p. 1275-1284.

Mihalić, S., Oštrič, M., and Krkač, M., (2011) Seismic microzonation: A review of principles and practice: *Geofizika*, v. 28, no. 1.

Miller, R. D., Xia, J., Park, C. B., and Ivanov, J. M., (1999b) Multichannel analysis of surface waves to map bedrock: *The Leading Edge*, v. 18, no. 12, p. 1392-1396.

Miller, R. D., Xia, J., Park, C. B., Ivanov, J., and Williams, E., (1999a), Using MASW to map bedrock in Olathe, Kansas, *in* Proceedings Expanded Abstracts, *Society of Exploration and Geophysics*, p. 433-436.

Mogren, S. (2020). Engineering bedrock depth estimation and ground response analysis of the northern Jeddah urban area, western Saudi Arabia. Journal of King Saud University-Science, 32(4), 2445-2453.

Muço, B. A., G. Aliaj, S. Elezi, Z. Grecu, B. Mandrescu, N. Milutinovic, Z. Radulian, M. Ranguelov, B. Shkupi, D. (2012) Geohazards assessment and mapping of some Balkan countries: *Natural hazards*, v. 64, no. 2, p. 943-981.

Navarro, M., García-Jerez, A., Alcalá, F., Vidal, F., and Enomoto, T. (2014) Local site effect microzonation of Lorca town (SE Spain): *Bulletin of Earthquake Engineering*, v. 12, no. 5, p. 1933-1959.

Nejad, M. M., Momeni, M. S., and Manahiloh, K. N. (2018) Shear wave velocity and soil type microzonation using neural networks and geographic information system: *Soil Dynamics and Earthquake Engineering*, v. 104, p. 54-63.

Olasunkanmi, N. K., Sunmonu, L. A., & Adabanija, M. A. (2020). Geophysical investigation for mineral prospect in Igbeti-Moro area, southwestern Nigeria. Kuwait Journal of Science, 47(3), 2-14.

Pitilakis, K., Gazepis, C., and Anastasiadis, A., (2004) Design response spectra and soil classification for seismic code provisions: 13th World Conference on Earthquake Engineering, Vancouver, B.C., Canada.

Rehman, F., & Harbi, H. M. (2018) Review of Natural Hazards and Disasters and their Impacts in Pakistan. Muslim Perspectives, III (2)

Rehman, F. E.-H., Sherif M., Harbi, H. M., Ullah , M. F., Riaz , O., Hassan, S., and Rehman, S. u., (2018b) Probabilisticseismic Hazard Assessment and Sensitivity Analysis for Bahrah Area, Saudi Arabia: *Bahria University Research Journal of Earth Sciences*, v. 3.

Rehman, F., Abdelazeem, M., Gobashy, M. M., Harbi, H. M., & ABUELNAGA, H. (2019a) Application of magnetic method to define the structural setting controlling the contaminated area of Wadi Bani Malik, east Jeddah, Saudi Arabia. Bollettino di Geofisica Teorica ed Applicata, 60(1).

Rehman, F., & El-Hady, S. M. (2017) Groundwater contamination: a brief review for Pakistan and Saudi Arabia. Muslim Perspectives, II (3).

Rehman, F., Alamri, A. M., El-Hady, S. M., Harbi, H. M., & Atef, A. H. (2017) Seismic hazard assessment and rheological implications: a case study selected for cities of Saudi Arabia along the eastern coast of Red Sea. Arabian Journal of Geosciences, 10(24), 540.

Rehman, F., El-Hady, S. M., Atef, A. H., and Harbi, H. M., (2016b) Multichannel analysis of surface waves (MASW) for seismic site characterization using 2D genetic algorithm at Bahrah area, Wadi Fatima, Saudi Arabia: *Arabian Journal of Geosciences*, v. 9, no. 8, p. 519.

Rehman, F., El-Hady, S. M., Faisal, M., Harbi, H. M., Ullah, M. F., Rehman, S., and Kashif, M., (2018a) MASW Survey with Fixed Receiver Geometry and CMP Cross-Correlation Technique for Data Processing: A Case Study of Wadi Fatima, Western Saudi Arabia: *Open Journal of Geology*, v. 8, no. 05, p. 463.

Rehman, F., El-hady, S. M., Harbi, H. M., Ullah, M. F., ur Rehman, S., Riaz, O., & Hassan, S. (2019b) Potential Seismogenic Source Model for the Red Sea and Coastal areas of Saudi Arabia. International Journal of Economic and Environmental Geology, 10(2), 26-31.

Rehman, F., El-Hady, S., Atef, A., and Harbi, H. M., (2016a) Probabilistic Seismic Hazard Assessment Methodology and Site Response Analysis Application to Seismic Microzonation: *Science International* (Lahore), v. 28, p. 2593-2606.

Rezaei, S., and Choobbasti, A. J. (2018) Evaluation of local site effect from microtremor measurements in Babol City, Iran: *Journal of Seismology,* v. 22, no. 2, p. 471-486.

Sadiq, S., Muhammad, A., Mandokhail, S. U. J., Rehman, M. U., Mehtab, A., Muhammad, N., & Adeel, M. B. (2021). Evaluation of Site Amplification Factors for Shallow Rock Sites of Islamabad, Pakistan. Kuwait Journal of Science, 48(2).

Sosson, M., Kaymakci, N., Stephenson, R., Bergerat, F., and Starostenko, V. (2010) Sedimentary basin tectonics from the Black Sea and Caucasus to the Arabian Platform: introduction: Geological Society, London, *Special Publications*, v. 340, no. 1, p. 1-10.

Talhaoui, A., Brahim, A. I., Aberkan, M. H., Kasmi, M., and Mouraouah, A. E. (2004) SEISMIC MICROZONATION AND SITE EFFECTS AT AL HOCEIMA CITY, MOROCCO: *Journal of Earthquake Engineering*, v. 8, no. 4, p. 585-596.

Tap, T. D., Ngan, N. N. K., & Vanb, N. T. (2020) Determination of shear wave velocity by using multichannel analysis of surface wave and borehole measurements: A case study in Ho Chi Minh City. Lowland Technology International, 22(2, Septemb), 200-200.

Tempa, K., Sarkar, R., Dikshit, A., Pradhan, B., Simonelli, A. L., Acharya, S., & Alamri, A. M. (2020) Parametric study of local site response for bedrock ground motion to earthquake in Phuentsholing, Bhutan. Sustainability, 12(13), 5273.

Touhami, S., Lopez-Caballero, F., & Clouteau, D. (2020) A holistic approach of numerical analysis of the geology effects on ground motion prediction: Argostoli site test. Journal of Seismology, 1-26.

Xia, J., Miller, R. D., Park, C. B., and Ivanov, J. (2000) Published, Construction of 2-D vertical shear wave velocity field by the multichannel analysis of surface wave technique, *in* Proceedings Proceedings of the symposium on the application of geophysics to engineering and environmental problems, Arlington p. 20-24.

Submitted: 21/08/2021
Revised: 03/02/2022
Accepted: 07/02/2022
DOI: 10.48129/kjs.12349

Kuwait J.Sci., Vol.50, No.(1B),January.2023,pp(125-139)

Maximum entropy model-based spatial sinkhole occurrence prediction in Karapınar, Turkey

Fatih Sarı[1, *], Mustafa Yalçın[2]

[1] *Dept. of Geomatic Engineering, Konya Technical University, 42250 Konya, Turkey*

[2] *Dept. of Geomatic Engineering, Afyon Kocatepe University, 03200 Afyonkarahisar, Turkey*

[*] *Corresponding author: fsari@ktun.edu.tr*

Abstract

Sinkholes in Karapınar and their rapidly increasing occurrence rate are considered one of the main hazards that threaten arable lands and human life. The sudden occurrence and unavoidable characteristics of sinkholes make them more dangerous and challenging to avoid. More than 300 sinkholes have been recorded in the Karapınar region of Konya province in Turkey. There are intensive agricultural activities in the region, and therefore over 60,000 water wells are used to meet the demand. Thus, drought, the effects of climate change and decreasing precipitation rate reveal stress on sinkhole occurrence due to the geological structure of the region and its high tendency to sinkholes since ancient times due to its volcanic history.

The primary purpose of this study is to predict possible sinkhole occurrence probabilities in Konya, Karapınar region based on historical occurrences and to report to the authorities to raise awareness about this problem. The Maximum Entropy (MaxEnt) model is applied for sinkhole susceptibility mapping by evaluating 17 variables affecting sinkhole occurrence in meteorological, topographic, environmental, and geological aspects. The results indicated that 458.52 km^2 (2.48%) of the study area is highly susceptible to sinkholes. 100 sinkholes were assigned as sample data, and 45 sinkholes were set as test data for the MaxEnt model. The AUC values of training data with 0.978 and test data with 0.963 were calculated where a good correlation was provided. The variables Annual Mean Temperature, Precipitation Seasonality (Coefficient of Variation) Geology, and precipitation, which are mostly responsible for sinkhole formations, have been calculated.

Keywords: Geographical information systems; karstic formations; maxent; sinkholes; susceptibility mapping

1. Introduction

In recent years, sinkholes have been considered a natural hazard that may cause significant damage to the environment. Since it is challenging to detect underground structures (groundwater, natural caves, etc.) and sudden occurrence characteristics, determining the exact location of sinkholes is

very hard unless a collapse or deformation is observed on earth. Sinkholes are closed subsidence areas formed by surface dissolution of bedrock that dissolve in karst (Miao *et al*., 2013). Karst rock areas are generally vulnerable to sinkholes and range from a few meters to hundreds of meters.

The main causes of sinkhole formation can be divided into lithological, hydrogeological, tectonic, and climatological groups. In addition, natural factors anthropogenic reasons also trigger the occurrence of sinkholes, such as urbanization, agricultural activities, and irrigation. Decayed organic matters, rich in organic and carbonic acids, accelerate the dissolution of carbonate rocks naturally. Vibration, water demand, agriculture, and urbanization on limestone accelerate the formation of sinkholes anthropogenically (Bayari *et al*., 2009). Volcanic history and karstic formations have made the region vulnerable to sinkholes since ancient times, and excessive use of groundwater for agricultural irrigation increases the rate of occurrence that can cause irreversible damage to human life and the environment (Shaban & Darwich 2011; Rahimi & Alexander 2013). Therefore, Karst formations are generally vulnerable to sinkhole occurrences and can be triggered by urbanization, climate change, and land-use and land cover regimes (Benhammadi & Chaffai 2015; Entezari *et al*., 2016).

Since the study area has great importance in terms of solar energy fields, agricultural activities, coal reserves, and planning to establish a thermal power plant after a few years, predicting and determining the sinkhole susceptibility areas become vital to ensure the economic income and prevent loss of investments. This high economic income also leads to the expansion of residential areas overlapped with limestone zones as existing in Karapınar city center is located on very limited and strong rock formations. In the literature, there are several studies focused on sinkhole occurrence prediction and generation of sinkhole susceptibility maps via Geographical Information Systems (GIS) (Özdemir 2015; Özdemir 2016; Orhan *et al*., 2020) Analytical Hierarchy Process (AHP) (Sarı 2017; Subedi *et al*., 2019), Multi-Criteria Decision Analysis Techniques (Sari *et al*., 2021) machine learning algorithms (Taheri *et al*., 2019) and frequency ratio (Elmahdy *et al*., 2020; Yong *et al*., 2020). These studies have focused on revealing the main reasons for sinkholes and determining the frequency of occurrence by considering several variables in topographic, geological and meteorological aspects. The MaxEnt method is used by Blazzard (2018) to examine climate relationships of Florida considering 9 variables which are related to climatic variables.

This study intends to move one step further to achieve more reliable and accurate predictions of sinkholes occurrence and susceptibility zones. The MaxEnt(Maximum Entrophy) model is applied to generate a sinkhole susceptibility map considering sinkhole occurrences are highly dependent on environmental, geological, topographic, meteorological, and anthropogenic factors as MaxEnt can reveal the spatial relationships among these factors. Besides assigning weights to variables, the MaxEnt model can determine the consistency of sample points in each variable and the intervals in which sinkholes usually occur. Thus, the weights and percent contributions are being determined by the MaxEnt model considering the sample distribution of points on variables. In this way, revealing and detecting the main reasons and mostly responsible variables for sinkhole occurrences may be specified without any user-defined weights or

classifications and may be identified independently. In the study following criteria were selected; Mean annual temperature, isothermality, temperature seasonality, (Precipitation Seasonality), well density, wetness, precipitation, faults solar radiation, water vapor, geology, settlements, roads, elevation, land-use, and slope

2. Material Methods

Generating sinkhole susceptibility map starts with several processes to generate variable maps. MaxEnt method requires setting all variable maps in same resolution and geographic boundary. The flowchart of the study is given in Figure 1.

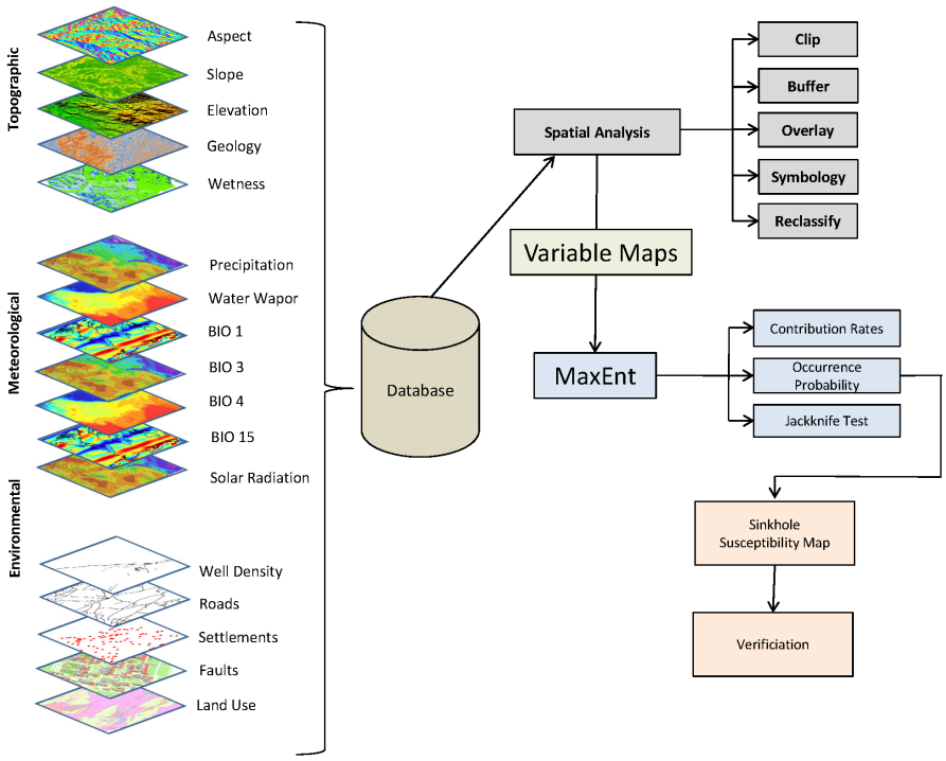

Fig. 1. Implementation model of the sinkhole susceptibility

2.1 Study area

The study area is located between 32°20’44.2’’ and 35°4’30.18’’ W longitude and 37°1’31.6’’ and 38°47’48.8’’ N latitude (in the WGS84 datum) with an area of 259.45 km^2, which refers to the named basin boundaries close to Konya. The study area boundaries are shown in Figure 2.

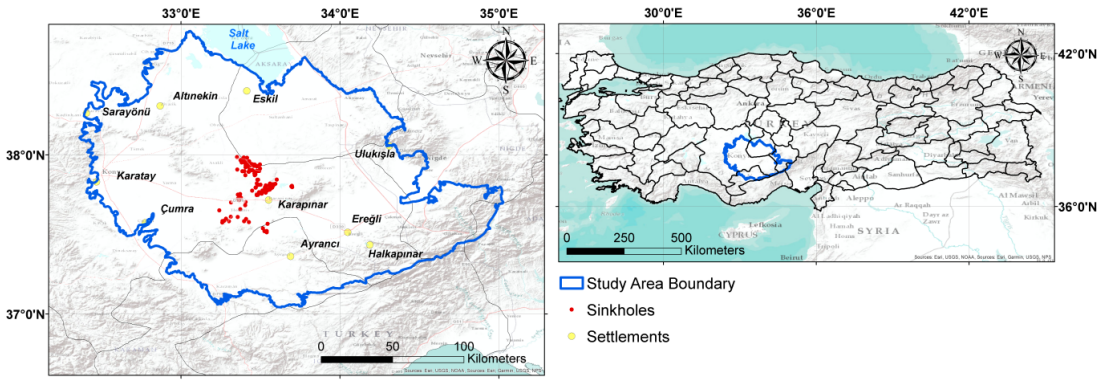

Fig. 2. The study area boundaries

The study area has very high temperatures in the summer season and a very cold climate in the winter season, with 24.3 °C and 2.1 °C on average. The study area has intensive agricultural activities with corn, sunflower, and sugar beet, as these crops require a high amount of water. Therefore, demand for water increases in the summer season, where groundwater is the primary source for irrigation. The sinkhole clusters are located on thick carbonate bedrocks as carbonate is highly susceptible to sinkholes. The geological map of the study area is shown in Figure 3.

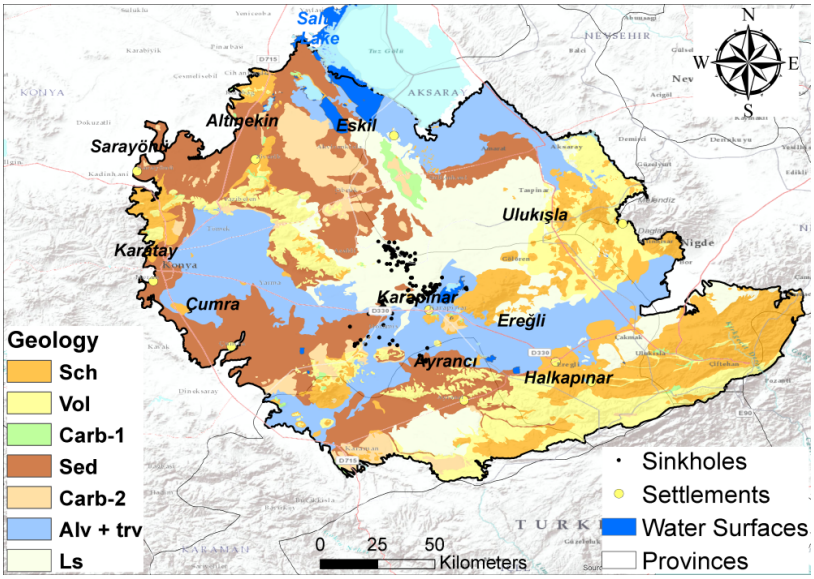

Fig.3. The geology map of the study area (Sch : Schist, Vol : Pyroclastic Rocks (Agg+tu+br), Carb-1 : Carbonate Rocks-1, Sed: Clastic Rocks (cong+ss+cs), Carb-2 : Carbonate Rocks-2, Alv+trv : Quaternary deposits, Ls : limestones). (Imperable-Semi Imperable Units: Sch, Pyroclastic Permeable Units: Others)

The sinkholes in the study area were defined as “cover-collapse” (Törk *et al*. 2013), and the ground collapse occurs when karstic limestone loses its strength due to several reasons as groundwater decreases, vibration, and decay. The main threat of this kind of sinkhole is the

capability to occur abruptly, and usually, it is being difficult to predict and escape from it. When evaluating the locations of sinkholes, formation is a composition of marl-claystone intercalated with limestone. In the plateau area, where old sinkholes are intensely developed, alternating limestones and marls are generally observed. According to Ulu *et al*. (1994), the thickness of the formation is approximately 450 m (Ayday & Alan 2020).

2.2 Maximum Entropy (MaxEnt) Model

MaxEnt is an algorithm based on a machine learning system used to determine their spatial distribution by evaluating point positions and layers. MaxEnt uses occurrence data to estimate the probability distribution of varieties based on maximum entropy theory(Phillips *et al*., 2006; Elith *et al*., 2011). The MaxEnt model can estimate the spatial distribution probability of the samples by evaluating the variables by adjusting the probability distribution of the maximum entropy. These models are based on iterative comparison of predictive (independent) variable values in occurrence (entity) regions with a large subsample extracted from the study area and used as non-realization values (Phillips *et al*., 2006; Elith *et al*., 2011).

MaxEnt estimates the probability of an event's target distribution by determining the probability distribution of the maximum entropy. In detail, the model defines the most overlapping value of each observation point and independent variables to determine the spread of species in each variable (Phillips *et al*., 2006). Thus, the Maxent model requires presence data (existing sinkholes) and independent variables to determine the distribution. The sinkhole occurrence is considered to be species to predict its distribution and mostly occurring variables and intervals. MaxEnt software allows the user to generate probable distribution via several parameters for learning and graphical result outputs. MaxEnt generates verification and accurate outputs based on AUC (Area Under the Curve) measures and jack-knife method.

2.3 Data Specification

Several spatial datasets are used to generate sinkhole susceptibility that affects sinkhole occurrences. Bioclimatic variables are related to precipitation and evaporation of water resources and were retrieved from WordClim (URL 1) database at 30 seconds (1 km^2) resolution. Bioclimatic variables are also related to agricultural activities, and irrigation, as groundwater resources are mostly used for irrigation. Therefore, high temperatures and low precipitation rates increase the water demand. Land use map and Wetness criteria are retrieved from the CORINE project (URL 2) at 20 x 20 meters resolution. Considering the existing sinkhole locations, it has been observed that they mostly overlapped with agricultural lands and have a triggering effect on sinkholes due to intensive agricultural activities, movements, and vibrations of heavy agricultural vehicles. Digital Elevation Model (DEM) data is retrieved from the ASTER GDEM database at 30 x 30 meters resolution, where slope and aspect criteria are derived from DEM data at the same resolution. Faults and geology criteria are retrieved from the Turkish Directorate of Mineral Research and Exploration institute at 1/25.000 scale. As frequently mentioned in research and studies, geological formations and fault movements have a decisive role in the occurrence rate of

sinkhole occurrence, and especially geological formations are the main factor in sinkhole occurrences. All the spatial variables and data resources are given in Table 1.

Table 1. Spatial data sources and units

Variables	Units	Data Source
BIO1 (Mean Annual Temperature)	C^O	WorldClim
BIO3 (Isothermality)	C^O	"
BIO4 (Temperature Seasonality)	C^O	"
BIO15 (Precipitation Seasonality)	C^O	"
Precipitation	mm/m^2	"
Solar Radiation	$(kJ\ m^{-2}\ day^{-1})$	"
Water Vapor	*kPa*	"
Geology	*Class*	1/25.000 Geology Map
Land-Use	*Class*	CORINE Project
Settlements	*Meter*	Derived from CORINE
Well Density	*%*	1/1000 Water Well Maps
Roads	*Meter*	OSM Database
Faults	*Meter*	1/25.000 Faults Map
Elevation	*Meter*	ASTER GDEM
Aspect	*Class*	Derived from ASTER GDEM
Slope	*%*	Derived from ASTER GDEM
Wetness	*Class*	Copernicus Web Site

3. Generating Sinkhole Occurrence Probability

To determine the sinkhole occurrence probability map via the MaxEnt model, all the variables given in Table 1 were uploaded to MaxEnt software. Current geographical distributions of sinkholes in Karapınar region were examined. In total, 145 existing sinkholes were considered where %70 of them as sample data and %30 of them as test data to verify the model. Sample and test point distributions are shown in Figure 4.

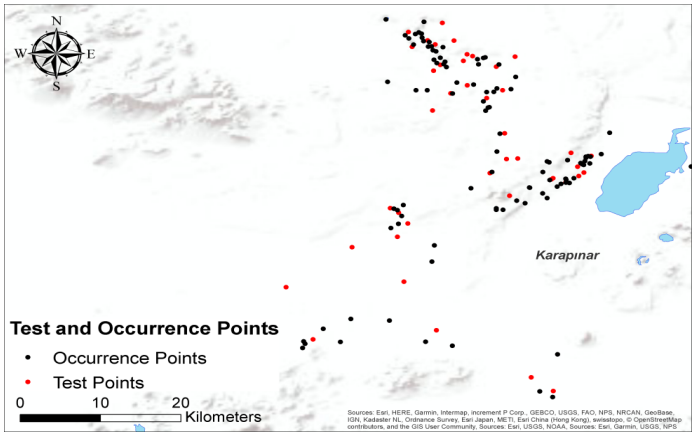

Fig. 4. Distribution of defined 100 sample and 45 test sinkhole points

The verification of the model can be done by using the AUC values of both sample and test data. The AUC values were obtained for the training data with 0.978 and for the test data with 0.963, where both values are quite similar and consistent. The AUC values also revealed that generated sinkhole susceptibility map is reliable and accurate. The AUC values and graphics are given in Figure 5.

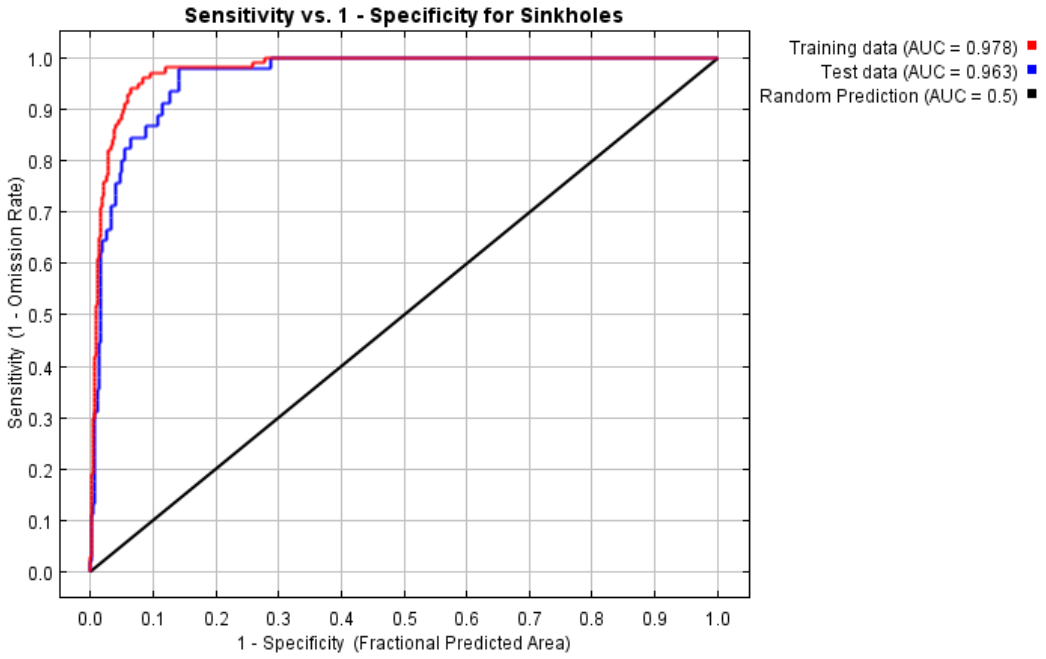

Fig. 5. AUC values for training and test dataTo determine the relativity of variables in terms of sinkhole occurrences, Jackknife test option in MaxEnt modeling software was used. As can be seen in Figure 5, mean annual temperature, precipitation seasonally, Geology and Precipitation variables were determined as highly responsible for sinkhole occurrence when examining randomly selected 100 existing sinkholes. While geological formations are the main decisive factors of sinkhole occurrences, precipitation and temperature are related to groundwater level decreasing which has a triggering effect on sinkholes. When used for insulation, the variables with the highest value are the annual average temperature, which alone seems to have the most useful information. The environmental variable that reduces the value the most when omitted is Geology, so it seems to have the most information not found in the other variables. Aspect, slope, faults, and wetness were determined as non-related to sinkhole occurrences, and as a result, 100 sinkhole locations were intersected with these variables without consistency. Besides this, elevation and isothermality can be accepted as highly related to sinkholes occurrences and should be considered. To determine the similarity and reliability of the MaxEnt sinkhole occurrence, a jackknife graphic was generated for only 45 test sinkhole locations (Figure 6). When jackknife graphics of both sample and test data were compared, it was found that the similarity results and the responsible variables were very similar to each other. This similarity can be accepted as one of the most effective ways to verify the MaxEnt sinkhole occurrence probabilities.

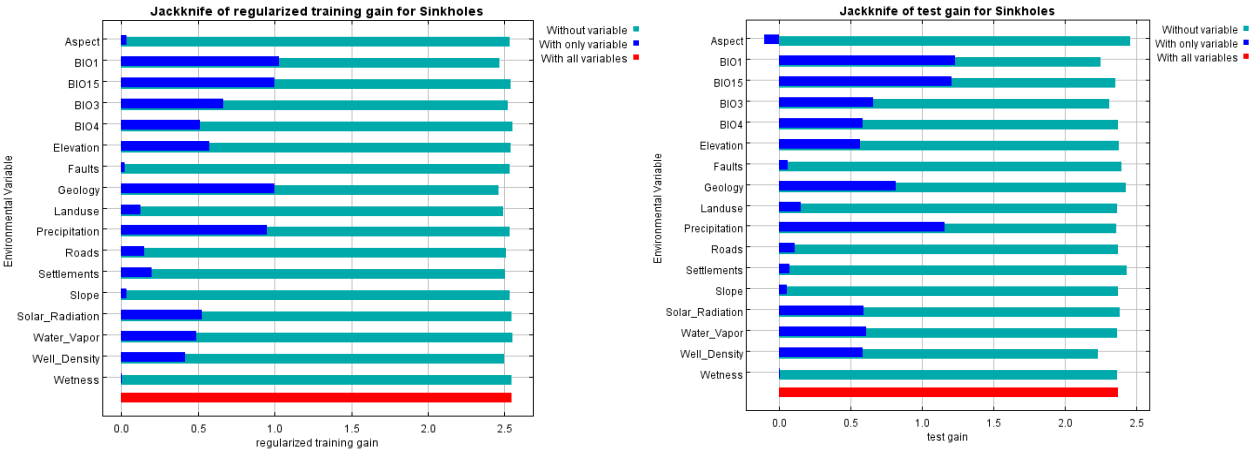

Fig. 6. Jackknife test results of training data and variables

At each iteration of the training algorithm, the increase in regular gain is added to the corresponding value in the initial guess. The values of the relevant variable on the training entity and background data are then randomly allowed as a second guess for each variable in turn. The model is standardized to the resulting decline in training AUC as a percentage and reassessed on allowable data. Estimates of the weights of the variables are given in Table 2.

Table.2. Spatial datasets, units and retrieved data sources

Variable	Percent Contribution	Variable	Percent Contribution
Geology	**34.9**	BIO3	**1.6**
BIO15	**18.8**	Faults	**1.3**
BIO1	**14**	Aspect	**0.7**
Land-Use	**6.9**	Water Vapor	**0.6**
Well Density	**6.7**	Elevation	**0.4**
BIO4	**5.8**	Precipitation	**0.4**
Solar Radiation	**3.2**	Wetness	**0.2**
Settlements	**2.7**	Slope	**0.0**
Roads	**1.7**		

To evaluate each variable and determine how each variable affects the MaxEnt prediction, response curves were generated. The curves show the marginal effect of changing precisely one variable, whereas the model may also take advantage of sets of variables changing together. In other words, response curves are helpful to detect the intervals of maximum effect of each variable to the prediction. The response curves also reveal the consistency of the variables considering all the sample data and their distribution within a variable. All the response curves are shown in Figure 7.

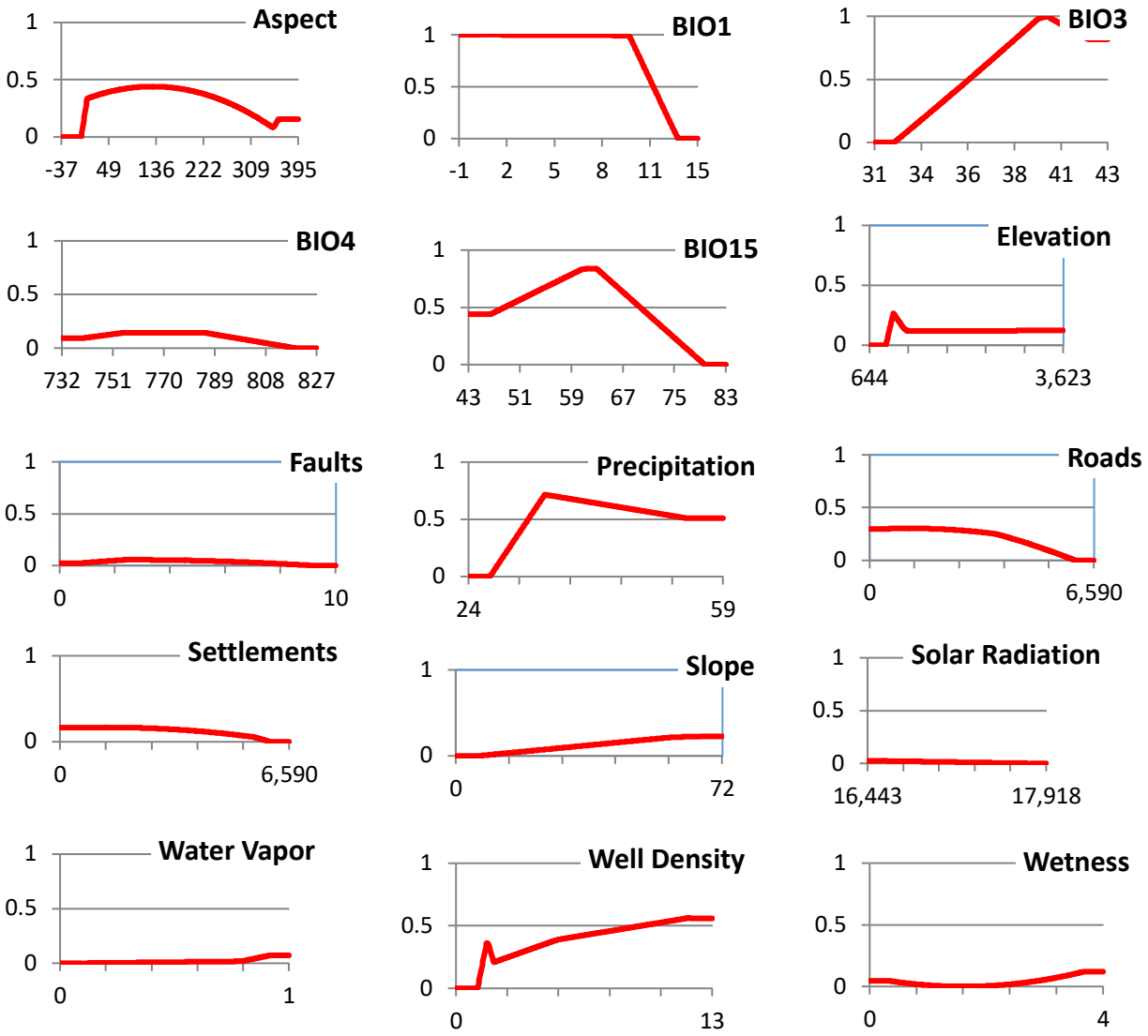

Fig.7. Response curves of each variable (1 = has highest relationship, 0= has no relationship)

All response curves of the variables have the same scale on the vertical axis; 1 denotes the highest correlation with sinkhole formation, 0 denotes relatedness with sinkhole formation. The horizontal axis of the graphs shows the minimum and maximum value of each variable in different units. Response curves are also useful for detecting specific ranges or values with the highest correlation of a variable through chart selections. For example, the variable BIO1 has a very high correlation with sinkhole formation, up to a value of 10, and becomes 0 when BIO1 reaches 13.5.

Geology and land-use response curves within categorical variables are shown in Figures 8 and 9. Sinkholes were mostly overlapped with Grasslands, Semi-Agricultural Lands, Pastures, and Sclerophyll land-use classes, where generally agricultural lands are accepted as highly susceptible to sinkholes (Figure 8). When considering the geological formations response curves, sinkholes were mostly overlapped with limestone karstic formations as they are the most prone to sinkholes (Figure 9).

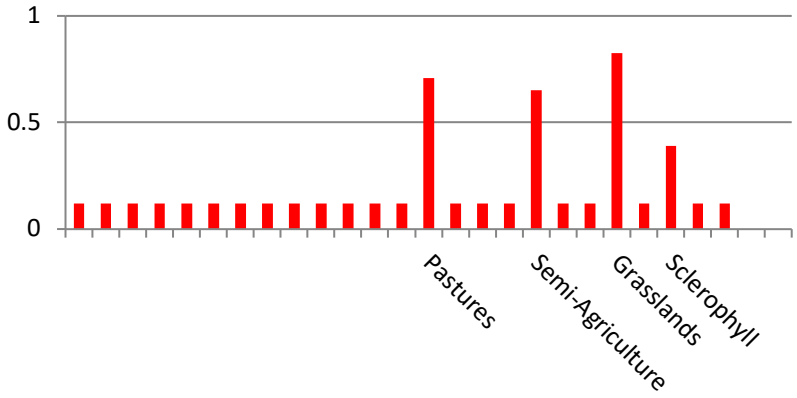

Fig. 8. Response curves of land-use variable (1-11 Urban areas, 12-22 Agricultural lands, 23-25 Forests, 26-31 Semi-natural areas)

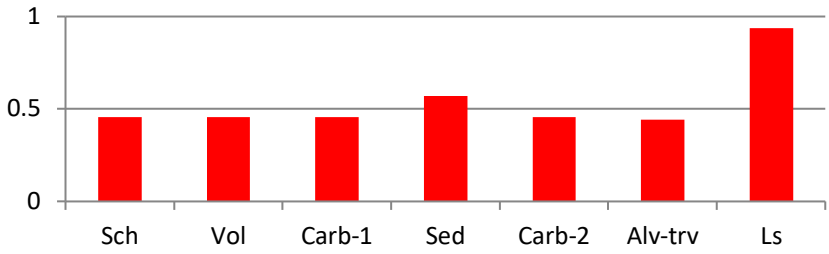

Fig. 9. Response curve of geology variable (The geological formations of the study area (Sch, schist; Vol, pyroclastic rocks (Agg+tu+br); Carb-1, carbonate rocks-1; Sed, clastic rocks (cong+ss+cs); Carb-2, carbonate rocks-2; Alv+trv, quaternary deposits; Ls, limestones) (imperable-semi imperable units, Sch; pyroclastic permeable units, others)

4. Discussion

Finally, a map of the regions susceptible to a possible sinkhole formation was created with the MaxEnt software (Figure 10). Accordingly, it has been determined that 458.52 km^2 of the study area is very vulnerable to sinkhole formation. Considering the existing and possible sinkholes, they are located close to the center of Karapınar and are very clearly clustered. The Natural Breaks Jenks Method was used to classify the areas susceptible to sinkhole formation. Most of the sinkholes outside the center of Karapınar are expected to occur on the Çumra region in a short time, following the limestone formations and intensive agricultural lands.

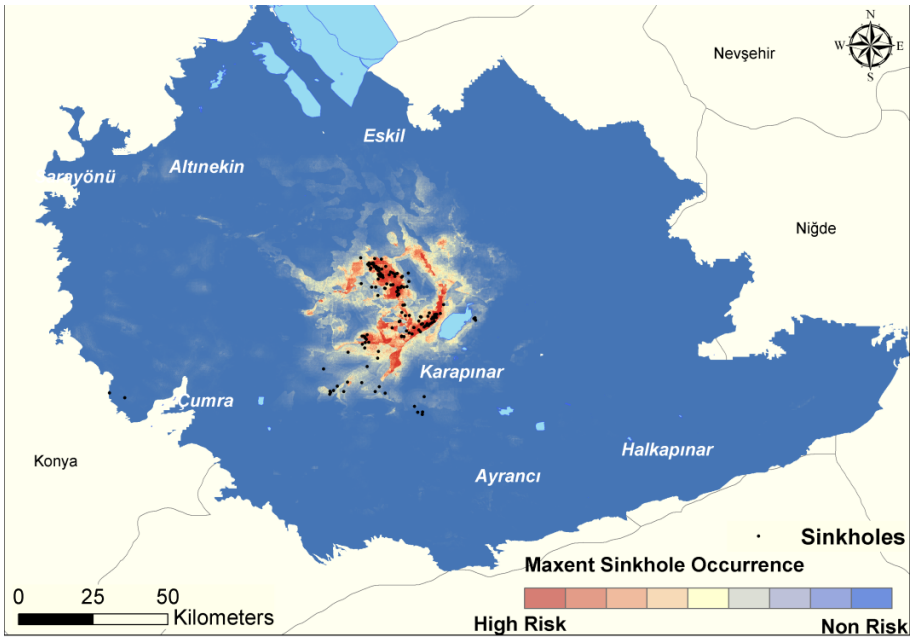

Fig. 10. MaxEnt possible sinkhole occurrence distribution map and risk zones

Another verification was performed to evaluate the overlap of 45 test sinkholes with a generated possible sinkhole distribution map. 27 of them (over 0.80) overlapped with highly susceptible areas and 11 (0.60-0.80) overlapped risk areas moderately. Only 8 of 45 test sinkholes were overlapped with non-risk zones, which are quite small compared to others (1-3 meter radius), and distributions were given in Figure 11.

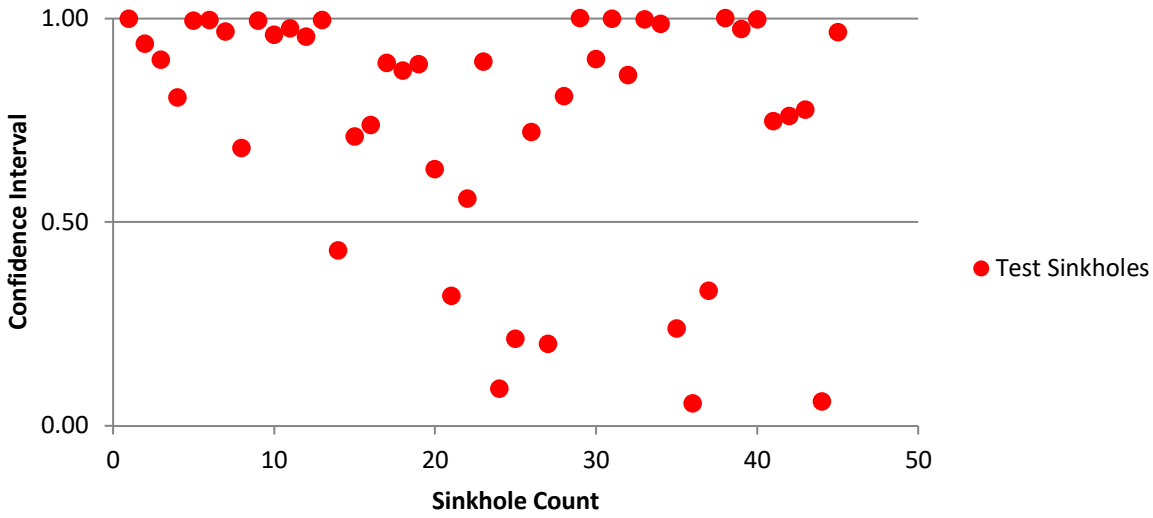

Fig. 11. Overlap of 45 test sinkholes points and MaxEnt risk values

The overlap of the test sinkholes and generated possible sinkhole distribution map are shown in Figure 12. Considering both high and moderate risk zone classes, 84.4 % of the test points overlapped with risk zones that can be accepted as reliable and accurate.

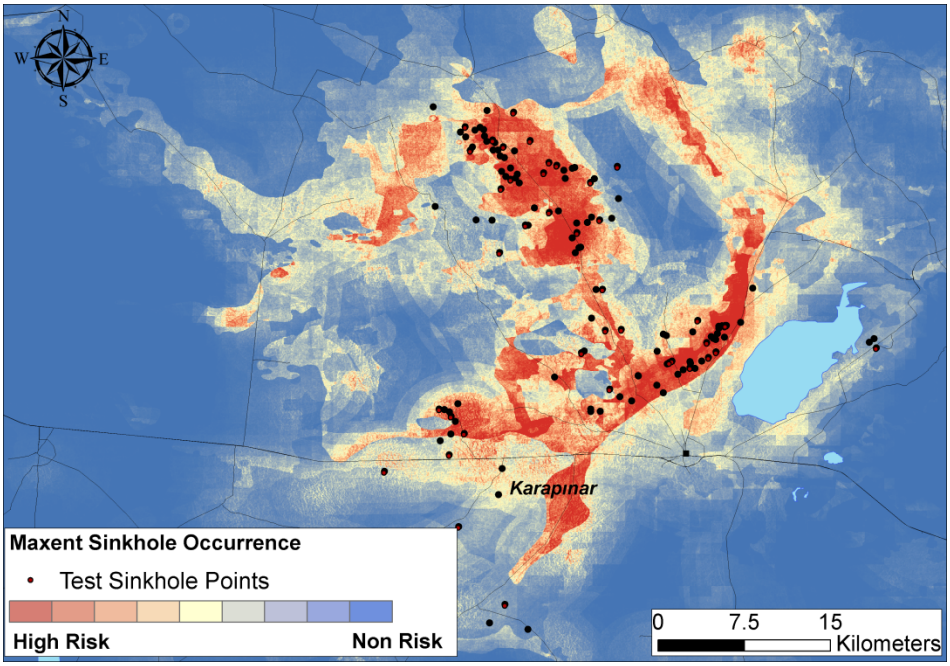

Fig. 12. Overlap of 45 test sinkholes points and MaxEnt possible sinkhole occurrence map

This study represents the relationship between variables and sinkhole occurrence probability by evaluating the spatial interaction of sinkholes without any user-defined parameter or weight. MaxEnt method determines this spatial relationship like Multivariate Statistical Analysis (D'Angella *et al*., 2015) and Frequency Ratio (Yılmaz 2007; Ozdemir 2015). On the other hand, most of the studies used techniques that require user-defined parameters based on Weighted Overlay and Multi-Criteria Decision Analysis methods (Oh & Lee 2010; Nachbaur & Rohmer, 2011; Al-Kouri *et al*., 2013; Perrin *et al*., 2015; Subedi *et al*., 2019; Orhan *et al*., 2020; Sarı *et al*., 2021). These techniques require user-defined weights and the weights are generally flexible due to the included variable counts and sinkhole distributions. When evaluating the weights, geology criteria were chosen as highest weight (Taheri et al., 2019; Subedi et al., 2019; Orhan et al., 2020; Sarı et al., 2021) other criteria weights have been specified differently than each other. Therefore, sinkhole occurrence probabilities were determined more realistic in MaxEnt method due to the excluded human-defined parameters.

5. Conclusion

This study presents the sinkhole occurrence predictions via the MaxEnt model by evaluating the sinkholes' similarity and reveals valuable information about factors that trigger sinkholes. Although this study aims to generate a susceptibility map for sinkholes, considering the economic

value of the study area, risk zones were generated to guide investments and projects such as solar energy field location determination, agricultural crop management, environmental planning, suitable site selection for urban settlement areas, irrigation and highway planning projects. Solar energy panels, cultural heritage, agricultural productivity, petroleum research investments, and coal reserve research structures are being threatened by sinkholes occurrence probability.

The growing rate of this natural disaster reveals stress on organizations and institutes to specify the prediction of sinkhole occurrences and prevention procedures urgently. The recent research generated sinkhole susceptibility maps via user-defined weights, intervals, and coefficients by using several methods. However, the sinkhole occurrences should be evaluated within its nature by only specifying the effects (variables) that trigger sinkhole formations. Thus, the MaxEnt method allows researchers to generate sinkhole locations that will probably occur by evaluating recent sinkhole locations and their similarity, intersection, and dependencies to variables regardless of user-defined specifications. Therefore, the most reliable and accurate susceptibility maps can be determined via the MaxEnt method. Additional criteria such as geodetic deformation measurements with GPS systems, groundwater level decreasing, and groundwater observations (level, chemical, and physical analysis) should be included to characterize the area more precisely and to take efficient and necessary precautions as soon as possible

References

Al-Kouri, O., Al-Fugara, A., Al-Rawashdeh, S., Sadoun, B. & Pradhan, B. (2013) Geospatial modeling for sinkholes hazard map based on GIS & RS data. Journal of Geographic Information System, **5**: 584-592.

Ayday, C., Alan, H. (2020) Eskişehir –Sivrihisar YHT Güzergahında Obruk Oluşumu ve Riskleri Hakkında Rapor. Jeoloji Mühendisleri Odası Yayınları 28 s

Bayari, S., Pekkan, E. & Özyurt, N. (2009) Obruks, as giand collapse dolines caused by hypogenic karstification in the Central Anatolia, Turkey: analysis of likely formation processes. Hydrogeology Journal **17**:327–345.

Benhammadi, H. & Chaffai, H. (2015) The Impact of Karsts structures on the urban environment in semi arid area Cheria plateau case (Northeast of Algeria). Electronic Journal of Geotechnical Engineering Volume 20(**8**): 2107-2114.

Blazzard, K. (2018) Geostatistical Analysis of Potential Sinkhole Risk: Examining Spatial and Temporal Climate Relationships in Tennessee and Florida (Doctoral dissertation, East Tennessee State University).

D'Angella A., Canora F. & Spilotro G. (2015) Sinkholes susceptibility assessment in urban environment using heuristic, statistical and Artificial Neural Network (ANN) models in evaporite karst system: A case study from Lesina Marina (southern Italy). Engineering Geology for Society and Territory, **5**: 411-414.

Elith, J., Phillips, S.J., Hastie, T., Dudık, M., Chee, Y.E. & Yates, C.J. (2011) A statistical explanation of MaxEnt for ecologists. Divers Distrib. 17(**1**):43–57. https://doi.org/10.1111/j.1472-4642.2010. 00725.x

Elmahdy, S.I., Mohamed, M.M., Al, T., Abdalla, J. & Abouleish, M. (2020) Land subsidence and sinkholes susceptibility mapping and analysis using random forest and frequency ratio models in Al Ain, UAE. Geocarto International, 37(**1**), 315-331

Entezari, M., Yamani, M. & Jafari, Aghdam M. (2016) Evaluation of intrinsic vulnerability, hazard and risk mapping for karst aquifers, Khorein aquifer, Kermanshah province: a case study. Environmental Earth Sciences. 75(**5**): Article number 435, Pages 1-10.

Miao, X., Qiu, X., Wu, S.S., Luo, J., Gouzie, D.R. & Xie, H. (2013) Developing efficient procedures for automated sinkhole extraction from Lidar DEMs. Photogrammetric Engineering & Remote Sensing, 79 (**6**), 545–554.

Nachbaur A. & Rohmer J. (2011). Managing expertinformation uncertainties for assessing collapse susceptibility of abandoned underground structures. Engineering Geology, 123 (**3**): 166–178. https://doi.org/10.1016/j.enggeo.2011.07.007

Oh H.J. & Lee S. (2010). Assessment of ground subsidence using GIS and the weight-of-evidence model. Engineering Geology, 115 (**1-2**): 36-48.

Orhan, O., Yakar, M. & Ekercin, S. (2020) An application on sinkhole susceptibility mapping by integrating remote sensing and geographic information systems. Arabian Journal of Geosciences.**13**, 886. https://doi.org/10.1007/s12517-020-05841-6

Özdemir, A. (2016) Sinkhole susceptibility mapping using logistic regression in Karapınar (Konya, Turkey). Bulletin of Engineering Geology and the Environment.**75**, 681–707.

Özdemir, A. (2015) Investigation of sinkholes spatial distribution using the weights of evidence method and GIS in the vicinity of Karapınar (Konya, Turkey). Geomorphology**245**:40–50

Perrin, J., Cartannaz C., Noury G. & Vanoudheusden E. (2015) A multicriteria approach to karst subsidences hazard mapping supported by weights-of-evidence analysis. Engineering Geology, **197**: 296-305. https://doi.org/10.1016/j.enggeo.2015.09.001

Phillips, S.J., Anderson, R.P. & Schapire, R.E. (2006) Maximum entropy modeling of species geographic distributions. *Ecological modelling*, *190*(**3-4**), 231-259.. https://doi.org/10.1016/j.ecolmodel. 2005.03.026

Rahimi, M. & Alexander, E.C. (2013) Locating Sinkholes in LiDAR Coverage of a Glacio-fluvial Karst, Winona County, MN.

Sarı F. (2017) Sinkhole Susceptibility Analysis For Karapinar/Konya Via Multi Criteria Decision Analysis. 4th International Workshop on GeoInformation Science.Safranbolu, Turkey.

Sarı, F., Kahveci, M., Altaş, M.S. & Tuşat, E. (2021) Evaluating sinkhole formation with multicriteria decision analysis:A case study in Karapınar-Konya, Turkey. Arabian Journal of Geosciences, 14(**4**), 1-15.

Shaban, A. & Darwich, T. (2011) The role of sinkholes in groundwater recharge in the high mountains of Lebanon. Journal of Environmental Hydrology 19.

Subedi, P., Subedi, K., Thapa, B. et al. (2019) Sinkhole susceptibility mapping in Marion County, Florida: Evaluation and comparison between analytical hierarchy process and logistic regression based approaches. Scientific reports, 9(**1**), 1-18.

Taheri, K., Shahabi, H., Chapi, K., Shirzadi, A., Gutiérrez, F. & Khosravi, K. (2019) Sinkhole susceptibility mapping: A comparison between Bayes-based machine learning algorithms. Land Degradation & Development, 30(7), 730-745.

Ulu, Ü., Bulduk, A.K., Saçlı, L., Ekmekçi, E., Taşkıran, M.A., Karataş, M., Adır, M., Öcal, H., Sözer, Ş., Arbas, A., Karabıyıkoğlu, M. (1994) İnlice-Akkiseve Cihanbeyli-Karapınar Alanının Jeolojisi. MTA Der Rap No:9720

Yilmaz I. (2007) GIS based susceptibility mapping of karst depression in gypsum: A case study from Sivas basin (Turkey). Engineering Geology, 90 (**1-2**): 89-103. https://doi.org/10.1016/j.enggeo.2006.12.004

Yong, K., Hyun, N., Ryan, S., Moataz, S. & Heejung, Y. (2020) Development of Sinkhole Susceptibility Map of East Central Florida. Natural Hazards Review, 21(**4**).

URL 1, WordClim Web Page. https://www.worldclim.org/data/index.html (Accessed on 18.12.2021)

URL 2, Copernicus Home Page. https://www.copernicus.eu/en (Accessed on 18.12.2021)

Submitted: 28/06/2021
Revised: 03/01/2022
Accepted: 07/01/2022
DOI: 10.48129/kjs.19149

Kuwait J.Sci., Vol.50, No.(1A),January.2023,pp(140-154)

Monitoring land cover dynamics utilizing a change vector analysis approach: a case study of al Najaf Province, Iraq

Ebtihal T AL-Khakani[1, *]; Huda M. Hamid[2]

[1] *Dept. of Physics, College of Education for Girls, University of Kufa al Najaf, Iraq*

[2] *Dept. of Soil and Water Resources, College of Agriculture, Al-Qasim Green University, Babylon, Iraq*

**Corresponding author: csiw512@gmail.com*

Abstract

Analysing information relevant to land cover changes is a fundamental issue in studies linked to environmental diversity. The use of multi-time satellite images at different scales allowed continuous observation of land cover changes. Due to significant changes in land cover, specifically in the decades 2000–2010 and 2010–2020, al Najaf Province was selected as the study area. This work aimed to study changes in land cover in Al Najaf Province from satellite imagery, using change vector analysis (CVA), through the last two decades (2000–2010 and 2010–2020). The enhanced vegetation index 2 (EVI2) and the dry bare soil index (DBSI) represented the vegetation and soil condition in the study region. They were estimated via images from the satellite Landsat-5 TM for March for the two years 2000 and 2010, and Landsat 8 OLI 2020 for the same month, then were considered the parameters for a land cover change analysis using the CVA. The outputs of the CVA were assessed on maps of land cover obtained through the supervised classification for the above-mentioned images. The results of the change vector magnitude found that the ratio of the changed area reached 46.58% and 56.35%, and the unchanged area was 53.42% and 43.65% for the periods (2000–2010) and (2010–2020), respectively. The results of the change direction revealed that the moisture reduction ratio was 26.93% and 4.85%, while the vegetation regrowth ratio was 15.81% and 38.79% for the same two periods, respectively. The results of the two periods considered exhibited that the EVI2-DBSI combination presented promising performance results with the overall accuracy of 0.90 and 0.92 and a kappa index of 0.867 and 0.852, respectively. As a result, the CVA technique offers a promising way to track environmental changes that are connected to the dynamics of land use/land cover in this region.

Keywords: Change vector analysis; dry bare soil index; enhanced vegetation index 2; land cover change; Landsat.

1. Introduction

The phrase land cover is often used to describe the general biophysical state of the land surface as well as giving information on the distribution of vegetation, water, soil, etc. The changes in

land cover resulting from several human and natural factors, represented by the changes of relative biophysical characteristics of the Earth's surface, have significant effects on the quality of environmental systems. So, the changes in the cover of land can represent the principal indices of environmental changes at various temporal and spatial scales (Polykretis *et al*., 2020).

The survey of land cover/use change is significant for the management of natural resources in the regional and local areas of the country (Sangpradid, 2018). Change detection may be defined as a methodology for distinguishing variations in the status of a target or phenomenon by monitoring them at various times (Tong *et al*., 2020). For studying the land cover changes of a particular area, it is essential to obtain the information that reveals its condition at different time intervals (Polykretis *et al*., 2020). Change detection utilising satellite imagery and a GIS platform is an effective method (Mohammed, 2021), where it is characterised by quickly collecting multi-spatial data and a multi-temporal resolution that allows the mapping of changes of land cover at various levels (Tong *et al*., 2020).

Depending on the methods of processing data for change detection, the techniques used were divided, according to Johnson & Kasischke (1998), into two major groups: (a) depending on the input data's spectral categorisation (classification) and (b) techniques that build on the radiometric changes for data with different dates, like band ratio, band difference, image difference obtained from band conversion (e.g., vegetation and soil indicators) and change vector analysis (CVA).

Vegetation cover or bare soil are often indicated as biophysical characteristics of the land surface. These characteristics can be measured using several spectral indices for vegetation and soil (Islam *et al*., 2016). The spectral indicators describe the conditions of vegetation and soil cover, respectively, for a particular area, employing a specific value range depending on the level of absorption/reflection from the surface of the Earth in the various parts of the electromagnetic spectrum or satellite bands (Münch *et al*., 2019). The relation between the spectral indicators and change detection of land cover is well established as a result of their commonly used application in this type of analysis.

The CVA technique has been employed by many researchers to study land cover changes, for example, detecting changes in the forests (Malila,1980), detecting the change of land cover in rural-urban regions (He *et al*., 2011), evaluating humid land dynamics (Landmann *et al*., 2013), detecting the changes in agricultural land use (Aravind, S., & Sivakumar, R.2016), observation of the changes of fuzzy shorelines (Dewi *et al*., 2017), and monitoring forest resources (Xiao-hui *et al*., 2021). The CVA method allows the user to classify various kinds of change concerning land cover dynamics in a given region (Ebrahimian, R., & Alesheikh, A. 2019). It provides the possibility to determine the nature of the change, in addition to its magnitude, where it is a powerful tool for detecting radiometric changes (Fernandes *et al*., 2014).

This research aims to detect the changes in land cover of Al Najaf Province employing the CVA technique. The CVA technique was applied using EVI2 and DBSI indices from Landsat satellite data for the two periods 2000–2010 and 2010–2020.

2. Materials and Methods

2.1. Study Site

Al-Najaf Province is situated in the southwest part of Iraq, at 70 m above sea level. It is 160 km from the capital, Baghdad, with an area of about 28,824 km^2. The study zone represents the north-eastern portion of the province (figure 1), with an area estimated at 2,112 km^2, and lies between latitude 31º 37′–32º 21′ N and longitude 44º 7′– 44º 37′ E. The area selected for the study includes the land cover types that experienced significant changes in the period 2000–2020. The region witnessed the transformation of significant parts of bare lands and agricultural areas into urban areas, in addition to considerable changes in water areas as a result of the large variation in total annual rainfall from 2000 to 2020 (General Authority for Meteorology) ,as indicated in figure 2, which influenced the large variations in vegetation cover.

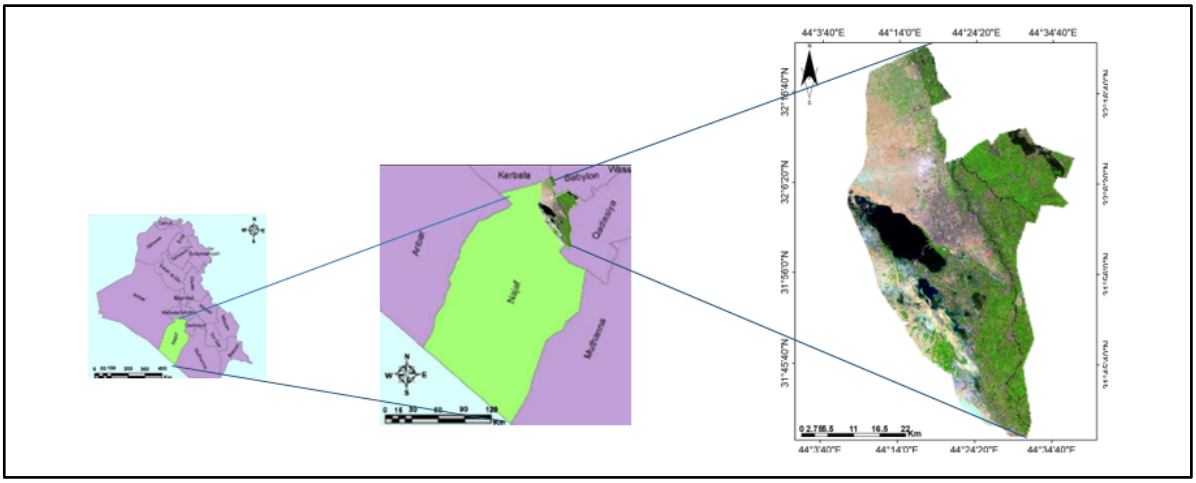

Fig. 1. Study area site. From left to right: location of al Najaf Province in Iraq, study site in al Najaf province and Landsat image (2020) for the study area (band combination RGB 3, 5, 7).

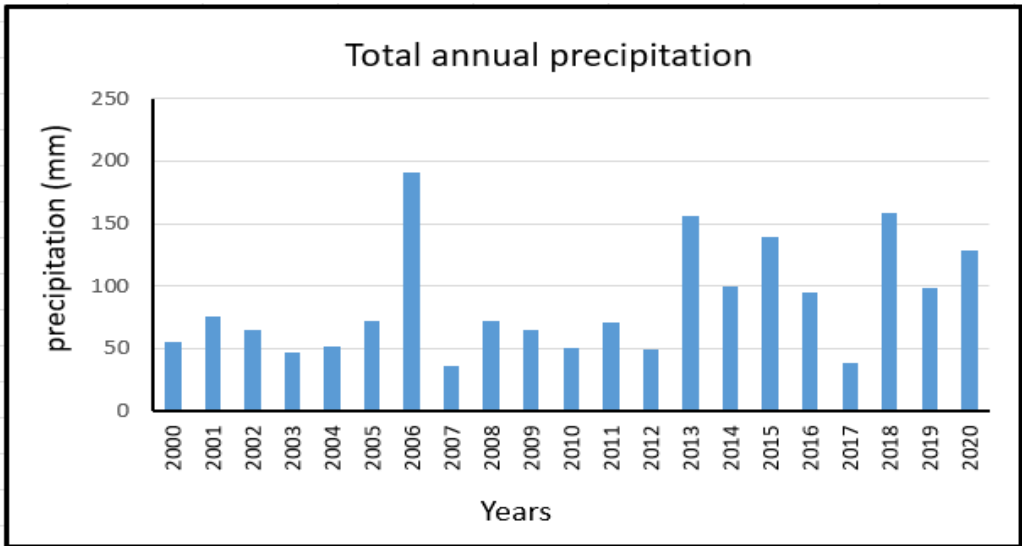

Fig. 2. Total annual precipitation for the period from 2000 to 2020.

2.2. Data utilised

In this research, Landsat satellite images for the period 2000–2020 were selected to assess the changes in the land cover of the study region. The time period was chosen based on the significant changes that occurred in the land cover and the availability of appropriate data for that period. All images, downloaded from http://landsat.usgs.gov, were cloud-free and were systematically rectified at downloaded. The multi-spectral imagery data with a resolution of 30 m were obtained for the Landsat-5 TM in March 2000 and 2010, and Landsat 8 OLI in March 2020, path/row 168/38. The data have been corrected to a Universal Transverse Mercator (UTM) projection via the WGS84 datum and zone 38. The dates of the images were chosen as they represent the peak of the vegetation growing season in the region (from March to May). The images for the three years were from the same month to reduce seasonal variation. Arc GIS 10.6 software was employed for pre-processing data, and Excel 2019 was utilised for the other analyses.

2.3. Spectral indices used

To evaluate the biophysical characterisation of the study region, two spectral indices have been employed after processing Landsat imagery data.

For measuring the changes of land cover for the studied region, the enhanced vegetation index 2 (EVI2) to describe vegetation conditions, and the dry bare soil index (DBSI) to describe the soil conditions of the zone, were computed from Landsat images. EVI2 is an improved version of NDVI. It reduces atmospheric effects, and it can be formulated according to the equation as follows (Jiang *et al*., 2008):

$$EVI2 = 2.5 \frac{\rho_{NIR} - \rho_{RED}}{\rho_{NIR} + 2.4 * \rho_{RED} + 1} \quad (1)$$

Where ρ_{NIR} and ρ_{RED} are the values of surface reflectance for near-infrared and visible red bands (Landsat-5 TM bands 4 and 3, and Landsat 8-OLI bands 4 and 5, respectively).

The EVI2, similar to NDVI, is a unit less variable, whose values range from -1 to 1. The value of 2.5 is the gain factor, the coefficient 2.4 is employed to reduce aerosol impacts and the value of 1 represents the soil adjustment factor utilised to reduce soil background influences.

The DBSI, created by Rasul *et al*. in 2018, improves differentiation between dispersed vegetation and bare soil to identify bare zones in dry climates. The values of the DBSI range from -2.0 to +2.0. The higher value is conformed to the bare soil area. The proposed formula for the DBSI is (Rasul *et al*., 2018):

$$DBSI = \frac{\rho_{SWIR1} - \rho_{Green}}{\rho_{SWIR1} - \rho_{Green}} - NDVI \quad (2)$$

2.4. Change vector analysis

CVA is a change detection method that exhibits the change as a vector, either in two- or multi-dimensional space. The idea of CVA includes the computation of spectral changes according to multi-temporal pairs of spectral indicators (Fernandes & Almeida, 2014). The computed change

vector involves basic information about the magnitude and direction of change, where it allows for mapping them between the dates specified, pixel by pixel (Polykretis *et al*., 2020).

If two components are used, the two-dimensional space is represented with two axes via a Cartesian coordinate system. The change vector consists of two points corresponding with the same pixel at two different times, where the beginning and ending points represent the pixel positions in EVI2-DBSI space on these two dates (Sangpradid, 2018). The change magnitude (M) is measured between the first (t1) and second (t2) dates, across the length of the change vector as in figure 3A where it is calculated utilising the Euclidean distance according to the formula:

$$M = \sqrt{(EVI2_{t2} - EVI2_{t1})^2 + (DBSI_{t2} - DBSI_{t1})^2} \quad (3)$$

Where $EVI2_{t1}$ and $EVI2_{t2}$ are the pixel values of the EVI2 index at the two dates of t1 and t2, respectively. As well, $DBSI_{t1}$ and $DBSI_{t2}$ are the values of pixels for the DBSI index for the same two dates.

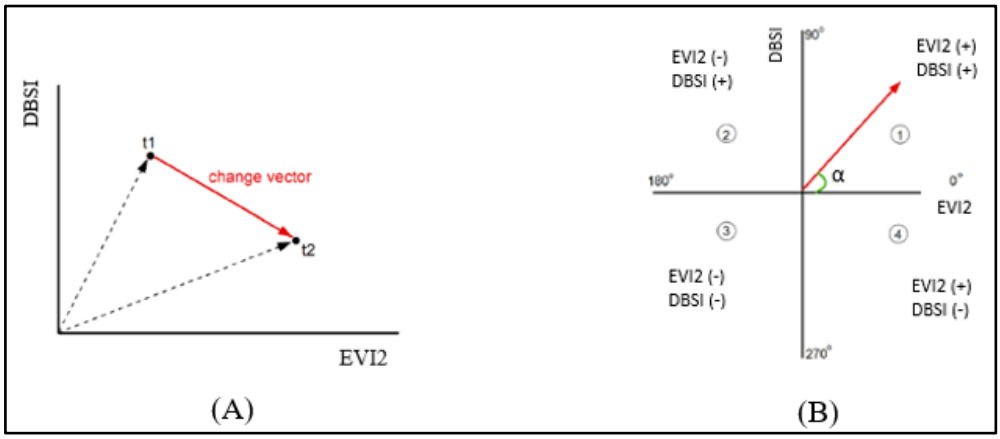

Fig. 3. The change vector analysis for space of EVI2-DBSI,
(A) the magnitude of change and (B) the direction of change.

A threshold is set according to standard deviations for the values of magnitude to differentiate between changed and unchanged portions from the study region. The direction of change is determined by computing the change vector angle, which varies with the number of components utilised. This angle refers to the kinds of changes that have occurred during two particular dates (Fernandes & Almeida, 2014), which describes the type of change concerning the directions of mutual change within the pixel units of the two components. In general, the number of direction classes is equivalent to 2n, where n represents the number of components or spectral bands (Karnieli *et al*., 2014). In this paper, two components (DBSI and EVI2) were employed as input, so the direction of change is classified into four categories of angles, or four quadrants, as shown in figure 3B. The change vector direction was calculated in a two-dimensional space, using the following equation:

$$\tan \alpha = \frac{DBSI_{t2} - DBSI_{t1}}{EVI2_{t2} - EVI2_{t1}} \quad (4)$$

Where, tan(α) represents the tangent of angle α.

Based on the directions of change within pixels in the DBSI and EVI2 components: Angle measurements between 0º–90º indicate an increase in both bands. The angles between 90º–180º represent an increase in the EVI2 and a decreased DBSI. Angle measurements between 180º–270º indicate a decrease in both components. Finally, the angles between 270º–360º refer to a decrement in EVI2 and an increase in DBSI (Fernandes & Almeida, 2014).

2.5. Methodology

In this research, the CVA technique has been applied to reveal the changes in land cover using two spectral indices, EVI2 and DBSI. The changes in magnitude in land cover for the studied area for the two periods 2000–2010 and 2010–2020 were estimated utilising equation (3) in ArcGIS software. Relying on prior expertise in change detection analysis, the standard deviation (ST) by the value of one from the average, has been specified as a threshold (Bayarjargal *et al*., 2006; Paz-Kagan *et al*., 2014; Volcani *et al*., 2005) for a distinction between changed and unchanged regions. In a similar way, the change level has been classified into low change and high change. The results of the change magnitude are displayed as maps graded into three classes: high change, low change and no change, for the two periods 2000–2010 and 2010–2020. The change direction has been determined based on the angles of the change vectors using equation (4).

Each of the four angle categories is associated with types of land cover changes for the study region. The angles 0º–90º represent the increment in both the EVI2 and DBSI indices. This category identifies areas of varying biomass or low humidity and is often associated with changes in agricultural zones. The angles 90º–180º, which correspond to a decrease of the EVI2 indicator and an increase of the DBSI indicator, represent the extension of bare soil or degraded areas. The angles 180º–270º, which conform to a decrease in both spectral indicators, represent water bodies or increased humidity. The range angles 270º–360º are connected with an increase and a decrease of the EVI2 and DBSI indicator values, respectively, which indicates the re-growth of vegetation cover, i.e., areas that experienced an improvement in land quality (Karnieli *et al*., 2014).

3. Results

3.1 The results of the EVI2 and the DBSI

The results of the EVI2 and the DBSI were assessed for the 2000, 2010, and 2020 Landsat imagery data. Figure 4 shows the results of the EVI2 for 2000, 2010, and 2020. The area of vegetation cover was lower in 2010 than it was in 2000, specifically in the south-eastern section of the region, while in 2020, vegetation increased in most eastern and south-eastern parts of the studied zone. Figure 5 displays the DBSI results for the period 2000–2020. The low values of the DBSI have accompanied the areas with a high vegetation density.

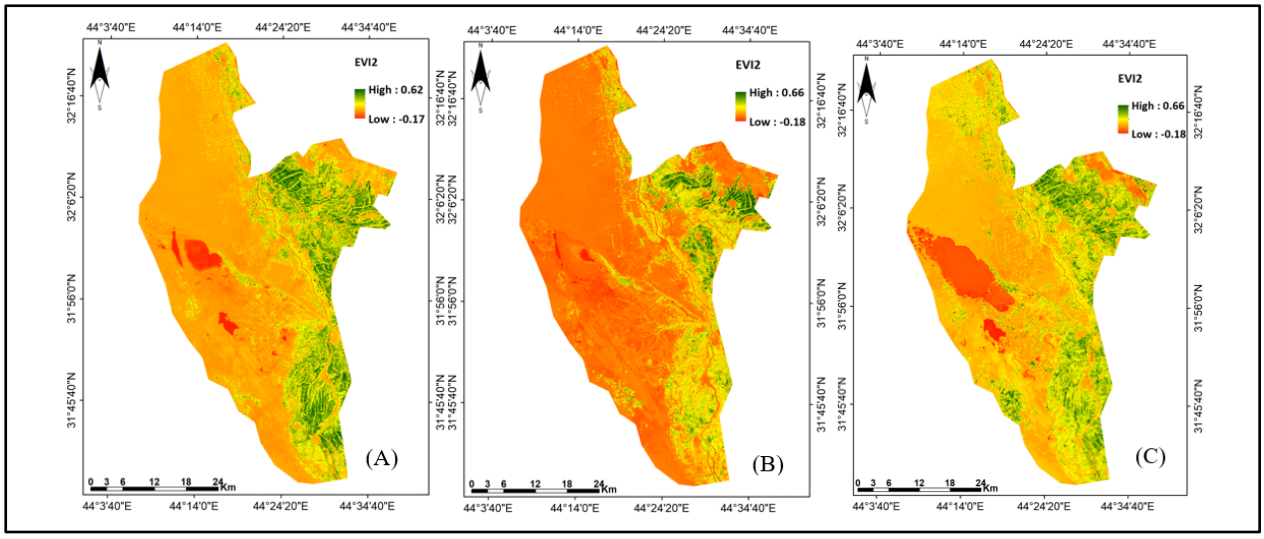

Fig. 4. Results of the enhanced vegetation index 2 for years (A) 2000, (B) 2010, and (C) 2020

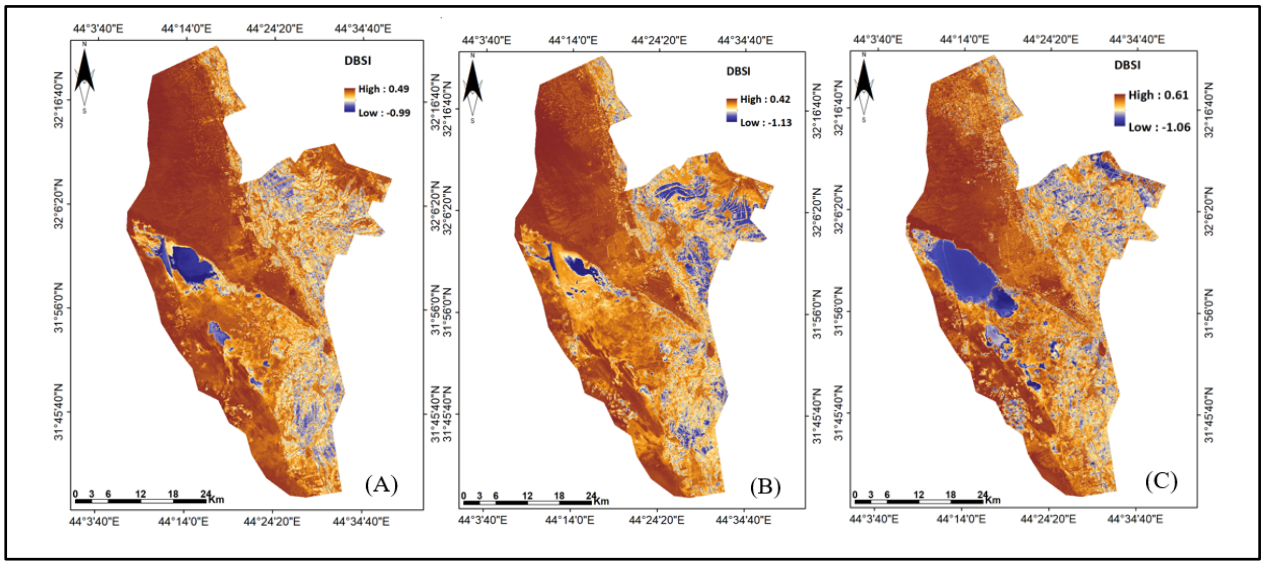

Fig. 5. Results of the dry bare Soil index for years (A) 2000, (B) 2010, and (C) 2020

3.2 Analysis of CVA

The outcomes of CVA have two parameters: the change magnitude and the change vector direction. Figure 6 A and B illustrate the maps of change magnitude generated by the EVI2-DBSI combination for the two periods 2000–2010 and 2010–2020.

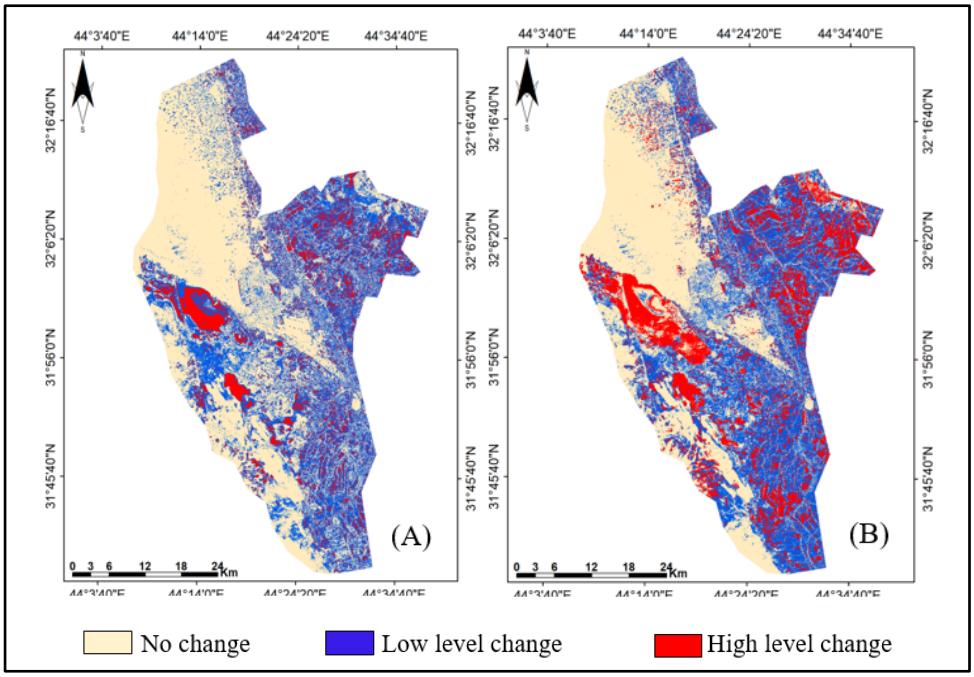

Fig. 6. Maps of change magnitude (A) for the period 2000–2010 and (B) for 2010–2020 from EVI2-DBSI combination.

Between 2000 and 2010, about 46.58% (983.9 km^2) of the study region suffered changes, as against 53.42% (approximately 1,128.54 km^2) unchanged, as in figure 6A. The area with low-level changes reached 754.76km^2, while high-level changes were 229.14 km^2, which were concentrated in the western section of the study site in the Bahr Al-Najaf depression and some of the zones of agricultural fields.

From 2010–2020, many changes occurred in large parts of the study site compared to the 2000–2010 period, as illustrated in figure 6B. Land totalling 56.35% (approximately 1,190.82 km^2) witnessed a change, while the rest, about 43.65% (921.82 km^2) showed no change. Of the total changing area, 36.4% (about 769.02 km^2) was associated with low-level changes, observed in most agricultural land, and 19.95% (about 431.54 km^2) had high-level changes, which were mainly concentrated in water zones as well as a few areas of bare soil.

Concerning the direction of change from 2000 to 2010, figure 7A, nearly 26.93% (approximately 577.33 km^2) of the study zone suffered biomass variation/moisture reduction, followed by about 15.81% (334.06 km^2) that experienced regrowth of vegetation cover, and 2.75% (approximately 31.60 km^2) witnessed a bare soil expansion. A small portion of the study zone equal to 1.09% (approximately 23.02 km^2) showed a water body/moisture increase.

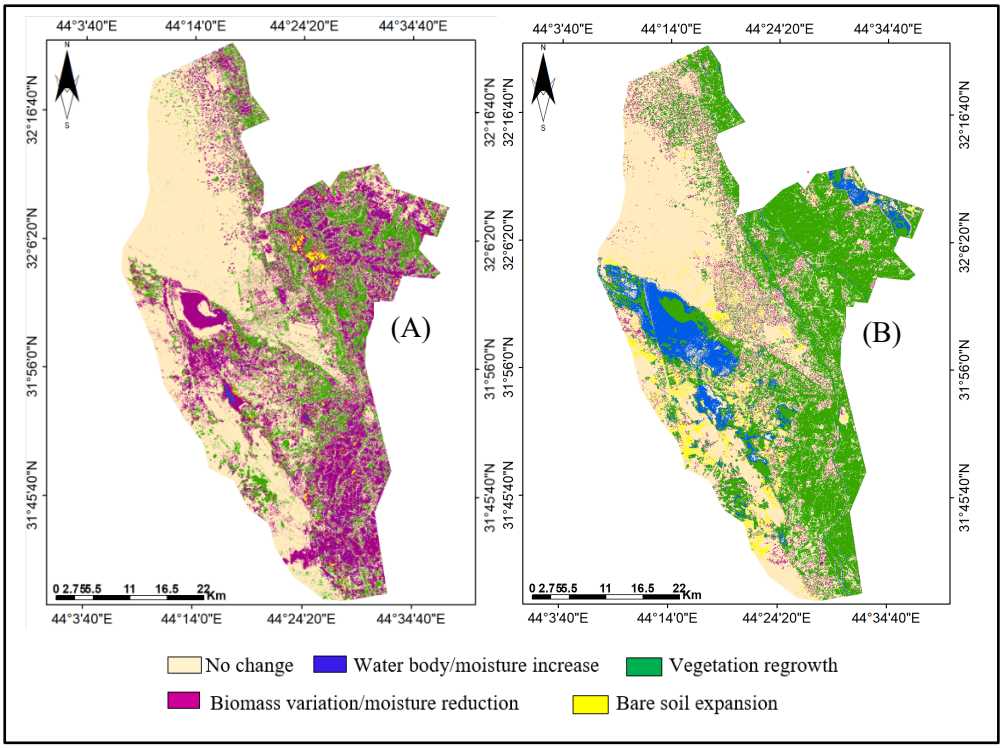

Fig. 7. Maps of change direction, left, for 2000–2010, and on the right, for 2010–2020, from EVI2-DBSI combination.

According to the change directions for the period 2010–2020 (figure 7B), a large part of the study area witnessed about 38.7% (5,096 km^2) of vegetation regrowth, according to the scattered spatial coverage of vegetation cover. There was an increase in water bodies/moisture of approximately 8.92% (183.08 km^2). A less extensive part, which is 4.85% (about 100.5 km^2), suffered a biomass variation/moisture reduction. Finally, the expansion of bare soil increased slightly, around 3.79% (approximately 67.03km^2). Figures 8 and 9 show the percentage of change magnitude calculated for the relative categories for each period.

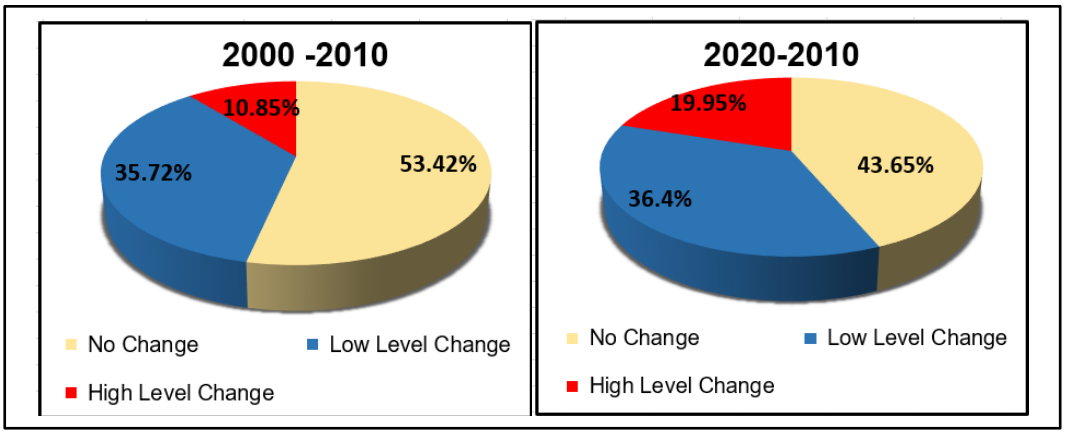

Fig. 8. Percentages of change magnitude classes for the two study periods.

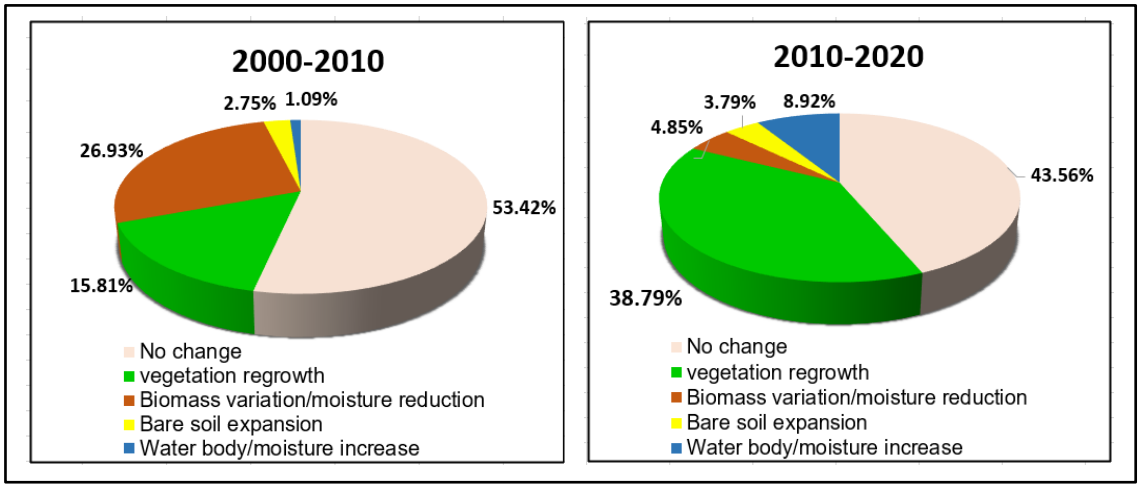

Fig. 9. Percentages of change direction classes for the two study periods.

3.3 Accuracy assessment

Accuracy evaluation of the CVA outputs was performed using the error (or confusion) matrix for defining the overall accuracy, and the kappa index (Equations 5 and 6) (Thakkar *et al*., 2017; Keshtkar & Alizadeh, 2017) was used to test the accuracy of results and compare them with actual reality. The confusion matrix is a two-dimensional table that enables the performance of an image classification method to be visualised. The truth data is represented by the table's columns (x-axis), while the classified image results are represented by the rows (y-axis) (or vice versa) (Congalton, 1991). The kappa coefficient ranges from 0 for very low accuracy to 1 for excellent accuracy. Because precise field-derived data was unavailable, new data produced through remote sensing was developed to establish reference data. It was generated utilising a supervised classification of Landsat satellite images to create detailed maps of land cover. On composite RGB colour images of 2000, 2010, and 2020, about 246 random sample zones were collected. Visual interpretation was used to designate these locations as a distinct land cover type, resulting in a total of five categories being represented. ArcGIS software was used to create a detailed map of land cover for each date, using the identified areas and a supervised classification method through a maximum likelihood classifier (MLC). The maximum-likelihood algorithm locates the likeness with an unknown data item and a defined dataset via a covariance matrix depending on the correlations within a dataset and the data distribution. To determine changing or non-changing regions through the periods 2010–2000 and 2020–2010, spatial analysis based on GIS was performed for pairs of these maps. The type of change was then assigned and named based on the change direction classes of CVA. Finally, for obtaining the statistics of overall accuracy and the kappa index, the specified information as reference data was compared with the outputs of CVA (the magnitude and direction of change) in confusion matrices.

$$Overall\ accuracy = \frac{Total\ number\ of\ correct\ samples}{Total\ number\ of\ samples.} \times 100 \quad (5)$$

$$K = \frac{(The\ diagonal\ elements\ sum \times sum\ of\ correct) - sum\ all\ of\ the\ (row\ total \times column\ total)}{Total\ of\ correct\ squared - sum\ of\ all\ the\ (row\ total \times column\ total)} \quad (6)$$

Table 1. The values of overall accuracy and kappa coefficient for the two time periods.

Period	Change/No Change (Magnitude)		Kind of Change (Direction)	
	Overall Accuracy	Kappa Index	Overall Accuracy	Kappa Index
2000-2010	0.901	0.849	0.885	0.867
2010-2020	0.921	0.879	0.829	0.852

4. Discussion

In this work, through the application of the CVA technique utilising two EVI2 and DBSI indexes, the land cover changes were located and evaluated for the time intervals 2000–2010, and 2010–2020. Vegetation and soil indicators were created based on images from the Landsat satellite obtained for March 2000, 2010, and 2020. CVA is a promising technique for observing the changes of land cover, with the ability to provide important qualitative and quantitative information regarding the dynamics of temporal and spatial land cover. The results of the CVA outputs (magnitude and direction of change) allow various magnitudes and types of change to be determined.

Compared to classification-based methods, the CVA technique can simultaneously analyse a combination of remotely sensed data to monitor the changes within categories of land cover. Such changes are obtained by observing the variation between consecutive satellite images without going into an uncertain classification (Karnieli *et al*., 2014).

The CVA results of the DBSI-EVI2 combination were mapped to define the spatial distribution for the change magnitudes and the types of land cover changes in the studied zone. The maps of magnitude in figures. 5A & B, showed that, for both periods evaluated, most of the study region was influenced via low-level changes. In addition, large areas remained unchanged. The high-level changes were significantly low in 2000–2010, but clearly increased in 2010–2020.

According to the change direction maps in figure 6A, the study area generally experienced a marked decrease in vegetation cover during the period 2000–2010. Indicating the decrease in regrowth areas at the expense of a raising in the degraded land area, that represent the biomass variations regions (or moisture reduction), where concentrated in the central, eastern, and south-eastern parts, with the expansion of bare soil areas. The spatial expansion of degraded or arid land can be attributed to reduced annual rainfall in this period (as illustrated in figure.2)

and droughts arising from poor land management. Also, the water bodies of the region, represented by the depression of Bahr Al-Najaf, witnessed a noticeable decrease in their levels during the same period due to the dwindling of the floodwaters that feed this depression.

Moreover, as seen in figure 6B, the period 2010–2020 witnessed an increase in regrowth zones, where cultivated areas expanded due to increased agricultural activity and rainfall levels rising from 50.3 mm in 2010 to 128.4 mm in 2020, as illustrated in figure 2. This was evident in the eastern and south-eastern portions of the studied region, where there was a significant decrease in areas of biomass variation/humidity reduction. Water bodies have expanded significantly compared to the previous period because of the increased flow of torrent water, which is the major source of water.

Confusion matrices have been utilised for evaluation of the accuracy of CVA outputs, based on change/non-change (magnitude) in addition to the type of change (direction), for the 2000–2010 and 2010–2020 periods. Table 1 offers the values of overall accuracy and the kappa coefficient calculated using these matrices, in accordance with (Landis, & Koch, 1977). These results are considered very acceptable.

5. Conclusion

Currently, remote sensing imagery and different analysis techniques provide further information to monitor and detect changes in land cover. CVA is a powerful and effective method to detect radiometric changes in the multi-spectral remote sensing data. The results of the CVA technique implementation using two components, EVI2 and DBSI, showed the ability to detect and classify different categories of changes concerning biomass gain and loss. The results demonstrated that the number of regions that did not change was higher than those with high-level and low-level changes through the two periods studied.

Between 2000 and 2010, there has been a decline in areas of regrowth and water bodies. From 2010 to 2020, regrowth zones and water bodies have increased as large areas of bare soil have shifted to agricultural use due to increased rainfall.

The CVA technique offered satisfactory results for the two study periods, as the overall accuracy of the final maps was 0.885 and 0.829, with a kappa index of 0.867 and 0.852 respectively, indicating that accurate change detection can be obtainable. The maps of change magnitude and direction could establish a fundamental rule for planners in determining changes of land cover and planning suitable land administration strategies.

ACKNOWLEDGEMENTS

The authors extend their thanks and great gratitude to Assistant Professor Dr. Khaleda Al-Mayali, Head of the Physics Department at the College of Education for Girls, University of Kufa, for her support and valuable comments.

References

Aravind, S., & Sivakumar, R. (2016). Agricultural land use change detection using change vector analysis in lower Velar Watershed. International Journal of Engineering Research & Technology, **4**(20), 1-6.

Bayarjargal, Y.; Karnieli, A.; Bayasgalan, M.; Khudulmur, S.; Gandush, C.; Tucker, C.J. (2006). A comparative study of NOAA-AVHRR derived drought indices using change vector analysis. Remote Sensing Environment, **105**(1), pp. 9–22.

Congalton, R. G. (1991). A review of assessing the accuracy of classifications of remotely sensed data. Remote Sensing of Environment, **37**(1), pp. 35–46.

Dewi R., Bijker W. and Stein A. (2017). Change Vector Analysis to Monitor the Changes in Fuzzy Shorelines. Remote Sensing, **9**(2), pp.1–28.

Ebrahimian, R., & Alesheikh, A. (2019). a Change Vector Analysis Method to Monitor Drought Using Landsat Data. The International Archives of Photogrammetry, Remote Sensing and Spatial Information Sciences, 42, 321-325.

Fernandes, P. J. F., & de Almeida Furtado, L. F. (2014). Change vector analysis to detect deforestation and land use/land cover change in Brazilian Amazon. Brazilian Geographical Journal: Geosciences and Humanities Research Medium, **5**(2), pp. 371–387.

General Authority for Meteorology and Seismic Monitoring / Climate Management / Republic of Iraq. Unpublished data.

He C., Wei A., Shi P., Zhang Q. and Zhao Y. (2011). Detecting land-use/land-cover change in rural-urban fringe areas using extended change-vector analysis. International Journal of Applied Earth Observation and Geoformation, **13**(4), pp. 572–585.

Islam, K., Jasimuddin, M., Nath, B., & Nath, T. K. (2016). Quantitative Assessment of land cover change using landsat time series data: case of Chunati Wildlife Sanctuary (CWS), Bangladesh. International Journal of Environment and Geoinformatics, **3**(2), pp. 45–55.

Jiang, Z., Huete, A. R., Didan, K., & Miura, T. (2008). Development of a two-band enhanced vegetation index without a blue band. Remote Sensing of Environment, **112**(10), pp. 3833–3845.

Johnson, R. D., & Kasischke, E. S. (1998). Change vector analysis: A technique for the multispectral monitoring of land cover and condition. International Journal of Remote Sensing, **19**(3), pp. 411–426.

Karnieli, A., Qin, Z., Wu, B., Panov, N., & Yan, F. (2014). Spatio-temporal dynamics of land-use and land-cover in the Mu Us sandy land, China, using the change vector analysis technique. Remote Sensing, **6**(10), pp. 9316–9339.

Keshtkar, H., Voigt, W., & Alizadeh, E. (2017). Land-cover classification and analysis of change using machine-learning classifiers and multi-temporal remote sensing imagery. Arabian Journal of Geosciences, **10**(6), pp. 1–15.

Landis, J. R., & Koch, G. G. (1977). The measurement of observer agreement for categorical data. *biometrics*, pp. 159–174.

Landmann T., Schramm M., Huettich C., and Dech S. (2013). MODIS-based change vector analysis for assessing wetland dynamics in Southern Africa. Remote Sensing Letters, **4**(2), pp. 104–113.

Malila, W. A. (1980). Change vector analysis: an approach for detecting forest changes with Landsat. In LARS symposia, pp. 326–335.

Mohammed, D. A. (2021). Integrated remote sensing and GIS techniques to delineate groundwater potential area of Chamchamal basin, Sulaymaniyah, NE Iraq. Kuwait Journal of Science, **48**(3), pp.1–16.

Münch, Z., Gibson, L., & Palmer, A. (2019). Monitoring effects of land cover change on biophysical drivers in rangelands using albedo. Land, **8**(2), pp. 1–28.

Paz-Kagan, T.; Panov, N.; Shachak, M.; Zaady, E.; Karnieli, A. (2014). Structural changes of decertified and managed shrub land landscapes in response to drought: Spectral, spatial and temporal analyses. Remote Sens. **6**(9), pp. 8134–8164.

Polykretis, C., Grillakis, M. G., & Alexakis, D. D. (2020). Exploring the impact of various spectral indices on land cover change detection using change vector analysis: A case study of Crete Island, Greece. Remote Sensing, **12**(2), pp,1–25.

Rasul, A., Balzter, H., Ibrahim, G. R. F., Hameed, H. M., Wheeler, J., Adamu, B., & Najmaddin, P. M. (2018). Applying built-up and bare-soil indices from Landsat 8 to cities in dry climates. Land, **7**(3), pp. 1–13.

Sangpradid, S. (2018). Change Vector Analysis using Integrated Vegetation Indices for Land Cover Change Detection. International Journal of Geoinformatics, **14**(4), pp.71–77.

Thakkar, K., Desai, V., Patel, A., & Potdar, M. (2017). Impact assessment of watershed management programs on land use/ land cover dynamics using remote sensing and GIS. Remote Sensing Applications: Society and Environment, Elsevier, 5, pp. 1–15.

Tong, S. S., Pham, T. L., Nguyen, Q. L., Le, T. T. H., Cao, X. C., Ahmad, A., & Tong, T. H. A. (2020). The Study of Land Cover Change Using Change Vector Approach Integrated with

Unsupervised Classification Method: A Case In Duy Tien (Vietnam). Geography, Environment, Sustainability, **13**(2), pp.175–184.

Volcani, A.; Karnieli, A.; Svoray, T. (2005). The use of remote sensing and GIS for spatio-temporal analysis of the physiological state of a semi-arid forest with respect to drought years. Forest Ecology and Management, 215, pp. 239–250.

Xiao-hui, W. A. N. G., Bing-xiang, T. A. N., Shi-ming, L. I., & Lin-yan, F. E. N. G. (2021). Object-oriented Forest Change Detection Based on Multi-feature Change Vector Analysis. Journal of Forest Research, **34**(1), 98-105

Submitted: 18/04/2021
Revised: 26/08/2021
Accepted: 02/11/2021
DOI: 10.48129/kjs.16391

Kuwait J.Sci., Vol.50, No.(1A),January.2023,pp(155-172)

Petrotectonic framework of Siwalik Group in Khairi Murat-Kauliar area, Potwar Sub-Basin, Pakistan

Syed K. Ali[1 *], Jahanzeb Khan[1], Muhammad S. Mughal[1], Muhammad R. Lashari[2], Ali G. Sahito[2], Fahad Hameed[1], Hafiz S. Bashir[1], Ahmer Bilal[1], Syed S. Razzaq[1]

[1]*Institute of Geology, University of Azad Jammu & Kashmir Muzaffarabad, Pakistan.*
[2]*Center for Pure and Applied Geology University of Sindh, Jamshoro Pakistan*

[*]*Corresponding author: Kamran.ali@ajku.edu.pk*

Abstract

The Khairi Murat-Kauliar area lies between the Salt Range Thrust (SRT) in the south whereas Main Boundary Thrust (MBT) in the north which is the part of the Potwar Sub Basin. Eocene to Recent rock succession is exposed in the study area. The selected siliciclastic Siwalik Group display various facies in a fluviatile environment, with different lithologies, and sedimentary features. The petrographic studies of Siwalik Group delineate different microfacies including feldspathic litharenite, litharenite and sub arkose. The provenance study of sandstones depicted the terrane of dissected arc and recycled orogeny, indicating that the detritus was received from sedimentary, metamorphic, plutonic and volcanic rocks from the northern domain of Indian Plate, Karakoram Ranges and Kohistan Island arc. The Siwalik sandstone also contains heavy mineral assemblage such as tourmaline, garnet, epidote, hornblende and chlorite. This heavy detritus assemblage depicted that the deposits were received from metamorphic and igneous origin. A modified dynamic depositional stages of the Siwalik Group with respect to Himalayan orogeny is further built using outcrop data, microfacies and heavy minerals analysis. According to this concept, the group was deposited along Himalayan uprising and thrusting, on the depository in targeted area. The Siwalik Group depicted different phase of Himalayan tectonics and these molasse sequence were deposited in a subsiding foreland basin under the conditions of rapid erosion and quick deposition.

Keywords: Dissected arc; heavy minerals; lith arenite; recycled orogeny; siwalik group.

1. Introduction

The Khairi Murat-Kauliar area located in the northeastern wedge of Potwar Sub-basin (Figure 1). Surface stratigraphy dominantly comprised of molasse sediments of Siwalik Group. These sediments indicate the initial stage of basin evolution as well as prone to less deformation as compared to underlying Paleogene strata (Drewes 1995; Kazmi & Jan, 1997; Riaz *et al.,* 2019).

The key problem related to molasses, that they need to be analyzed in the capacity of their mineral assemblage, variation in microfacies and provenance determination. Petrography of the rock component of molasse belongs to Himalayan foreland domain has been executed by various workers.

Chaudhri, (1972) discussed initially the petrogenesis of Siwalik sediments of the northwestern Himalayas, India. Sigdel & Sakai (2013) worked on Siwalik sandstones of Karnali River section, Nepal and suggested different tectonic stages of Himalaya. Bilal, & Khan, (2017) described the petrography and provenance of Kuldana Formation, Kalamula and Khursheedabad area, Kahuta, Azad Kashmir. Goswami & Deopa, (2018) investigated the petrotectonic setting of the provenance of Lower Siwalik of Himalayan foreland basin, Kumaun Himalaya, India. Farooqui *et al.,* (2022) worked on Ispikan Conglomerate and concluded that the provenance of Ispikan detritus was located to the north composed of plutonic and volcanic rocks with minor metamorphic rocks. The present study has been conducted for litho facies and microfacies analysis as well as the distribution of heavy minerals in the Siwalik's; this is necessary to understand and identify the different tectonic stages in Potwar foreland stratigraphic framework.

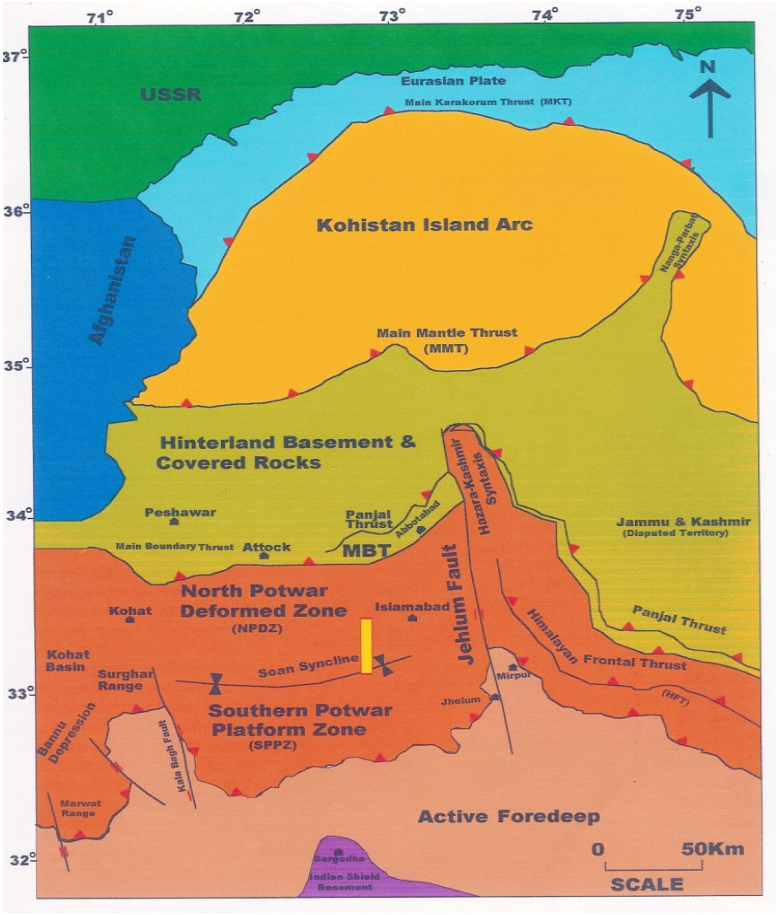

Fig. 1. Tectonic map of Northwest Himalayas, Pakistan. Yellow rectangle displayed the study area (modified after Khan *et al.* 1986).

2. Geological Setting and Stratigraphy

Potwar Sub-Basin is a broad Himalayan foreland basin, located on northwestern margins of Indian Plate. The imbricated and deformed zone in the northern Potwar over the Salt Range thrust sheet is called Northern Potwar Deformed Zone (NPDZ) (Jaswal, 1990: Figure 1). Salt Range Thrust bound

the Potwar sub-basin in the south; represent the marginal foreland fold-and-thrust belt of Pakistan. In the Early Miocene, deformation propagated southward near the MBT, where unmetamorphosed lower Tertiary rocks are thrusted over Neogene molasse. In the latest phase in Pakistan, thrusting is transferred to the Salt Range Thrust where deformation is as young as 0.4 Ma (Yeats *et al.,* 1984). The Potwar sub-basin is nearly undeformed south of the Soan River but is deformed on its northern and eastern margins. Eastern Potwar represents strong deformation as compared to central and western Potwar (Figure 2). Southern Potwar though has been pushed at last twenty kilometers southward, yet it has been undergone almost no internal deformation, except broad, gently folded anticlines (Khan *et al.,* 1986). This phenomenon is due to the weak evaporite decollement and to the increase in the basement slope (Jaume and Lillie, 1988). The Siwalik Group is widely exposed in the northern and southern limbs of Soan Syncline. These strata are non-marine, time transgressive molassic facies that represents the erosional product of southward advancing Himalayan Thrust sheets. Thickness of molasse strata is about 5 km below the Soan Syncline (Lillie *et al.,* 1987). The Siwaliks have been deposited during the last 13 Ma. Top of Murree Formation is dated as 17 Ma. Johnson *et al.,* (1979) suggested that the fluvial and fluvio-deltaic Rawalpindi Group deposits indicate the initiation of significant Himalayan uplift. In the study area, exposed rocks ranges from Eocene to Recent. The stratigraphy of this domain displays tremendous outcrops along Khairi Murat Range (Figure 2; Table 1). Shah (2009) divided Siwalik Group into four formations which are Chinji, Nagri, Dhok Pathan and Soan Formations.

3. Methods and Material

The outcrops of Siwalik Group were recorded, sampled, and measured using standard procedures. Detailed analyses were performed to identify distinct litho facies intervals based on sedimentological properties such as lithology, depositional texture (Figure 3). About 120 samples of Siwalik Group were collected from various locations. For thin section preparation, samples were sent to the Hydrocarbon Development Institute of Pakistan (HDIP), Islamabad. Petrographic microscopy is used to analyzed thin sections by reflected and transmitted light with the help of Leica-DM-750P. To evaluate the provenance, several petrographic observations and parameters were recorded and measured. The classification of sandstone is based on an assessment of the percentages of the various grain types present in thin sections. Sandstones are classified by triangular diagram (McBride, 1963) with end members of quartz (Q), feldspar (F) and lithic fragments (L). The provenance of sandstone is determined from QFL provenance discrimination diagram of Dickinson *et al.,* (1983). Dickinson present four major provenance terrains i.e. stable craton, basement uplift, magmatic arc and recycled orogen. Stable cratons and basement uplifts form the continental blocks. Magmatic arcs included the continental and island arcs associated with subduction, and these are areas of volcanic, plutonic rocks and metamorphosed sediments. Recycled orogens are uplifted and deformed supracrustal rocks, which form mountain belts. Finally, a dynamic provenance stages are developed, based on the dynamics of the paleo-tectonics of northern margin of the Indian Plate, emphasizing the paleo geographic relevance of the Siwalik deposits.

4. Results and Discussion

The petrographic investigations related to the Siwalik set using the classification scheme of McBride, (1963) and Dickinson *et al.,* (1983) are as follows:

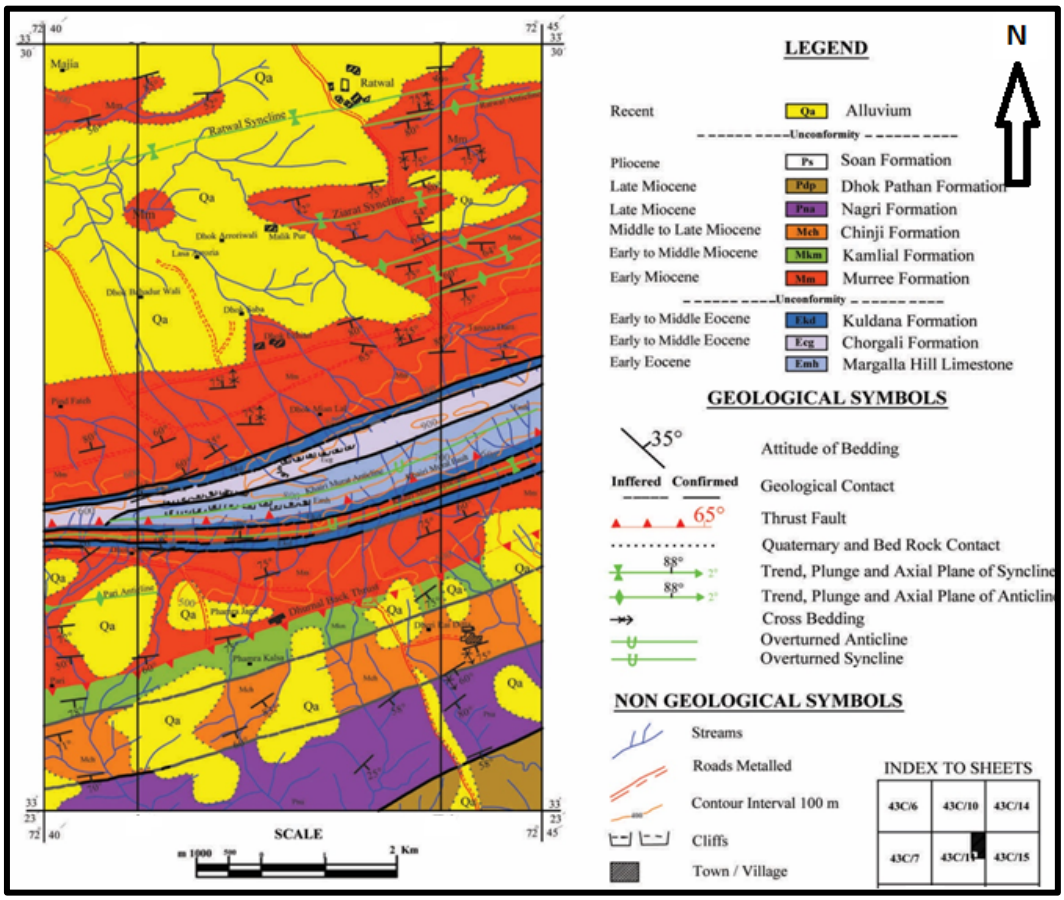

Fig. 2. Geological map of Khairi Murat-Kauliar area, Potwar Sub-Basin, Pakistan (after Kamran *et al.,* 2011).

Table 1. Surface stratigraphic sequence of the study area.

Epoch		Formation	Description
Recent		Alluvium	Silt & clay.
Pleistocene	SIWALIK	Soan Formation	Conglomerate.
Pliocene		Dhok Pathan Formation	Clay and sandstone with conglomerate
Pliocene		Nagri Formation	Massive sand stone with subordinate clays.
Miocene		Chinji Formation	Variegated clays with sandstone.
Miocene		Kamlial Formation	Sandstone.
Miocene		Murree Formation	Sandstone and clays.
Eocene		Kuldana Formation	Variegated color shale
Eocene		Chorgali Formation	Limestone with shale.
Eocene		Margalla Hill Limestone	Nodular limestone with shale.

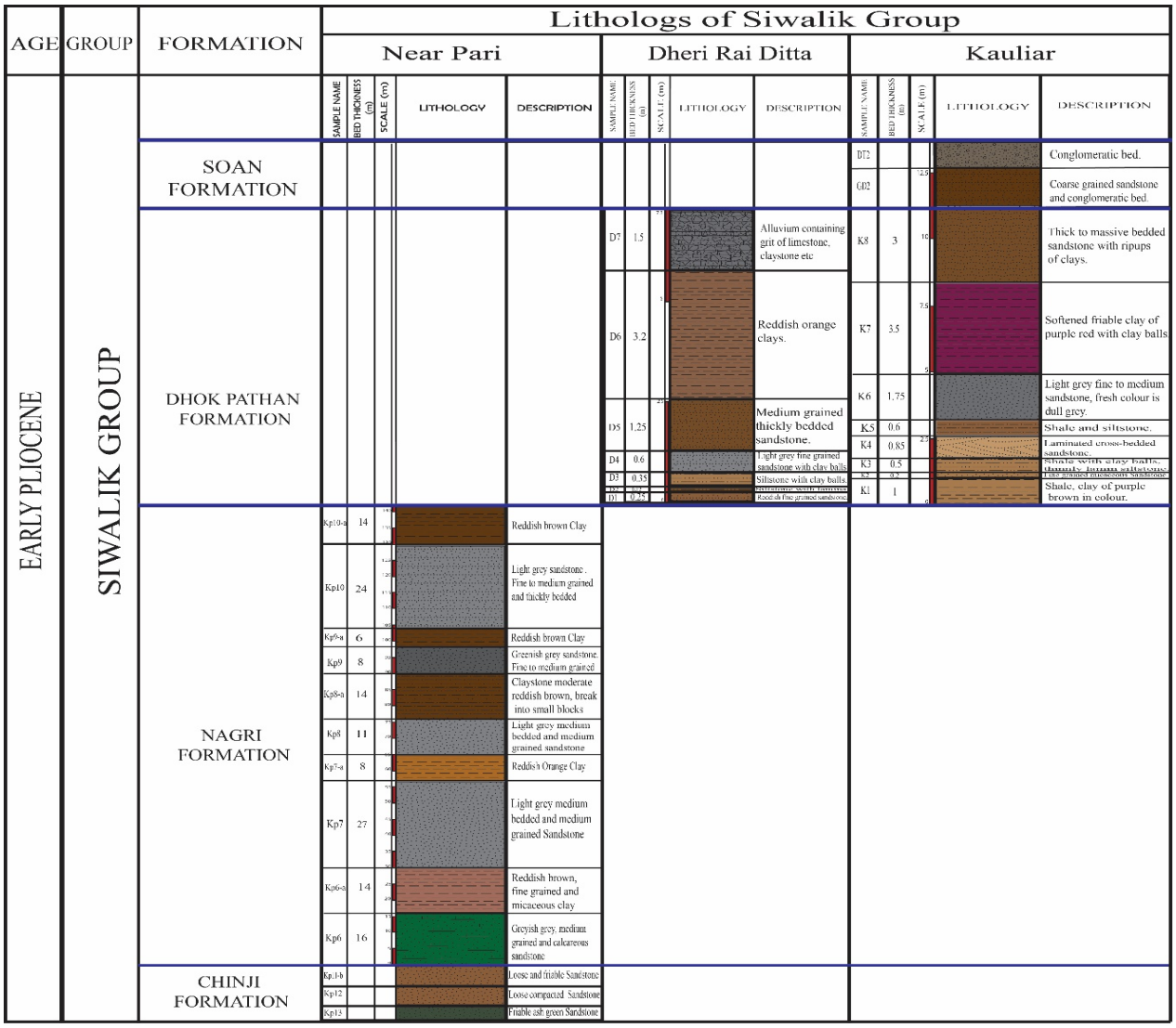

Fig. 3. Lithologs of Chinji, Nagri, Dhok Pathan and Soan Formations near Kauliar, Potwar Sub-Basin Pakistan.

4.1 Chinji Formation

Chinji Formation consists of dominantly brick red clay alternating with sandstone. Three samples were selected for petrographic study which delineates three microfacies (Figure 4).

4.1.1 Litharenite

On QFL diagram, one sample is recognized as litharenite. This type of sandstone is coarse grained, light grey to ash grey, soft and calcareous (Table 2). The texture is angular to sub angular and poorly sorted. Lithic fragments include sedimentary, metamorphic, igneous and volcanic rocks. The flakes of mica (5%), are frequently present. Litharenite sample falls in category of recycled orogen (Figure 5).

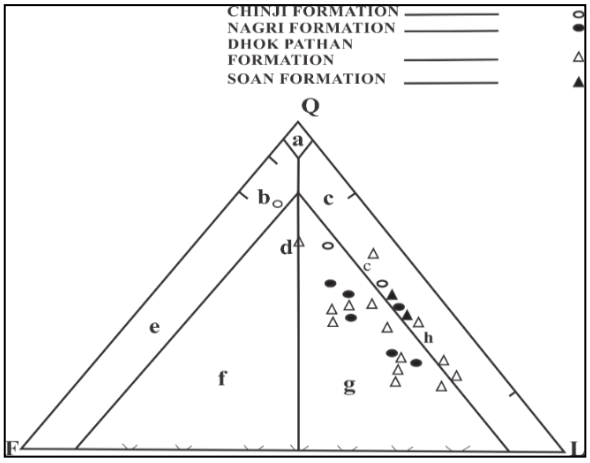

Fig. 4. QFL diagram (modified after McBride, 1963) of the Siwalik Group. The fields are: (a) Quartz arenite, (b) Sub arkose, (c) Sub Litharenite, (d) Lithic sub arkose, (e) Arkose, (f) Lithic arkose, (g) Feldspathic litharenite, (h) Lith arenite

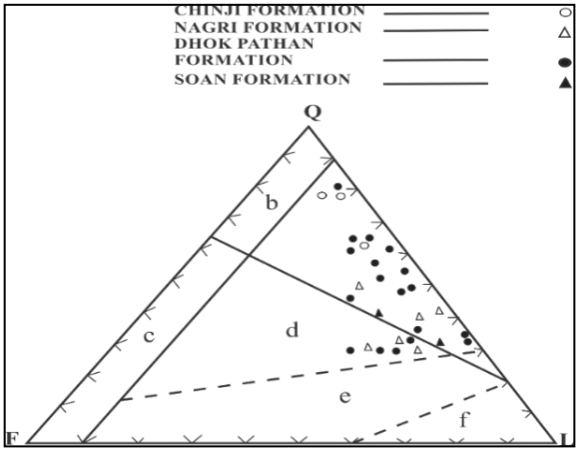

Fig. 5 QFL provenance discrimination diagram (Dickinson *et al.,* 1983) of the Siwalik Group. The fields are: (a) Recycled orogen, (b) Transitional continent, (c) Basement Uplift, (d) Dissected arc, (e) Transitional arc, (f) Undissected arc

Table 2. Modal percentage composition of sandstone of Chinji Formation

	Qm	Qp	Pl	Mc	L	Mus	Bt	Tm	C.M.	Ep	Gt	O.M	Class	Prov
$Kp_{11\text{-}b}$	30	06	4	2	20	02	3	1	05	2	--	10	Litharenite	R.O
Kp_{12}	30	10	4	2	12	02	7	4	-	3	1	15	L.Sub arkose	R.O
Kp_{13}	35	10	6	2	12	02	5	2	03	2	--	10	Sub-arkose	R.O

Abbreviations: Qm = Monocrystalline quartz, Qp = Polycrystalline quartz, Pl = Plagioclase, Mc = Microcline, L = Lithic Fragments, Ca = Calcite, Mus. = Muscovite, Bt = Biotite, Tm = Tourmaline, C.M =Clay minerals, Ep = Epidote, Gt = Garnet, O.M= Ore Minerals, Prov.= Provenance, R. O=Recycled orogen, D. A= Dissected arc

4.1.2 Lithic Sub arkose

Sample no. Kp_{12} is acknowledged as lithic subarkose in QFL diagram (Figure 4). The sandstone of this facie is coarse grained, brownish, grayish and soft. Concavo-convex contacts are observed between the quartz grains of mono and polycrystalline nature. Overall sub-angular to sub-rounded grains are seen with undulatory quartz. Feldspar flakes are mostly plagioclase nature with microcline. Lithic grains are received from metamorphic, igneous and sedimentary rocks. Tourmaline displays pleochroism out of pink-light green (Figure 6-a). A detrital matrix present in the lithic subarkose consists of calcite. According to QFL diagram the provenance is recycled orogen (Figure 5).

4.1.3 Subarkose

Sample no. Kp_{13} of lower Chinji Formation realized as subarkose (Figure 4). This is brownish, soft and coarse-grained sandstone. Texturally, this type of sandstone is well-sorted having a grain-supported fabric. Presence of monocrystalline along with polycrystalline quartz grains with sutured contacts depicted the presence of compaction. Plagioclase and microcline are present in fewer amounts. Lithic fragments found to be received out from igneous, sedimentary and metamorphic rocks. Deformed flakes of mica are also present consisting of stable muscovite and unstable biotite (Figure 6-b). Minor heavy minerals are also present in subarkose including tourmaline (2%) and epidote (4%). Calcite cement is dominant, whereas ferruginous and silica cements are also present in subarkose. According to QFL diagram, the provenance is recycled orogen (Figure 5). Diagenetic process such as cementation, replacement, mechanical compaction and authigenic overgrowth of quartz are common in this facie.

4.2 Nagri Formation

Six rock samples for petrographic studies were taken from the Nagri Formation's base to top. On the basis of petrography Nagri Formation are classified into two microfacies.

4.2.1 Feldspathic Lith arenite

Five samples (Kp_6, Kp_7, Kp_8, Kp_9 and $Kp_{11\text{-}a}$) are recognized as feldspathic Lith arenite (Figure 4; Table 3). This facie is comprised of grey sandstone interbedded with red clays. Quartz grains are found to be monocrystalline with subordinate polycrystalline quartz. Undulose quartz grains also occur in the rock. Feldspar includes plagioclase and microcline. The feldspar alters into sericite and clay minerals. Lithic fragments include quartz mica schists along with phyllite and slates. Clasts belongs to sedimentary rocks are of sandstone, shale, and older limestones. The flakes of micas are randomly oriented throughout the rocks (Figure 6-c, d). The cementing material is dominantly calcium carbonate. Calcite cement comprising microcrystalline aggregates and mosaic of anhedral sub hedral crystals. According to QFL diagram provenance of the two samples is recycled orogen. Three sample falls in dissected arc (Figure 5)

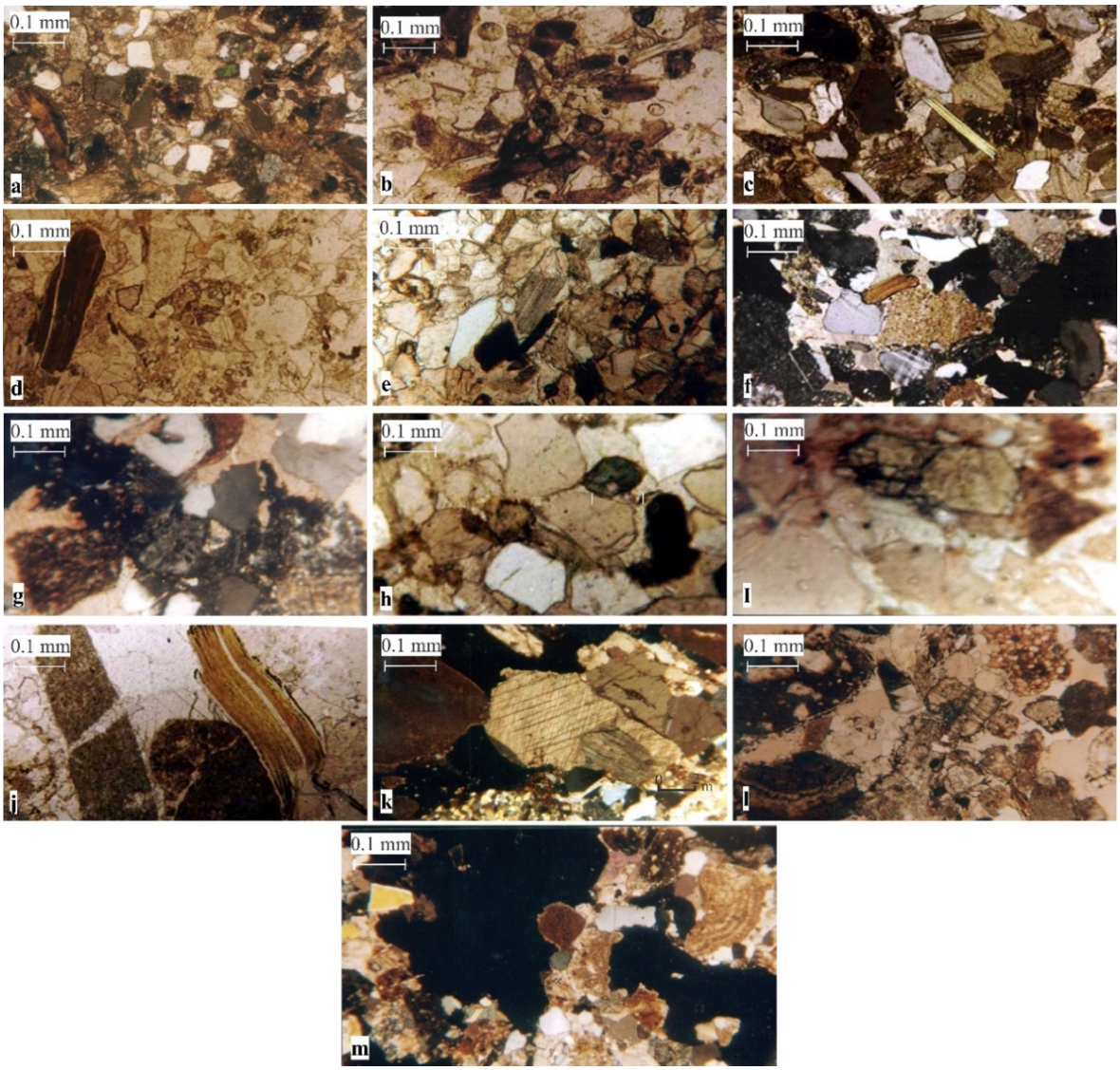

Fig. 6. Photomicrographs of sandstones of Siwalik Group (a) Lithic subarkose facie of Chinji Formation (Kp_{12}) showing green tourmaline in upper right portion, biotite flakes in lower left portion, and growth of calcite crystal between the pore spaces (Cross Nicol. x8). (b) Sub arkose facie of Chinji Formation (Kp_{13}) showing flakes of biotite at lower central portion, tourmaline grain at upper right and light brown garnet at central right portion (PPL. x8). (c) Feldspathic litharenite facie of Nagri Formation (Kp_8) showing plagioclase at upper central portion and muscovite in central portion (Cross Nicol. x8). (d) Feldspathic litharenite facie of Nagri Formation (Kp_7) showing large flake of biotite at left portion and green tourmaline in central right portion (PPL. x8). (e) Litharenite facie of Nagri Formation (Kp_{10}) showing well-developed cleavage in calcite crystal in the central portion (PPl. x10). (f) Feldspathic litharenite facie of Dhok Pathan Formation (Hc_6) showing microcline at lower central portion, shale fragment at center and biotite at upper right portion (Cross Nicol. x4). (g) Feldspathic litharenite facie of Dhok Pathan Formation (Dk_2) showing sutured contacts of quartz grains and development of embayment in quartz grain at upper central portion (Cross Nicol. x10). (h) Feldspathic litharenite facie of Dhok Pathan Formation (Dk_8) showing green, sub rounded tourmaline

at upper right portion, light brown garnet at center and quartz overgrowth at center left portion (PPL. x10). (i) Feldspathic litharenite facie of Dhok Pathan Formation (Hc_2) showing large, fractured light green tourmaline grain (PPl. x10). (j) Litharenite facie of Dhok Pathan Formation (Hc_5) showing large deformed biotite at right portion and fine-grained volcanic lithics (PPL. x10). (k) Litharenite Facie of Dhok Pathan Formation (Hc_4) showing crystals of calcite at central part and polycrystalline quartz at lower left portion (Cross Nicol. x2.5). (l) Litharenite facie of Soan Formation (GD_2) showing bioclasts at lower left portion and central portion and fragment of sandstone at upper right portion (PPL. x2.5). (m) Litharenite facie of Soan Formation (Dt_4) showing bioclasts at upper right portion and lithics of shale at the central portion (PPL. x2.5).

.

Table 3. Modal percentage composition of sandstone of Nagri Formation.

	Qm	Qp	Pl	Mc	L	Ca	Mus	Bt	Tm	Ep	Gt	O.M	Class	Prov
Kp_6	22	07	10	04	24	15	05	05	01	02	1	08		D.A
Kp_7	19	05	05	04	35	12	04	04	02	02	1	07		D.A
Kp_8	19	06	08	03	30	15	05	03	01	03	1	06	Feldspathic Lith arenite	D.A
Kp_9	22	08	07	03	20	15	05	05	02	03	1	10		R. O
Kp_{10}	20	08	02	03	25	13	04	07	03	03	1	12		R. O
$Kp_{11\text{-}a}$	22	08	07	04	15	20	04	02	03	03	1	12	Lith arenite	R. O

4.2.2 Lith arenite

According to QFL diagram, one rock sample (Kp_{10}) is recognized as Lith arenite (Figure 4). The sandstone is grey to greenish grey, coarse grained, hard and calcareous. Lithic grains consist of resistant sedimentary, metamorphic and igneous rocks. Quartz grains are common and display wavy extinction. Feldspar grains present in minute amount (5%). Detrital micas (2-9%), along with muscovite is much more common. A suite of heavy minerals present comprising epidote, tourmaline and garnet. Calcite occurs as pore filling cement and form microcrystalline mosaic, cavity filling textures and also forming poikilotopic texture in which big crystals are interlocked irregularly (Figure 6-e). According to QFL diagram the provenance is recycled orogen (Figure 5). Calcite cementation took place before the main phase of silica cement, thus preventing the quartz overgrowth as nearly all pores were already occupied. The other diagenetic process is the compaction indicated by sutured contacts of quartz grains due to deep burial process called pressure solution.

4.3 Dhok Pathan Formation

Dhok Pathan Formation consists of cyclic deposits of clay and sandstone and forms the multi sandstone story (Figure 7). Sandstone is greyish, green, medium bedded, coarse grained and characterized by calcareous concretions. The clasts of igneous and volcanic rocks of variable sizes are embedded occasionally. Fifteen samples are classified into three microfacies.

Fig. 7. Multi sandstone story and clays of Dhok Pathan Formation near Kauliar, Potwar sub basin.

4.3.1 Feldspathic Litharenite

Nine samples (Bc_3, Hc_2, Dk_1, Dk_2, Dk_5, Dk_7, Dk_8, Dp_5 and Hc_6) are recognized as feldspathic litharenite (Figure 4; **Table 4**). This facie consists of sub-angular to sub rounded grains and grain size varies from fine to medium grained (Figure 6-f). Quartz grains are monocrystalline with subordinate polycrystalline. At few places authigenic over growth of silica around quartz grains have been observed. Some contacts of quartz grains are sutured (Figure 6-g). Feldspar grains are sub angular and include plagioclase and microcline. Lithic fragments are received from igneous, metamorphic and sedimentary rocks. Muscovite and biotite occur as small flakes. Minor clay minerals occur in the matrix but these are extremely fine grained. Some accessory minerals like tourmaline, epidote, rutile and garnet (Figure 6-h) are also present. Tourmaline found as light green showing moderately pleochroism from brownish green to dark brown (Figure 6-i). Garnet grains present rarely and these are sub angular to sub rounded. Epidote occurs as anhedral to subhedral grains showing various colors. The calcite is very important constituent of cement. According to QFL diagram, the provenance of seven rock samples is recycled orogen and two rock samples fall in dissected arc (Figure 5).

4.3.2 Lith arenite

According to QFL diagram five rock samples are recognized as Lith arenite (Figure 4). The sandstone is grey to greenish grey, coarse grained, hard and calcareous. This facie consists of lithics of low-grade metamorphic rocks and sedimentary rocks. Some carbonate lithics contain bioclasts are also present in rock samples. Feldspar grains present in relatively small amount.

Table 4. Modal percentage composition of sandstone of Dhok Pathan Formation.

	Qm	Qp	Pl	Mc	L	Ca	Mu	Bt	Tm	Hb	Ep	Gt	O.M	Class	Prov
BC_3	15	10	05	03	35	15	03	01	01	--	01	01	03		D.A
Hc_2	20	10	05	02	30	15	02	02	01	01	01	01	07		R.O
Dk_1	15	07	07	03	30	20	03	03	01	01	02	01	08		D.A
Dk_2	20	10	05	03	25	25	01	02	01	01	01	01	05		R.O
Dk_5	25	07	07	03	20	20	05	03	01	--	01	01	07	Feldspathic Litharenite	R.O
Dk_7	15	07	05	03	25	20	07	05	01	01	01	01	09		D.A
Dk_8	25	10	06	02	20	20	03	03	01	--	02	01	07		R.O
Dp_5	15	07	05	03	15	32	03	04	01	--	01	01	12		R.O
Hc_6	30	10	05	04	25	10	03	04	01	--	01	01	06		R.O
Bc_{1-a}	20	07	03	02	25	20	03	02	01	01	01	01	12		R.O
Dp_{16}	35	07	03	03	15	10	05	05	01	--	01	01	12	Lith arenite	R.O
Dp_{17}	25	10	03	02	15	20	06	05	02	01	02	01	10		R.O
Hc_4	10	10	05	01	45	10	02	01	--	--	01	--	10		D.A
Dp_7	30	10	05	03	10	20	02	08	02	--	01	01	06	Lithic sub-arkose	R.O

Detrital flakes of biotite and muscovite are frequent, which may possibly derive from metamorphic source (Figure 6-j). Some heavy minerals also increase in litharenite including tourmaline, garnet, epidote and hornblende. Calcite occurs as pore filling cement. Calcite crystals form microcrystalline mosaic or cavity filling poikilotopic texture (Figure 6-k). According to QFL diagram, the provenance of four rock samples is recycled orogen, while one rock sample fall in dissected arc (Figure 5).

4.3.3 Lithic Sub arkose

One sample (Dp_7) is recognized as lithic sub arkose in accordance with QFL diagram (Figure 4). The sandstone of this facie is brownish and soft. Both mono and poly-crystalline quartz grains are found having concavo-convex contacts. Grains shapes are found as sub-angular to sub-rounded. Feldspar grains are dominantly plagioclase and microcline with perthite texture. Lithic fragments are received from metamorphic, sedimentary and igneous rocks. Deformed flakes of biotite and muscovite are present. Minor heavy minerals are also present including tourmaline, garnet, hornblende and epidote. Cement consists of calcite. According to QFL diagram, the provenance is recycled orogen (Figure 5). The first diagenetic process is authigenic quartz overgrowth. The second common pore filling materials are calcite and clay minerals occur in patches and took place before the main phase of silica cement. The third diagenetic process is closer packing of grains due to mechanical compaction. Albitization of K-feldspar and calcic plagioclase is also observed in some rock samples.

4.4 Soan Formation

This formation consists of compact, very large sized conglomerate bodies with subordinate interbeds of sandstone, siltstone and clay. The conglomerate consists of pebbles and boulders of different sizes. The formation contains pebbles and boulders of quartzite, granite, metamorphic, volcanic, limestone and sandstone ranging in size from 2 to 10 cm in diameter. Two samples were taken from the Soan Formation and classified into one microfacie ((Figure 4).

4.4.1 Litharenite

According to QFL diagram two samples are recognized as litharenite (Figure 4). The sandstone is light grey and grayish to reddish. These are coarse grained, poorly sorted, sub angular, conglomeratic sandstones **(**Table 5**)**. Litharenite contains about 45% or more lithic grains exceeding feldspar and quartz grains including all types of resistant sedimentary, metamorphic, igneous and volcanic rocks. The sedimentary lithics were derived from sandstone, clay stones, mudstone, shale, chert and carbonates (Figure 6-l). Feldspar present in relatively small amount (8%). Some Eocene bioclasts are also present (Figure 6-m). The most common cement is calcite. Some crystals of calcite are present as detrital grains with clear boundaries and not act as cement. Litharenite is immature sandstones and reflect provenance in the most effective manner because lithics carry by themselves the obvious proofs of their origin. Modal data indicate a provenance of recycled orogen (Figure 5).

Table 5. Modal percentage composition of sandstone of Soan Formation

S. No.	Qm	Qp	Pl	Mc	L	Ca	Mu	Bt	Tm	CM	Bio-clasts	O.M	Class	Prov
DT_4	15	12	02	03	30	10	02	02	01	05	01	10	Lith-	R.O
GD_2	20	10	02	04	35	10	01	02	01	04	01	07	arenite	R.O

5. Heavy minerals in sandstone of Siwalik Group

Heavy minerals include many kinds of opaque and non-opaque or transparent minerals. According to Abbasi and Khan (1990) the common heavy minerals in the sediments of the Siwalik Group are epidote, garnet, tourmaline, zircon, mica, amphibole, kyanite and staurolite.

5.1 Opaque Minerals

In almost all the samples, the opaque minerals comprise the major bulk of the heavy concentrate. This group consists of hematite, ilmenite, magnetite and few pyrite. Ilmenite has a steal grey, sub-metallic lusture, magnetite has a silver gray lusture, hematite possesses a reddish brown and pyrite shows a brass yellow color under reflected light. The percentage of total opaque minerals range from 47-54% **(**Table 6**)**.

5.2 Tourmaline

Grains of tourmaline are irregular prismatic and strongly pleochroic. Inclusion and zoning are also present, and it varies from 8-11% (Figure 6-a, d, h, i).

5.3 Epidote

Epidote occurs as anhedral to subhedral grain and show typical green color with marked pleochroism to greenish yellow color. It varies from 9-14%.

5.4 Garnet

It is most predominant in all the samples and is mostly pink or colorless. Grains are irregular and sub angular, but some rounded grains are also observed. Percentage of garnet grains varies from 2-8% (Figure 6-h).

Table 6. Heavy mineral percentage in sandstone of Siwalik Group

Sr. No.	Formation	Epidote%	Garnet %	Biotite %	Tourmaline%	Hornblende%	Opaque %	Chlorite%
1	CHINJI	11	02	23	10	--	54	Traces
2	NAGRI	14	06	23	10	Traces	47	Traces
3	DHOK PATHAN	09	08	24	08	03	48	Traces
4	SOAN	10	05	21	11	--	53	--

5.5 Hornblende

Grains of hornblende are flat, prismatic and irregular in shapes. Color of the grains is green, bluish green to olive green. It varies from traces to 3%.

6. Provenance of Siwalik Group

According to Hubbard *et al.,* (2021) the continental collision process has made a large contribution to continental growth and reconfiguration of craton basin throughout Earth history. The molasse of the study area has direct relationship with uplifting sequences. According to Critelli & Garzanti (1994) during Miocene, when highly metamorphosed rocks of the Himalaya were carried southward, the mountain range began to rise to dramatic heights, and huge amounts of detritus started to feed the Siwalik foreland basin of Indus and Bengal Fans. The field investigations and petrographic evaluations of the sandstone also reflected that the detritus was eroded away from uprising Himalayan and were finally unlade in the Indus depression. These provenance studies are also supplemented with the evaluation of heavy minerals.

6.1 Provenance of Chinji Formation

The Chinji Formation is found as litharenite, lithic subarkose and subarkose and these are derived from the recycled orogen. Some quartz grains are polycrystalline and some show undulatory extinction. According to Mughal *et al.,* (2018) the polycrystalline quartz and undulatory quartz grains were derived from the felsic plutonic igneous rocks (granite), high grade metamorphic rocks and older sandstone provenances. The microcline and albite indicates that the granitic and gneissic rocks were exposed at the time of the deposition of sediments. The lithics are of metamorphic and sedimentary origin. The metamorphic clasts are of slates, phyllite, schist and gneisses. Kamran *et al*., (2011) shows that during the deposition of the Kamlial Formation (below the Chinji Formation), the more metamorphic and plutonic rocks eroded during the uplift of the Himalayan orogenic belt. Similarly, the presence of rock fragments and microfacies suggest that the sediments of Chinji Formation were also derived from the metamorphic and plutonic origin of northern margin of Indian Plate.

6.2 Provenance of Nagri Formation

The Nagri Formation is characterized as feldspathic litharenite and litharenite. These microfacies are derived from recycled orogen and dissected arc. The feldspar increases with respect to the underlying formation, which indicates that the igneous rocks were uplifted and eroded at this time. The sedimentary lithics dominate the metamorphic and igneous lithics. The garnet grains are also present in Nagri Formation and according to Abbasi & Khan, (1990) the major source of garnet in molasse sediments is interpreted as the metamorphic belts of the Indian plate exposed along its northern margin. The lenses of conglomerates consisting of igneous, metamorphic and sedimentary rock fragments. Thus it can be concluded that the abundance of garnet, increase of volcanic lithics and volcanic conglomerates of basalt and andesite show that the Kohistan magmatic arc was uplifted and eroded during the deposition of Nagri Formation.

6.3 Provenance of Dhok Pathan Formation

The sandstone is mainly feldspathic litharenite to litharenite and lithic subarkose. These microfacies were derived from recycled orogen and dissected arc. The feldspar increases throughout the formation. More abundant plagioclase in sandstones indicates it was derived from volcanic rocks (Boggs, 2006). Phenocrysts of microcline, perthite and quartz are also present. The metamorphic rock fragments include quartz mica schist and garnet mica schist. Igneous rock fragments are granite and granite gneiss and fine-grained volcanics. These lithics show that the uplift and erosion of Kohistan Island arc and northern margin of the Indian Plate was continued during the deposition of this formation. The garnet grains are also present and these are derived from medium to high-grade metamorphic and plutonic rocks of the Indian Plate including Tanol Formation and Besham Basement rocks. Blue green amphiboles first appear in this formation. The presence of green and brown hornblende indicates that Kamila amphibolites of Kohistan Island arc were exposed at the time of deposition of Dhok Pathan Formation. During the field investigations the conglomerates of andesite, rhyolite, diorite, phyllite, slates, schists and quartzite are found. The sedimentary particles are of Sakesar and Margalla Hill Limestones showing their derivation from rocks exposed along MBT. The conglomerates also strengthen the fact that northern margin of the Indian Plate, Kohistan Island arc and probably mélanges zones were provenance for this formation. Volcanic rocks are also exposed in southeastern Kohistan like Alai and Babusar area. Kohistan Island arc at this time was not only uplifted but was sufficiently unroofed to provide plutonic detritus. The presence of porphyritic granite clasts in the Dhok Pathan Formation suggests the uplifting and unroofing of the Mansehra Granite. The provenance study of Dhok Pathan Formation suggests that detrital material derived from the plutonic, volcanic, metamorphic and sedimentary rocks of uplifting Himalayan collision belt in the north.

6.4 Provenance of Soan Formation

The Soan Formation is mainly consisting of Lith arenite facie. The lithic fragments of limestone of Lockhart, Sakesar, Margalla and Chorgali Formations are also present. This suggests that uplift of

Kala Chitta Range along MBT and Khairi Murat Range was responsible for providing detritus of the rocks exposed due to faulting. This evidence is supported by the presence of bioclasts derived from Eocene rocks present in Soan Formation. Similarly, the clasts of intrabasinal conglomerates and higher proportion of sandstone rock fragments suggest that rocks of Siwalik Group were also involved during the deposition of Soan Formation due to uplifting of nearby ranges.

7. Modal composition of sandstone and their implications for tectonics

Petrographic data provide different compositional stages which were recorded in sandstone during the field observation and petrographic studies.

7.1 Stage I: Chinji Formation

The rock fragments and detritus minerals reveal that Indian Plate after collision was continuously pushing the Asian landmass, which resulted ongoing uplifting and erosion of northern margin.

7.2 Stage II: Nagri Formation

Nagri stage shows entrance of volcanic rock fragments. This indicates that volcanic Island arc was eroded and detritus was deposited in this sandstone. The clasts of metamorphic, plutonic rocks and increase in garnet contents suggest that unroofing of the basement sequence in the north was initiated.

7.3 Stage III: Dhok Pathan Formation

The petrographic and field study exhibit that detritus of granitic rocks, high grade metamorphic rocks, volcanics and sedimentary rocks present in this sandstone was derived from the crustal and sub crustal rocks of northern margin of Indian Plate. This suggests that tectonics was active resulting in exposure of deep crustal rocks of the Indian Plate and Kohistan Island arc. Tectonic activity also migrated southward and resulted in deformation, uplifting and thrusting in the northern Potwar region.

7.4 Stage IV: Soan Formation

This formation indicates that in addition to the tectonic activity the northern Potwar basin was locally faulted and folded. The thrust faults were developed due to continued uplifting of the Himalayan fold-and-thrust belt and southward progradation of tectonics. These thrust faults cut and exposed the Tertiary sequence onto the surface. The rock fragments of these sequences provide further evidence that thrust tectonics was initiated and propagated towards Potwar sub-basin. The major thrusting and faulting events at the time of deposition are MBT and Khairi Murat Fault. These faults exposed Eocene carbonates above molasse deposits.

8. Conclusion

The study area is a zone of the active foreland fold-and-thrust belt related to the Himalayas. In this zone carbonate deposition was stopped at the end of Early Eocene time due to the increase of orogenic uplift. As a result of this tectonic activity a major unconformity was formed on the top of the Eocene

carbonate and clastic sediments of Kuldana Formation. The molasse sediments of Rawalpindi and Siwalik Groups deposited during Miocene to Pleistocene time. Petrographic evaluation related to the Siwalik Group displays variegated types of microfacies comprising feldspathic litharenite, litharenite as well as sub arkose. Study of provenance depicted dissected arc along with recycled orogeny, deducted that the material was received from the metamorphic, volcanic, plutonic and sedimentary sources present to the northern edge of Indian Plate, Kohistan Island arc as well as Karakoram Ranges in northern Pakistan. Northern Indian Plate's edge displays a detailed sequence of low-grade metamorphic to eclogite facies. Heavy mineral assemblage contains opaque minerals, garnet, tourmaline, rutile, epidote and hornblende. These typical minerals also showed that the sediments of these deposits came from the northern edges of Indian Plate. Petrographic analysis depicted that Siwalik suit were unlading in a subsiding foreland basin along the foothill under the environment of fast erosion leading to quick deposition. These deposits indicate inverted stratigraphy of the northern margin of the Indian plate showing the older metamorphic rocks of Kohistan Island Arc and Karakoram Range in younger Dhok Pathan and Soan Formations. Siwalik deposits also indicating the fluviatile environment of deposition which is the product of the Himalayan orogeny. During the deposition of Siwalik Group, the tendency of sediment deposition was north to south along perfect fluvial system. As a result, the Siwalik succession's thickness rises from north to south over the Potwar Sub basin.

ACKNOWLEDGMENTS

We are very thankful to the Director of Institute of Geology, UAJK, Muzaffarabad for his facilitation during this research work.

References

Abbasi I. A, Khan M. A, (1990) Heavy mineral analysis of molasse sediments, Trans Indus Ranges, Kohat, Pakistan. Geol Bull Univ Peshawar 23: 215-229.

Bilal A, & Khan M. S, (2017) Petrography and provenance of Sandstone and studies of shale of Kuldana Formation, Kalamula and Khursheedabad area, Kahuta, Azad Kashmir. Ear. Sci. Malay. 1: 21–31.

Boggs Jr, (2006) Principles of Sedimentology and Stratigraphy, fourth ed. University of Oregon, Pearson Education, New Jersey, Pp. 662.

Chaudhri R. S, (1972) Petrogenesis of Siwalik sediments of the northwestern Himalayas. Bull Indian Geol Soc India 13: 399-402.

Critelli, S. & Garzanti, E. (1994) Provenance of the Lower Tertiary Murree red beds (Hazara-Kashmir Syntaxis, Pakistan) and initial rising of Himalayas. Sedimentary Geology 89: 265-284.

Drewes, H. D, (1995) Tectonics of the Potwar Plateau region and the development of syntaxes, Punjab, Pakistan. Bull 2126 https://doi.org/10.3133/b2126

Dickinson W. R, Beard L. S, Brackenridge G. R, Exjavec J. L, & Ferguson R. C, (1983) Provenance of North American Phanerozoic Sandstones in Relation to Tectonic Setting. Geol Soc Amer Bull (94): 222-235.

Farooqui, M. A, Rehman, K. U, Yaseen, A, Roohi, G, & Umar, M., (2022) Petrography, geochemistry and depositional model of Ispikan Conglomerate, Makran Accretionary Prism, Southwest Pakistan. Kuwait J. Sci., Vol.49, No. (1), 1-25.

Goswami P. K. and Deopa, T. (2018) Petrotectonic setting of the provenance of Lower Siwalik sandstones of Himalayan foreland basin, southeastern Kumaun Himalaya, India. Wiley Island Arc Res Art pp 1-12.

Hubbard M, Mukul M, Gajurel A. P, Ghosh A, Srivastava V, (2021) Orogenic Segmentation and Its Role in Himalayan Mountain Building. Front. Earth Sci., 23 April 2021 | https://doi.org/10.3389/feart.2021.641666.

Jaswal, T. M., 1990. Structure and evolution of Dhurnal oil field, Northern Potwar Deformed Zone, Pakistan. Unpub. M. S. Thesis Oregon State University Corvalis, US.

Jaume, S. C., and Lillie, R. J., (1988) Mechanics of the Salt Range Potwar Plateau, Pakistan. A fold-and-thrust belt underlying by evaporites. Tectonics. V. 7: 57-71.

Johnson, G. D., Johnson, N. M., Opdyike, N. M., TahirKheli R. A. K., (1979) Magnetic reversal stratigraphy and sedimentary tectonic history of the upper Siwalik Group, Eastern Salt Range. In: Farah, A. and Dejong, K. A. (eds.), Geodynamics of Pakistan, Geol. Surv. Pakistan, 149-165.

Kamran S. M, Khan M. S, Siddiqi, M. I., (2011) Petrography of Sandstone of Molasse Deposits (Rawalpindi Group) and their tectonic setting from Khairi-Murat Area, Potwar Sub-basin, Pakistan. Pakistan Jour. Hydrocarbon Res. Vol. 20, (June 2010), 15-25.

Kazmi, A. H. & Jan, M. Q, (1997). Geology and Tectonics of Pakistan, Graphic Publisher, 554p.

Khan M. A, Ahmed R, Raza H. A, Kamal A, (1986) Geology of petroleum of Kohat-Potwar depression, Pakistan. Amer Assoc Petrol Geol Bull 70: 369-414.

Lillie, R. J., Johnson, G. D., Yousuf, M., Zaman, A. S. H., and Yeats, R. S., (1987). Structural development within the Himalayan Foreland fold-and-thrust belt of Pakistan. Canada Soc. Petrol. Geol., Mem. 12: 379-392.

McBride E. F, (1963) A Classification of Common Sandstones. Jour Sed Petrol 33: 664-669.

Mughal S. M, Zhang C, Du D, Zhang L, Mustafa S, & Hameed F. (2018) Petrography and provenance of the Early Miocene Murree Formation, Himalayan Foreland Basin, Muzaffarabad, Pakistan. Jour Asia Earth Sci doi: https://doi.org/10.1016/ j. jseaes.2018.04.018.

Riaz M, Nuno P, Zafar T, Ghazi, S, (2019) 2D Seismic Interpretation of the Meyal Area, Northern Potwar Deform Zone, Potwar Basin, Pakistan. Open Geosciences 11; 1-16. https://doi.org/10.1515/geo-2019-0001

Shah S. M. I, (2009) Stratigraphy of Pakistan. Geol Surv Pakistan Mem 22: Pp 400.

Sigdel A, & Sakai T, (2013) Petrography of Miocene Siwalik Group sandstones, Karnali River section, Nepal Himalaya: Implications for source lithology and tectonic setting. Jour Nepal Geol So 46: 95-110.

Yeats, R. S., Khan, S. H. and Akhtar, M., (1984) Late Quaternary deformation on the Salt Range of Pakistan. Geol. Soc. Amer. Bull. V. 95: 958-966.

Submitted: 06/12/2021
Revised: 21/02/2022
Accepted: 08/03/2022
DOI: 10.48129/kjs.17577

Prediction of petrophysical properties through comparative post-stack inversion techniques using advance Neural Networking

Pal Washa S. Rathore [1, *], Matloob Hussain[1], Muhammad B. Malik[1], Sher Afgan[2]

[1] *Dept. of Earth Sciences, Quaid-i-Azam University, Islamabad, Pakistan*
[2] *Institute of Geology, University of the Punjab, Lahore 54000, Pakistan*

[*]*Corresponding author: palwashashahzad97@gmail.com*

Abstract

The sophisticated seismic inversion methodology develops the relationship between the interpreted seismic data and the elastic properties to discerning the desired facies in the reservoir characterization. The study is focused on the C-interval sand of the Lower Goru Formation by utilizing Post-stack Time Migration (PSTM) 3D seismic and borehole logs of six wells. The challenges in the facies discrimination arise due to various complexities, i.e., lithological variability and acquisition sensitivity of recording tools. Various quantitative interpretation techniques such as Band limited inversion, Model-Based inversion, and Stochastic inversion are developed to handle the limitations effectively and precisely access the producing facies. A comparative analysis is performed for the heterogeneous sands by employing these QI techniques and evaluating their effectiveness. The inverted seismic attributes are further utilized in the petrophysical properties estimation through Probabilistic Neural Networking (PNN) algorithm to distinguish litho-facies by developing a petro-elastic relationship. Probabilistic Neural Networking works best for the heterogeneous reservoir's petrophysical properties estimation, especially sand reservoirs with shales intercalation. The concluding results declare the efficiency of all applied techniques for potential sand zones, especially the Stochastic inversion. The petrophysical properties volume of clay and effective porosity, estimated from the Stochastic inversion attribute, matched with the results of the blind well, resolute precisely the reservoir potential, and delineated the depositional environment of the three segregated sand bodies.

Keywords: Band limited inversion; Geo-statistical methods; Model-Based inversion; Probability Neural Networking; Stochastic inversion.

1. Introduction

The increase in energy demand of the world has increased the need to adopt sophisticated computational techniques to explore and produce hydrocarbons (Ehsan *et al*., 2018). The pre-and post-stack inversion of seismic data is now considered an essential tool of the modern exploration industry used for field development (Moosavi & Mokhtari, 2016; Abdulkareem, 2022). The interpretation and reliability of the inverted seismic data allow the scientists to develop the pre-

stacked and post stacked seismic inversion techniques. This technique increases the data reliability and reduces the risks of exploring hydrocarbons, as mapping gas-bearing sand facies using conventional techniques is challenging (Osita *et al*., 2022; Shahzad *et al*., 2022). So, this combination of seismic and well log interpretation is essential to discriminate the gas and wet sand facies quantitatively (Al-Sulaimi & Al-Rawaih, 2004). The inversion technique helps generate the reservoir rock's elastic properties that indicate the hydrocarbon zones (Adesanya *et al*., 2021). For this research work, the post stacked seismic and well log data are acquired from a hydrocarbon field located in the Middle Indus Basin, Pakistan. The geological map of the study area is shown in (Figure 1). The post-stack inversion is a stable technique usually used for the model building based on the estimated impedance of the subsurface horizons. This enables the explorations to monitor the reservoir properties during the production phase of the field and aids in decision making (Pyrcz *et al*., 2014). Petrophysical properties derived from the Neural Networking technique play a significant role in determining the areas between the wells and away from the wells having good reservoir properties (Razak, 2010; Rijks & Jauffred, 1991). The present work performs the Band-limited inversion, Model-Based inversion, and Stochastic inversion. These three inversion techniques were performed and comparatively analyzed in terms of accuracy to interpret the best-suited inversion technique. The probabilistic neural networks are a technique that can be used to efficiently identify shale layers as C-interval sands of Lower Formation consist of alternating layers of sand and shale, reducing the risk associated with exploration and production in shaly reservoirs. This method will improve the strategy adopted for exploring and developing hydrocarbon fields.

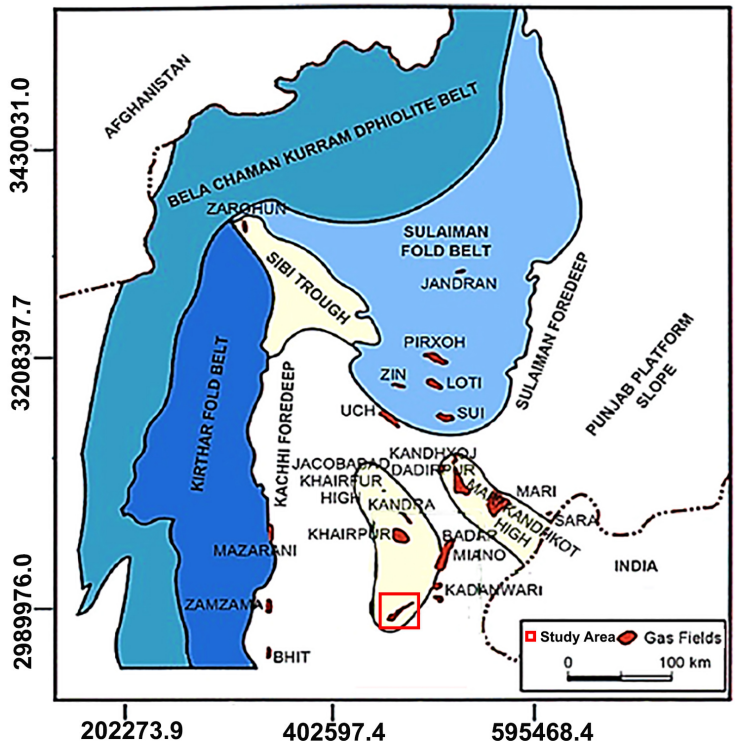

Fig. 1. Geological Map of Middle Indus Basin with highlighted Study area, Pakistan.

2. Geological Settings

The study area lies in the Middle Indus basin of Pakistan, which is a prolific hydrocarbon-bearing basin of Pakistan (Asghar, 2021; Miraj *et al*., 2021). The study area is situated in the Sukkur Rift zone along the southeastern margin of Jacobabad-Khairpur High (Zaigham & Mallick, 2000; Kadri, 1995; Kazmi & Jan, 1997; Ahmed *et al*., 2004). The geological setting of the area reveals that the Punjab Platform occupies the northeastern side. On the northern and northwestern sides, the Sulaiman Fold Belt is present. At the west of the study area, Kirthar Fold Belt is present (Miraj *et al*., 2021). Rajasthan Shelf and Indian Shield are present on the eastern side of the study area (Kadri, 1995). The prolific reservoir of this region belongs to the Cretaceous age (Afzal *et al*., 2009). The structural traps in this area were developed during the uplifting of Jacobabad Khairpur high during the Cretaceous (Quadri & Shuaib, 1986). The uplifting of the Ranikot Formation resulted in the pinch-out against the Jacobabad-Khairpur high (Kazmi & Jan, 1997).
The complete Cretaceous section of the study area is cut by a deep-rooted wrench faulting system developed due to the collision of the Indian and Eurasian plates (Burg *et al*., 2005). The hydrocarbon migration and trapping occurred during the Mesozoic and Tertiary during the crustal thrusting (Kazmi & Jan, 1997). Sembar Formation is acting as a proven source of rock in the area. The lithology of the Sembar Formation mainly consists of black shale (Khalid *et al*., 2014). C-interval sands of the Lower Goru Formation act as reservoir rock in this area. The lithology of the Lower Goru Formation comprises alternating layers of sand and shale, which depicts the deltaic environment of deposition (Berger *et al*., 2009).

3. Data and Methodology

The data for the present research has been acquired from DGPC. Data include 3D seismic volume (in SEG-Y format) survey data spanning an area of roughly 15 km^2, and well logs data from six wells lying in the vicinity were used. In this work, a variety of wireline logs were employed and interpreted. After that, post-stack inversion was done. Post-stack inversion approaches are the numerous techniques used to turn stacked seismic data into quantifiable rock physics characteristics. From post-stack inversion results only, acoustic impedance can be acquired, but Pre-stack inversion may provide acoustic and shear impedance. Some post-stack inversion methods are Band limited inversion, Model-Based inversion, and Stochastic inversion.

The advantage of this inversion is that they may combine multiple geophysical data with seismic data to improve inversion findings (Contreras *et al*., 2006). The combination of log and seismic data is used to improve the vertical resolution. The Stochastic inversion method is an initial model, and it utilizes a random Gaussian prior that encompasses the spectrum. Because input seismic lacks high- and low-frequency bands, the inversion procedure does not limit the frequency components of the original model (Varela *et al*., 2006). The workflow for performing this inversion, as shown in (Figure 3), includes extraction of wavelet, seismic tie, generating low-frequency models, petrophysical and PNN training. The probabilistic Neural Networking (PNN) technique helps manage shale packages within the sand (Khan *et al*., 2021).

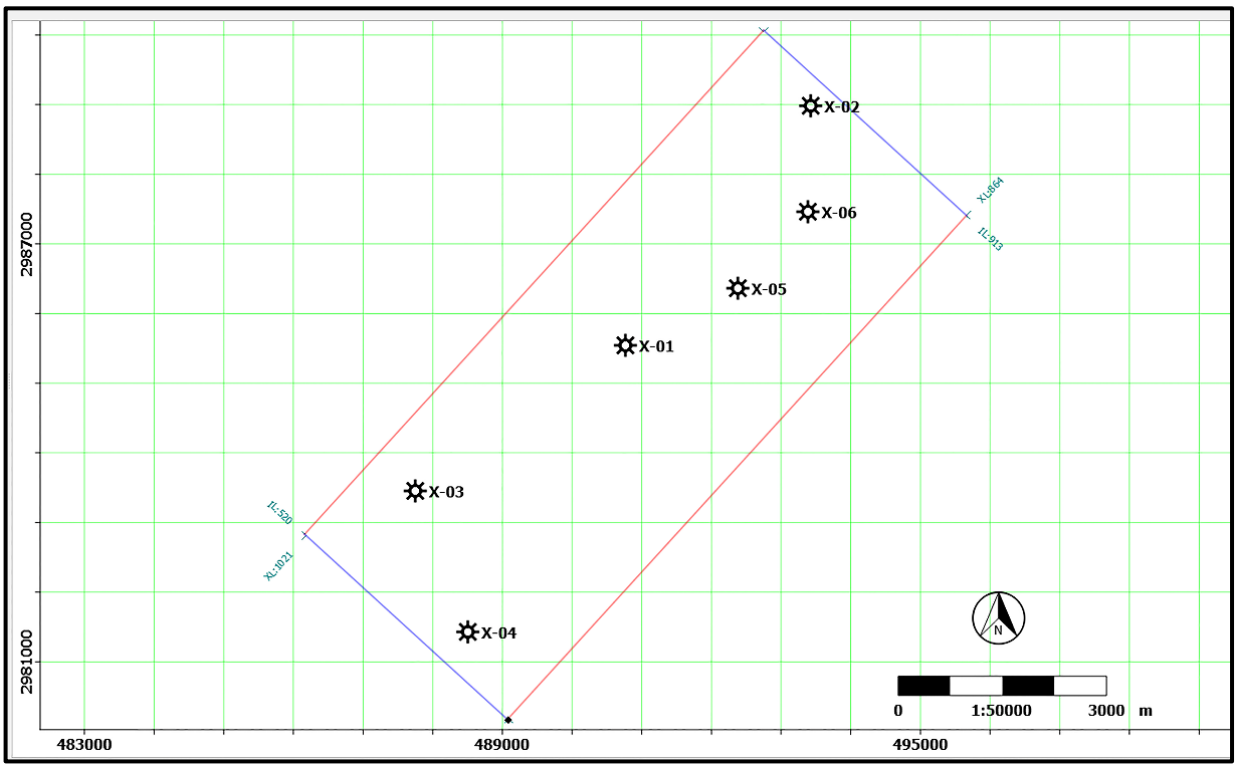

Fig. 2. Base map of the study area including wells (X-01, X-02, X-03, X-04, X-05, and X-06).

3.1 Petrophysical Analysis

The petrophysical analysis of all the wells was performed to obtain the clay volume and effective porosity values. Petrophysical interpretation of C-interval sand of the Lower Goru Formation was carried out in all wells (X-01, X-02, X-03, X-04, X-05 and X-06). The log plot of X-05 is shown in (Figure 4), where the first track is the lithology track displaying SP, Caliper and Gamma-Ray Log. The second track is known as the depth track, and it displays the depth of the well in meters. The third track represents the three resistivity logs: deep resistivity, Moderate resistivity, and shallow resistivity (ResD, ResM and ResS). The fourth track is also known as the porosity track as it displays the porosity logs, including the density log, sonic log, and neutron log. The first four tracks display the input logs, whereas the last four tracks display interpreted logs. The volume of clay is displayed in the sixth track showing the Lower Goru Formation. In the fifth interpretation, average/total porosity has been displayed. The average neutron-density porosities are used for the determination of average porosity. Effective porosity was displayed in the seventh track, calculated from the total porosity. In the last track, the water saturation of the Lower Goru Formation is displayed. Water saturation was calculated using the Indonesian equation.

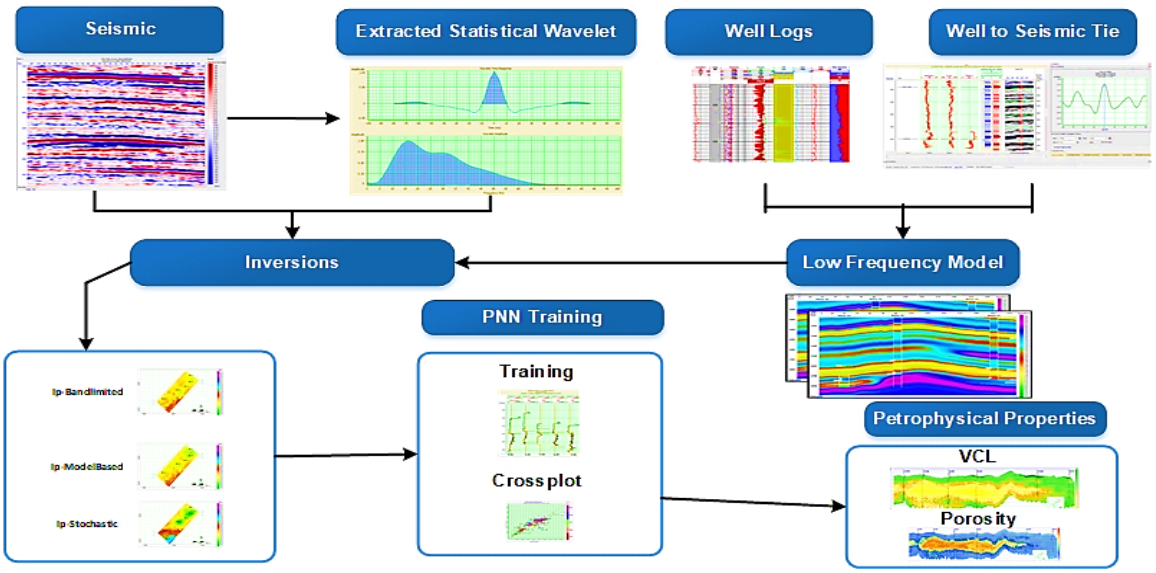

Fig. 3. Workflow for the study.

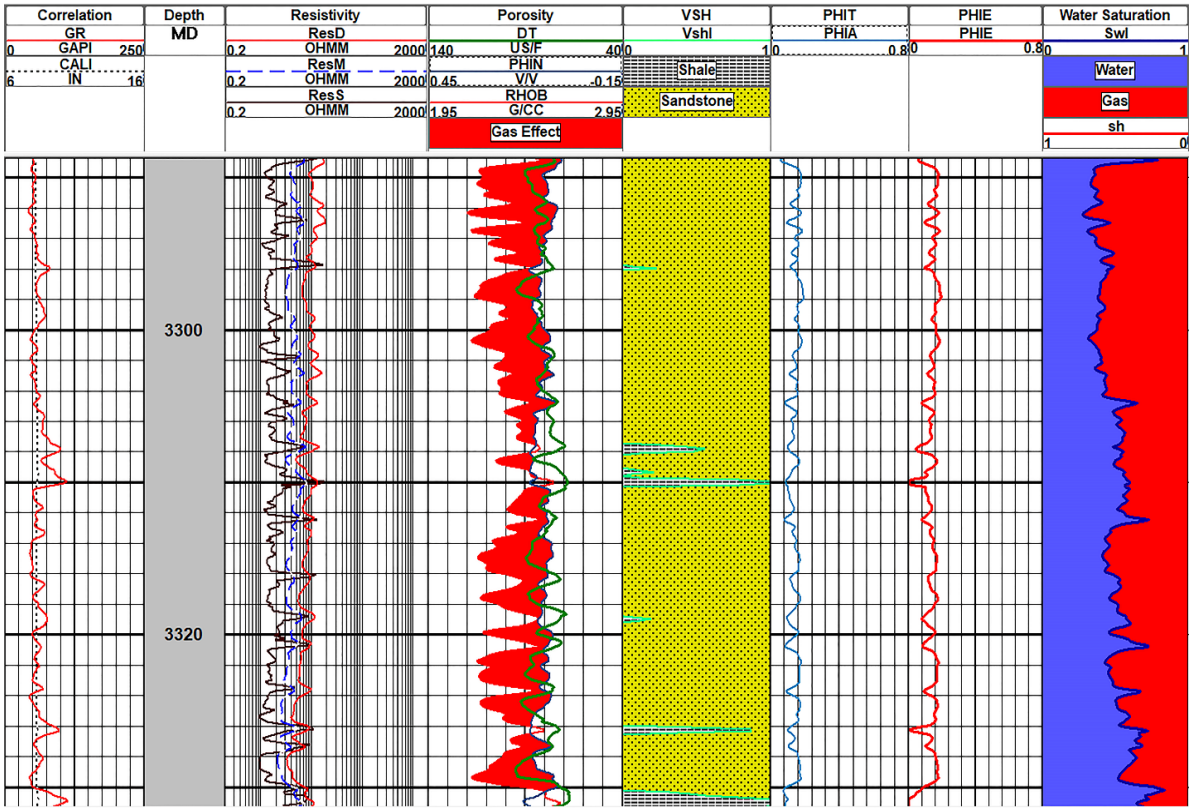

Fig. 4. Petrophysical interpretation of well logs.

3.1. Wavelet Extraction

Wavelet estimated on the seismic database helps deliver true reflectivity series. As a result of the earth's reflectivity convolution with the source wavelet, the seismic trace is obtained. The wavelet extraction procedure includes the statistical estimation of wavelets from the seismic cube. As shown in (Figure 5), the extracted wavelet is obtained by using an operator that gives an initial correlation between real and synthetic data when convoluted with the reflectivity series of well (Jain, 2013). The extraction time window was set from 1600 to 2400 milliseconds with a wavelength of 160 milliseconds.

3.2. Well to Seismic Tie

After wavelet extraction, the next step was to perform well to seismic tie of Lower Goru Formation in all the wells. A synthetic seismogram helps generate well seismic ties and identify events corresponding to reservoir sands (Chukwuemeka, 2021). The logs used for seismic to well tie include Gamma Ray, Sonic and density log. The correlation is done on seismic inline 793, and one zone, "Lower Goru Formation", is marked. In (Figure 6), red traces are actual traces, and the blue traces are synthetic traces having a maximum coefficient of 77%.

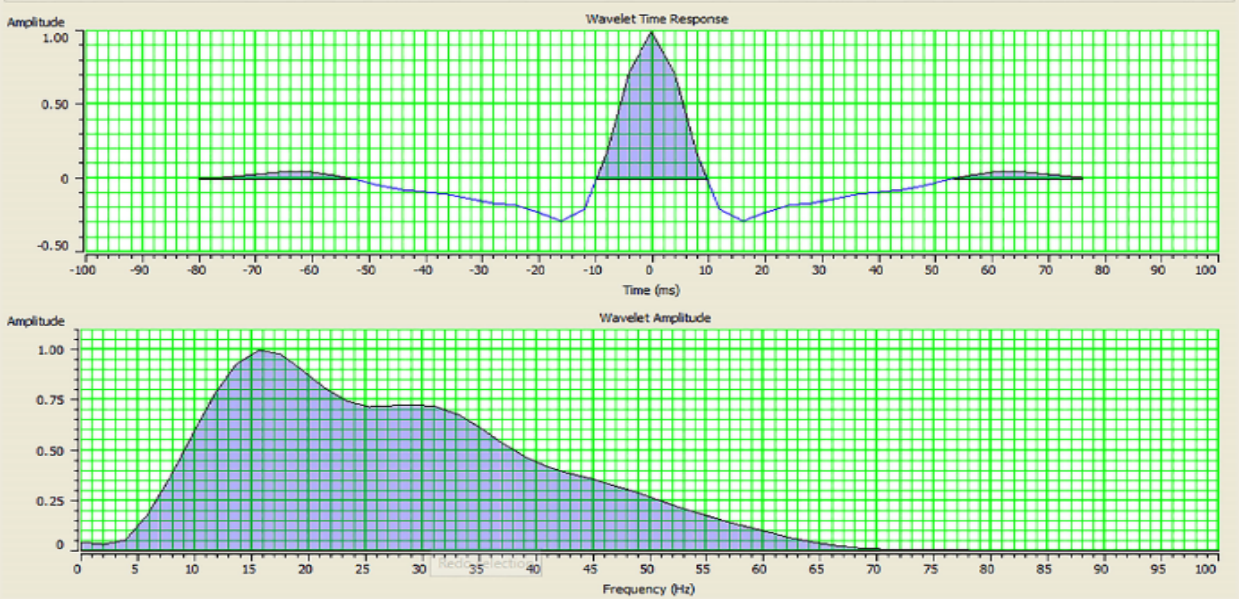

Fig. 5. Extracted Wavelet from seismic cube.

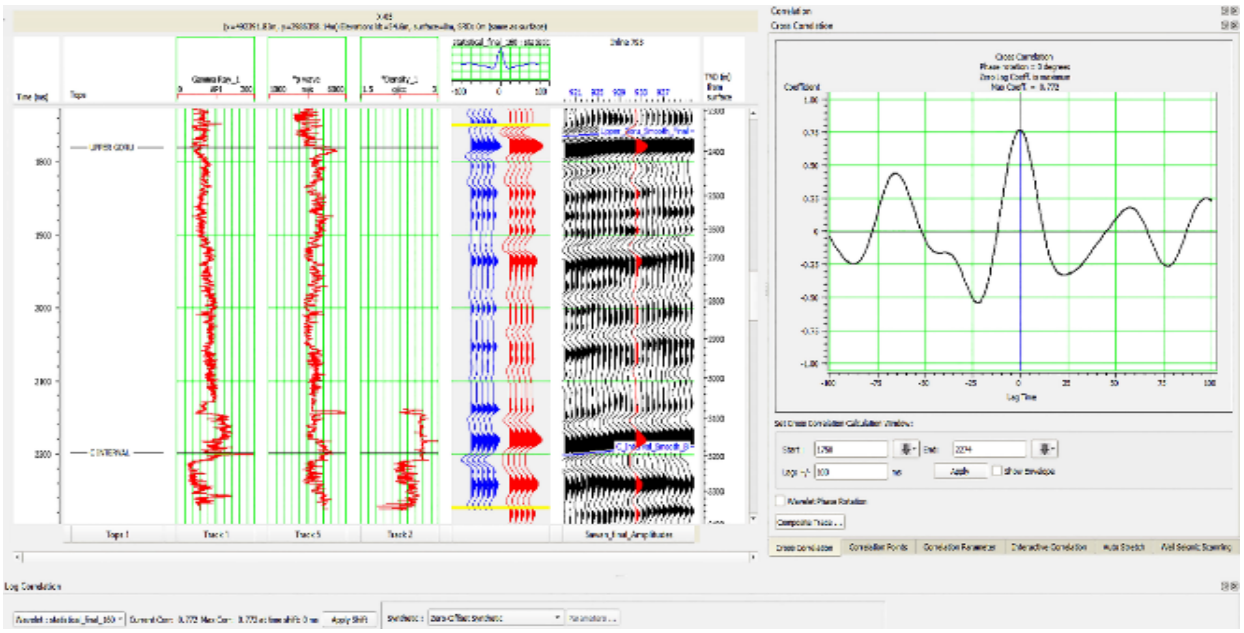

Fig. 6. Well to seismic tie where red curves are indicating actual trace and blue curves are indicating the synthetic trace generated with the help of wavelet extracted from seismic cube.

3.3. Band limited Inversion

Waters invented the Seismic Approximate Impedance Log (SAIL) inversion method in 1978 (Waters, 1978). The help of which velocities and well logs can be stacked for acquiring impedance values from low-frequency data. Ferguson and Margrave proposed a new impedance inversion technique on SAIL dubbed Band limited inversion in the year 1996. The technique utilizes low frequencies data of 2 Hz and 10 Hz (Ferguson & Margrave, 1996). With the help of inversion methodology, the post-stack seismic data was converted into an impedance, density, and P-wave velocity. Defining the relationship between the trace and seismic impedance is the first step of this methodology. As a result, the normal incidence reflection coefficient is defined as

$$r_i = \frac{Z_{i+1} - Z_i}{Z_{i+1} + Z_i} \tag{1}$$

Here, Zi is the seismic impedance of the jth layer, and ri is the seismic reflectivity of jth and (j+1) the interface. By solving the equation for impedance (j+1) the layer, it will become

$$I_{j+1} = I_1 \exp(\gamma \sum_{k=1}^{j} S_k) \tag{2}$$

A robust approach that delivers a smooth and continuous output is Band-limited inversion. In contrast to Band-limited inversion, model-Based inversion gives a blocky result with greater geological information. Both approaches, however, may be beneficial in determining the location of hydrocarbon resources.

3.4.Model Based inversion

This inversion is done by inverting a seismic trace restricted by an a priori model to increase resolution. A basic initial acoustic impedance model is convolved with the wavelet in a model-based inversion to create a synthetic response compared with the real trace. Iteratively altering the acoustic impedance model until the discrepancy between the inverted and seismic traces is decreased to a threshold value. As a solution, a model with a minor difference is approved. Model-Based inversion can produce excellent findings even with inadequate well and seismic quality.
In model-Based inversions, a generalized linear inversion method is utilized. This method assumes that the interpreters are familiar with the seismic trace and wavelet. Moreover, attempts were made to change the initial guass model until the computed trace matches the real trace to an acceptable degree (Gavotti *et al*., 2013). The model is changed many times until the synthetic, and actual seismic traces show the minimum difference. The basic strategy of the inversion algorithm is to solve the function provided in the equation and quantify any changes in synthetic data from real data (Gavotti *et al*., 2013)

$$J = weight_1 x(S - W * R) + weight_1 x(M - H * R) \quad (3)$$

S is an actual seismic trace, R is RC series, W has extracted wavelet, and H is integration operator.

3.5.Stochastic inversion

Stochastic inversion is a method for predicting reservoir parameters distant from the well, which are critical inputs for reservoir modelling. The method incorporates interdisciplinary data from various sources and enables the creation of several earth-model realizations that consider both seismic and good log data. It is also helpful in highlighting the uncertainties in quantifiable data. The earth-model estimate is restricted by seismic, regional geostatistics, and acoustic impedance data from logs to fit the area's known geological trends (Nanda, 2016).

It's a statistical method that generates several different model realizations that meet the observed data. It utilizes the following convolution model:

$$S(t) = R(t) * W(t) + N(t), (1) \quad (4)$$

Where S(t) is the symbol for seismic trace, R(t) represents the reflectivity, W(t) is the wavelet and N(t) represent the random noise.

4. Geo-statistical methods

Geo-statistical methods help predict geophysical parameters from well data and seismic data (Pyrcz *et al*., 2014). A probabilistic Neural Network was utilized to compute the volume of clay and effective porosity volume from seismic data. The input data for training include petrophysical well logs (X-01, X-02, X-04, X-05 and X-06) along with 3D seismic cube and inverted results

from Band limited, Model-Based and Stochastic algorithms. Inverted results from all three methods are used to estimate the volume of clay and effective porosity volume.

The objective of using geo-statistical methods is to apply a neural network algorithm for clay volume and effective porosity estimation over the whole 3D seismic volume. The first step in accomplishing the objective is building a relationship between seismic and well data via the training process. When the relationship is successfully established, it will be applied to the whole seismic volume. The analysis window for the volume of clay in the wells (X-01, X-02, X-04, X-05 and X-06) is shown in (Figure 7). The black curve in the log track is the value of the actual volume of clay in wells, whereas the red curve is for the predicted volume of clay. The horizontal yellow lines demarcate the analysis window of the wells' data volume of clay. The training process results using a series of attributes show a 0.9398 (93%) correlation between used wells' actual and predicted porosities (Figure 7). In (Figure 8), the cross plot between the actual volume of clay and the predicted volume of clay for the Stochastic inversion using probabilistic neural networks (PNN).

The analysis window for effective porosities in the wells (X-01, X-02, X-04, X-05 and X-06) is shown in (Figure 9). The curves in the log track (Figure 9) are the porosity values in which the black curve indicates the actual porosity, whereas the red curve indicates predicted porosity. The horizontal yellow lines demarcate the analysis window of wells data effective porosity. The training process results using a series of attributes show a 0.94436 (94%) correlation between the actual and predicted porosities of used wells (Figure 9). Using the probabilistic neural networks (PNN) approach, the cross plots between actual porosity and predicted porosity for the Stochastic inversion were plotted (Figure 10). In the cross plot, the predicted porosity is on Y-axis, and the Actual porosity is on X-axis. On the right side, a colour bar is present, and it shows different wells.

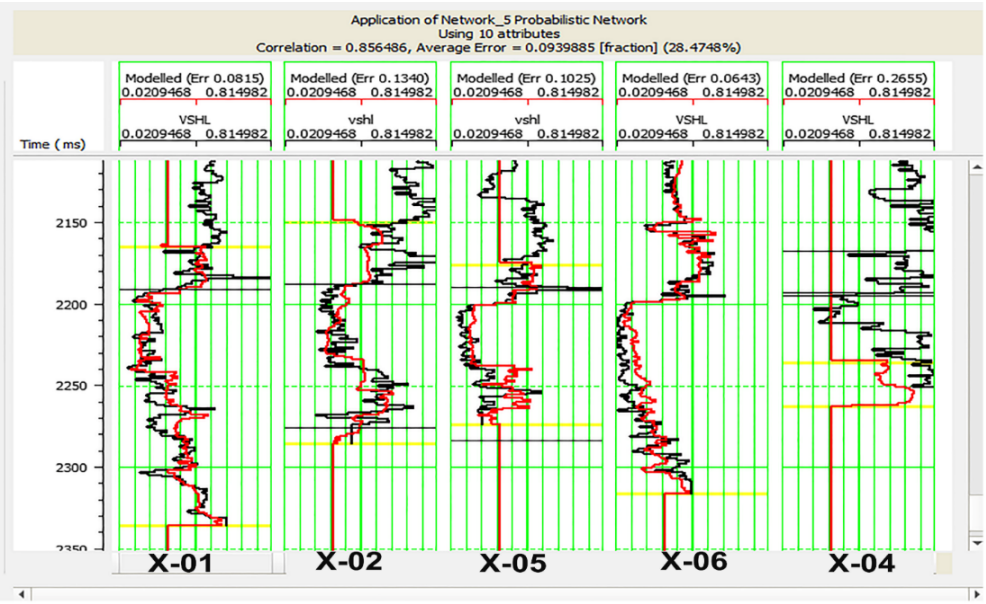

Fig. 7. Analysis of Actual volume of clay (black curve) and predicted volume of clay (red curve) along with the analysis window demarcated above and below by horizontal yellow lines.

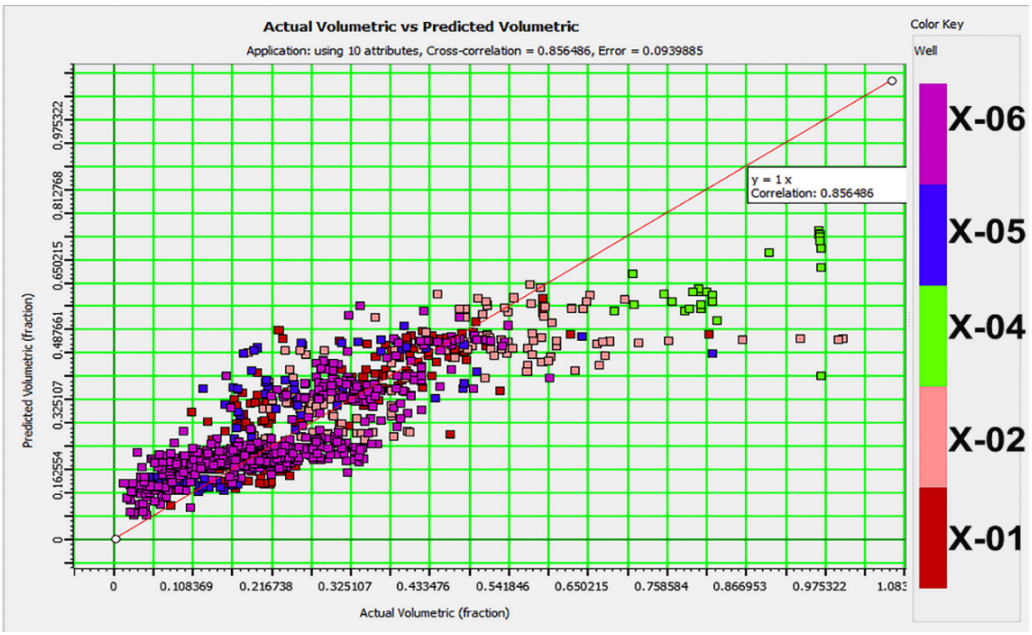

Fig. 8. The cross plot between the actual volume of clay and predicted volume of clay of wells (X-01, X-02, X-04, X-05 and X-06).

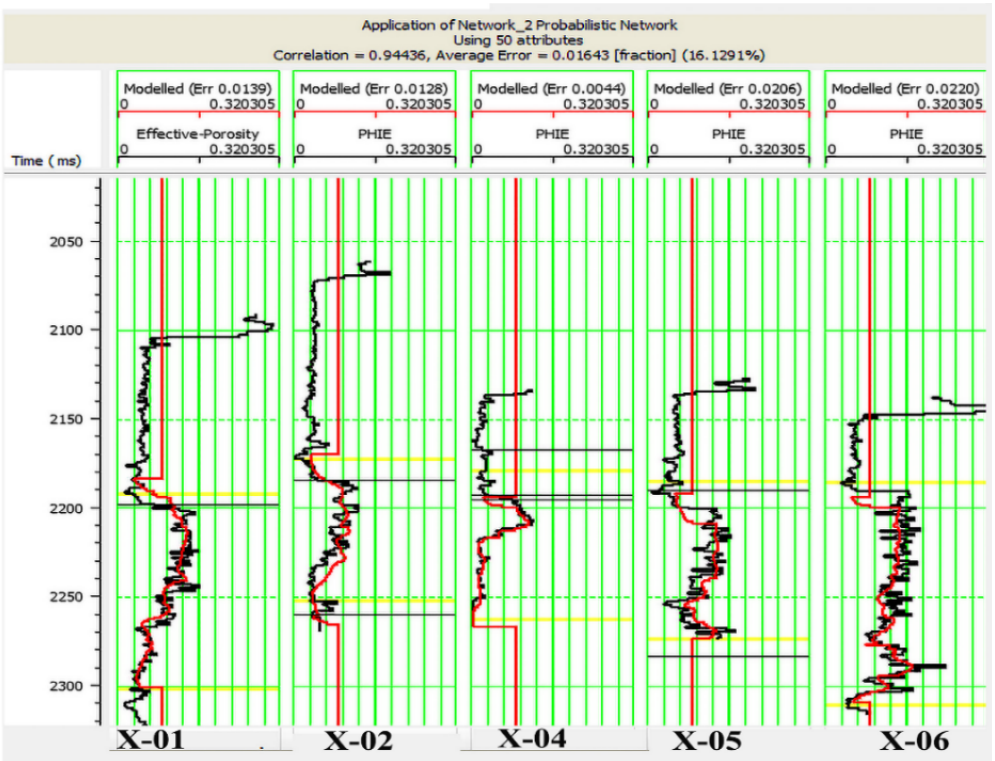

Fig. 9. Analysis of Actual porosity represented by black curve and predicted porosity by red curve along with the analysis window demarcated above and below by horizontal yellow lines.

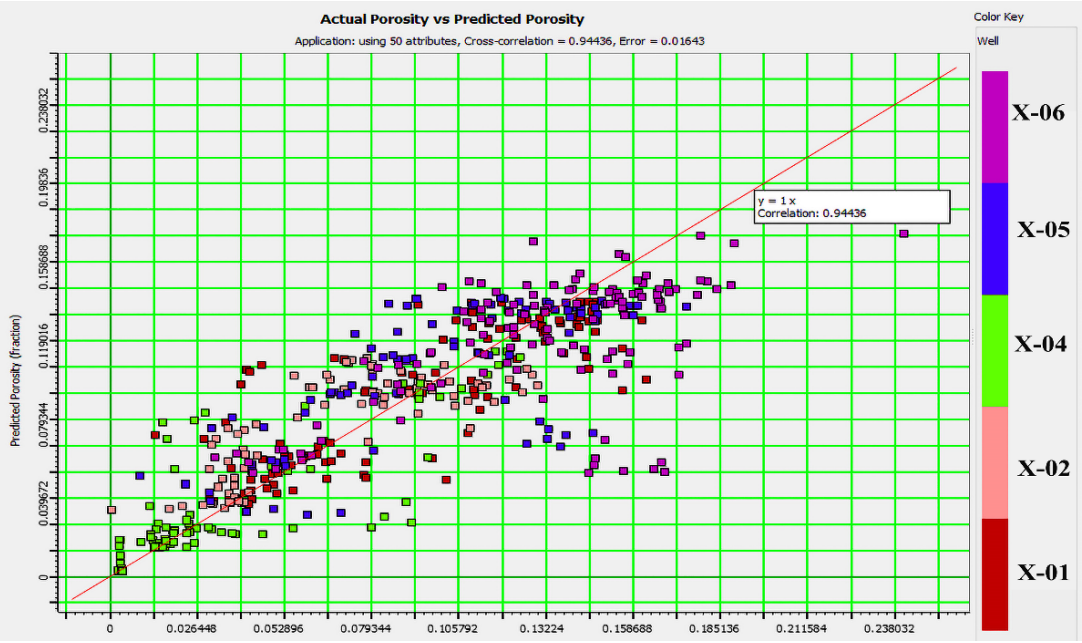

Fig. 10. The cross plot between actual and predicted porosity of wells (X-01, X-02, X-04, X-05 and X-06).

5. Results and Discussion

The study aimed to improve the reservoir characterization of the C-interval sand of the Lower Goru Formation by using different sophisticated inversion techniques (Band limited, Model-Based inversion, and Stochastic inversion) and comparatively analyzed their results. For this purpose, integrating datasets, including seismic and well logs, was utilized to link geological and geophysical information. These inversion techniques successfully delineated isolated sand bodies sandwiched between high impedance (10000-12000 m/s g/cc) shale packages. In addition, Impedance values ranging from 7000-to 10000 m/s g/cc are assigned to the gas-bearing sands and illustrate the potential of the study area (Ibrahim, 2007). These alternative sand-shale facies (clarified by their impedances) are deposited under a deltaic environment followed by forced regression and transgression. Stochastic inversion provided a better result than Band limited inversion and Model-Based inversion (Figures 11a and b). It resolved possible potential sand facies effectively with an improved resolution and provided the best realistic model of subsurface geology (Figure 11c). Stochastic inversion separated the North-eastern part of the study area dominated by clean sand bodies indicating the proximal shore face deposits. In contrast, shale content increases on the Southwestern side, signifying the distal part.

Furthermore, inversion results are trained by the probabilistic neural network algorithm for petrophysical properties estimation i.e., Volume of clay and effective porosities. These petrophysical attributes characterizes the reservoir quality and minimize the exploration risk of targeted potential Lower Goru sands (Khan *et al*., 2021; Khan *et al*., 2022). Stratigraphic slices of

Volume of clay by taking average values within C-interval sand of the Lower Goru Formation are generated for all PNN derived results (Band limited, Model-Based and Stochastic) (Figures 12a, b and c). In comparison, the stochastic map provided improved facies distribution that is aligned with geological setting. The map highlighted three different facies such as clean sands (10-30%) passing through X-01, X-05 and X-06 wells, shaly sand (30-35%) encounter at well X-03 while shale facies (>45%) at well location X-04 (Figure 12c). All these facies are verified by the petrophysical evaluation of each well.

Similarly, effective porosities map is generated with average values of C-interval sand of the Lower Goru Formation extracted by the training of inversion results through PNN algorithm i.e., Band limited, Model-Based and Stochastic (Figures 13a, b and c). Likewise, Stochastic inversion resolved the heterogeneous porosities of reservoir sands more efficiently. The map shows high effective positives of 10-12% in the clean sand facies, 8-10% in the shaly sand facies and minimum effective porosities of about 0-1% for the shales.

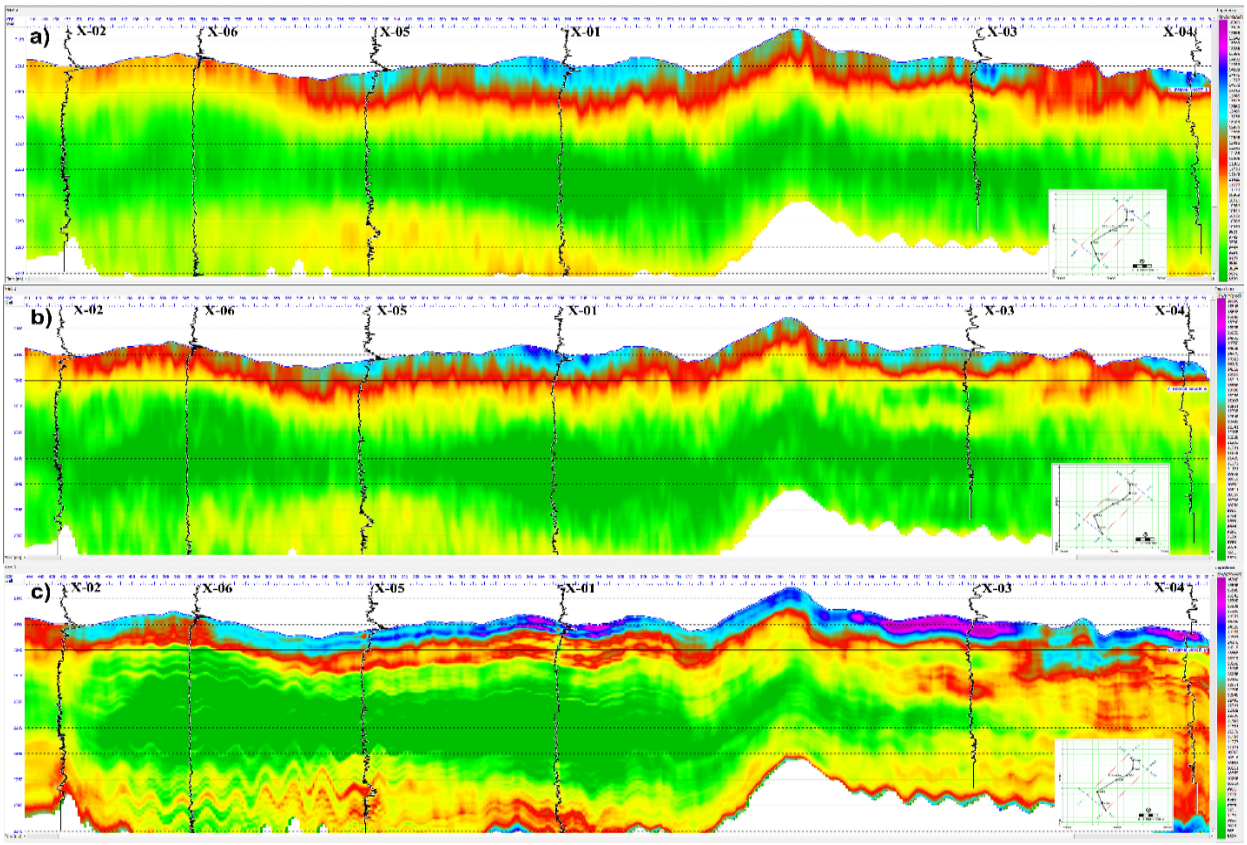

Fig. 11. P impedance for (a) Bandlimited Inversion (b) Model-Based inversion (c) Stochastic inversion.

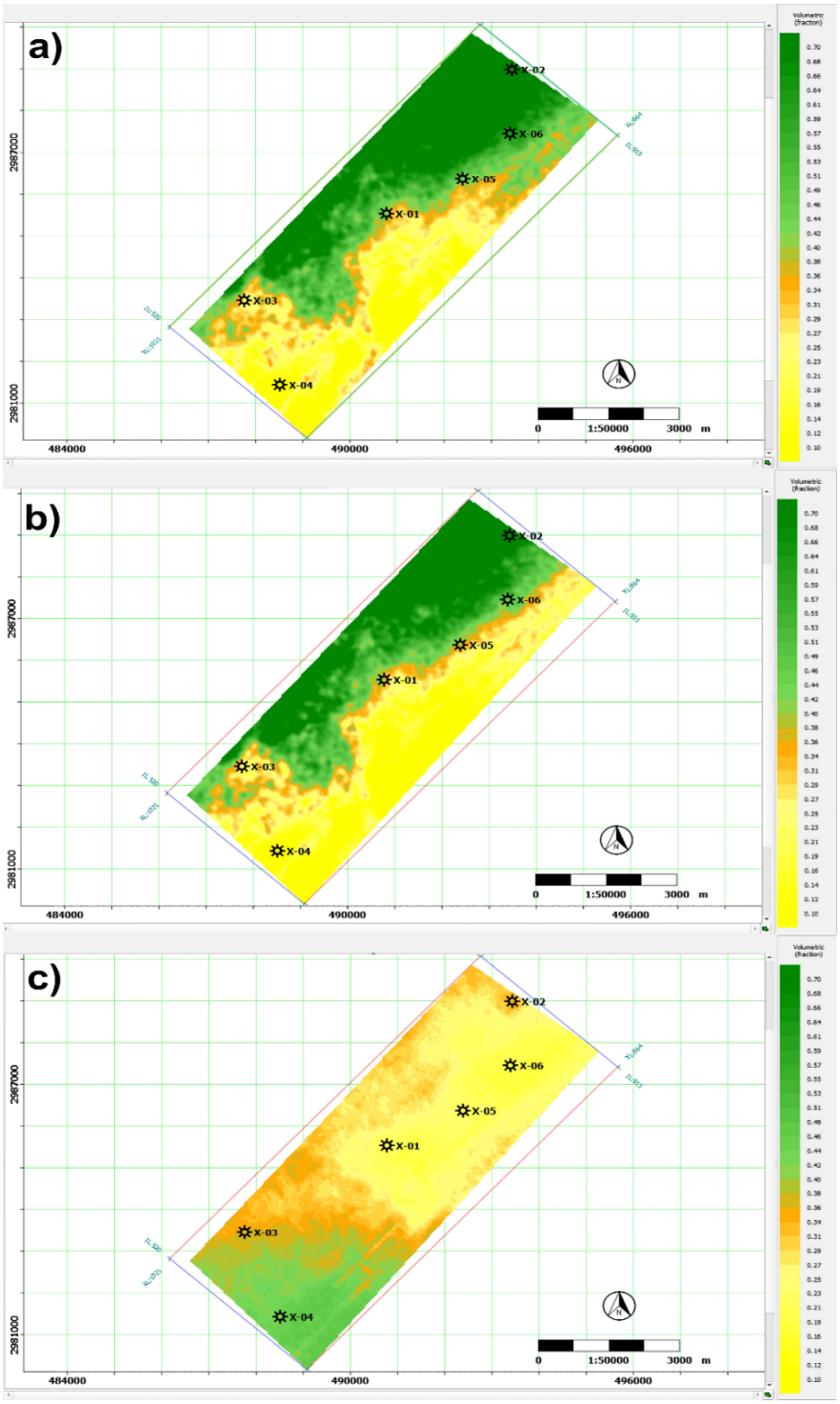

Fig. 12. Estimation of Volume of clay (Vclay) of C-interval sands of Lower Goru Formation using post-stack inversion techniques including (a) Band limited Inversion (b) Model-Based inversion (c) Stochastic inversion.

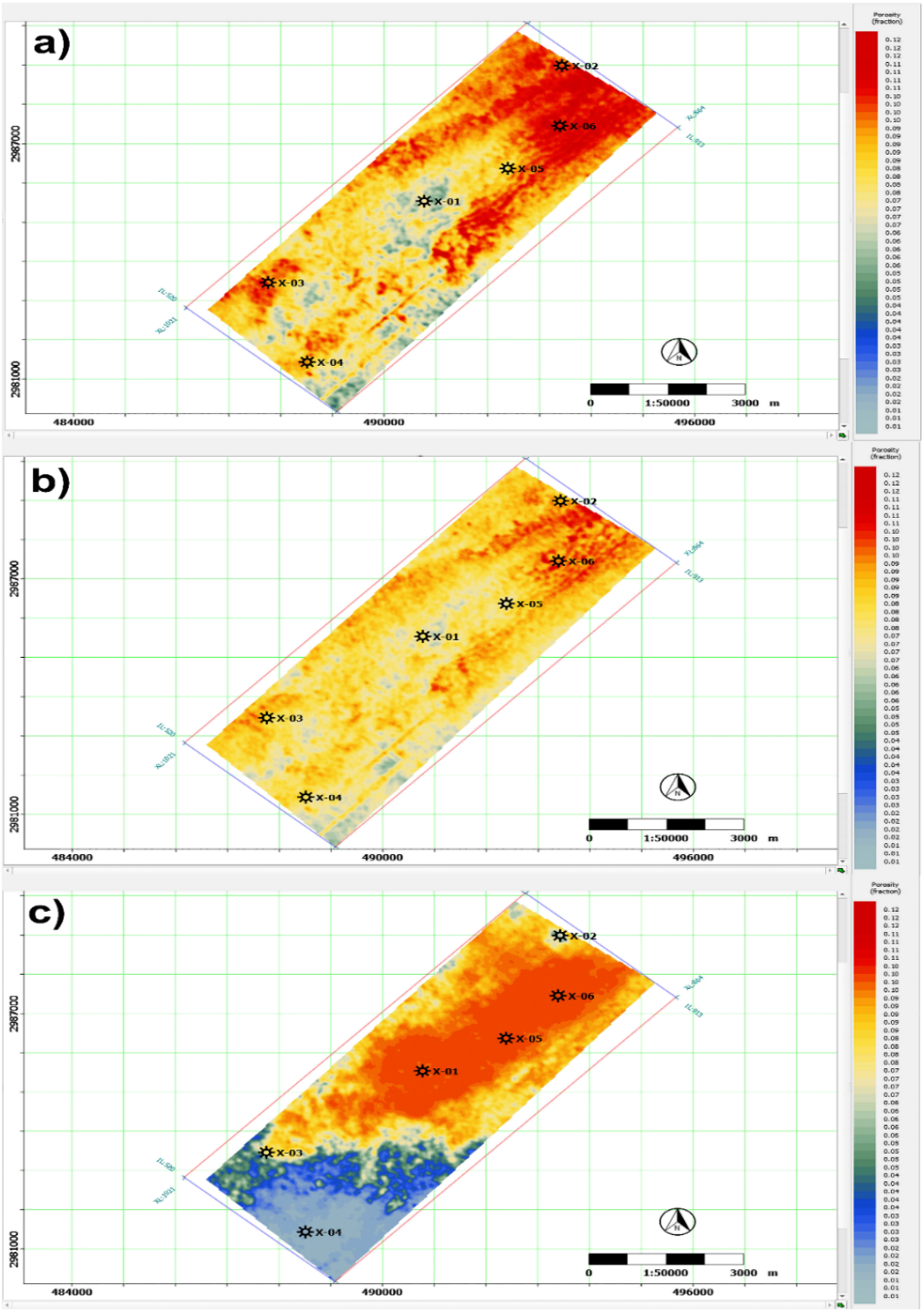

Fig. 13. Effective porosity estimation of C-interval sands of Lower Goru Formation using post-stack inversion techniques including (a) Band limited Inversion (b) Model-Based inversion (c) Stochastic inversion.

6. Conclusion

The comparative analysis among three seismic inversion techniques (Band limited inversion, Model-Based inversion and Stochastic inversion) successfully characterizes the reservoir facies of C-interval sands of the Lower Goru Formation. The highly resolved Stochastic inversion best differentiates between producing and non-producing reservoir facies. The PNN trained stochastic attributes for petrophysical properties to illuminate potential sands with low P-impedances, high effective porosity, and low clay volumetric. The results are in accordance with interpreted wells (X-04 was kept blind) and geological settings. Hence Stochastic inversion overcomes many problems effectively, such as assessing heterogeneity and quality of the reservoir. The north-eastern wells (X-01, X-05, X-06 and X-02) have clean sand facies with a low volume of clay and high effective porosity delineating the main producing facies. Whereas, moving towards the southwestern side, the wells (X-03 and X-04) have finer sediments, greater shale volume, and low effective porosity resulting in poor reservoir quality.

ACKNOWLEDGEMENT

We are very thankful to the Directorate General of Petroleum Concessions (DGPC) for providing the seismic and petrophysical data used in the present research.

References

Abdulkareem, L. (2022). AVO analysis for high amplitude anomalies using 2D pre-stack seismic data. Kuwait Journal of Science, 49(2).

Adesanya, O. Y., Adeoti, L., Oyedele, K. F., Afinotan, I. P., Oyeniran, T., & Alli, S. (2021). Hydrocarbon reservoir delineation using simultaneous and elastic impedance inversions in a Niger Delta field. Journal of Petroleum Exploration and Production Technology, 11(7), 2891-2904.

Afzal, J., Williams, M., & Aldridge, R. J. (2009). Revised stratigraphy of the lower Cenozoic succession of the Greater Indus Basin in Pakistan. Journal of Micropalaeontology, 28(1), 7-23.

Ahmad, N., Fink, P., Sturrock, S., Mahmood, T., & Ibrahim, M. (2004). Sequence stratigraphy as predictive tool in lower goru fairway, lower and middle Indus platform Pakistan.

Al-Sulaimi, J. S., & Al-Ruwaih, F. M. (2004). Geological, structural, and geochemical aspects of the main aquifer systems in Kuwait. KUWAIT JOURNAL OF SCIENCE AND ENGINEERING., 31(1), 149-174.

Asghar, H. (2021). Organic geochemistry and mineralogical characterization of the Paleocene Ranikot Formation shales in selected areas of southern Indus Basin Pakistan. KUWAIT JOURNAL OF SCIENCE.

Berger, A., Gier, S., & Krois, P. (2009). Porosity-preserving chlorite cements in shallow-marine volcaniclastic sandstones: Evidence from Cretaceous sandstones of the Sawan gas field, Pakistan. AAPG bulletin, 93(5), 595-615.

Burg, J. P., Célérier, B., Chaudhry, N. M., Ghazanfar, M., Gnehm, F., & Schnellmann, M. (2005). Fault analysis and paleostress evolution in large strain regions: methodological and geological discussion of the southeastern Himalayan fold-and-thrust belt in Pakistan. Journal of Asian Earth Sciences, 24(4), 445-467.

Chukwuemeka, A. P. (2021). Application of Seismic Inversion in Estimating Reservoir Petrophysical Properties: Case Study of Jay field of Niger Delta. KUWAIT JOURNAL OF SCIENCE.

Contreras, A., Torres-Verdín, C., & Fasnacht, T. (2006). AVA simultaneous inversion of partially stacked seismic amplitude data for the spatial delineation of lithology and fluid units of deepwater hydrocarbon reservoirs in the central Gulf of Mexico. Geophysics, 71(4), E41-E48.

Ehsan, M., Gu, H., Akhtar, M. M., Abbasi, S. S., & Ehsan, U. (2018). A geological study of reservoir formations and exploratory well depths statistical analysis in Sindh Province, Southern Lower Indus Basin, Pakistan. KUWAIT JOURNAL OF SCIENCE, 45(2).

Ferguson, R. J., & Margrave, G. F. (1996). A simple algorithm for band-limited impedance inversion. CREWES Research Report, 8(21), 1-10.

Gavotti, P., Lawton, D. C., Margrave, G., & Isaac, J. H. (2013, June). Model-Based Inversion of Low-Frequency Seismic Data. European Association of Geoscientists & Engineers.

Ibrahim, M. (2007). Seismic inversion data, a tool for reservoir characterization/modeling, sawan gas field—A case study. In Proceedings of the Annual Technical Conference.

Jain, C. (2013). Effect of seismic wavelet phase on post stack inversion. In 10th Biennial Int. Conf. & Exposition, Kochi (p. 410).

Kadri, I. B. (1995). Petroleum Geology of Pakistan: Pakistan Petroleum Limited. Karachi, Pakistan.

Kazmi, A. H. (1979). Active fault systems in Pakistan. Geodynamics of Pakistan, 285-294.

Kazmi, A. H., & Jan, M. Q. (1997). Geology and Tectonics of Pakistan Graphic Publishers. ISBN: 9698375007, 9789698375003, 554.

Khalid, P., Qayyum, F., & Yasin, Q. (2014). Data-driven sequence stratigraphy of the Cretaceous depositional system, Punjab Platform, Pakistan. Surveys in Geophysics, 35(4), 1065-1088.

Khan, Z. U., Lisa, M., Hussain, M., & Ahmed, S. A. (2021). Gas-bearing sands appraisal through inverted elastic attributes assisted with PNN approximation of petrophysical properties. KUWAIT JOURNAL OF SCIENCE.

Khan, Z. U., Lisa, M., Hussain, M., & Ahmed, S. A. (2022). Gas-bearing sands appraisal for Zamzama Gas field in Pakistan through inverted elastic attributes assisted with PNN approximation of petrophysical properties. Kuwait Journal of Science, 49(4).

Miraj, M. A. F., Javaid, H., & Ahsan, N. (2021). An integrated approach to evaluate hydrocarbon potential of Jurassic Samana Suk Formation in Middle Indus Basin, Pakistan. KUWAIT JOURNAL OF SCIENCE, 48(4).

Moosavi, N., & Mokhtari, M. (2016). Application of post-stack and pre-stack seismic inversion for prediction of hydrocarbon reservoirs in a Persian Gulf gas field. International Journal of Geological and Environmental Engineering, 10(8), 853-862.

Nanda, N. C. (2016). Seismic data interpretation and evaluation for hydrocarbon exploration and production: A practitioner's guide. Springer.

Osita, M. C., Abbey, C. P., Oniku, A. S., Okpogo, E. U., Sebastian, A. S., & Dabari, Y. M. (2022). Application of seismic inversion in estimating reservoir petrophysical properties: Case study of Jay field of Niger Delta. Kuwait Journal of Science, 49(2).

Pyrcz, M. J., & Deutsch, C. V. (2014). Geostatistical reservoir modeling. Oxford university press.

Quadri, V. U. N., & Shuaib, S. M. (1986). Hydrocarbon prospects of southern Indus basin, Pakistan. AAPG bulletin, 70(6), 730-747.

Razak, M. H. A. (2010, March). Application of 3D Seismic Multi-Attribute and Neural Network Technique for Reservoir Prediction: A Case Study for the Marrat Formation, Kuwait. In GEO 2010 (pp. cp-248).

Rijks, E. J. H., & Jauffred, J. C. E. M. (1991). Attribute extraction: An important application in any detailed 3-D interpretation study. The Leading Edge, 10(9), 11-19.

Shahzad, Y., dos Reis, R. P., & Henriques, M. H. (2022). A Hydrocarbon Resource Plays in Southern Pakistan´ s Indus Basin.

Varela, O. J., Torres-Verdín, C., & Sen, M. K. (2006). Enforcing smoothness and assessing uncertainty in non-linear one-dimensional prestack seismic inversion. Geophysical Prospecting, 54(3), 239-259.

Waters, K. H., Palmer, S. P., & Farrell, W. E. (1978). Fracture detection in crystalline rock using ultrasonic shear waves (No. LBL--7051). California Univ...

Zaigham, N. A., & Mallick, K. A. (2000). Prospect of hydrocarbon associated with fossil-rift structures of the southern Indus basin, Pakistan. AAPG bulletin, 84(11), 1833-1848.

Submitted: 17/01/2022
Revised: 17/04/2022
Accepted: 10/05/2022
DOI: 10.48129/kjs.18279

Reservoir evaluation of the eastern Tethyan Middle Eocene Larger Benthic Foraminifera dominated carbonates from Pakistan.

Anwar Qadir[1*], Khurram Shahzad[2], Mehran Khan[3], Waqar Ahmad[3]

[1]*Dept. of Earth Sciences, The University of Haripur, Haripur, Pakistan*
[2]*Institut für Geologie, Universität Hamburg, Hamburg, Germany*
[3]*Dept. of Earth and Environmental Sciences, Bahria University, Islamabad, Pakistan.*

[*] *Corresponding Author: anwarq@uoh.edu.pk*

Abstract

The Eocene Large Benthic Foraminiferal limestones of the Tethyan margins are proven hydrocarbon reservoirs. This study examines the controls on porosity and permeability development of the producing Middle Eocene Pirkoh Member of the Eastern Tethys using well core data from Well Zx-01 from the Punjab Platform area, Central Indus Basin, Pakistan.

The standard petrographic and core analysis techniques were adopted to determine these controls. Petrographic studies revealed three microfacies comprising bioclastic packstone to floatstone, bioclastic wackestone and mud-wackestone microfacies. The allochems belong to benthic foraminifera including *Nummulites* sp*., Discocyclinids* sp*.., Coralline algae, Assilina* sp*., Lockhartia* sp*.,* Coralline algae and Gastropods along with the other bioclastic debris. These allochems were found embedded in the micritic matrix with extensive cementation of calcite. The diagenetic events included cementation, compaction, dolomitization, fracture filling and neomorphism. Based on microfacies, the environment of deposition is interpreted to be a high-energy zone of the middle ramp in shallow marine environment. Subsurface core indicates that the porosity of the reservoir is low to high ranging between 6 to 27.47% and permeability is found low to fair ranging between 0.03 to 7.73 mD, found closely related to microfacies and diagenetic modifications. This study is a first attempt to document the reservoir facies of the non-reefal carbonates of the Pirkoh limestone that would help to exploit the reservoir's potential of the carbonate platforms developed in similar settings worldwide.

Keywords: Carbonates reservoir characterization, greenhouse carbonates; large benthic foraminifera; middle Eocene; Pakistan.

1. Introduction

Carbonate platforms are the most promising hydrocarbon reservoirs containing more than 60% of the world's oil and gas reserves (Burchette, 2012; Abdullah, 2020). Reef constructors have remained the primary constituent of the giant carbonate reservoirs. Tropical shallow marine carbonates of late Paleocene to early Oligocene are characterized by the dominance of Large Benthic Foraminifera (LBF) (Höntzsch *et al.*, 2013; Bahman, 2022).

Recent developments in sequence stratigraphy gained the interest of petroleum geologists in identifying carbonate reservoir facies in the subsurface seismic images (Sarg, 1988; Handford and Loucks, 1993; Markello *et al.*, 2008; Garland *et al.*, 2012; Shahzad *et al.*, 2018; Shahzad *et al.*, 2019; Miraj *et al.* 2021; Asaad, 2021). The lack of understanding of the petrographic details also impacts the production and artificially enhanced fluid flow in the carbonate system. According to the traced research gap, this paper analyzes the in-situ reservoir characteristics of the middle Eocene Pirkoh limestone as a case study using industrial analysis techniques and petrography of the core data.

Pirkoh Member contains abundant Large Benthic Foraminifera (LBF) and serves as proven reservoir hosting the hydrocarbons in the Central Indus Basin such as Mari and Qadirpur gas fields (Khan *et al.*, 2016). It is a shallow producing reservoir at the depth of 610 m located on the Punjab Platform, therefore, the effect of burial is minimum with regionally stable tectonics, in comparison with the fractured Eocene carbonate reservoir of Sulaiman and Potwar Fold belts. Therefore, it represents an ideal workable example for establishing the depositional system of the Eocene carbonate reservoirs.

Currently, there is a lack of publicly available data concerning the evaluation of the Pirkoh Member. Therefore, it was decided to investigate the lithofacies, porosity, permeability, and the effect of diagenesis on the reservoir properties using core data and petrographic analysis techniques. Furthermore, efforts were made to assess reservoir quality and to make these data more widely available in the literature.

1.1 Regional Settings

The study area is in the Punjab Platform of the Central Indus Basin, west of Pakistan (Figure.1). It is located on the northwestern margin of the Indian Plate. This area represents the Cenozoic convergence between the Indian and the Eurasian Plates with the closure of the Neo Tethys in Eocene (Kazmi & Jan 1997). The Punjab Platform is a westward gently dipping monocline that extends from the Aravalli craton (Indian Shelf) and Bikaner–Nagaur Basin in the east to the Sulaiman Fold-thrust belt and Sulaiman Depression in the west originated due to the Himalayan orogeny. The study area is bounded by two main features of geological significance i.e., the Sargodha High and the Mari Kandhkot High in the north and south respectively. The Punjab part of the platform remained undisturbed during Late Cretaceous (Khalid *et al.*, 2014).

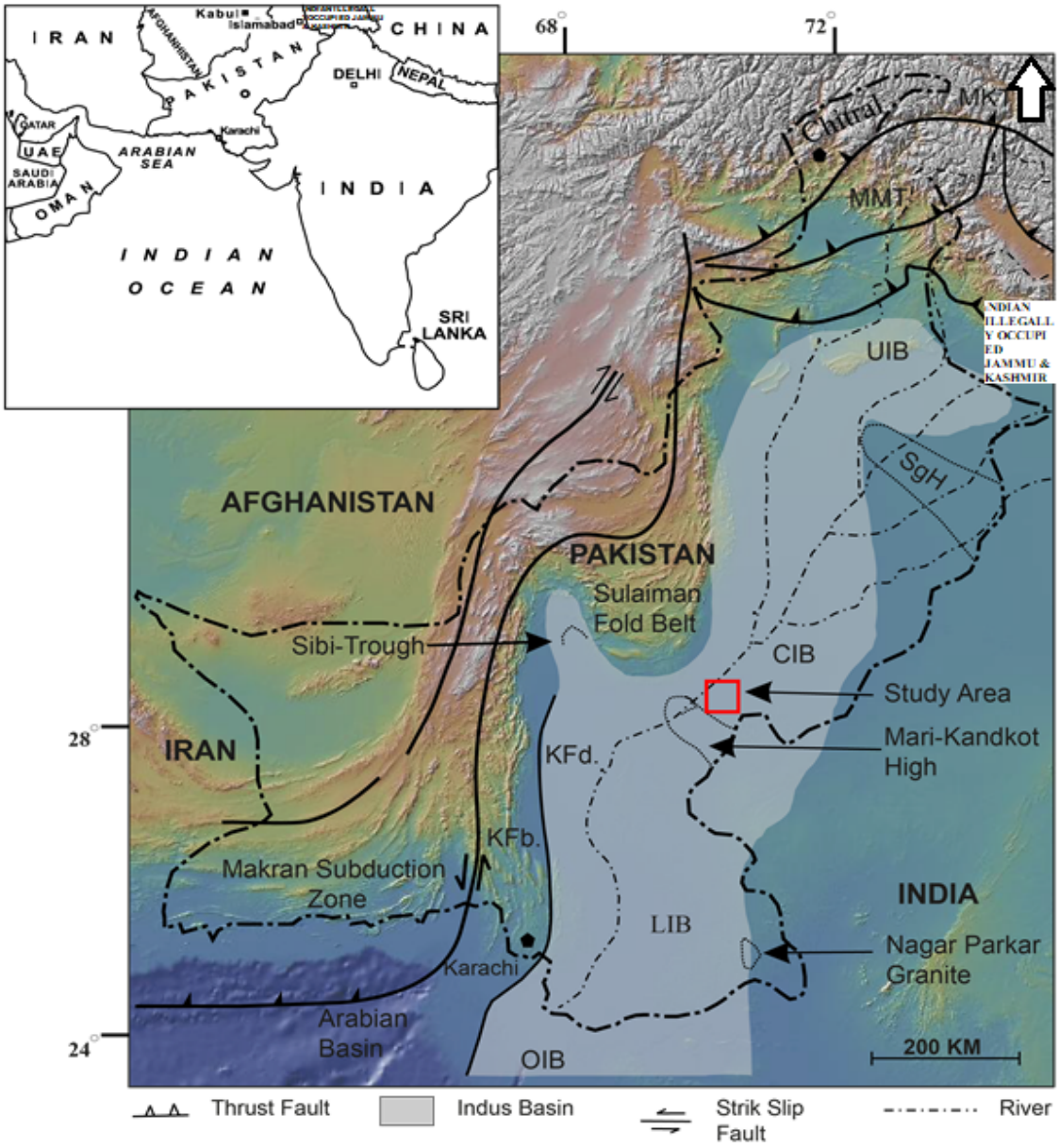

Fig. 1. Regional map of Pakistan with major tectonic and structural elements. Shaded zone shows the extent of Greater Indus Basin (onshore) (after Afzal et al 2009). Main Karakoram Thrust (MKT), Main Mantle Thrust (MMT), Main Boundary Thrust (MBT), Kohistan (island) Arc (KA), Upper Indus Basin (UIB), Central Indus Basin (CIB) Lower Indus Basin (LIB), Kirthar Foldbelt (KFb), Kirthar Foredeep (KFd).

During the Eocene, the western continental margin of Indian Plate was covered by the shallow, neritic, passive margin carbonates. Additionally, this plate was located near or at the equator during the Eocene (Shahzad *et al.*, 2018; Shahzad *et al.*, 2019). These shallow marine deposits were rich in LBFs and crop out in the series of doubly plunging north-south to NNW-SSE anticlines and elongate anticlinal ridges separated by broad synclines in the mountain areas of the Sulaiman-Kirthar Fold belts (Figure. 2a). Furthermore, these reservoirs were also encountered in Central Indus Basin and their correlative succession in the Northern and Southern Indus Basin (Siddiqui, 2004).

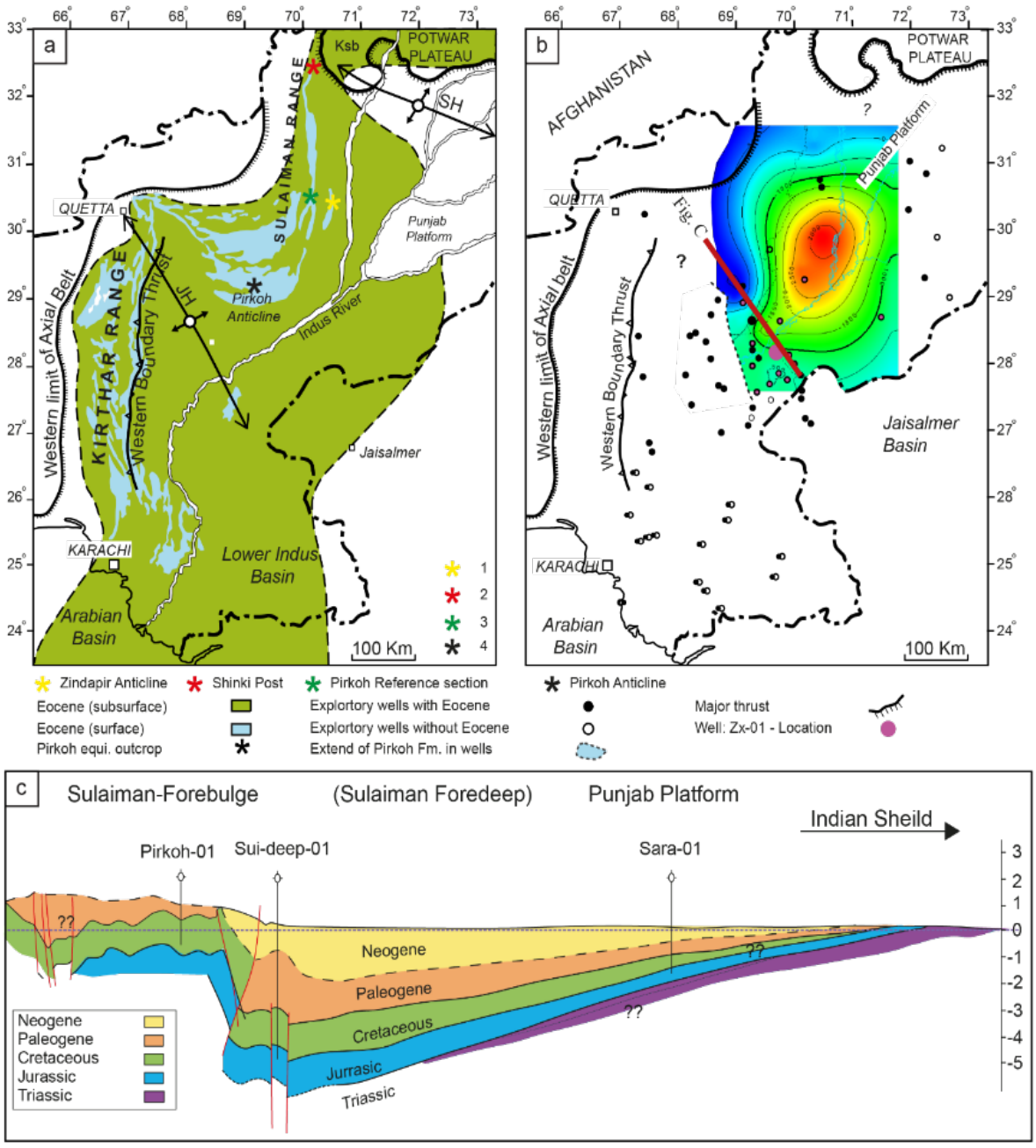

Fig. 2. a) A detailed map of location with type locality and regional extension of Eocene strata. b) Lateral extension of Pirkoh Member on Punjab Platform found in exploratory wells in the subsurface. The red line shows the regional cross-section in figure c. c) Regional geological cross-section along the red line in figure b. Depths in meter with standard above mean sea level (modified from Siddiqui, 2004; Wandrey *et al.*, 2004). Outcrops 1. Zindapir Anticline, 2. Sirki Post, 3. Pirkoh Reference Section, 4. Pirkoh Anticline.

1.2 Stratigraphy and Petroleum System of Well Zx-01

In Sulaiman Kirthar geological province, the sedimentary succession of the region is comprising stratigraphic units, i.e. (i) Precambrian basement rocks, (ii) Permian to Eocene shallow-marine shelf to deep marine strata, and (iii) Oligocene to Holocene molasse deposits (Figure. 2 and 3). Shallow marine to estuarine limestone interbedded with the calcareous shales makes up the Eocene succession. A biostratigraphic subdivision of the Eocene succession was developed based on the diagnostic planktic and benthic foraminiferal assemblages (Ali *et al.*, 2018). These deposits record the final stages of the diachronous closure of Tethyan seaway in Priabonian times in the Indus Basin (Kazmi and Abbasi, 2008).

Cretaceous and Paleocene rocks revealed good potential source characteristics in exploratory wells in the periphery of the studied area (Khan and Raza, 1986; Afzal *et al.*, 1997; Qayyum *et al.*, 2016; Ehsan *et al.*, 2018). The shales of the Drazinda Formation, which in places lies conformably above Pirkoh Member, act as a cap/seal rock along with the sealing beds of the Pirkoh Formation (Figure. 3) (Siddiqui, 2004).

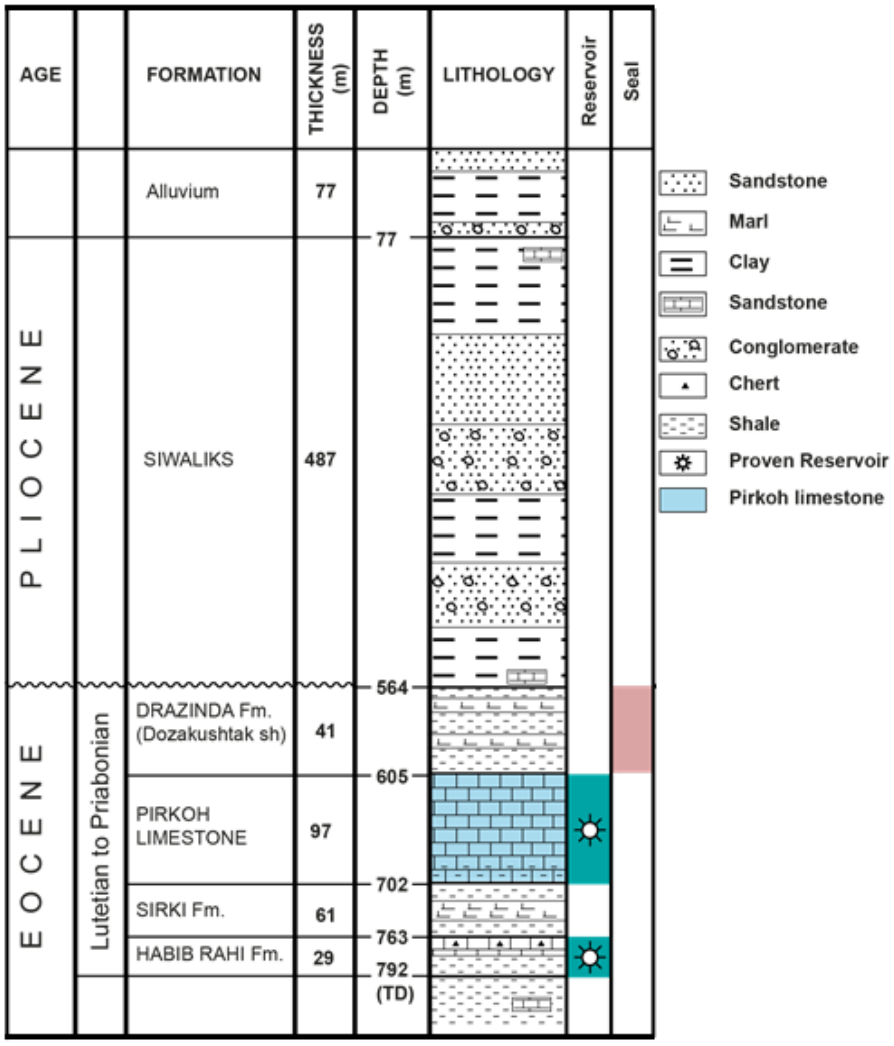

Fig. 3. Sedimentary Stratigraphic column encountered in the well Zx-01.

2. Material and methods

Thirty plug samples were taken from the Pirkoh Member that was encountered in the exploratory well Zx-01 well. The samples were taken at suitable intervals to prepare thin sections for the microfacies analysis, and reservoir characterization including porosity and permeability determination. The methodology adopted for this research was based majorly on core analysis techniques (Flügel, 2004). The Dunham classification (Dunham, 1962) was used for microfacies while the porosity and permeability, parameters were analyzed using Core Measurement System (CMS) 300 under standard protocols.

2.1 Petrography

Fourteen thin sections were prepared from core samples. Classification, depositional environment's interpretations, diagenetic alterations, and biostratigraphy were studied according to the standard procedures (Embry and Klovan, 1971; Flügel, 2004; Serra Kiel *et al.*, 1998).

2.2 Core Analysis

Thirty plug samples were taken at the regular intervals from 9 m long cores with the help of the plugging machine. These were then oven dried and weights were measured. The diameter and length of these plugs were measured using the Vernier Caliper. The bulk volume and permeability was calculated by the following formula.

$$\text{Bulk Volume} = (\text{diameter})^2 \times \text{length} \times 3.14 / 4 \quad (1)$$

$$Q = \frac{KA(P1-P2)}{(\mu L)} \quad (2)$$

Where:

Q = flow rate
K = permeability
A = area
P1 – P2 = pressure drop
L = path length
μ = dynamic viscosity (aka absolute viscosity or viscosity

3. Result and Discussion

3.1 Carbonate microfacies

Three microfacies were distinguished and described below:

3.1.1 MF1: Bioclastic Packstone to floatstone with Large Benthic Foraminifera (LBF)

The MF1 consists of light grey to brownish grey, fossiliferous, hard, and compact limestone. The MF1 is found in four thin sections (Table 1). *Nummulites* sp. and *Discocyclina* sp. are the dominant skeletal grains found in these microfacies (Figure. 4). Apart from these two, *Lockhartia* sp. And coralline algae with other bioclastic grains were also found. The common size of the skeletal grains ranged between 2 to 3 mm. The grains are

poorly sorted and embedded in the micrite matrix. The cementation of calcite is also observed in these facies. The grain to matrix ratio found in this microfacie is 4:1.

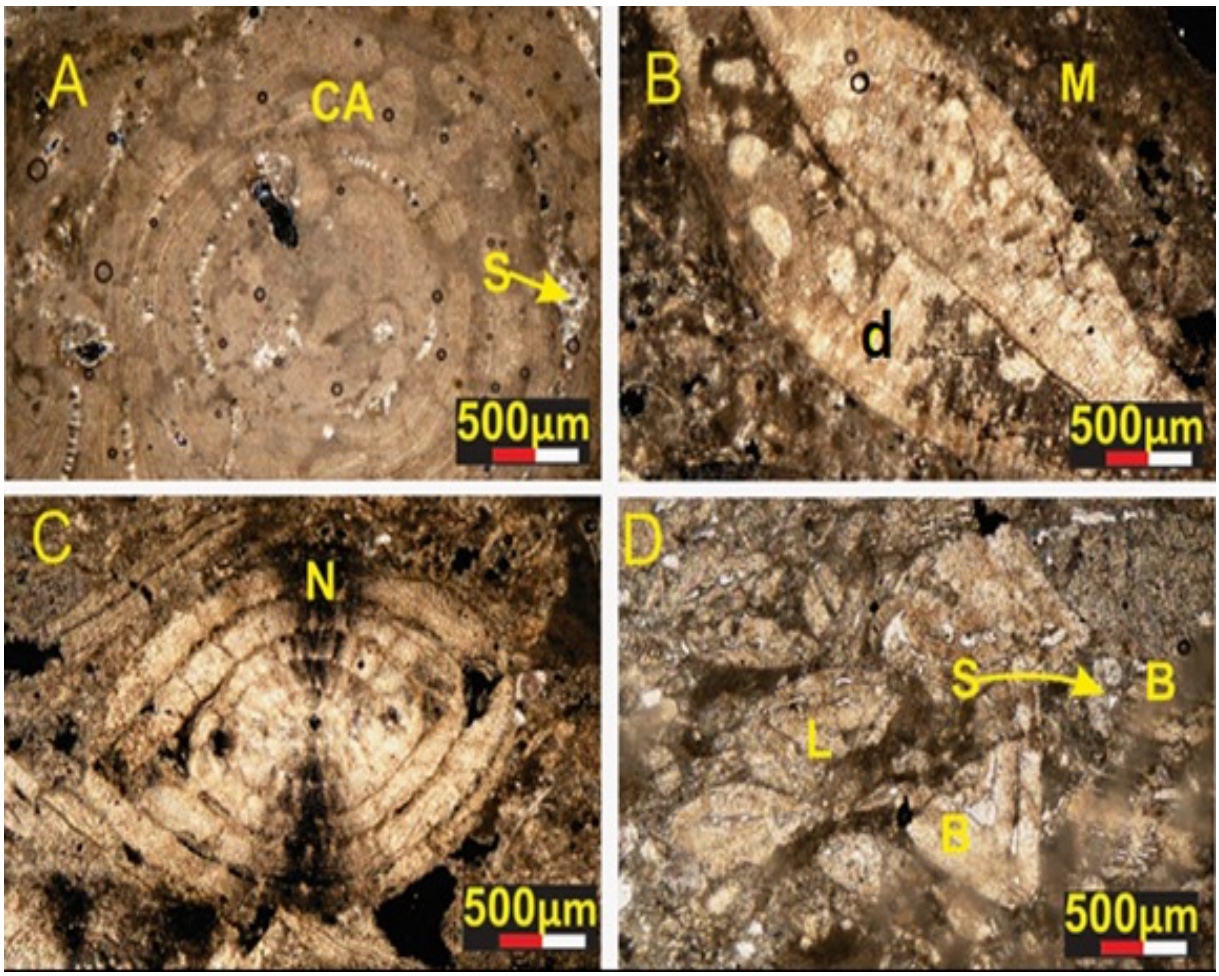

Fig. 4. Bioclastic packstone to floatstone Microfacies with Large Benthic Foraminifera (MF1), identified in Pirkoh Member, Zx-01. A: Coralline Algae(CA), spar (S). B: Micrite matrix (M), *Discocyclina* sp.(d). C: *Nummulites* sp. (N). D: *Lockhartia* sp. (L), spar cement (S) and broken fragments (B).

The MF1 represents shallow water settings with a relatively high-energy environment in oligotrophic and tropical conditions (Hallock and Glenn 1986; Hallock 1987). An abundance of LBF reflects the deposition in the middle ramp, below the Fair-Weather Wave Base (Figure.7). The occurrence of Nummulitids represents a water depth of less than 100 m (Hallock and Glenn, 1986; Hallock, 1987).

Table 1. Core sample analysis results discussed in this study.

Serial No.	Confining Pressure	Depth	Analysis No.	Porosity	Permeability		Samples
					Horizontal	Klinkenberg	
	Psi	(m)		%	(md)	(md)	
1	1000	610.3	A	16.27	1.14	0.84	■
2	1000	610.6	B	23.46	3.24	2.41	■
3	1000	610.9	C	21.29	1.95	1.42	
4	1000	611.2	D	14.27	0.51	0.47	
5	1000	611.5	E	11.10	0.12	0.08	
6	1000	611.8	F	12.43	0.12	0.08	■
7	1000	612.1	G				
8	1000	612.4	H	8.99	0.03	0.02	
9	1000	612.7	I	14.06	0.31	0.22	
10	1000	613.0	J	12.96	0.35	0.21	■
11	1000	613.3	K	25.96	7.73	6.14	■
12	1000	613.6	L	24.13	6.34	4.85	■
13	1000	613.9	M	23.18	4.07	3.50	
14	1000	614.2	N				
15	1000	614.5	O	6.24	0.03	0.02	
16	1000	614.8	P	13.86	0.11	0.06	■
17	1000	615.1	Q	12.23	0.48	0.27	
18	1000	615.4	R				■
19	1000	615.7	S	24.60	4.36	3.38	■
20	1000	616.0	T	20.31	2.76	2.04	
21	1000	616.3	U	27.47	1.94	1.45	■
22	1000	616.6	V	18.44	0.56	0.38	
23	1000	616.9	W	13.64	0.27	0.18	■
24	1000	617.2	X	16.04	1.18	0.85	■
25	1000	617.5	Y	12.29	1.37	1.05	
26	1000	617.8	Z	12.83	1.12	0.86	■
27	1000	618.1	A-1	10.29	0.12	0.07	■
28	1000	618.4	B-2	11.77	0.15	0.09	
29	1000	618.7	C-3	12.89	0.19	0.12	
30	1000	619.0	D-4	17.02	0.88	0.62	■

3.1.2 MF2: Bioclastic wackestone

The MF2 consists of medium grey to brownish grey colored, fossiliferous limestone. The MF2 is identified in nine thin sections (Table. 1). The allochems identified in these microfacies (Figure. 5) include *Nummulites* sp., Discocyclinids, *Assilina* sp., Coralline algae and *Lockhartia* sp. The grain size ranges from 1 to 2 mm. The fossil chambers of grains are often filled with the spar. These grains are mostly cemented by spar and calcite and micrite is also present as a matrix. The grain to matrix ratio in MF2 is 2:3 that shows a sixty percent matrix.

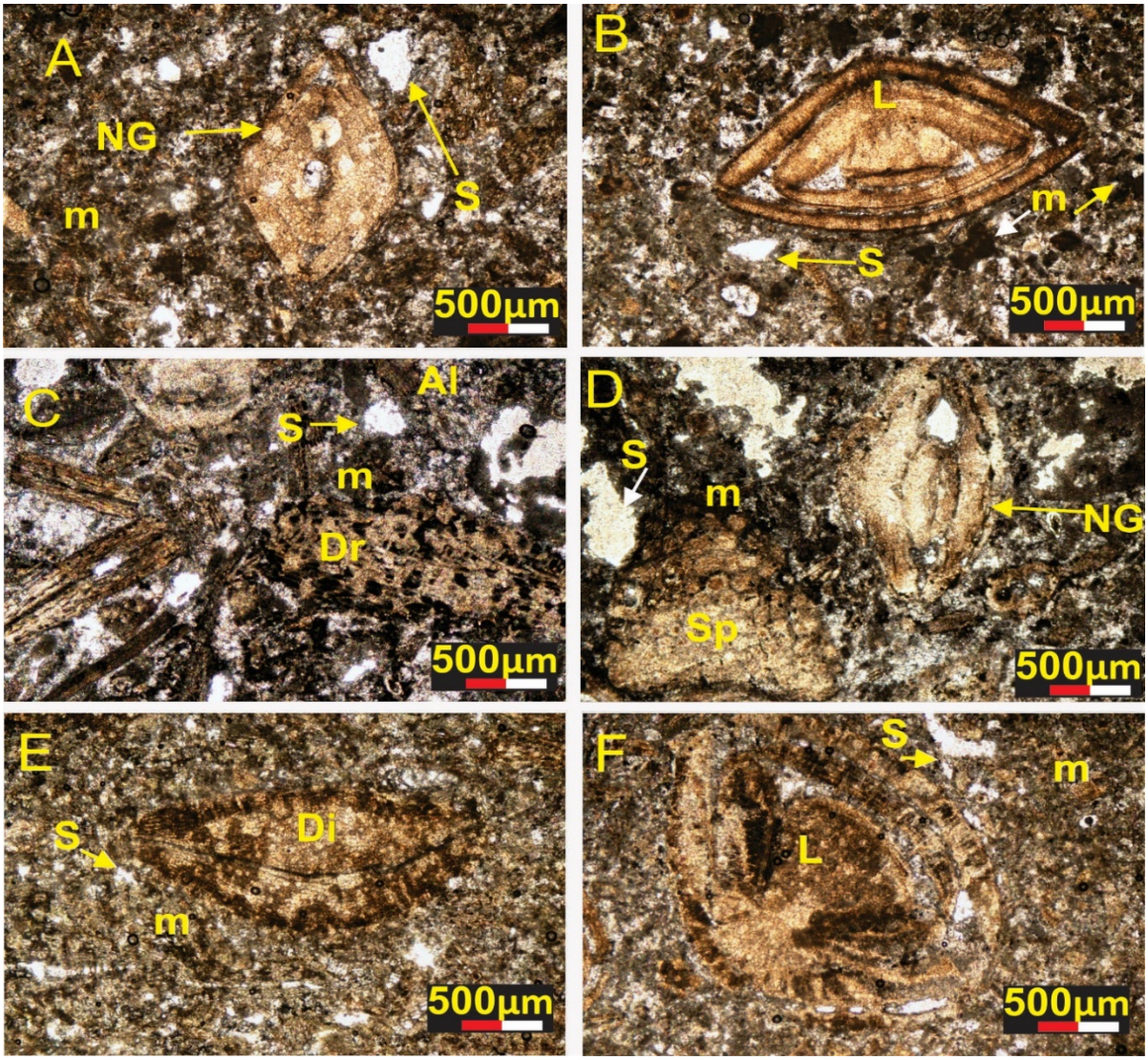

Fig. 5. Bioclastic wackestone Microfacies (MF2), identified in Pirkoh Member, Zx-01. A: *Nummulites globulus* (NG), Spar (S) as cement, matrix (m). B: Micrite matrix (m), spar (S), *Lockhartia* sp. (L). C: Spar cement (S), matrix (m), fragment of *Discocyclina ranikotensis* (DR), Calcareous algae Halimeda (Al). D: Sponge (Sp), *Nummulites globulus* (NG), Spar as cement (S), matrix (m). E):*Discocyclina* sp. (Di), Spar (S) as cement, matrix (m). F: *Lockhartia* sp. (L), Spar (S) as cement, matrix (m).

These features represent shallow marine environment in oligotrophic setting under the tropical to subtropical climatic conditions (Hallock and Glenn 1986; Hallock 1987). The occurrence of coralline algae represents high light penetration. Increased cement and bioclast represents agitated waters (Figure. 7) (Hallock and Schlager, 1986; Hallock, 1987)

3.1.3 MF3: Mudstone-wackestone microfacies

The MF3 consists of grey to brownish grey colored, hard, fractured limestone. The MF3 is identified in two thin sections (Table 1). The grains to matrix ratio in this microfacies are about 1:4. The allochems identified include *Assilina* sp.,

Discocyclinids and *Lockhartia* sp. with bioclasts (Figure. 6). The grains are less than 1mm in size. These grains are cemented majorly by spar. These grains are mostly supported by mud and cemented by microcrystalline calcite, whereas spar is minor.

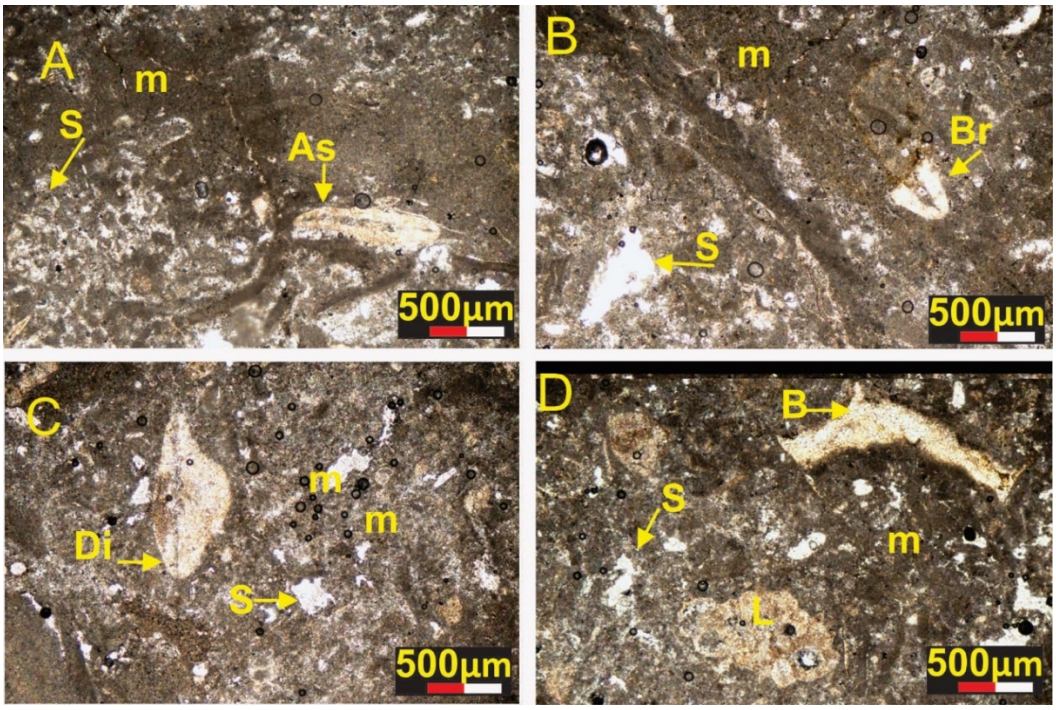

Fig. 6. Mudstone-wackestone microfacies (MF3), identified in Pirkoh Member, Zx-01. A: *Assilina laminose* (As), spar (S) as cement, matrix (m). B: Broken fragments (Br), spar (S) as cement, matrix (m). C: Discocyclinids (Di), spar (S) as cement, matrix (m). D: *Lockhartia* sp. (L), spar (S) as cement, matrix (m), broken fragment of bioclast (B).

The excessive occurrence of lime mud, broken, reworked and scarce LBF of MF3 represents calm shelf conditions and is interpreted to be deposited below the Fair-Weather Wave Base (FWWB) and above Storm Wave Base (SWB), upper and lower slope in non-rim setting or open carbonate platforms also confirmed by the other authors (Afzal *et al.*, 1997; Abbas1999). (Figure. 7)

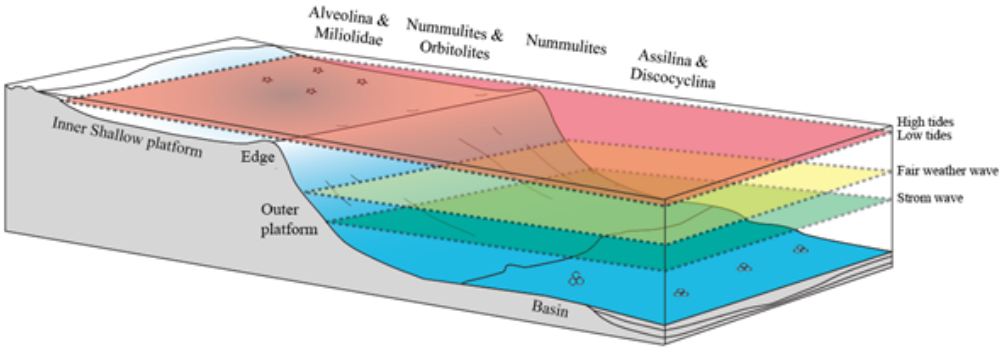

Fig. 7. A block diagram showing the distribution of the Large Benthic Foraminifera and environments of deposition.

3.2 Diagenesis

The identified diagenetic features include micritization, cementation, dissolution, reworked grains, fracture filling, neomorphism, compaction and dolomitization.

3.2.2 Micritization and cementation

The effect of micritization is observed in all three microfacies. The micritization is found from 20 to 80 percent in the three defined microfacies. MF2 and MF3 contain allomicrite (Figure. 8B) matrix related to abrasion and bioerosion (Flugel, 2004). It was also found that the MF3 contains micritic envelopes, indicating original aragonite (Figure. 8A) (Swei and Tucker, 2012).

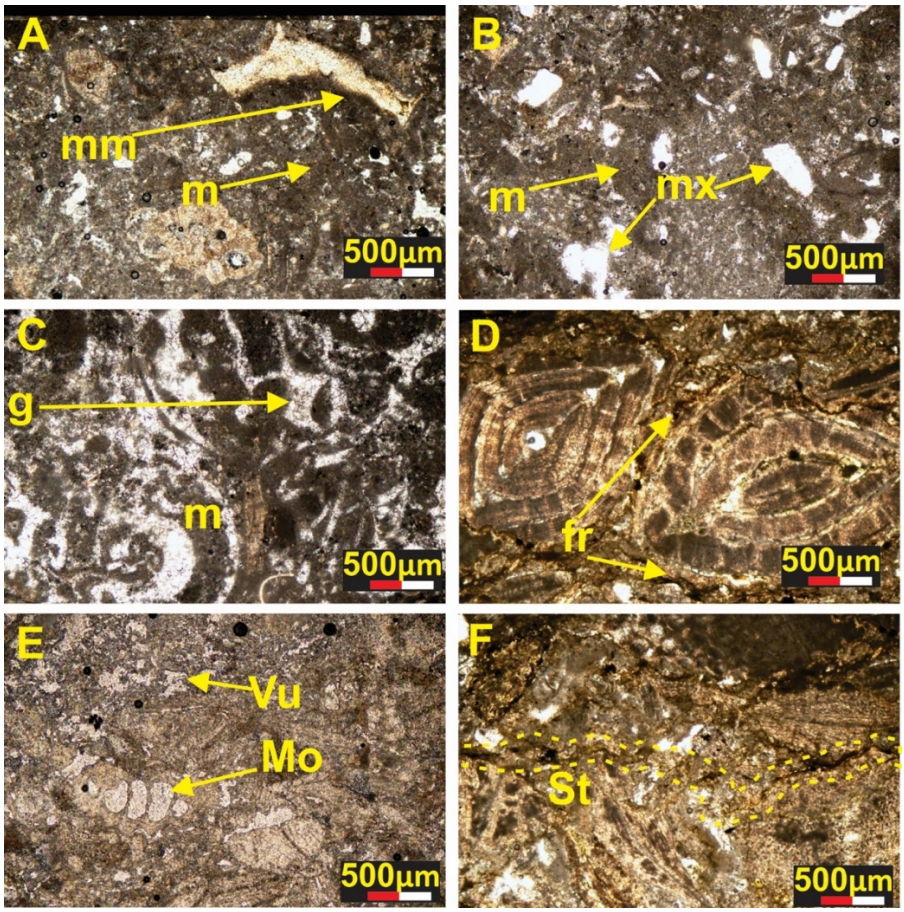

Fig. 8. Diagenetic features in Pirkoh limestone. A: Microbial micrite (Mm) in micrite matrix (m). B: pores filled by microcrystalline calcite (mx) and micrite (m) as matrix. C: granular cement fabric (g). D and E: fabric selective dissolution, fractures (fr), vuggy pore spaces (Vu) and molds (Mo). F: Stylolites (St).

The MF2 and MF3 mostly show microcrystalline (Figure. 8B) and granular (Figure. 8C) cement fabric comprising of calcite and dolomite minerals. Mostly this cement fills intraskeletal pores confirming the meteoric-vadose burial environment (Flügel, 2004). Apart from these cements, MF1 and MF2 display pyrite-filled pores and fractures that confirms the burial environment (Figure. 9C).

3.2.3 Neomorphism

Aggrading neomorphism has been extensively observed in many samples indicating a meteoric phreatic environment. The final stage of aggrading neomorphism is not found in any sample. This confirms the initial phase of aggrading neomorphism in this limestone.

3.2.4 Dissolution and compaction

Dissolution developed secondary porosity that includes molds, vugs, intra-particle and inter-particle pores i.e., fabric selective and non-fabric selective (Figure. 8D and 9B). Both physical (Figure. 9C) and chemical compaction (Figure. 8F) types were found in the form of abundant compaction features in MF1 and MF2. Furthermore, it is also apprehended that this compaction took place in the late stage of diagenesis.

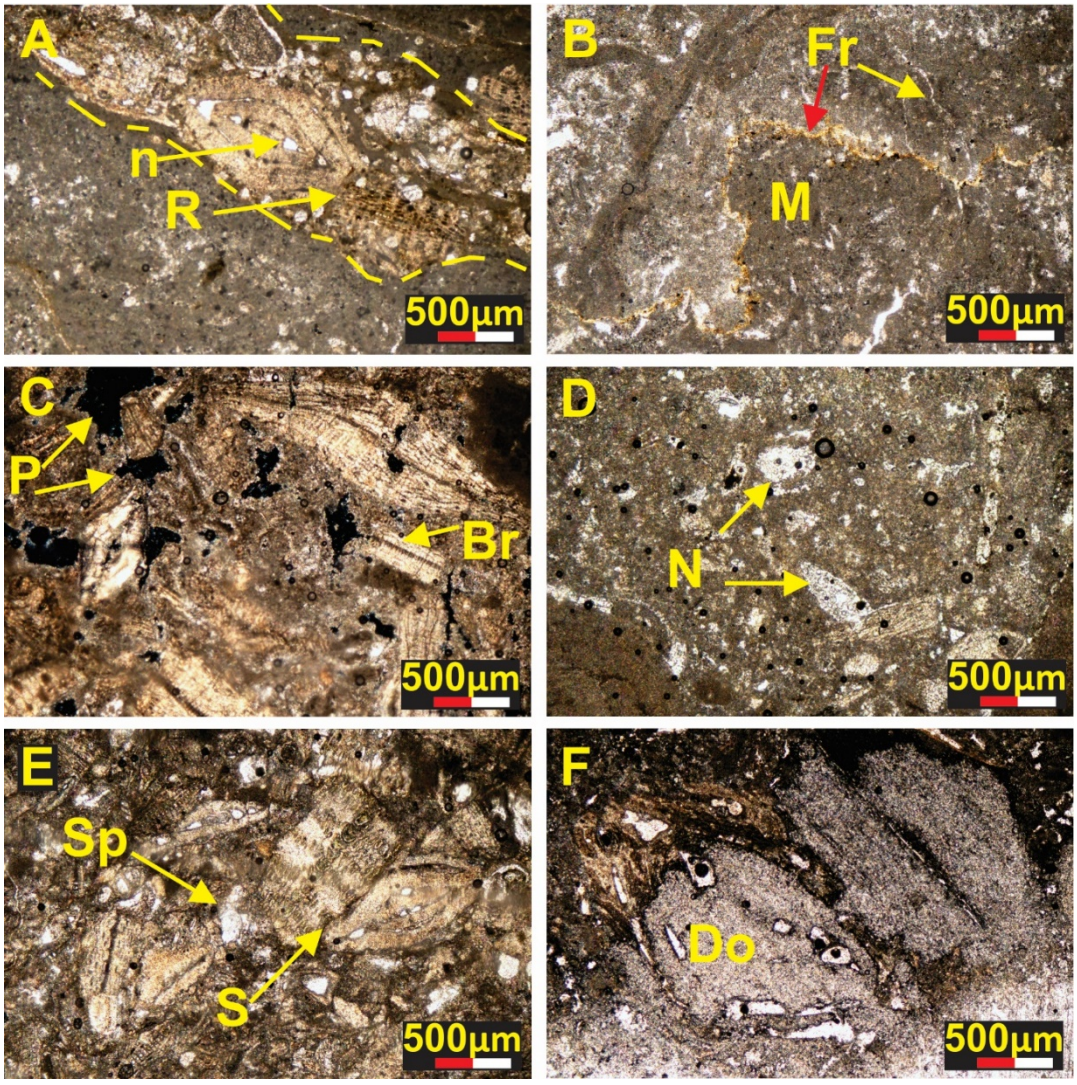

Fig. 9. Diagenetic features in Pirkoh limestone. A: Reworked sediments (R) including redeposited *Nummulites* sp. (n) and other bioclast in a fracture (marked by red dotted and dashed lines). B: fracture filling (Fr), two stages of fractures, an older stage shown by red arrow and a younger stage of fracture filling shown by white colored arrow. Micrite (M). C: pyritization (P) and broken fragments of bioclast (Br). D: Neomorphism (N). E: suturing (S). Spar (Sp). F: selective dolomitization (Do).

3.2.5 Dolomitization

The secondary type of dolomitization was observed in many thin sections (Figure. 9F). This type of dolomitization is termed fabric selective dolomitization and is an indicator of shallow water burial. MF2 and MF3 displayed fabric selective dolomitization.

3.3 Porosity and Permeability

The reservoir statistics based on the porosity and permeability test by the laboratory petrophysical measurements show porosity ranges between 6.24% to 27.47% with a mean value of 16.51%. The permeability varies from 0.11 to 6.59 mD whereas 2/3 of the samples show less than 1.5 mD (Figures. 10 and 11). Compared with the microfacies, Bioclastic wackestone shows the highest porosity which is 27.47 % as well as the lowest i.e., 6.21 % (Figure. 11).

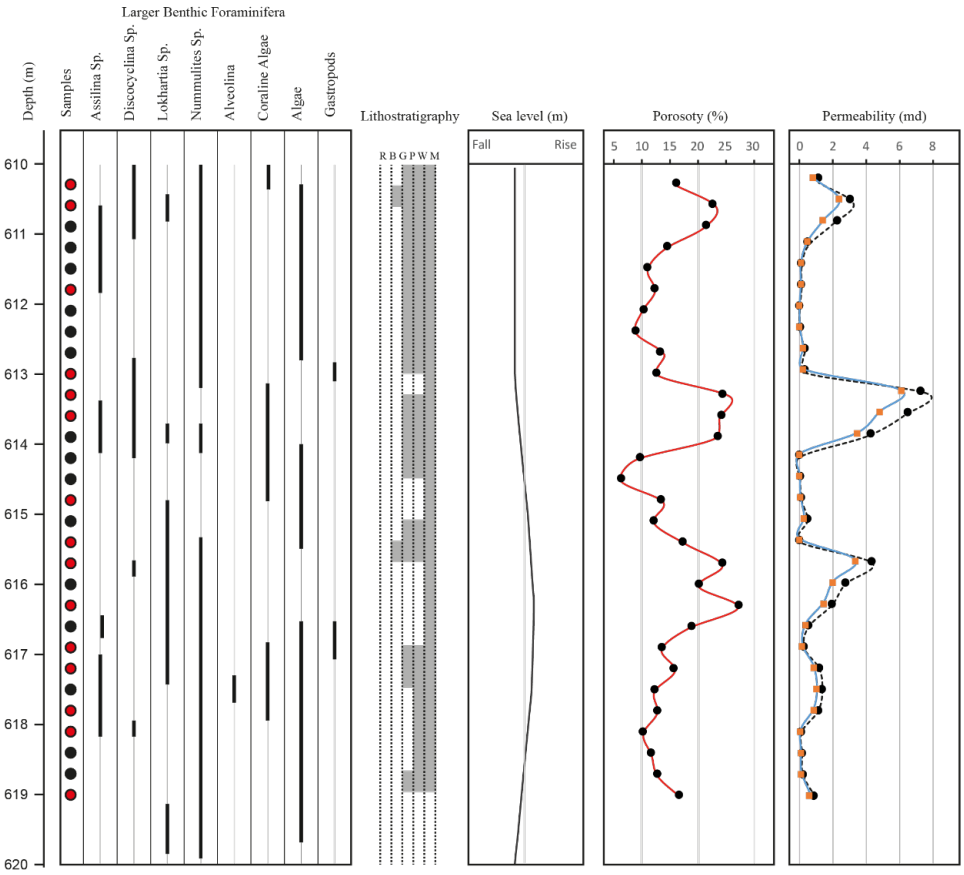

Fig. 10. Vertical distribution of microfacies, lithofacies, porosity and permeability with respective sea level curve in the study area.

Results show a reservoir potential of the Pirkoh Member with good to very good porosity. The primary porosity as interparticle and intraparticle porosity is the result of the depositional setting of varying grain size and void spaces in the foraminifera chambers such as Nummulitids (Jorry *et al.*, 2006). However, most of the depositional porosities are reduced due to cementation and compaction (Figures 8 and 9). Early cementation has reduced the

depositional porosity. This was shown by pores and foraminiferal chambers that were subsequently occluded by complete or partial cementation by pyrite, calcite. Apart from this, visible filled molds were also found. These cements and molds were derived from matrix dissolution along stylolites at the mesogenetic stage (Figures. 8 and 9). Microfractures, open-closed fractures, and cemented fractures were all identified (Figure. 8D). Some of these fractures may act as a conduit of fluid flow, while others may act as a barrier to the reservoir fluids in the event of stylolites formation (Figure. 8F).

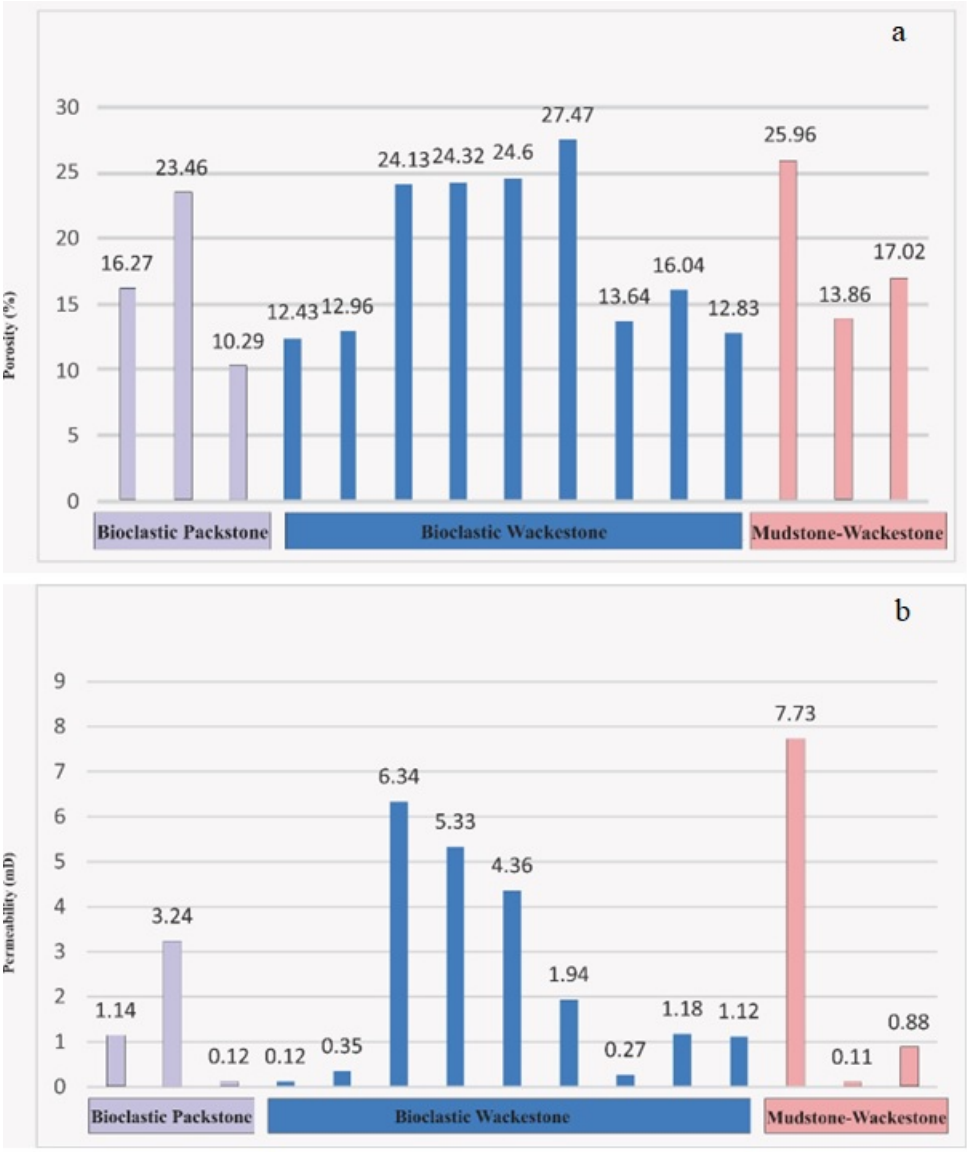

Fig. 11. Graphical distribution of the porosity (a) and permeability (b) with respect to microfacies.

A plot of porosity versus permeability (Figure. 12) reveals that permeability and porosity are correlated in an increasing trend suggest that permeability is directly related to the carbonate components and depositional framework. The reasons for the low permeability (Figure. 10) at certain intervals could be due to the argillaceous nature of limestone along with some diagenetic events including cementation, compaction and neomorphism.

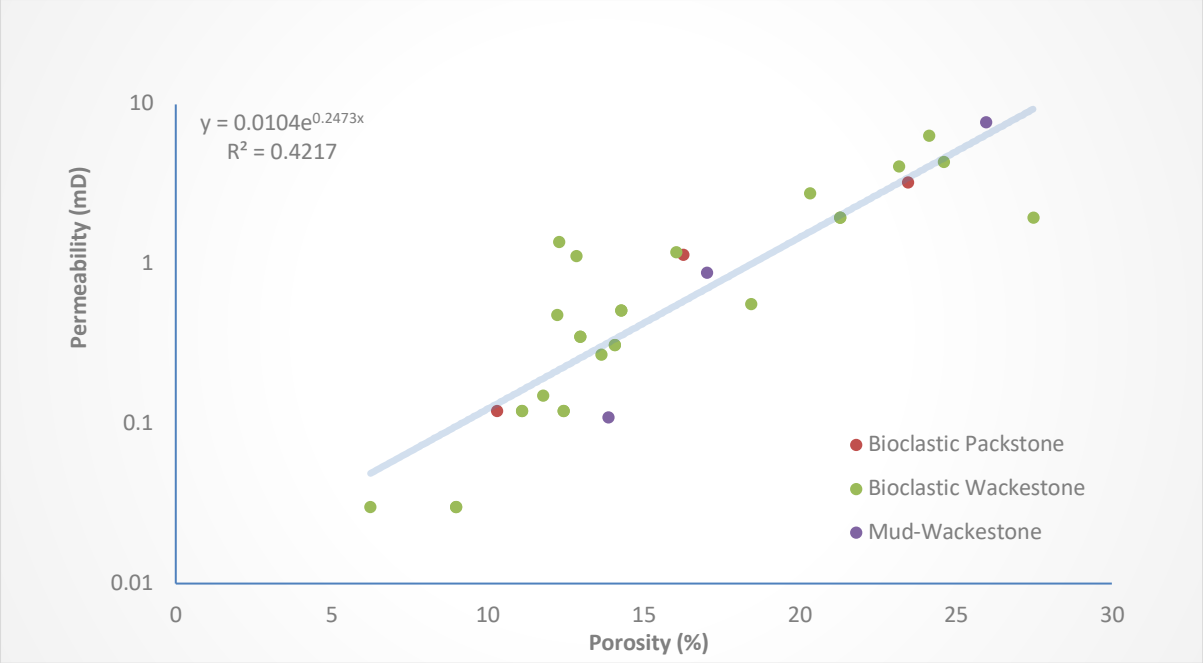

Fig. 12. Scatter-graph between Porosity and Permeability of Pirkoh Member.

4. Conclusions

The sedimentological studies show that the carbonate platform is predominantly composed of the *Nummulites* sp., *Lockhartia* sp., *Discocyclina* sp., and *Assilina* sp., and Coralline algae with micrite of the Middle Eocene age. This fossil assemblage represents a carbonate ramp setting developed in an oligotrophic tropical environment. Amongst three microfacies, bioclastic wackestone, bioclastic packstone to floatstone and mud-wackestone, reservoir potential of the carbonate is good with low to high porosity (6.24% to 27.47%), and low to fair permeability (0.11-6.59 mD). Variations in porosity and permeability are related to the depositional environment as well as other diagenetic processes that operated during the burial phase and altered the reservoir quality. The observed porosity is intra- and interparticle primary porosity and the secondary porosity developed due to fracturing and dissolution that enhanced the reservoir potential. Post burial diagenesis and the presence of clay or marly lithologies are potential reasons for low permeability. The findings of this study demonstrate good reservoir properties of the Eocene carbonates and help to correlate the vertical facies distribution of the reservoir characteristics.

ACKNOWLEDGMENTS

The authors would like to thank the Directorate General of Petroleum Concession (DGPC), Ministry of Petroleum and Natural Resources, Pakistan for providing well data. Hydrocarbon Development Institute of Pakistan and Oil and Gas Development Company, Pakistan is thanked for providing services for core analysis. Furthermore, we extend our gratitude to the editorial team and the reviewers for suggesting improvements in this manuscript.

References

Abbas, G. (1999). Microfacies, depositional environments, diagenesisdiagenesis, and porosity development in Limestone horizons of Kirthar Formation (Middle Late Eocene) in frontal parts of Sulaiman fold belt and adjoining areas, Pakistan. Unpublished PhD Thesis submitted to University of Punjab, Pakistan.

Abdullah, S.O. (2020). Biostratigraphic analysis of the K/Pg boundary using calcareous Nannofossil from Sulaimani area, Kurdistan Region, Iraq. *Kuwait Journal of Science*, *47*(4).

Afzal, J., Khan, A.M. & Shafique, N.A. (1997). Biostratigraphy of Kirthar Formation (Middle to Late Eocene), Sulaiman Basin, Pakistan. *Pakistan Journal of Hydrocarbon Research*, *9*,: 15-33.

Afzal, J., Williams, M. & Aldridge, R.J. (2009). Revised stratigraphy of the lower Cenozoic succession of the Greater Indus Basin in Pakistan. Journal of MicropalaeontologyMicropaleontology 28:, 7–23. https://doi.org/10.1144/jm.28.1.7

Ali, N., Özcan, E., Yücel, A.O., Hanif, M., Hashmi, S.I., Ullah, F., Rizwan, M. & Pignatti, J. (2018). Bartonian orthophragminids with new endemic species from the Pirkoh and Drazinda formations in the Sulaiman Range, Indus Basin, Pakistan. Geodynamica Acta 30:, 31–62. https://doi.org/10.1080/09853111.2017.1419676

Asaad, I.S. (2021). Lithostratigraphy and microfacies analysis of Avanah Formation (Middle Eocene) in Gomaspan section northeast Erbil City, Iraqi Kurdistan region. *Kuwait Journal of Science*.

Bahman, F.K. (2022). Organic geochemical and petrographical characteristics of the major lower cretaceous petroleum source rock (Makhul Formation) in Kuwait-Arabian Gulf. *Kuwait Journal of Science*, *49*(1).

Burchette, T.P. (2012). Carbonate rocks and petroleum reservoirs: a geological perspective from the industry. Geological Society, London, Special Publications 370,: 17–37. https://doi.org/10.1144/SP370.14

Dunham, R.J. (1962). Classification of Carbonate Rocks According to Depositional Texture. In W. E. Ham, (ed) Classification of Carbonate Rocks. American Association Petroleum Geologists Memoirs 1:, 108-121.

Ehsan, M., Gu, H., Akhtar, M.M., Abbasi, S.S. & Ehsan, U. (2018). A geological study of reservoir formations and exploratory well depths statistical analysis in Sindh Province, Southern Lower Indus Basin, Pakistan. Kuwait Journal of Science, 45(2).

Embry, A.F. & Klovan, J.E. (1971). A Late Devonian Reef Tract on Northeastern Banks Island, N.W.T. Bulletin of Canadian Petroleum Geology 19:, 730–781.

Flügel, E. (2004). Microfacies of Carbonate Rocks - Analysis, Interpretation and Application. Springer Berlin Heidelberg, Berlin, Heidelberg.

Garland, J., Neilson, J., Laubach, S.E. & Whidden, K.J. (2012). Advances in carbonate exploration and reservoir analysis. Geological Society, London, Special Publications 370:, 1–15. https://doi.org/10.1144/SP370.15

Hallock, P. (1987). Fluctuations in the trophic resource continuum: A factor in global diversity cycles.? Paleoceanography 2:, 457–471. https://doi.org/10.1029/PA002i005p00457

Hallock, P. & Glenn, E.C. (1986). Larger Foraminifera: A Tool for Paleoenvironmental Analysis of Cenozoic Carbonate Depositional Facies. Palaios 1:, 55–64. https://doi.org/10.2307/3514459

Hallock, P. & Schlager, W. (1986). Nutrient excess and the demise of coral reefs and carbonate platforms. PaAlLaAiIoOsS 1:, 389. https://doi.org/10.2307/3514476

Handford, C.R. & Loucks, R.G. (1993). Carbonate Depositional Sequences and Systems Tracts--Responses of Carbonate Platforms to Relative Sea-Level Changes: Chapter 1.

Höntzsch, S., Scheibner, C., P. Brock, J. & Kuss, J. (2013). Circum-Tethyan carbonate platform evolution during the PalaeogenePaleogene: the Prebetic platform as a test for climatically controlled facies shifts. Turkish Journal of Earth Sciences 22:, 891–918. https://doi.org/10.3906/yer-1207-8

Jorry, S.J., Hasler, C.A. & Davaud, E. (2006). Hydrodynamic behaviourbehavior of Nummulites: implications for depositional models. Facies 52:, 221–235. https://doi.org/10.1007/s10347-005-0035-z

Kazmi, A.H. & Abbasi, I.A. (2008). Stratigraphy & historical geology of Pakistan (p. 524). Peshawar, Pakistan: Department & National Centre of Excellence in Geology.

Kazmi, A.H. & Jan, M.Q. (1997). Geology and Tectonics of Pakistan. Karachi, Graphic Publishers.

Khalid, P., Qayyum, F. & Yasin, Q. (2014). Data-Driven Sequence Stratigraphy of the Cretaceous Depositional System, Punjab Platform, Pakistan. Surv Geophys 35:, 1065–1088. https://doi.org/10.1007/s10712-014-9289-8

Khan, M., Arif, M., Ali, N., Yaseen, M., Ahmed, A. & Siyar, S.M. (2016). Petrophysical parameters and modelling of the Eocene reservoirs in the Qadirpur area, Central Indus Basin, Pakistan: implications from well log analysis. Arab J Geosci 9:, 425. https://doi.org/10.1007/s12517-016-2373-2

Khan, M.A. & Raza, H.A. (1986). The role of geothermal gradients in hydrocarbon exploration in Pakistan. J Petroleum Geol 9:, 245–258. https://doi.org/10.1111/j.1747-5457.1986.tb00388.x

Markello, J.R., Keopnick, R.B., Waite, L.E. & Collins, J.F. (2008). The Carbonate Analogs Through Time (Catt) Hypothesis and the Global Atlas of Carbonate Fields—A Systematic and Predictive Look at Phanerozoic Carbonate Systems, in: Lukasik, J., Simo, J.A. (Toni) (Eds.), Controls on Carbonate Platform and Reef Development. SEPM (Society for Sedimentary Geology). https://doi.org/10.2110/pec.08.89

Miraj, M. A. F., Javaid, H., & Ahsan, N. (2021). An integrated approach to evaluate hydrocarbon potential of Jurassic Samana Suk Formation in Middle Indus Basin, Pakistan. Kuwait Journal of Science, 48(4).

Qayyum, F., Hanif, M., Mujtaba, M., Wahid, S. & Ali, F. (2016). Evaluation of source rocks using one dimensional maturity modeling in Lower Indus Basin, Pakistan. Arabian Journal of Geosciences 9. https://doi.org/10.1007/s12517-015-2244-2

Sarg, J.F. (1988). Carbonate sequence stratigraphy, in: Sea-Level Changes: An Integrated Approach (SEPM Special Publication No. 42).

Serra-Kiel, J., Hottinger, L., Caus, E., Drobne, K., Ferrandez, C., Jauhri, A.K, Less, G., Pavlovec, R., Pignatti, J., Samso, J.M., Schaub, H., Sirel, E., Strougo, A., Tambareau, Y., Tosquella, J. & Zakrevskaya, E. (1998). Larger foraminiferal biostratigraphy of the Tethyan Paleocene and Eocene. Bulletin de la Société Géologique de France 169:281–299

Shahzad, K., Betzler, C., Ahmed, N., Qayyum, F., Spezzaferri, S. & Qadir, A. (2018). Growth and demise of a Paleogene isolated carbonate platform of the Offshore Indus Basin, Pakistan: effects of regional and local controlling factors. International Journal of Earth Sciences 107,: 481–504. https://doi.org/10.1007/s00531-017-1504-7

Shahzad, K., Betzler, C. & Qayyum, F. (2019). Controls on the Paleogene carbonate platform growth under greenhouse climate conditions (Offshore Indus Basin). Marine and Petroleum Geology 101,: 519–539. https://doi.org/10.1016/j.marpetgeo.2018.12.025

Siddiqui, N.K. (2004). Sui Main Limestone: Regional geology and the analysis of original pressures of a closed-system reservoir in central Pakistan. AAPG Bulletin 88:, 1007–1035. https://doi.org/10.1306/012004200150

Swei, G.H. & Tucker, M.E. (2012). Impact of Diagensis on reservoir quality in ramp carbonates: Gialo Fromation (middle Eocene), Sirt Basin, Libya. Journal of Petroleum Geology 35:, 25–47. https://doi.org/10.1111/j.1747-5457.2012.00517.x

Wandrey, C.J., Law, B.E. & Shah, H.A. (2004). Sembar-Goru/Ghazij Composite Total Petroleum System, Indus and Sulaiman-Kirthar Geologic Provinces, Pakistan and India, in: Petroleum Systems and Related Geologic Studies in Region 8, South Asia: U.S. Geological Survey Bulletin 2208-C, 2208-C. U.S. Geological Survey Bulletin, Pp. 23.

Submitted: 21/08/2021
Revised: 03/02/2022
Accepted: 07/02/2022
DOI: 10.48129/kjs.15597

Using isotopes for dating and residence time of groundwater in an aquifer, a case study at Al-Najaf, Middle Iraq

Arshad W.A. Al-Enezy[1], Mohanad R.A. Al-Owaidi[2*], Mohammed L. Hussein[3]

[1]*General Commission of Groundwater, Najaf, Ministry of Water Resources, Najaf, Iraq*

[2]*Dept. of Applied Geology, College of Science, University of Babylon, Babylon, Iraq*

[3]*Dept. of Building and Construction Engineering Technologies, Al-Mustaqbal University College, Babylon, Iraq*

[*]*Corresponding Author: sci.mohanad.rasim@uobabylon.edu.iq*

Abstract

Groundwater is the main source of sustaining life in the Najaf Desert that helps sustain human and animals' lives. The aquifer of the Dammam Formation is considered the main source of groundwater in the study area. The isotope elements have been used as a geochemical indicator to determine the age, direction of flow and the effect of rainwater of this area. The values of stable isotopes $\delta^{18}O$ and $\delta^{2}H$ range between -2.56‰ to -1.99‰, and between 7.12‰ to -4.84‰ with an average of -2.32‰ and -6.20‰ in rainfall respectively. Their values range from -3.26‰ to -2.01‰ for $\delta^{18}O$, and from -27.00‰ to -16.21‰ for $\delta^{2}H$ with an average of -2.70‰ and -22.27‰ in the Dammam groundwater respectively. The groundwater is old and does not mix with new water, because tritium has not been not detected. Furthermore, the $\delta^{18}O$ and $\delta^{2}H$ values show that the rainwater, which feeds the aquifer does not come from the continental lands. They represent a humid and cold climate, as well as a considerable amount of rainfall in the past. Analyses of ^{14}C indicate that the groundwater dates back to approximately 4176 years ago. The groundwater is moving from the west and southwest directions to the north and northeast directions.

Keywords: Dammam; groundwater; najaf; radioactive isotopes; stable isotopes.

1. Introduction

The groundwater is studied in Al-Najaf Governorate, middle Iraq where the desert covers most of its territory. The inhabitants of this area live in small towns and villages, and many of them are Bedouins leading a pastoral life. The study area is characterized by the absence of rivers, and during most months of the year there is no surface water except for a few rainy days. As such, the inhabitants of the area rely on groundwater for their whole needs. The study area contains a large reserve and significant quality of groundwater in the Dammam aquifer. It is a wonderful groundwater system which is not deep but is near to the surface (Al-Enezy, 2019 and Aladwani, 2022).

Many hydrological studies use environmental isotopes to provide evidence for the knowledge of water sources, quality, water age, groundwater recharge, and movement of groundwater (Izbicki *et al.*, 1998). Groundwater quality is affected by the interaction of rocks with various water bodies, geochemical evolution, and salinity, as well as polluting processes (Clark & Fritz, 1997, Wilopo & Putra, 2021). Isotopes are some particular elements that have the same atomic number but have a different atomic weight, including hydrogen atoms (^{1}H, ^{2}H, and ^{3}H). This means that they have the same atomic number; yet, they have different mass numbers greater than the atoms of the same chemical elements. This can create a tight bond which requires a high amount of energy to break the nucleus into its constituent nucleons (Kendall & Caldwell, 1998).

This study aims to determine the groundwater dating in the area under scrutiny. The aims can be fulfilled by using radioactive isotopes. Delineation of recharge and discharge zones and the movement paths of groundwater have been performed by identifying the newest groundwater age for each region. Stable isotope analysis of rainwater compositions aims to determine the origin of the air mass in the region. Stable isotope analysis for groundwater is deployed to check out the mixture of the new and old waters. As a result, the stable isotopes are used to determine the origin of salination. The coordinates of the study area are at the latitudes 31º8′43.74″- 31º26′8.38″ and longitudes 44º02′42.33″- 44°30′52.30″ which span approximately over 9630 km^2 (Figure 1).

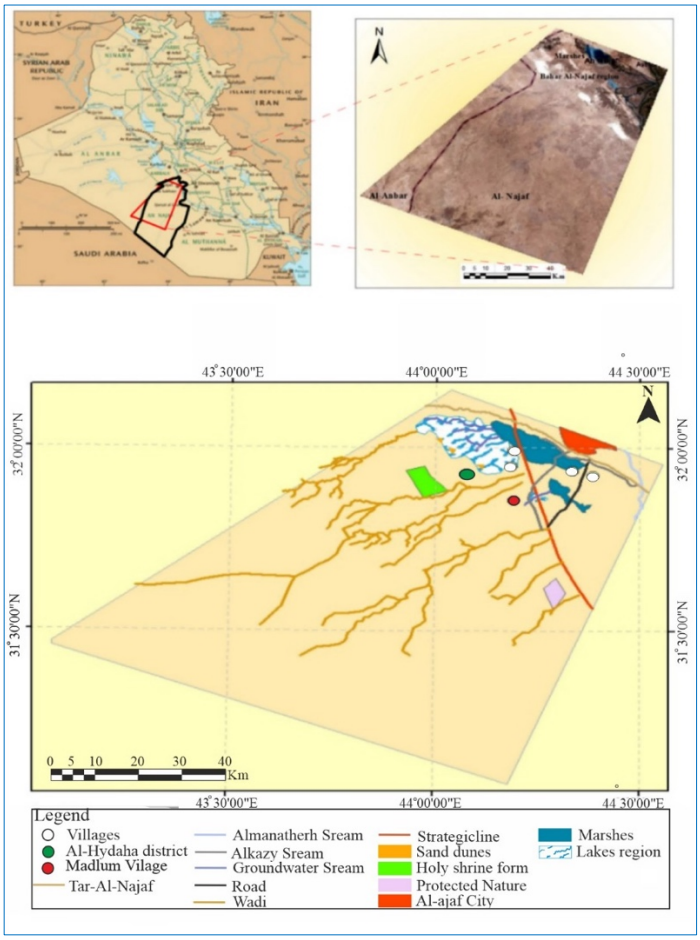

Fig. 1. Location and features map of the study area.

2. Geological setting

2.1 Geological description

The region is located within the boundaries of the Salman Subzone including the stable shelf which is characterized by its simple structures (Buday, 1980). From the newest to the oldest, the stratigraphic sequence arranges over Dibdibba, Injana, Nfayil, Euphrates, and Dammam formations (Al-Owaidi *et al.*, 2021).

Geomorphologically, Bahr-Al-Najaf depression is filled with water and many breeding fish lakes occupy the east side of the study area (Al-Owaidi *et al.*, 2021). A few reliefs are seen to rise gradually from the north and northeast to the south and southwest, approximately over 50m of the sea level for every 10-15 km (Jassim & Goff, 2006). The valleys Haussab, Al-Kharr, and other smaller ones including Al-Rhimawi and Abo Kumssat are subsumed under the study area. The Abu Jir Fault zone, extending to the eastern side, forms the stable shelf boundary. It has played an important role in controlling the groundwater movement in the study area.

2.2 Hydrological setting

Although the studied area is affected by a dry desert climate, yet; rainfall sometimes occurs in spring and summer seasons resulted from a severe intermittent rain once every several years. These rainfall events have caused a shallow flow of rainwater and created many temporary and ephemeral rivers in the desert, which all flood the large valleys downwards. The Dammam aquifer (Dammam Formation) is the main supplier of groundwater in the southern desert of Iraq and in Kuwait as well. (Al-Ruwaih, 1993).

3. Analysis Methods

Six samples of rainfall were collected in the time course of six months (January, February, March, April, May, and June/ 2020) to determine the stable isotopes $\delta^{18}O$ and $\delta^{2}H$ of rainwater. Twelve groundwater samples were tapped from wells (during January 2020), following the procedure of the International Atomic Energy Agency (IAEA) (2009) instructions applied to the analysis of ^{2}H and ^{18}O isotope concentration. The samples were collected in polyethylene (PE) containers (impermeable to light) each of 30 ml capacity. The stable isotope samples were analyzed at UC Davis Stable Isotope Facility, Department of Plant Sciences, on Shields Avenue, Davis, California, 95616, USA.

Three samples were analyzed for Tritium (^{3}H), and other four samples were analyzed for radiocarbon (^{14}C) which have been collected as radioactive isotopes in order to determine the groundwater age. For proper analysis of ^{14}C depending on IAEA, 2.5 gm of carbon must be obtained. Ordinarily, this amount can be precipitated from a total of 120 liters of water samples depending on the alkalinity of groundwater (Geyer *et al.*, 1993). Then, concentrated NaOH was added to raise the pH of the sample to about 11; then about 150 gm of $BaCl_2$ powder was added and the mixture was stirred well for 10 minutes leaving it to precipitate for an hour. Later, 1 liter of distilled water was pulled from the bottom of the container to precipitate. Finally, the samples were analyzed by using a Tri-Carb 3110TR along with low activity liquid scintillation analyzer (LSA) (PerkinElmer, Inc., Waltham, MA, USA), in the laboratory of the Department of Water Analysis/ Ministry of Science and Technology/ Iraq. The sample coordinates are shown in Table 1.

Table 1. Studied wells coordinate

Well No.	Longitude	Latitude	Elevation
W.1	44°15'47.506"E	31°55'13.294"N	6m
W.3	44°15'59.034"E	31°48'50.250"N	22m
W.6	44°18'46.106"E	31°50'30.144"N	21m
W.8	44°20'12.412"E	31°55'14.818"N	8m
W.9	44°14'07.575"E	31°51'15.225"N	30m
W.11	44°14'33.919"E	31°51'50.946"N	29m
W.13	44°16'22.212"E	31°45'34.115"N	39m
W.17	44°12'13.641"E	31°52'13.636"N	35m
W.20	44°08'55.239"E	32°00'46.465"N	17m
W.22	44°05'37.221"E	32°01'56.412"N	23m
W.27	44°05'15.475"E	32°00'25.549"N	29m
W.31	44°08'43.012"E	31°57'07.715"N	32m
W.1	44°15'47.506"E	31°55'13.294"N	6m
W.22	44°06'02.202"E	32°01'08.589"N	21m
W.12	44°14'33.919"E	31°51'50.946"N	25m
W.39	44°5'09.765"E	31°13'00.082"N	26.5m

4. Results

4.1 Stable isotopes

After analyses, the stable isotopes in rainfall water and groundwater samples are described below.

4.1.1 Stable isotopes in rainfall samples

The stable isotope composition ($\delta 1^8O$ and δ^2H) in rainwater indicated that the lowest value was measured in January and the highest value in June. The isotopic composition values were recorded between -2.56‰ and -1.99‰ and between -7.12‰ and -4.84‰ for $\delta^{18}O$ and ^2H with an average of -2.32‰ and -6.3‰ respectively (Table 2).

Table 2. Rainwater values of $\delta^{18}O$ and δ^2H during 2020

Stable Isotope	Jan.	Feb.	Mar.	Apr.	May	Jun	Min.	Max.	Average
δ^2H	-7.12	-7.03	-6.91	-6.89	-4.91	-4.84	-7.12	-4.84	-6.3
$\delta^{18}O$	-2.56	-2.52	-2.45	-2.41	-2.1	-1.99	-2.56	-1.99	-2.32

4.1.1.1 Deuterium-excess

D-excess values are an index that shows the physical-chemical characteristics of water if it is evaporated (Tsujimura *et al.*, 2007). A typical character that shows the origin of air masses from which the precipitation is formed is a deuterium excess. D-excess reflects the prevailing conditions during the evolution and the interaction or the mixing up of air mass with the

locations of precipitations. However, the value d defines a slope of eight and is calculated for any precipitation sample as the equation (1) below can show (Faucher *et al.*, 2020):

$$d = \delta^2 H - 8 \times \delta^{18} O \quad (1)$$

Under conditions of 100% humidity, the vapor will be in isotopic equilibrium with seawater, but when the humidity is lower than 100%, excess deuterium can be found in the rain. Thus, the increase of deuterium is attributed to isotopic exchange, moisture, and lower humidity conditions. The values signal the importance of recycled continental vapors, if they are higher than 100.5 (Table 3) (Clark & Fritz,1997).

Table 3. Values of D-excess in precipitation

Months	d-excess values
January	13.04
February	13.45
Mar	12.69
April	12.39
May	11.89
Jun	11.08
Min	11.08
Max	13.45
Average	12.23

4.1.2 Stable isotopes in groundwater

The stable isotope composition of groundwater samples ranged from -3.26‰ to -2.01‰ for $\delta^{18}O$ and from -27.00‰ to -16.21‰ for $\delta^{2}H$ with an average of -2.70‰ and -22.27‰ respectively (Table 4).

Table 4. Values of $\delta^{18}O$ and $\delta^{2}H$ in the groundwater during 2020

Sample ID	$\delta^{2}H$	$\delta^{18}O$
W.1	-25.65	-3.14
W.3	-21.64	-2.67
W.6	-26.16	-3.14
W.8	-27.00	-3.26
W.9	-25.80	-2.99
W.11	-22.42	-2.70
W.13	-26.47	-3.17
W.17	-25.67	-3.02
W.20	-17.91	-2.22
W.22	-16.21	-2.01
W.27	-17.23	-2.16
W.31	-16.41	-2.10
min	-27.00	-3.26
max	-16.21	-2.01
average	-22.27	-2.70

4.1.2.1 D-excess in the groundwater

Deuterium excess is a measurement of non-equilibrium conditions during the evaporation of water in a relatively humid conditions (Sebastian *et al.*, 2010). Groundwater D-excess values ranged from -1.91‰ to -0.39‰, with an average of -0.66‰ (Table 5).

Table 5. d-excess of groundwater samples

Wells ID	**W.1**	**W.3**	**W.6**	**W.8**	**W.9**	**W.11**	**W.13**	**W.17**	**W.20**	**W.22**	**W.27**	**W.30**
D-excess	-0.5	-0.26	-1.02	-0.92	-1.91	-0.82	-1.13	-1.49	-0.19	-0.13	0.05	0.39
Min.	-1.91					Max.	0.39				Avg.	-0.66

4.1.2.2 Origin salinity

The origin of salinity and mechanisms of groundwater salinization can be determined successfully by deploying stable isotopes (IAEA, 2009). The relationship between $\delta^{18}O$ and Ec can be used to detect groundwater salinity. Salinization originates from the dissolution of the salts. This means that there are no accompanying notable changes in the stable isotopic composition. Yet, the existing of sensitive changes in the stable isotopic composition are due to the presence of the mixing or the evaporating processes (IAEA, 2001).

4.2 Radioactive isotopes in groundwater

Radioactive isotopes ^{3}H and ^{14}C can be used to measure the time and the environmental radionuclides used to estimate the age or the circulation of groundwater (Mook, 2000).

4.2.1 Tritium (^{3}H)

Tritium, the radioisotope of hydrogen (^{3}H), here had been relatively abundant: (0.5×10-5%). Tritium is continual and can be produced in small quantities in the upper atmosphere by the interaction of cosmic rays with gaseous nitrogen and thermonuclear weapons testing (Clark and Fritz, 1997). It can be used to provide information about the residence time and groundwater movement. Tritium has a short-live reaching to no more than 12.32 years, and its concentration is realized as tritium units TU (Fetter, 2001). In this study, tritium had not been detected in the samples (TU= zero) due to its short half-life.

4.2.2 Carbone-14

Carbone-14 exists in several naturally occurring isotopes, ^{12}C, ^{13}C, and ^{14}C. It is formed in the atmosphere by the bombardment of ^{14}N cosmic radiation (Faure & Mensing, 2005). The long half-life, 5730 years, of ^{14}C makes it useful for the late Quaternary period (Godwin, 1962). Carbon-14 activities are expressed as present and modern carbon (pMC): the fractions of CO_2, and dissolved inorganic carbon (DIC). Dissolved organic carbon (DOC) is derived from the living biomass record of ^{14}C activities, which is close to the modern atmospheric level of ~100 (pMC) (Faure & Mensing, 2005).

Radiocarbon dating of DIC in groundwater was based on the radioactive decay of ^{14}C. Rainwater infiltrated the soil whereby the DOC contained much ^{14}C during groundwater

recharge. The carbonic acid dissolved the old soil carbonate devoid of the ^{14}C (DIC). Other physical and chemical processes in the aquifer affected the ^{14}C activity of DIC. The radiocarbon age of DIC must be converted into actual age.

The second step involves the correction of the ^{14}C value controlled by geochemical reactions in the aquifer (Clark & Fritz, 1997).

5. Discussion

Depending on the values of stable isotopes $\delta^{18}O$ and $\delta^{2}H$ for rainwater (Table 2), the equation (2) of the Najaf Meteoric Water Line (NMWL) of the study area was linear

$$\delta^2 H = 4.5\delta^{18}O + 4.32 \quad (2)$$

The slope 4.5 pointed to the enrichment process of isotope composition which was more than the Global Meteoric Water Line (GMWL) due to the fractionation process, where the NMWL could be governed by the local climate factors such as a temporal change in the moisture source and the seasonal variations (Durowoju *et al.*, 2019) (Figure 2).

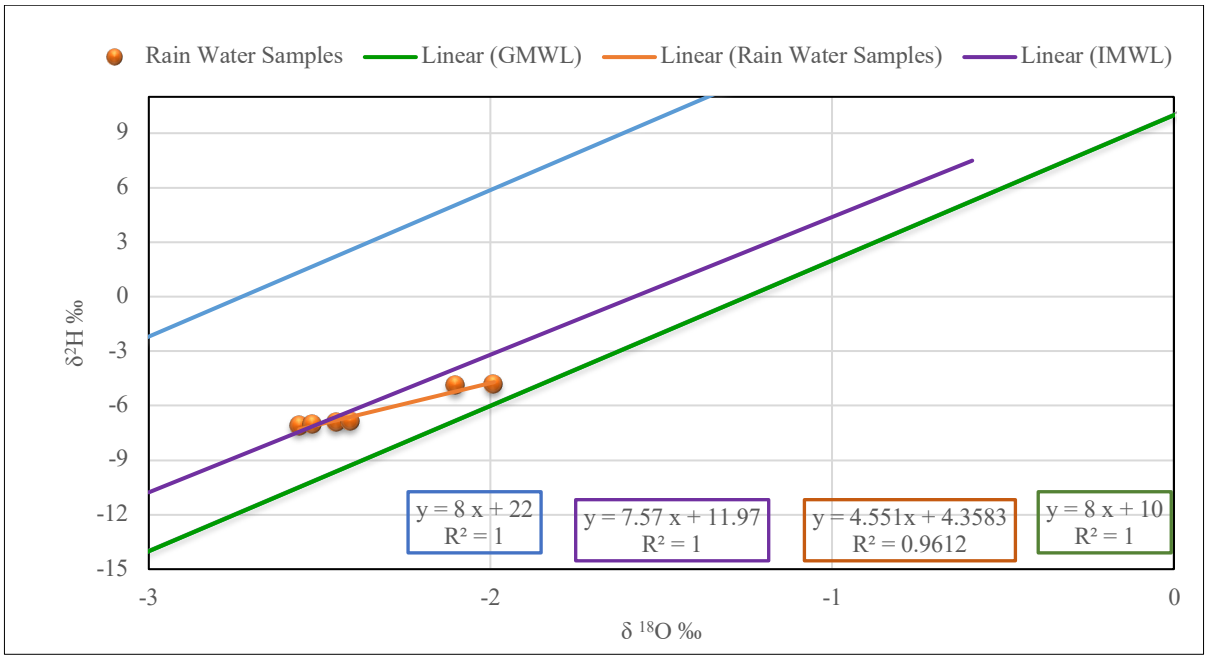

Fig. 2. NMWL of rainwater samples with GMWL, Eastern Mediterranean Meteoric Water Line (EMWL) and Iraqi Meteoric Water Line (IMWL)

The enrichment of stable isotopes can increase along with the increasing temperature degrees (Positive relationship) (Clark & Fritz, 1997). Furthermore, the variations of the values of $\delta^{18}O$ and $\delta^{2}H$ can be attributed to the passage of air mass from the Mediterranean Sea loaded with humidity to affect the line slope (Kattan, 1997). The NMWL was shifted to the GMWL and approached IMWL due to the influence of Mediterranean air masses.

All d-excess values of rainwater were less than 10.5 (Table 3). This pinpointed the source of air masses, which was not coming from the continent lands (Figure 3). The Mediterranean region is characterized by a relatively low humidity and distinctive vapor formation conditions (Gat & Carmi, 1970).

Figures 4 and 5 show the positions and distribution of $\delta^{18}O$ and $\delta^{2}H$ of wells respectively, and the interpolations of enrichment of $\delta^{18}O$ and $\delta^{2}H$ within the study area respectively.

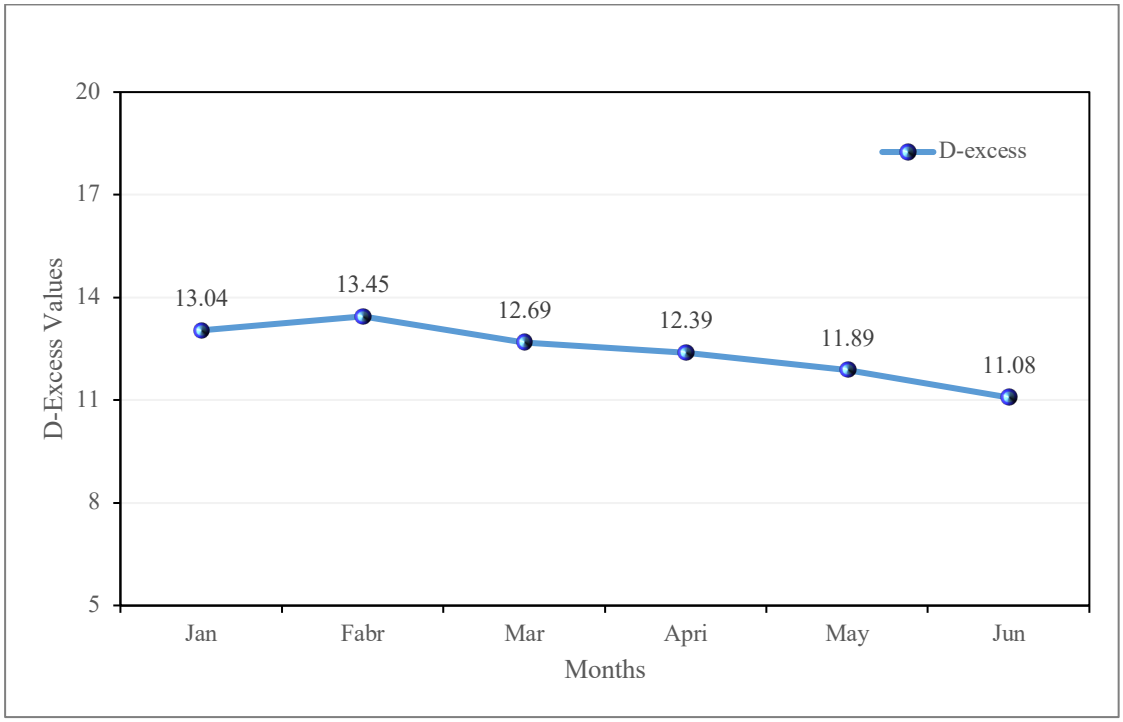

Fig. 3. D-excess variation versus monthly precipitation

Groundwater stable isotope values were compared with GMWL, IMWL and NMWL (Figure 6) where the slope and the regression interception line of groundwater was: $\delta^{2}H= 9.09\ \delta^{18}O+ 2.305‰$.

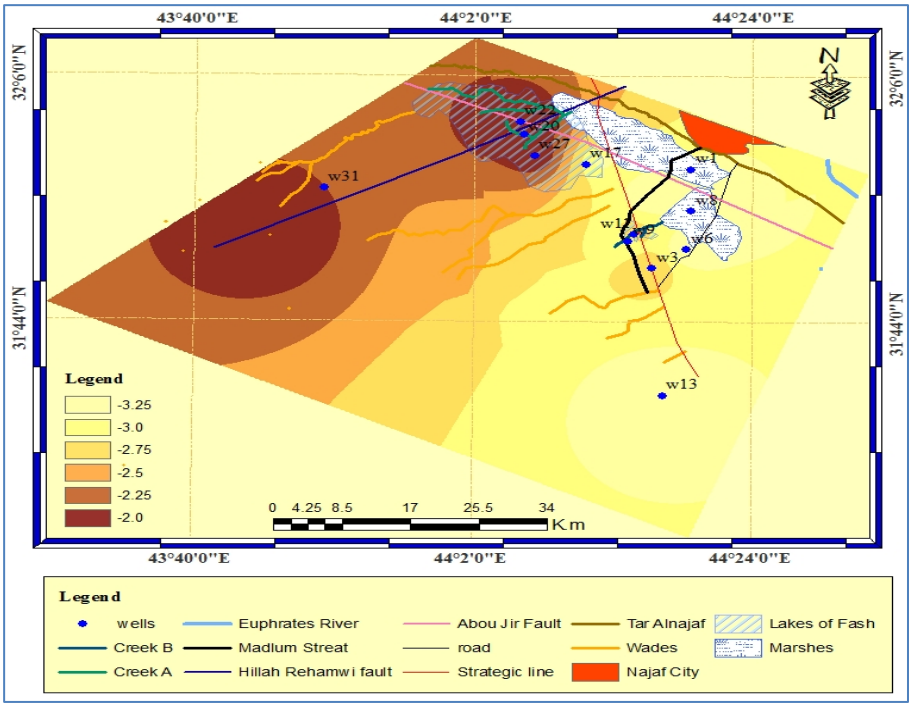

Fig. 4. Stable isotopes wells positions and the interpolations of enrichment for $\delta^{18}O‰$

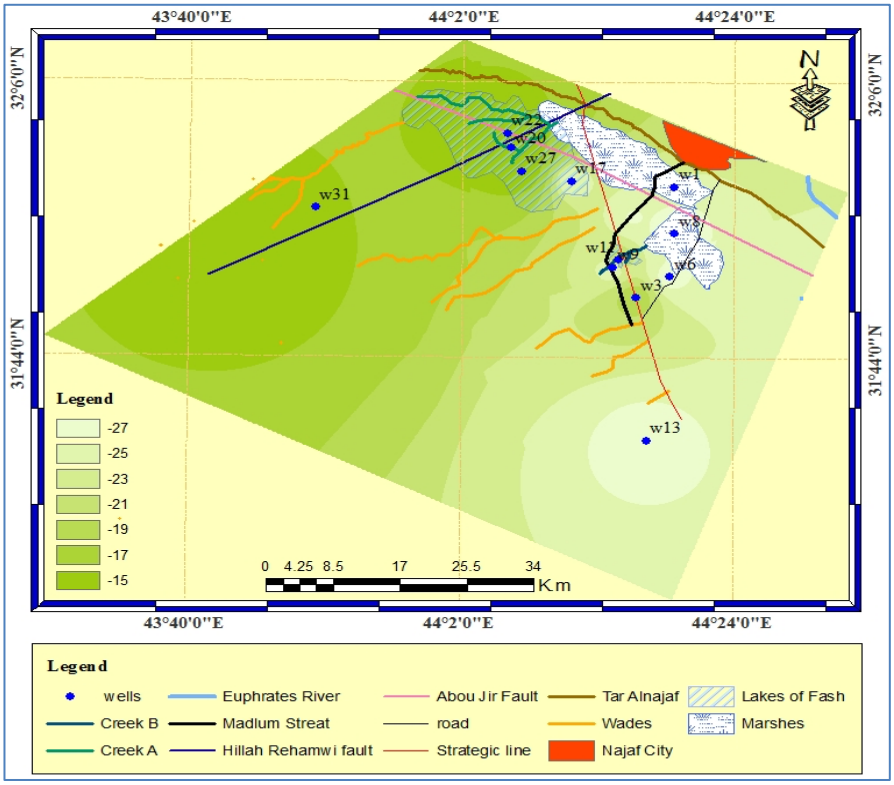

Fig. 5. Stable isotopes and the interpolations of enrichment for δ^2H‰

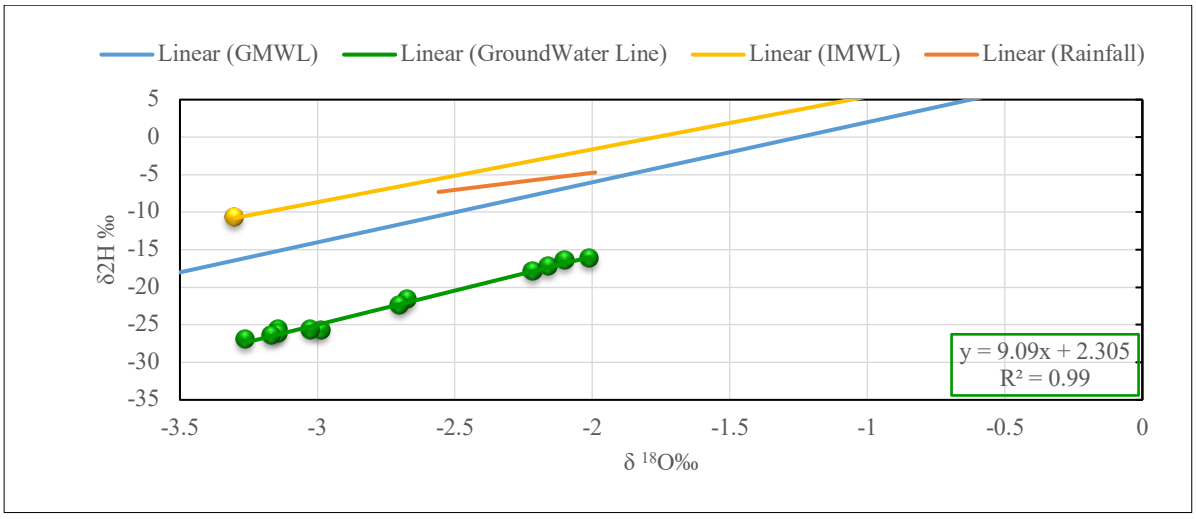

Fig. 6. δ^2H and $\delta^{18}O$ relation of groundwater samples compared to the GMWL and the IMWL

The source and evolution process of groundwater in a specific location can be determined based on the groundwater's relationship with hydrogen and oxygen isotopes in meteoric water (Liu & Yamanaka, 2012).

All groundwater samples were located beneath the three lines IMWL, GMWL and NMWL. This indicated that there was no intermixing between them recently. Consequently, the results suggested that the groundwater came from higher regions. In addition, the $\delta^{18}O$ and δ^2H depletion in the groundwater referred to a humid, cold climate and a high amount of rainfall in the past. Therefore, the values of $\delta^{18}O$ and δ^2H in the groundwater samples were significant as being lower than the values of $\delta^{18}O$ and δ^2H in the rainwater samples due to the natural

evaporation and variation of stable isotope content in the rainwater. Based on the distribution positions of data points of δ^2H and $\delta^{18}O$ diagram, three groups were distinguished from stable isotope components (Table 6 and Figure 7).

Table 6. Mean values of $\delta^{18}O$ and δ^2H for groundwater groups

Groups	$\delta^{18}O‰$			$\delta^2H‰$		
	Min	Max	Average	Min	Max	Average
Group A	-3.26	-2.99	-3.12	-27.00	-25.65	-26.18
Group B	-2.70	-2.67	-2.69	-22.42	-21.64	-22.03
Group C	-2.22	-2.01	-2.12	-17.91	-16.21	-16.98

Group A included six groundwater samples with a ratio of 50%, withdrawn from wells W.1, W.6, W.8, W.9, W.13, W.17 (Figure 8).

Group B contained two samples of groundwater with a ratio of 16.60%, within wells W.3 and W.11. Group C had four samples with a ratio of 33.33%, within wells W.20, W.22, W.27, and W.30. As a result, these groups created a movement of groundwater from the west and southwest to north and northeast affected by the regional Abu-Jir fault. Notable changes between $\delta^{18}O$ and Ec (Figure 9) were detected, where the salinity origin resulted from the dissolution processes. This revealed that a groundwater-confined aquifer did not witness a mixing with modern water recently. As a consequence, this was an indicator of very old age. The age corrections of ^{14}C in the studied samples based on radioactive decay (t) was carried out by using the equation (3) (Kalin, 2000):

$$t = -8267 \times ln\,(at^{14}C/ao^{14}C) \quad (3)$$

Where: $a_t{}^{14}C$: the measured value of (pMC), a_o ^{14}C: initial activity (100%).

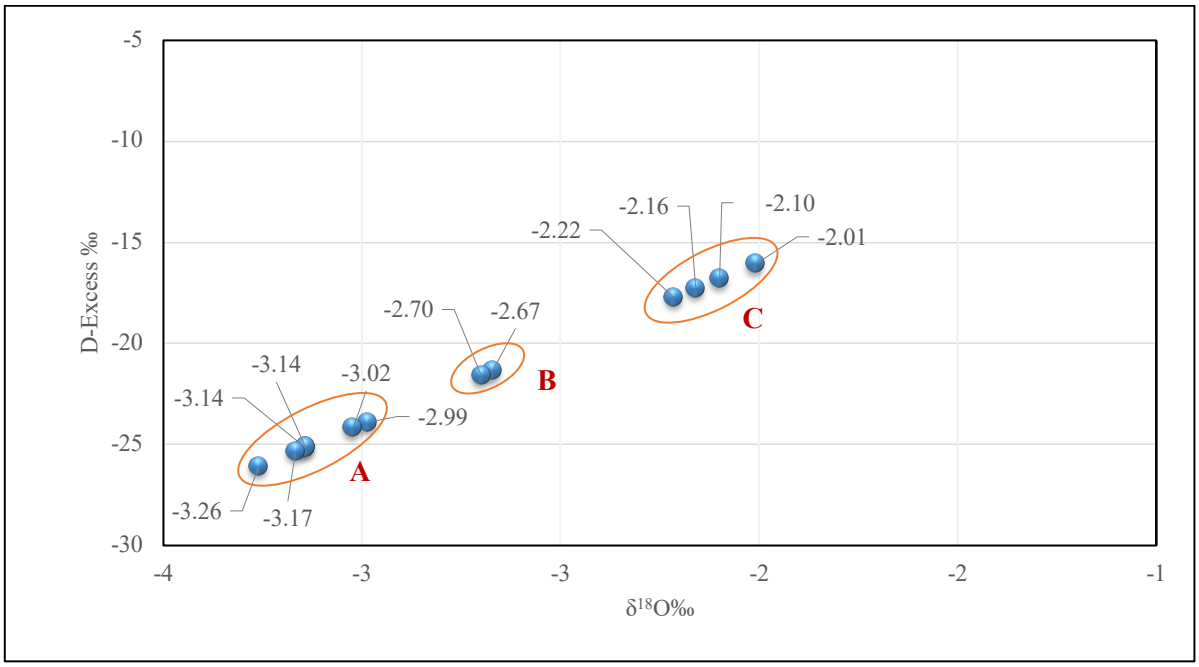

Fig. 7. Groundwater groups depending on $\delta^{18}O$ and δ^2H diagram

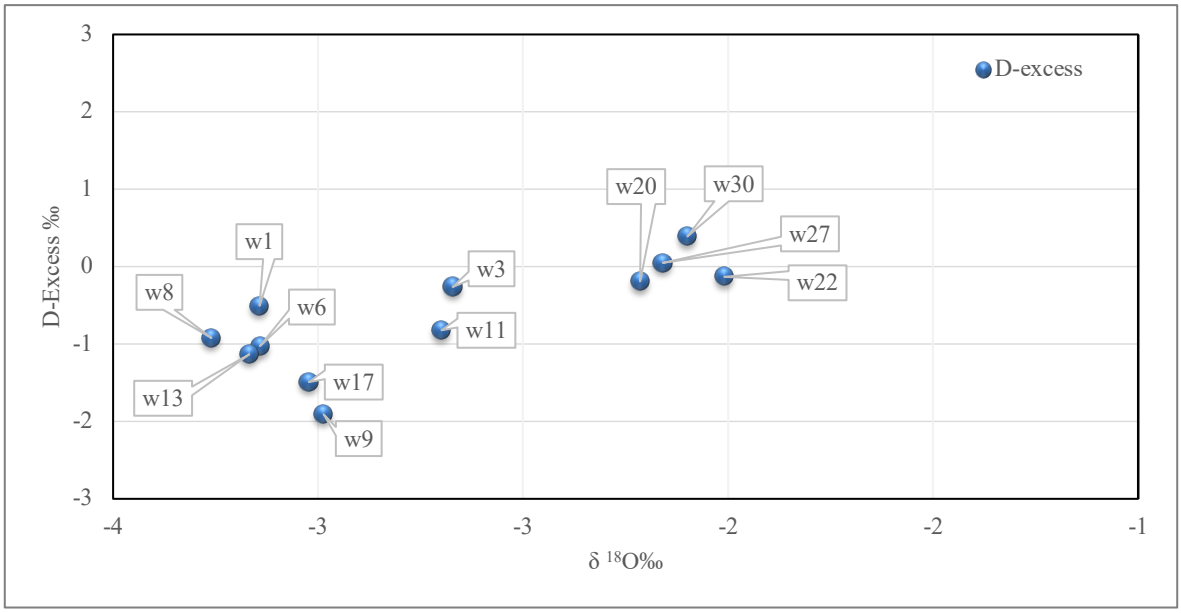

Fig. 8. Relationship between d-excess and $\delta^{18}O‰$ in the groundwater samples

The correction of the $\delta\,^{14}C$ age, and the carbonate dissolutions was fulfilled by using ^{13}C mixing model which must be accounted for to get q (corrections of carbonate dissolution) equation (4) (Pearson & Hanshaw, 1970):

$$q = (\delta^{13}C_{DIC} - \delta^{13}C_{carb})/(\delta^{13}C_{soil} - \delta^{13}C_{carb}) \quad (4)$$

Where: $\delta^{13}C_{DIC}$: measured ^{13}C in the groundwater (DIC). $\delta^{13}C_{soil}$: $\delta^{13}C$ of the soil CO_2 (usually close to -20‰). $\delta^{13}C_{carb}$: $\delta^{13}C$ of the carbonate dissolution (usually close to 0.0‰). The results pointed to the average residence time of groundwater that had come up to 4176 years (Table 7).

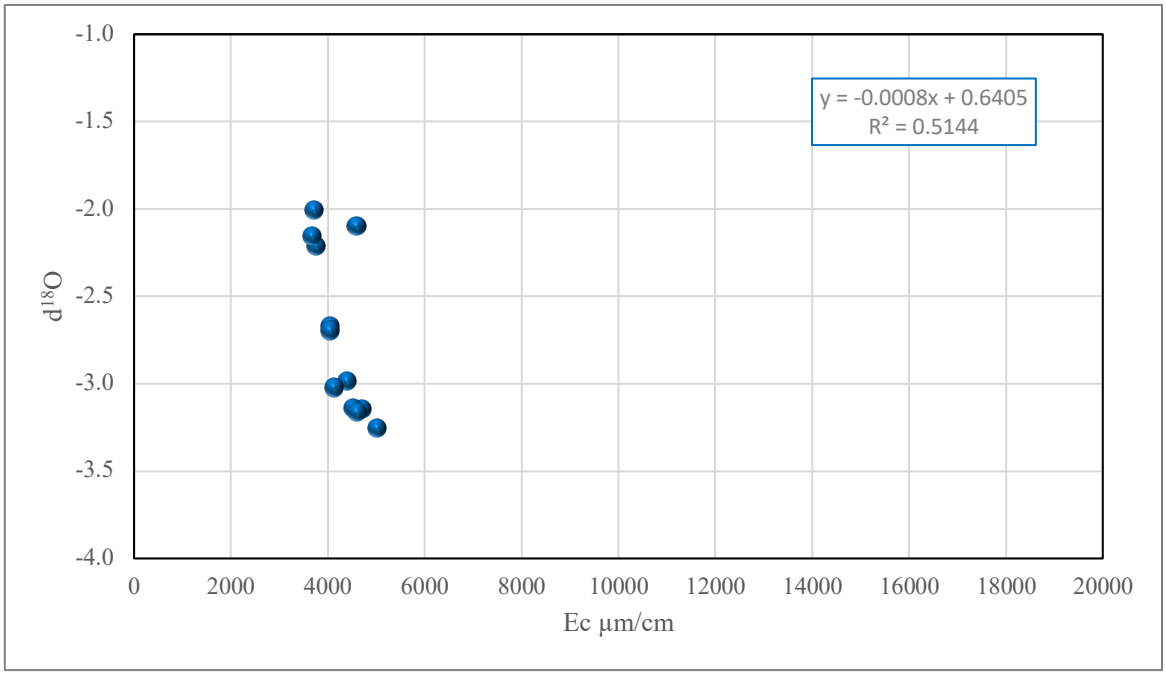

Fig. 9. Relationship between mean δ^{18} O with Ec

Table 7. Groundwater samples ages

No.	Well no.	pMC	t. year
1	W.1	50	5726
2	W.22	70	3603
3	W.12	60	4877
4	W.39	80	2498
Average		-	4176

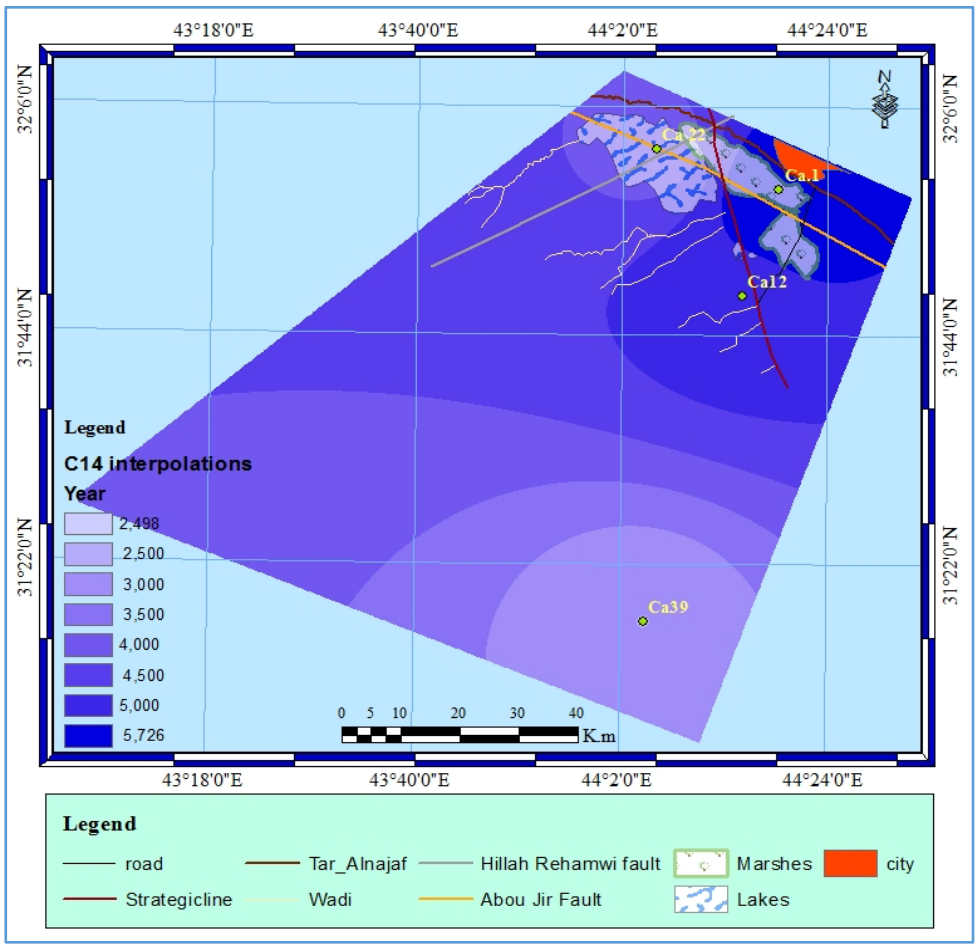

Fig. 10. Groundwater distribution of age

A contrast in groundwater ages was observed, depending on the sites of sampling ^{14}C, where the well W.39 contained a groundwater age reaching to 2498 years. It could have an age of less than the age of other samples in the study area, due to its location at the beginning of recharging area (Figure 10).

Well W.1 contained a ground water aging 5726 years due to its location in a confined aquifer as being far from the recharging area, and because of its location in the west of the Abu-Jir fault. Well W.22 contained a water age of 3602 years, due to its location in the high discharging zone (flowing well with high discharge), being distinguished by fractures facilitating the renewal of the water process where the increased pumping can increase the proportion of modern contribution (Clark & Fritz, 1997).

6. Conclusions

The stable isotope composition of rainwater indicated that the lowest values were measured in January and the highest value was in June. The values were recorded between -2.56‰ and -1.99‰ and between 7.12‰ and -4.84‰ for $\delta^{18}O$ and ^{2}H respectively, with an average of -2.32‰ and -6.20‰ respectively.

The linear equation of the NMWL was $\delta^{2}H= 4.5\ \delta^{18}O+ 4.32$ with a slope of 4.5. It reflected the enrichment process of the isotope composition due to the fractionation process. The NMWL was governed by the local climate factors. The sources of air masses were not coming from continental lands, depending on d-excess values (less than 10.5).

Groundwater stable isotope composition samples of the Dammam aquifer ranged between -3.26‰ and -2.01‰ of $\delta^{18}O$ and between -27.00‰ and -16.21‰ of $\delta^{2}H$ with an average of -2.70‰ and -22.27‰ respectively. The slope and the interception of the regression line of groundwater was $\delta^{2}H= 9.09\delta^{18}O+ 2.305$‰.

All samples of groundwater were located beneath the two lines GMWL and NMWL, and they did not match with the precipitation line NMWL. However, NMWL located above the line of GMWL indicated that there was not an intermixing between them recently. The results indicated that the groundwater was imported from a high elevation above the sea level with a more altitude than its current location. Furthermore, the depletion of $\delta^{18}O$ and $\delta^{2}H$ in the groundwater reflected a humid and cold climate and a high amount of rainfall in the past.

Based on the distribution of data point positions for the $\delta^{2}H$ and $\delta^{18}O$ diagram, three groups were distinguished from the stable isotope components of groundwater. They were: Group A, Group B and Group C. The relationship between $\delta^{18}O$ and Ec showed that the origin of salinity resulted from processes of dissolution.

The age of groundwater was determined via an existing ratio of ^{14}C in the groundwater of the study area. The mean age of groundwater was approximately 4176 years. The groundwater movement reflected that there was a difference in the age of groundwater of many places in the study area.

ACKNOWLEDGEMENTS

The authors are very grateful to the Department of Water Analysis staff/ Ministry of Science and Technology/ Iraq and General Commission for Groundwater/ Department of Najaf for their invaluable help.

Reference

Aladwani, N.S. (2022) Qualitative and quantitative analysis of the crust base structure using Kuwait gravity anomaly maps in the determination of new oil fields. Kuwait Journal Science, 49(2):1-16.

Al-Enezy, A.W. (2019) Hydrochemical, hydrogeological and isotopic investigation of groundwater in Dammam Aquifer at Southern Desert, West of Najaf Governorate. Ph.D. thesis, Collage of Science, University of Basrah, Iraq.

Al-Owaidi, M.R.A., Al-Enezy A.W.A. & Hussein M.L. (2021) Hydrogeochemical properties and the exhaustion groundwater reserve from Dammam aquifer at Al-Najaf Governorate, middle Iraq. Journal of Physics: Conference Series, IOP Publishing. Doi:10.1088/1742-6596/1999/1/012158

Al-Ruwaih, F.M. (1993) Studies of groundwater chemistry of the A1-Shagaya Field-D, Kuwait. Kuwait Journal of Science, 20(1): 127-143.

Buday, T. (1980) The Regional geology of Iraq, Stratigraphy and Paleogeography. Dar Al-Kutib Publication House, University of Mosul Pp. 445.

Clark, I., & Fritz, P. (1997) Environmental isotopes in hydrogeology. CRC Press Taylor & Francis Group, New York Pp. 343.

Durowoju, O.S., Odiyo, J.O. & Ekosse, G.E. (2019) Determination of isotopic composition of rainwater to generate local meteoric water line in Thohoyandou, Limpopo Province, South Africa. Water SA: 45(**2**):183-189.

Faucher, B.; Lacelle, D.; Fisher, D.A.; Weisleitner, K. & Andersen, D.T. 2020. Modeling δ^2H-$\delta^{18}O$ Steady-State of Well-Sealed Perennially Ice-Covered Lakes and Their Recharge Source: Examples from Lake Untersee and Lake Vostok, Antarctica. Frontiers in Earth Science, 8: 220. https://doi.org/10.3389/feart.2020.00220

Faure, G. & Mensing, T.M. (2005) Isotopes: Principles and applications, 3rd ed. John Wiley & Sons, USA Pp. 897.

Fetter, G.W. (2001) Applied Hydrology, 4th ed. New Jersey, Prentice Hall, Pp. 320.

Gat, J. R. & Carmi, I. (1970) Evolution of the isotopic composition of atmospheric waters in the Mediterranean Sea area. Journal of Geophysical Research, 75(15): 3039-3048. https://doi.org/10.1029/JC075i015p03039

Geyer, S., Wolf, M., Wassenaar, L.I. & Fritz, P. (1993) Isotope investigations on fractions of dissolved organic carbon for ^{14}C groundwater dating p. 359-380, In Isotope techniques in the study of past and current environmental changes in the hydrosphere and the atmosphere. International Atomic Energy Agency (IAEA), Vienna (Austria); Proceedings series; Pp. 623.

Godwin, H. (1962) Half-life of radiocarbon. Nature 195 – 984.

IAEA (2001) GNIP Maps and Animations, International Atomic Energy Agency, Vienna. Accessible at http://isohis.iaea.org

IAEA (2009) Global Network of isotopes in precipitation, the GNIP Database Accessible http://isohis.iaea.org

Izbicki, J.A., Wesley, R.D. & Mendez. O.G. (1998) Chemistry and isotopes composition of groundwater along a near Newmark Area, San Bernardino, California. Water-Resources Investigations Report 97-4179 U.S. Geological Survey. 32 P.

Jassim, S.Z. & Goff, J.C. 2006. Geology of Iraq. Dolin, Prague and Moravian Museum, Brno, 431 p.

Kalin, R.M. (2000) Radiocarbon dating of groundwater systems: in Cook, P.G. and Herczeg, A.L., eds., Environmental Tracers in Subsurface Hydrology: Kluwer Academic Publishers, p. 111-144.

Kattan, Z. (1997) Chemical and isotopes study of precipitation in Syria. Journal of arid Environments, 35(4): 601-615.

Kendall, C. & Caldwell, E.A. (1998) Fundamentals of isotope geochemistry, In: Kendall C., and McDonnell J.J. (Eds.), Isotope tracers in catchment hydrology, Elsevier Science, Amsterdam, PP. 51-86.

Liu, Y. & Yamanaka, T. (2012) Tracing groundwater recharge sources in a mountain–plain transitional area using stable isotopes and hydrochemistry. Journal of Hydrology, 464–465: 116–126. https://doi.org/10.1016/j.jhydrol.2012.06.053

Mook, W.G. (2000) Environmental isotopes in the hydrological cycle; principles and applications, Vol. 2. International Atomic Energy Agency, Vienna, 122 P.

Pearson, F.J. & Hanshaw, B.B. (1970) Sources of dissolved carbonate species in groundwater and their effects on carbon-14 dating; In: Isotope Hydrology, 1970, Vienna, IAEA; 271-286.

Sebastian, F.M., Jess, F., Hanno, M. & Marwan, N. (2010) Strong influence at water vapor source dynamic on stable isotopes in precipitation observed in south Meghalaya, India. Earth and planetary science letters, 292(1): 212-220.

Tsujimura, M., Abe Y., Tanaka T., Shimada J., Higuchi S., Yamanaka T., Davaa G. & Oyunbaatar D. (2007) Stable isotopic and geochemical characteristics of groundwater in Kherlen River basin, a semi-arid region in eastern Mongolia. Journal of Hydrology, 333(1):47-57.

Wilopo, W. & Putra, D.P.E. (2021) Groundwater Fluctuation Patterns and Groundwater Recharge Estimation in Unconfined Aquifer of Yogyakarta City, Indonesia. Kuwait Journal of Science, 48(2):1-11.

Submitted: 09/11/2021
Revised: 20/04/2022
Accepted: 21/04/2022
DOI: 10.48129/kjs.17107